SHAPE MEMORY ALLOYS FOR VIBRATION ISOLATION AND DAMPING

A Dissertation

by

LUCIANO G. MACHADO

Submitted to the Office of Graduate Studies of
Texas A&M University
in partial fulfillment of the requirements for the degree of

DOCTOR OF PHILOSOPHY

December 2007

Major Subject: Aerospace Engineering

SHAPE MEMORY ALLOYS FOR VIBRATION ISOLATION AND DAMPING

A Dissertation

by

LUCIANO G. MACHADO

Submitted to the Office of Graduate Studies of
Texas A&M University
in partial fulfillment of the requirements for the degree of

DOCTOR OF PHILOSOPHY

Approved by:

Chair of Committee,	Dimitris C. Lagoudas
Committee members,	James Boyd
	Johnny Hurtado
	Tamás Kalmár-Nagy
	Alan Palazzolo
Head of Department,	Helen L. Reed

December 2007

Major Subject: Aerospace Engineering

ABSTRACT

Shape Memory Alloys for Vibration Isolation and Damping. (December 2007)
Luciano G. Machado, B.S., Federal Center of Technological Education of Rio de
Janeiro - RJ, Brazil; M.S., Military Institute of Engineering - RJ, Brazil;
Chair of Advisory Committee: Dr. Dimitris C. Lagoudas

This work investigates the use of shape memory alloys (SMAs) for vibration isolation and damping of mechanical systems. The first part of this work evaluates the nonlinear dynamics of a passive vibration isolation and damping (PVID) device through numerical simulations and experimental correlations. The device, a mass connected to a frame through two SMA wires, is subjected to a series of continuous acceleration functions in the form of a sine sweep. Frequency responses and transmissibility of the device as well as temperature variations of the SMA wires are analyzed for the case where the SMA wires are pre-strained at 4.0% of their original length. Numerical simulations of a one-degree of freedom (1-DOF) SMA oscillator are also conducted to corroborate the experimental results. The configuration of the SMA oscillator is based on the PVID device. A modified version of the constitutive model proposed by Boyd and Lagoudas, which considers the thermomechanical coupling, is used to predict the behavior of the SMA elements of the oscillator.

The second part of this work numerically investigates chaotic responses of a 1-DOF SMA oscillator composed of a mass and a SMA element. The restitution force of the oscillator is provided by an SMA element described by a rate-independent, hysteretic, thermomechanical constitutive model. This model, which is a new version of the model presented in the first part of this work, allows smooth transitions between the austenitic and the martensitic phases. Chaotic responses of the SMA oscillator are evaluated through the estimation of the Lyapunov exponents. The Lyapunov exponent estimation of the SMA system is done by adapting the algorithm by Wolf and co-workers. The main issue of using this algorithm for nonlinear, rate-independent, hysteretic systems is related to the procedure of linearization of the equations of motion. The present work establishes a procedure of linearization that allows the use of the classical algorithm. Two different modeling cases are considered for isothermal and non-isothermal heat transfer conditions. The evaluation of the Lyapunov exponents shows that the proposed procedure is capable of quantifying chaos in rate-independent, hysteretic dynamical systems.

To my grandfather José Pedro Filho, for his 100^{th} birthday, and to my family.

ACKNOWLEDGMENTS

I would first and foremost like to thank Jesus and all my spiritual masters and friends for all the help that I received during my life, specially during my graduate studies.

I wish to express my gratitude to Dr. Dimitris Lagoudas, my advisor and chair of my Ph.D. advisory committee, for his guidance and support throughout the development of this research work. I appreciate all the classes, technical discussions, conferences and professional meetings that I had the opportunity to attend and interact with him. I have learnt a great deal from him and I am grateful.

I would like also to express my thanks to my advisory committee: Dr. James Boyd, Dr. John Hurtado, and Dr. Alan Palazzolo. All of them have greatly contributed to my academic and professional formation. I really enjoyed attending their courses and working with them during the development of my research work. I also want to thank Dr. Suman Chakvorty for substituting as a committee member durring my thesis defense.

I would like to express my sincere thanks to Dr. Marcelo Savi for helping me during my Master of Science degree program and during the development of my Ph.D. dissertation. He has always been a role model for me as a great researcher and great friend.

I have been very lucky and fortunate to work with my colleges and friends Gary Seidel, Bjoern Kiefer, Peter Popov, Darren Hartl and Parikshith Kumar. They have certainly contributed to the development of my Ph.D. dissertation and to my professional growth. I am also grateful for the interactions on both personal and professional levels that I had with my colleagues and friends Piyush Tahkre, Khrishnendu Haldar, Pam McConal, Rodney Inmon, Andrew Sinclair and Lesley Weitz.

On a personal level I want to thank my beloved wife, Rosane, my parents, Gilberto and Tarcilia, and my brother, Renato, for their support with prayers and words of encouragement in all the steps of my life. They have always been my foundation. I am sure that it would have been impossible for me to receive my Ph.D. degree without their support and love.

Also on a personal level I would like to thank all the help and support that I have received from the Brazilian community in College Station. A special thanks are also due to Marcel and Katia Amstalden, Luis and Marcia de Ávila, Claudine de Bona, Arley Prado, Jairo Nunes, Josely Figueiredo, Gilvan Yogui, Paulo Fortes, Carmen Gomes, Georgia Barros and Cassia Marchon. They have been my family here in the US.

Finally, I would like to acknowledge my home country Brazil for the financial support that allowed me to come to the USA and pursue my Ph.D. degree for four years. I would also like to acknowledge the financial support of USAFOSR.

TABLE OF CONTENTS

CHAPTER Page

I INTRODUCTION 1

- A. General Aspects of Shape Memory Alloys 1
  - 1. Phenomenology of Phase Transformation in SMAs . . 2
  - 2. Shape Memory Effect 6
  - 3. Pseudoelasticity 7
- B. Literature Review on Thermomechanical Constitutive Models for SMAs 10
- C. Literature Review on SMAs (Nonlinear) Dynamical Systems 15
- D. Outline of the Present Research 19

II CONTINUUM DESCRIPTION OF SHAPE MEMORY ALLOYS 22

- A. Kinematics of SMAs 22
- B. Conservation (Balance) Laws 23
  - 1. Conservation of Mass 24
  - 2. Conservation of Linear Momentum 25
  - 3. Conservation of Angular Momentum 26
  - 4. Conservation of Energy 26
  - 5. Entropy Inequality - Second Law of Thermodynamics 27
- C. Need for Constitutive Equations 28
- D. Constitutive Equations 29
  - 1. Constitutive Assumptions for SMAs 32

III THERMOMECHANICAL CONSTITUTIVE MODEL FOR SMAS 35

- A. Choice of Internal State Variables 35
- B. Kinematic Assumptions 36
- C. Constitutive Assumptions for the SMA Material 36
  - 1. Evolution of Internal State Variables and Kuhn-Tucker Conditions 38
- D. One-dimensional Reduction and Identification of the Material Parameters 43
- E. Closed-Form Solutions 49

CHAPTER Page

IV THERMOMECHANICAL COUPLING IN SHAPE MEMORY ALLOYS 54

  1. Adiabatic Conditions 56
  2. Non-isothermal Conditions 57

 A. Characterization of SMA Elements for Different Heat Transfer Processes and One-dimensional Reduction of the Model 60
  1. 1-D Reduction of the Model 61
  2. Material Parameter Characterization and Model Parameter Calibration 62
  3. Closed-Form Solutions for Adiabatic and Non-Isothermal Conditions 63

V NUMERICAL IMPLEMENTATION OF THE CONSTITUTIVE MODEL 65

 A. Review of Important Equations 67
 B. Return Mapping Algorithm 69
  1. Closest Point Projection Return Mapping Algorithm - I 69
   a. Thermoelastic Prediction 71
   b. Transformation Correction 72
  2. Closest Point Projection Return Mapping Algorithm - II 77
   a. Thermoelastic Prediction 80
   b. Transformation Correction 81
 C. Numerical Simulations of the Constitutive Model Using Return Mapping Algorithm 88
  1. Comparison of Return Mapping Algorithm Implementations 88
  2. Comparison of Tensile Test on a SMA Wire with Numerical Simulations 94
  3. Investigation of the Stress-Relaxation Phenomenon on SMAs 96
  4. Numerical Simulations: Different Strain Rates and Stress Relaxation Test 99

VI NONLINEAR DYNAMICS OF A PASSIVE VIBRATION ISOLATION AND DAMPING DEVICE 103

CHAPTER Page

A. Experimental Investigation 103
  1. Material Parameter Characterization 105
  2. Experimental Vibration Test 106
B. Numerical Simulations of a Passive Vibration Isolation SMA Device 115
  1. One-Degree of Freedom Shape Memory Alloy Oscillator 115
  2. Constitutive Model for SMAs 117
  3. Material Characterization and Numerical Implementation of the Model 119
C. Comparison of Experimental Results with Numerical Simulations 121

VII CONSTITUTIVE MODEL FOR POLYCRYSTALLINE SHAPE MEMORY ALLOYS WITH SMOOTH TRANSFORMATION HARDENING 130

A. Thermomechanical Constitutive Model for SMA 131
  1. Basic Equations 131
  2. Hardening Function 135
B. One-dimensional Reduction and Identification of the Material Parameters 139
C. Numerical Implementation and Numerical Evaluation of the Transformation Hardening Function 146
D. Comparison with Experimental Tests 148
E. Comparison of the Current Model's Predictions with Calorimetric Results 149

VIII CHAOTIC VIBRATION OF A ONE-DEGREE OF FREEDOM SHAPE MEMORY OSCILLATOR 157

A. Single-Degree of Freedom Hysteretic Oscillator 158
  1. Constitutive Model for Polycrystalline SMAs with Smooth Transformation Hardening 160
B. Numerical Implementation of the Constitutive Model and Integration of the Equations of Motion 166
C. Numerical Simulations 168
  1. Free Vibration 169
  2. Forced Vibrations 170
    a. Forced Vibration - Isothermal Conditions 170
    b. Forced Vibrations - Non-Isothermal Conditions . 172

CHAPTER Page

D. Lyapunov Exponents 174
  1. Linearization Process of a SMA Dynamical Hysteretic System 175
  2. Equivalent Viscous Damping 178
  3. Lyapunov Exponents Estimation 180
    a. Forced Vibrations - Isothermal Conditions 180
    b. Forced Vibrations - Non-Isothermal Conditions . 181

IX CONCLUSIONS AND FUTURE WORK 192

REFERENCES 197

VITA 209

LIST OF TABLES

TABLE Page

I Need for constitutive equations 29

II Thermodynamic potentials 31

III Definitions of the model parameters of Boyd and Lagoudas model . . 43

IV Values of the material parameters of a typical SMA wire 51

V Closest point projection implicit return mapping algorithm-I 78

VI Closest point projection implicit return mapping algorithm-II 89

VII Values of a SMA material parameters used on the comparison of the return mapping algorithms 93

VIII Values of the material parameters of the SMA wires used on the passive vibration isolation and damping device 108

IX Values of material parameters typical of the SMA wire used to calibrate the constitutive model with smooth hardening transitions . 146

X Definition of the model parameters of the constitutive model with smooth hardening transitions 146

XI Values of material parameters of the SMA specimen used to calibrate the constitutive model with hardening smooth transitions for calorimetric tests 154

XII Values of material parameters of the SMA specimen used to calibrate the Boyd and Lagoudas model for calorimetric tests 154

XIII Definitions of the model parameters of the normalized constitutive model with smooth hardening transitions 168

XIV Normalized values of SMA material parameters used on the SMA oscillator 169

LIST OF FIGURES

FIGURE Page

1 Temperature-induced phase transformation of an SMA without mechanical loading (Lagoudas *et al.* [1]). 4

2 SMA phase diagram showing temperature-induced phase transformation with mechanical loading(Lagoudas *et al.* [1]). 5

3 Schematics of the SME on a SMA showing the detwinning of the material with applied stress (Lagoudas *et al.* [1]). 7

4 Schematics of the SME on a SMA showing the unloading and subsequent heating to austenite under no load condition (Lagoudas *et al.* [1]). 8

5 Schematic of stress-strain-temperature-induced exhibiting the SME for a typical NiTi SMA (Lagoudas *et al.* [1]). 9

6 Phase diagram with a possible pseudoelastic loading path (Lagoudas *et al.* [1]). 10

7 Isothermal pseudoelastic loading cycle (Lagoudas *et al.* [1]). 11

8 Experimental stress *vs.* strain curves for different temperatures (Lagoudas *et al.* [1]). 47

9 Isothermal pseudoelastic loading paths. Stress *vs.* temperature. . . . 52

10 Isothermal pseudoelastic stress *vs.* strain curves for different temperatures (Lagoudas *et al.* [1]). 52

11 Stress *vs.* temperature plot of isobaric loading paths (Lagoudas *et al.* [1]). 53

12 Strain *vs.* temperature plot of isobaric loading paths (Lagoudas *et al.* [1]). 53

13 Determination of the heat convection coefficient. 63

FIGURE Page

14 Strain *vs.* temperature and stress *vs.* plots - comparison of isothermal and adiabatic conditions (Lagoudas *et al.* [1]). 64

15 Comparison of return mapping algorithm implementations. 92

16 Comparison of an experimental tensile test performed with numerical simulations. 95

17 Comparison of stress-relaxation test at room temperature with numerical simulations. 97

18 Comparison of stress-relaxation test at room temperature - isothermal and non-isothermal loading paths. 101

19 Simulation of uniaxial loading / unloading tests of a SMA wire for different strain rate inputs. 102

20 SMA passive vibration isolation and damping device. 104

21 Modes of vibration of the device. 105

22 Stress-Strain curves of the pseudoelastic SMA wires used on the experimental vibration test. 107

23 Transmissibility curves for the up and down sine sweep tests at the temperature of T=25 °C. 110

24 Transmissibility curve for 1g and 2g up and down sine sweep test at the temperature of T=25 °C. 112

25 Temperature variation of the SMA wires for up and down sine sweep tests. 114

26 One-degree of freedom SMA oscillator. 116

27 Comparison of experimental and numerical transmissibility curve and temperature variation for up sine sweep test with acceleration amplitude of 1.0g. 122

28 Comparison of experimental and numerical transmissibility curve and temperature variation for up sine sweep test with acceleration amplitude of 2.0g. 126

FIGURE Page

29 Comparison of experimental and numerical transmissibility curve and temperature variation, for down sine sweep test with acceleration amplitude of 1.0g. 127

30 Comparison of experimental and numerical transmissibility curve and temperature variation for down sine sweep test with acceleration amplitude of 2.0g. 128

31 Analysis of the numerical transmissibility curve for down sine sweep test with acceleration amplitude of 2.0g. 129

32 Stress-strain curves of the current model: smooth transitions between the phases. 140

33 Stress-strain curves of current model, at different temperatures. . . . 144

34 Comparison of current model (dark lines) with experimental results (light lines). Stress *vs.* strain curves at temperatures of T=313K, T=303K, and T=298K. 150

35 Comparison of experimental results with Boyd and Lagoudas and current model. 151

36 Comparison of the quadratic polynomial model with experimental DSC results. 155

37 Comparison of current model with experimental DSC results. 156

38 Single-degree of freedom hysteretic oscillator. 158

39 Stress *vs.* strain and temperature *vs.* time curves: comparison of isothermal, non-isothermal and adiabatic cases. 170

40 Free response of the SMA oscillator: stress *vs.* strain and phase portrait curves. 171

41 Bifurcation diagram for isothermal conditions. 171

42 Forced response of the SMA oscillator for $\hat{F} = 0.008$ and $\hat{\omega} = 0.356$, isothermal conditions. 183

FIGURE Page

43 Forced response of the SMA oscillator for $\hat{F} = 0.008$ and $\hat{\omega} = 0.397$Hz, isothermal conditions. 184

44 Bifurcation diagram for non-isothermal conditions. 185

45 Forced response of the SMA oscillator for $\hat{F} = 0.008$ and $\hat{\omega} = 0.356$. . 186

46 Forced response of the SMA oscillator for $\hat{F} = 0.008$ and $\hat{\omega} = 0.397$. . 187

47 Bifurcation diagrams, non-isothermal conditions. 188

48 Lyapunov exponents. 189

49 Lyapunov exponents calculation. 189

50 Lyapunov exponents for $\hat{F} = 0.008$ and $\hat{\omega} = 0.356$ and $\hat{\omega} = 0.397$, isothermal conditions. 190

51 Lyapunov exponents and bifurcation diagrams for the case of isothermal conditions. 190

52 Lyapunov exponents for $\hat{F} = 0.008$ and $\hat{\omega} = 0.356$ and $\hat{\omega} = 0.397$, non-isothermal conditions. 191

53 Bifurcation diagram with Lyapunov exponents for the case of non-isothermal conditions. 191

NOMENCLATURE

β	Scalar parameter used in the general trapezoidal rule
$\mathbf{a}$	Arbitrary vector
$\boldsymbol{\alpha}$	Effective thermal expansion coefficient tensor
$\boldsymbol{\alpha}^A$	Thermal expansion coefficient tensor of austenitic phase
$\boldsymbol{\alpha}^M$	Thermal expansion coefficient tensor of martensitic phase
$\mathbf{b}$	Body force vector
$\boldsymbol{\mathcal{S}}$	Effective compliance fourth-order tensor
$\mathbf{E}$	Green-Lagrange strain tensor
$\boldsymbol{\varepsilon}$	Infinitesimal strain tensor
$\boldsymbol{\varepsilon}^d$	Infinitesimal strain tensor generated during the detwinning process
$\boldsymbol{\varepsilon}^{in}$	Infinitesimal inelastic strain tensor
$\boldsymbol{\varepsilon}^p$	Infinitesimal plastic strain tensor
$\boldsymbol{\varepsilon}^{t-r}$	Transformation strain at the reversal of phase transformation
$\boldsymbol{\varepsilon}^{th}$	Infinitesimal thermoelastic strain tensor
$\boldsymbol{\varepsilon}^t$	Transformation strain tensor
$\mathbf{g}$	Thermal gradient vector
$\mathbf{n}$	Unit normal vector

$\boldsymbol{\nabla}$	Gradient vector operator
$\mathbf{q}$	Heat flux vector
$\mathbf{r}$	Position vector
$\boldsymbol{\sigma}$	Cauchy stress tensor
$\boldsymbol{\sigma}'$	Deviatoric stress tensor
$\mathbf{u}$	Displacement vector
$\mathbf{v}$	Velocity of a material point
$\boldsymbol{\zeta}$	Internal state variable vector
Δ	Denotes difference in fields between phases
δ_L	Lower wire displacement
δ_U	Upper wire displacement
$\hbar$	Enthalpy
$\boldsymbol{\Lambda}$	Transformation tensor
Ω	Region occupied by an SMA body
μ_1	Model parameter for Boyd and Lagoudas model
μ_2	Model parameter for Boyd and Lagoudas model
ω	Excitation circular frequency
$\partial\Omega$	Boundary surface of the region occupied by an SMA body
Φ	Transformation function

π	Thermodynamic force conjugated to ξ
ψ	Helmholtz free energy
ρb^A	Model parameter for Boyd and Lagoudas model
ρb^M	Model parameter for Boyd and Lagoudas model
ρ	Mass density
ρ^e	Electrical resistivity
σ^{Af}	Austenitic transformation finish stress at a given temperature
σ^{As}	Austenitic transformation onset stress at a given temperature
σ^{Mf}	Martensitic transformation finish stress at a given temperature
σ^{Ms}	Martensitic transformation onset stress at a given temperature
ξ	Martensitic volume fraction
A_f^σ	Austenitic finish temperature at a given stress level
A_s^σ	Austenitic start temperature at a given stress level
A_f	Austenitic finish temperature at zero stress level
A_s	Austenitic start temperature at zero stress level
c	Effective specific heat capacity
c^A	Specific heat capacity austenitic phase
c^M	Specific heat capacity of martensitic phase
E^A	Elastic modulus of austenitic phase

E^M	Elastic modulus tensor of martensitic phase
f	Hardening function
F_L^{SMA}	Force exerted by the lower wire
F_U^{SMA}	Force exerted by the upper wire
G	Gibbs free energy
g	Gravitational acceleration
H	Maximum uniaxial transformation strain
h	Heat convection coefficient
J	Magnitude of the current density
M	Mass of a SMA body
m	Mass of the oscillator
M_f^σ	Martensitic finish temperature at a given stress level
M_s^σ	Martensitic start temperature at a given stress level
M^d	Detwinned martensite
M^t	Twinned martensite
M_f	Martensitic finish temperature at zero stress level
M_s	Martensitic start temperature at zero stress level
n_1	Model parameter for constitutive model with smooth hardening transitions
n_2	Model parameter for constitutive model with smooth hardening transitions

n_3	Model parameter for constitutive model with smooth hardening transitions
n_4	Model parameter for constitutive model with smooth hardening transitions
r	Heat source supply
s	Entropy per unit mass
S^A	Compliance fourth-order tensor of austenitic phase
S^M	Compliance fourth-order tensor of martensitic phase
s_0	Effective specific entropy at reference state
s_0^A	Specific entropy austenitic phase
s_0^M	Specific entropy of martensitic phase
t	Time
T_0	Temperature at reference state
T_∞	Temperature of surrounding environment
u	Internal energy per unit mass
u_0	Effective specific internal energy at reference state
u_0^A	Specific internal energy austenitic phase
u_0^M	Specific internal energy of martensitic phase
x	Mass displacement
Y^*	Material parameter associated with internal dissipation
z	Base displacement

CHAPTER I

INTRODUCTION

A. General Aspects of Shape Memory Alloys

Shape Memory Alloys (SMAs) represent a class of materials that have the property of recovering apparent permanent strains when subjected to a proper thermomechanical path (Otsuka and Wayman [2]). The key property that drives the shape recovery is the martensitic phase transformation that takes place in the SMAs during thermal and/or mechanical loadings (Patoor *et. al* [3]). The martensitic transformation is a shear-dominant diffusionless solid-state phase transformation occurring by nucleation and growth of the (product) martensitic phase from the (parent) austenitic phase (Olson and Cohen [4], Otsuka and Ren [5]).

The SMA properties have been known since 1930s. In 1938, Greninger and Mooradian observed the shape memory effect in Cu-Zn and Cu-Sn alloys (Mandovani [6], and Hodgson *et.al* [7]). In 1951, Chang and Read experimentally observed the shape memory effect due to changes in resistivity of a Au-Cd alloy. However, only in the 1960s that SMA started to received some attention. In 1962, Buehler and coworkers [8] in the U.S. Naval Ordnance Laboratory (NOL) discovered the shape memory effect in a equi-atomic NiTi alloy while investigating materials useful for heat shielding. Still in the 1960s, Raychem Corporation developed the first SMA industrial application in the aerospace industry called Cryofit for pipe couplings in F-14 fighter aircraft (Wayman and Harrison [9]). In 1975, Andreasen, from Iowa University, made the first implant of a superelastic orthodontic device (Mandovani [6], Machado and Savi [10]).

The journal model is International Journal of Engineering Science.

1. Phenomenology of Phase Transformation in SMAs

SMAs have two crystallographic phases with distinct crystal structure and material properties: the austenitic and martensitic phases. The austenitic phase is only stable at high temperatures and has a cubic crystal structure. The martensitic phase, on the other hand, is only stable at low temperatures, and can be induced by either stress or temperature loadings. When a shape memory alloy undergoes a martensitic phase transformation, it transforms from the high-symmetry, austenitic phase to the low-symmetry, martensitic phase. The martensitic transformation that occurs in shape memory alloys is associated with mobile interfaces between the austenitic and martensitic phases (Patoor *et. al* [3]). These interfaces are capable of backward movement during the reverse transformation by shrinkage of the martensitic plates rather than nucleation of the parent phase. This phenomenon leads to a crystallographically reversible transformation (Otsuka and Wayman [2], Patoor *et. al* [3]). The martensitic transformation has some well-defined characteristics that distinguish it among other solid state transformations (Patoor *et. al* [3]):

- It is associated with an inelastic deformation of the crystal lattice with no diffusive process involved. It results from a cooperative and collective motion of atoms over distances smaller than the lattice parameters. The absence of diffusion makes the martensitic phase transformation almost instantaneous (Nishiyama [11]).

- Parent and product phases coexist during the phase transformation, and as a result there exists an invariant plane, which separates the parent and product phases. The invariant plane is called habit plane.

- Stress and temperature have a large influence on the martensitic transformation.

Transformation takes place when the free energy difference between the two phases reaches a critical value (Delaey [12]).

- Since the crystal lattice of the martensitic phase has lower symmetry than that of the austenitic phase, several variants of martensite can be formed from the same austenitic phase crystal (Vos *et al.* [13]).

Depending on the type of transformation experienced by these alloys, the crystal structure of martensite can be either monoclinic or orthorhombic (Otsuka and Ren [14], Wu and Lin [15]). Each martensite crystal formed can have a different orientation direction, which is called a variant. Martensitic variants can be organized into two distinct forms. When the martensitic phase is induced by temperature, the martensitic variants arrange themselves into a "self-accommodated" form. This assembly of martensitic variants is called *twinned* martensite (M^t). On the other hand, when the martensitic phase is induced by an applied load, all the variants rearrange into a specific variant orientation. This assembly of variants is called *detwinned* or reoriented martensite (M^d) (Lagoudas *et al.* [1]).

In the absence of load, the martensitic transformation takes place upon cooling, where the crystal structure changes from austenite into martensite. The transformation from austenite to martensite is called *forward* transformation. This transformation results in the formation of several martensitic variants, up to 24 for a typical NiTi (Lagoudas *et al.* [1]). The arrangement of variants occurs in such a way that the average macroscopic shape change is negligible, resulting in twinned martensite. On the other hand, when the material is heated from the twinned martensitic phase, the crystal structure transforms back to austenite. The phase transformation from martensite back to austenite is called *reverse* transformation. The forward and the reverse martensitic phase transformation happen in specific interval of temperature, where four characteristic temperatures can be defined. During the forward transformation, austenite begins to transform into martensite at the martensitic start temperature (M_s) and finishes at the martensitic finish temperature (M_f). Similarly, during heating the reverse transformation initiates at the austenitic start temperature (A_s) and the transformation is completed at the austenitic finish temperature (A_f). A schematic of the martensitic transformation under no load is shown in Fig. 1.

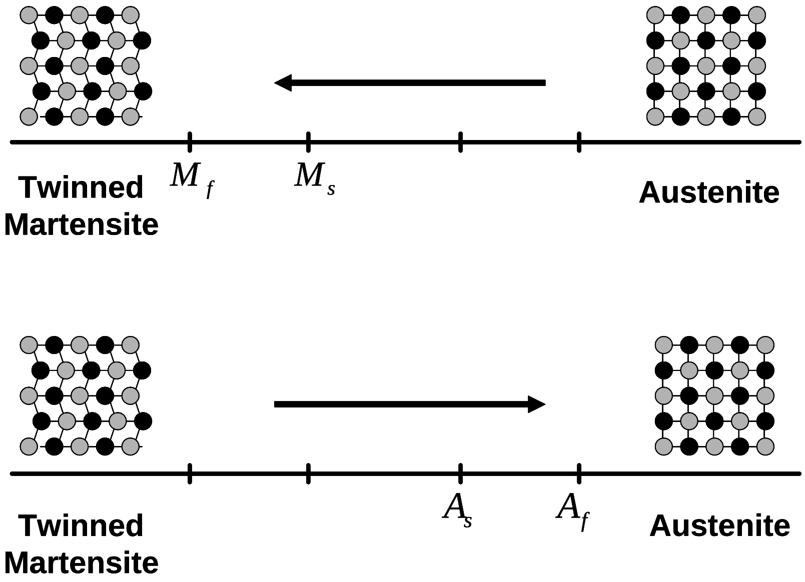

Fig. 1. Temperature-induced phase transformation of an SMA without mechanical loading (Lagoudas *et al.* [1]).

Due to the displacive nature of the martensitic phase transformation, applied stress plays a key role (Popov [16]). During phase transformation in the presence of applied stress, the austenitic phase transform directly into detwinned martensite, producing a shape change. A further heating of the SMA will lead to a shape recovery, while the load is still applied. It is important to note that the transformation temperatures are greatly influenced by the level of applied stress, as depicted in Fig. 2.

Under an applied load with a corresponding stress σ the new transformation temperatures are represented as (M_f^σ, M_s^σ , A_s^σ, A_f^σ) for martensitic finish, martensitic start, austenitic start and the austenitic finish temperatures, respectively.

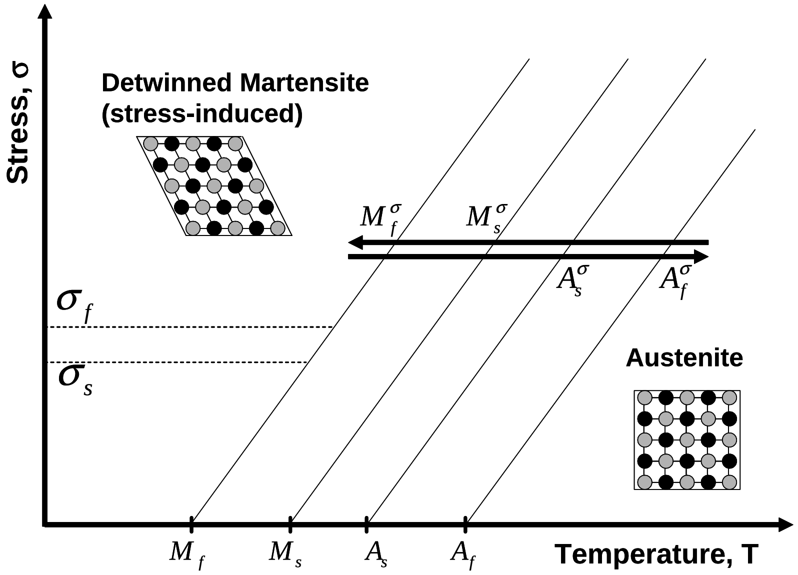
Stress, σ
Detwinned Martensite
(stress-induced)
M_f^σ
M_s^σ
A_s^σ
A_f^σ
σ_f
σ_s
Austenite
M_f
M_s
A_s
A_f
Temperature, T

Fig. 2. SMA phase diagram showing temperature-induced phase transformation with mechanical loading(Lagoudas *et al.* [1]).

Another important aspect of martensitic transformation is that it is accompanied by the release of heat (exothermic phase transformation). On the other hand, the reverse martensitic transformation is an endothermic phase transformation, accompanied by absorption of heat (Entchev [17]). This fact leads to a strong thermomechanical coupling on the SMA behavior. The thermomechanical coupling will be explored in the following chapters.

The *Shape Memory Effect* and the *Pseudoelasticity* are the key phenomena that distinguish SMAs from other conventional materials. They are associated with the way that the phase transformation takes place. These two effects are explained next.

2. Shape Memory Effect

If a mechanical load is applied to a SMA sample in the twinned martensitic phase, the martensitic variants can be reoriented (or detwinned) into a specific variant. The detwinning process leads to a macroscopic shape change (Fig. 3) and the deformed configuration is retained after the unloading (Fig. 4). A posterior heating of the SMA to a temperature above A_f results in reverse phase transformation, and consequently, in complete shape recovery (Fig. 4). If the SMA is then cooled to a temperature below M_f the austenite transforms back into twinned martensite and no associated shape change is observed. This process of detwinning and shape recovery under heating is called Shape Memory Effect (SME) (Otsuka and Wayman [2], Lagoudas *et al.* [1]). Note that the detwinning process occurs in a interval of stress. The minimum stress required for detwinning initiation is called detwinning start stress (σ_s), whereas the complete detwinning of martensite corresponds to the stress level denominated as the detwinning finish stress (σ_f).

Figure 5 shows the shape memory effect in the stress-strain-temperature space. Consider a SMA sample at a temperature greater than A_f (Point A). The SMA is cooled down to a temperature below M_f, point B, and the austenite is transformed into twinned martensite without any shape change. Afterwards, stress is applied on the SMA sample and the twinned martensite is reoriented into detwinned martensite, up to the point C. At point C the SMA is completely in the detwinned martensitic phase. Inelastic strains are formed during the detwinning process and are not recovered under unloading (Point D). Then the SMA sample is heated up to a temperature above A_f. During the heating step the reverse transformation occurs (points E-F) and all the detwinned martensite is transformed into austenite. As a result, all the inelastic strains are recovered. A further cooling from point A to B transforms the

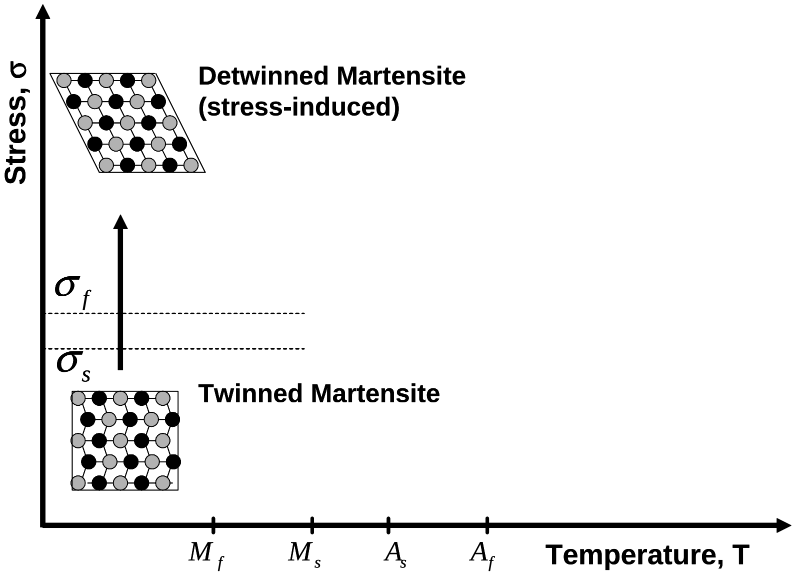
Stress, σ
Detwinned Martensite
(stress-induced)
σ_f
σ_s
Twinned Martensite
M_f
M_s
A_s
A_f
Temperature, T

Fig. 3. Schematics of the SME on a SMA showing the detwinning of the material with applied stress (Lagoudas *et al.* [1]).

austenite into twinned martensite again and no residual strain is observed.

3. Pseudoelasticity

In addition to thermally induced phase transformation, another way to induce phase transformation is to apply a sufficiently high mechanical load to the SMA in the austenitic phase. Detwinned martensite is then formed directly from the austenitic phase. During this loading step, inelastic strains due to phase transformation are formed. Upon unloding the detwinned martensite transforms back into austenite and if the temperature of the SMA is above A_f all the transformation strains are recovered. This is the so-called pseudoelastic effect (Otsuka and Wayman [2], Lagoudas *et al.* [1]). If the SMA is load and unload in a temperature above M_s but below A_f, only part of the transformation strains is recovered. The stress levels at which the martensite

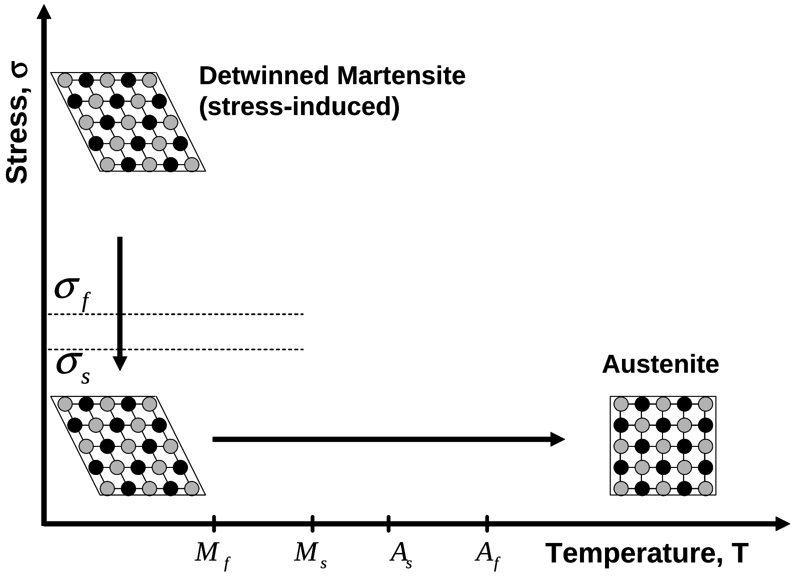

Fig. 4. Schematics of the SME on a SMA showing the unloading and subsequent heating to austenite under no load condition (Lagoudas *et al.* [1]).

transformation initiates and completes are denoted by σ^{Ms} and σ^{Mf}, whereas the stress levels at which the material initiates and completes its reverse transformation to austenite are denoted by σ^{As} and σ^{Af}, respectively. A schematic of an isothermal pseudoelastic loading path in the stress-temperature space is presented in Fig. 6.

Figure 7 presents the pseudoelastic effect in the stress *vs.* strain plot. Consider then a SMA sample at a temperature greater than A_f subjected to an applied stress. At first the SMA, which is in the austenitic phase, behaves in a elastic way. When the stress level reaches the value of σ^{Ms} the forward phase transformation starts and the austenite is transformed into detwinned martensite. The forward phase transformation ends when the stress level reaches the value of σ^{Mf}. For further loading the SMA, which now is in fully martensitic phase, behaves again in a elastic way. Upon unloading the SMA still behaves elastically, until the stress level reaches the value of

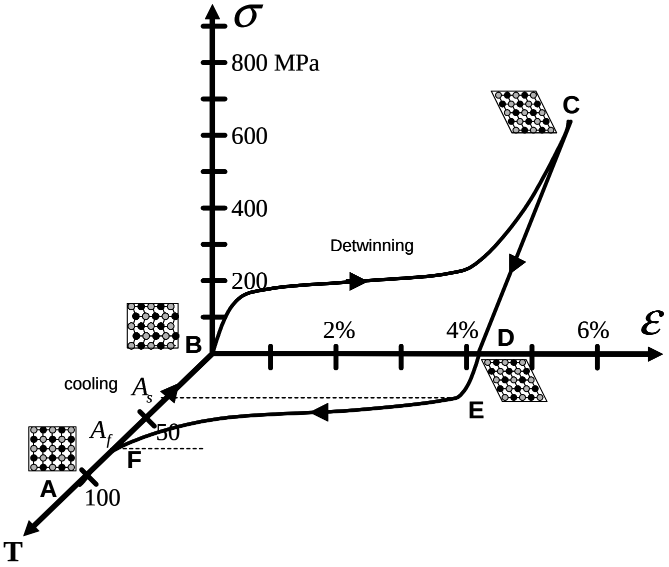

Fig. 5. Schematic of stress-strain-temperature-induced exhibiting the SME for a typical NiTi SMA (Lagoudas *et al.* [1]).

σ^{As}. At this point the reverse phase transformation takes place and the detwinned martensite transforms back into austenite. The reverse transformation is completed when the stress reaches the value of σ^{Af}. For further unloading the SMA behaves in a elastic way and no residual or permanent strain is observed. It is important to emphasize that the forward and reverse phase transformation paths do not coincide. As a result, a loop of hysteresis can be observed in the stress *vs.* strain plot. The area of the loop is related to the amount of energy dissipated by the material. This property of energy dissipation can be used to attenuate undesired vibrations of a mechanical system, for example, and will be explore in this work in the following chapters.

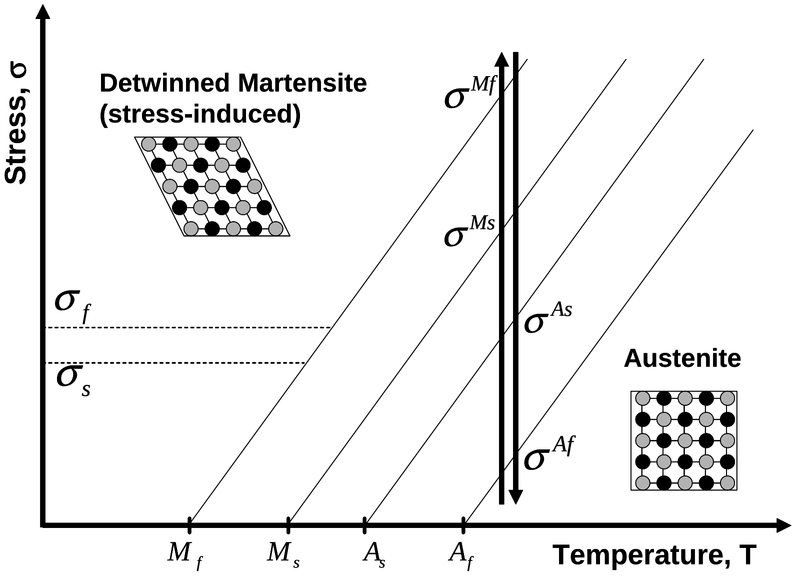
Stress, σ
Detwinned Martensite
(stress-induced)
σ^{Mf}
σ^{Ms}
σ^{As}
σ^{Af}
σ_f
σ_s
Austenite
M_f
M_s
A_s
A_f
Temperature, T

Fig. 6. Phase diagram with a possible pseudoelastic loading path (Lagoudas *et al.* [1]).

B. Literature Review on Thermomechanical Constitutive Models for SMAs

A substantial research effort has been conducted over the past three decades with the aim of developing constitutive models that can predict SMA thermomechanical behavior (Tanaka and coworkers [18, 19], Liang and Rogers [20], Brinson [21, 22], Berveiller *et al.* [23], Lagoudas and coworkers [24–27], Auricchio and Sacco [28, 29], Rajagopal and Srinivasa [30, 31], and Savi *et al.* [32]). A comprehensive review of SMA constitutive models can be found in (Lagoudas *et al.* [33], Patoor *et al.* [3]). These constitutive models can be divided into two different groups: micromechanics-based models and phenomenological models (Lagoudas *et al.* [33], and Patoor *et al.* [3]). The micromechanics-based models utilize information about the microstructure of the SMA to predict its macroscopic responses. Since, in reality, it is a very difficult task to obtain an exact representation of the microstructure of a material,

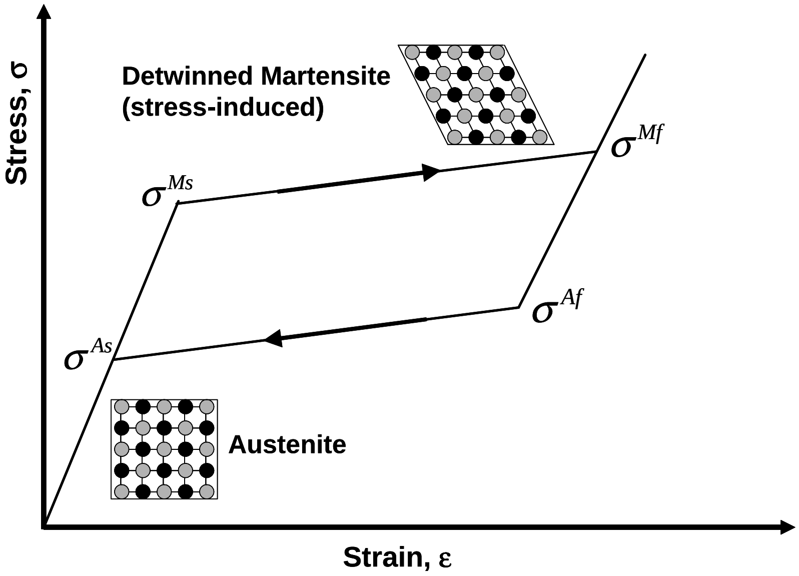

Fig. 7. Isothermal pseudoelastic loading cycle (Lagoudas *et al.* [1]).

these models utilize homogenization techniques, so that the effective SMA properties can be predicted [33]. Some examples of microscopic models can be found at Berveiller et al. [23], Sun and Hwang [34, 35], Lagoudas and Bhattacharyya [36], and Nae *et al.* [37], Anand and Gurtin [38]. Phenomenological models, on the other hand, do not directly depend on material parameters at the microscopic level, but on a set of parameters at the macroscopic level that are determined through experimental observations. These models rely on continuum thermomechanics with internal variables to account for the changes in the microstructure due to phase transformation (Lagoudas *et al.* [25], and Lagoudas *et al.* [33]). Some of the firsts macroscopic models are Falk [39], Brinson [22], Boyd and Lagoudas [24], Tanaka [18], Tanaka *et al.* [19], Liang and Rogers [20]. Later, Lagoudas and coworkers [25] unified the models by Boyd and Lagoudas [24], Tanaka [18],and Liang and Rogers [20] under the same thermodynamic framework, where the only difference lied in the transformation hardening function. For a more complete list and discussion about micromechanics-based and phenomenological models the interested reader is referred to Lagoudas *et al.* [33].

A key aspect in the SMA behavior is the strong thermomechanical coupling that occurs during phase transformation. Even though temperature is an interval variable for most of the constitutive models, just a few of them explicitly consider the thermomechanical coupling[40]. Most of the constitutive models predicts the stress-strain behavior of the SMA under the assumption of isothermal regime. This assumption is only valid for very slow strain rates, or when the heat transfer medium is enough to remove (or supply) latent heat due to phase transformation to prevent any significative variation in the temperature. One of the first attempts to model the thermomechanical problem was done by Leo *et al.* [41]. The authors have considered the model proposed by Falk [39] coupled with the heat equation. Later, Bhattacharyya *et al.* [42] theoretically and experimentally investigated the transient thermoelastic problem of a large force and large strain actuator using a thermoelectric heat exchange mechanism. A one-dimensional model of a thermoelectric unit cell with a SMA junction was developed and the transient thermoelectric response during a heat exchange process from or to the SMA junction were evaluated for different applied electric current densities. The governing equation for the one-dimensional heat conduction problem was considered, where the convective heat transfer was included as a source term. In that work, the change in the heat capacity of the SMA during forward and reverse martensitic phase transformations was described by empirical expressions as functions of the transformation temperatures and the current temperature. The change in the volume fraction of martensite was modeled by considering an exponential model. Later, Lagoudas and Bhattacharyya [36] considered the effect of a variable actuating load and a constant load applied as boundary conditions for the same SMA actuator. The thermomechanical coupling problem was accounted for by implementing an iterative scheme.

Benzaoui *et al.* [43] conducted an numerical-experimental study on a SMA wire actuator. At first, a loaded SMA wire was subjected to different resistivity heating input rate. The results have shown no significant change in the shape or width of the hysteresis on the strain-temperature space due to different resistivity heat input rate. Afterwards, a constitutive model originally proposed by Leclercq and Lexcellent [44] was extended to incorporate the thermomechanical coupling on SMA. The model is based on plasticity, and the coupling is considered by integrating the heat equation. It should be noticed that the authors did not investigate the strain rate input effect on the pseudoelastic response of SMAs. Peyroux *et al.* [45] propose a constitutive model for SMAs that assumes an intrinsic dissipation identically to zero, and takes into account the thermomechanical coupling. The model was implemented in a finite element code, where the time discretization utilized an implicit integration scheme. At first, experimental results were presented, where the influence of different loading paths, loading rates, and room temperature were investigated. Later, a finite element analysis of two bi-dimensional structures (a dog-bone specimen and a self-tightening ring) were conducted, where the thermomechanical coupling was considered. Prahlad and Chopra [46] described a modeling approach to incorporate the effects of the non-quasistatic loading rates on the extensional behavior of an SMA wire. The model utilizes rate forms for stress and martensitic volume fraction proposed by Brinson [21], and temperature and temperature rates are not prescribed but are derived from energy conservation of the material. Experimental results under a variety of loading conditions were conducted for comparison with the numerical simulations.

The thermomechanical coupling on SMAs can also leads to the appearance of other types of phenomena such as transformation induced creep and transformation induced stress relaxation. Matsui *et al.* [47] have experimentally investigated the stress relaxation and creep phenomena on TiNi shape memory alloys. Some tensile tests with different loading path at different constant strain and/or stress rate, with partial and full loop of hysteresis, were conducted. The authors concluded that the effect of creep and stress relaxation do not arise as a function of time as in viscoelastic materials but, in fact, due to temperature variations from phase transformations. Lim and McDowell [40] conducted several biaxial tension (or compression)-torsion proportional and non-proportional loadings for thin-wall SMA tubes. During uniaxial tensile tests at different loading / unloading strain rates some points were selected to hold constant strain (and stress) for five minutes, so that the effect of stress-relaxation and creep could be investigated. Afterwards the authors proposed a micromechanics-based model capable of simulating proportional and nonproportional loading paths. Later, Lim and McDowell [48] implemented a 3-D finite element form of their micromechanics-based model to study the thermomechanical coupling on SMAs. A 3-D mesh was constructed to simulate intergranular interactions in a polycrystal SMA. Numerical simulations regarding and disregarding thermomechanical coupling were performed and compared with experimental results in the average sense for uniaxial and shear loading cycles. Simulations with thermomechanical coupling investigated the stress-strain response of a uniaxial tensile tests for two different strain rates, where the effect of stress relaxation could be also obtained for loading paths that combine quasi-static and non-quasi-static loadings. Lexcellent and Rejzner [49] revisited the experimental results obtained by Lim and McDowell [40] for biaxial (tension(or compression)-torsion) proportional and non-proportional loading, including creep and stress-relaxation tests. The authors extended the constitutive model proposed by Raniecki and Lexcellent [50] so that the biaxial proportional loadings could be considered. The heat equation was integrated, so that temperature variation due to stress-induced phase transformation could be contemplated. Balandraud *et al.* [51, 52] proposed a one-dimensional constitutive model that takes into account temperature variations on the SMA due to stress-induced phase transformation, and also can predict stress-relaxation and creep phenomena. Specifically, the model considers the existence of a temperature variation due to phase transformation, but neglects the classical thermomechanical coupling. Recently, Auricchio and Petrini [53] investigated the mechanical response of a hybrid composite, in which SMA wires, previously deformed, are activated by electrical current heating and try to recover its original shape. A 3D phenomenological model that couples the thermal, electro and mechanical problem was considered. The coupled problem is solved by splitting the problem into a sequence of uncoupled problem and then searching for the global solution using an iterative procedure on the three partitions.

C. Literature Review on SMAs (Nonlinear) Dynamical Systems

The hysteretic behavior of pseudoelastic SMAs results in a high dissipation capacity that can be used to attenuate undesired vibrations of a mechanical system or structure (Williams *et al.* [54], Salich*et al.* [55], Saadat*et al.* [56], Lagoudas*et al.* [57],and Machado and Lagoudas [58]). Even though SMA evolving thermomechanical properties and high dissipation capacity are very interesting characteristics to be explored in passive vibration isolation systems, they can also lead to a very complex dynamical response, in some cases leading to chaotic response. Chaotic responses imply that two very close but different orbits can diverge in the course of time, and consequently, chaos is related to long-term unpredictability. Therefore, it is of fundamental importance to study the nonlinear dynamical response of SMA systems. Many researchers have investigated the complex dynamical response of SMA systems, including the possibility of chaotic responses. Feng and Li [59], for example, numerically and experimentally investigated the dynamical response of a mechanical system consisting of a mass, a SMA bar and a linear viscous damper. The constitutive model proposed by Graesser and Cozzarelli [60] was used to simulate the behavior of the SMA bar. The effect of stress-induced phase transformation on the resonance frequency and peak response near the resonance was also investigated. In particular, period-three response was found for some forcing parameters, as well as a period-doubling cascade, in which chaotic motion was observed in the presence of a bias load.

Savi and coworkers ([61], [62], [63]) also studied the dynamical response of a single-degree of freedom (S-DOF) oscillator composed of a mass, a linear damper, and an SMA element, with special attention to chaotic motions. A polynomial constitutive model, proposed by Falk [39], was used to describe the restitution force of the SMA. Lyapunov exponents were used to quantify chaotic motion of the SMA oscillator for certain ranges of excitation force and temperature. Savi and Pacheco [62], and Machado *et al.* [64] analyzed coupled shape memory oscillators, considering a two-degree of freedom oscillator, for free and forced vibration cases. It was shown that chaos, and even hyper-chaos, can be associated with the presence of one or more positive Lyapunov exponents. It is important to mention that the polynomial model proposed by Falk [39] is a nonlinear polynomial model that establishes the thermomechanical equilibrium curve due to a change of crystallographic phase, but does not properly describe the hysteretic behavior of the SMA. The damping effect related to the SMA material was considered by assuming a linear viscous damping representing the amount of damping for a steady state solution. Therefore, the estimation of the Lyapunov exponents was performed by directly employing the algorithm by Wolf *et al.* [65]. Alternatively, Savi *et al.* [66] have numerically investigated the dynamic response of a S-DOF SMA oscillator, where the restitution force was described by a constitutive model with internal constraints (Paiva *et al.* [67]). Tensile-compressive asymmetry of the SMA behavior was also studied, presenting chaotic-like and multi-stability response of the SMA oscillator.

Lacarbonara *et al.* [68] investigated the nonlinear response and bifurcations of an S-DOF shape memory oscillator. A thermomechanical model based on the work by Ivshin and Pence [69] was utilized to describe the nonlinear constitutive behavior of the shape memory element of the oscillator. It was shown that a rich class of solutions, including discontinuity of frequency responses, quasi-periodicity and chaos could arise in nearly adiabatic conditions. Bernardini and Rega [70] also studied the nonlinear dynamics of a single-degree of freedom pseudoelastic SMA oscillator. A constitutive model for the oscillator restoring force developed in a thermomechanical framework that allows the prediction of temperature variations due to dynamical loading was proposed. The authors have shown that non-regular responses occur around the jumps between different branches of frequency-response curves. Bifurcation diagrams were used to describe the transition from periodicity to chaotic motion.

Khan *et al.* [71], and Lagoudas *et al.* [72] investigated the pseudoelastic response of shape memory alloys on passive vibration isolation through numerical simulation and experimental correlation. A physically based simplified SMA model and an empirical model based on system identification (Preisach model) were adapted to simulate the force-displacement response of pseudoelastic SMA tubes (modeled as non-linear hysteretic spring elements). An extensive parametric study on a nonlinear hysteretic dynamic system, representing an actual SMA damping and on a passive prototype device, was conducted. Several tests were performed to explore the response of the SMA vibration isolation device. The results have shown that variable damping and tunable vibration isolation response can be achieved based on a combination of different parameters such as excitation levels, mass and pre-compression of the pseudoelastic

SMA spring elements.

Lagoudas *et al.* [57] conducted a numerical and experimental investigation on a passive vibration and isolation damping device where the main elements were pseudoelastic SMA wires. The device, a mass connected to a frame by two SMA wires, was subjected to a series of continuous sinusoidal acceleration functions in the form of a sine sweep. Frequency responses and transmissibility of the device were analyzed. The temperature of the wires during the dynamic test were also measured. The experimental results have shown that the transmissibility curves present a discontinuity related to the nonlinear damping introduced by the hysteretic behavior of the SMA wires. In addition, temperature variations of the wires were observed, related to the stress induced martensitic phase transformation. The numerical simulations of a one-degree of freedom SMA oscillator were conducted. The configuration of the SMA oscillator was based on the device, where a thermomechanical constitutive model proposed by Boyd and Lagoudas [24] was implemented to simulate the constitutive behavior of the SMA wires. Machado and Lagoudas [58] revisit the experimental results presented in Lagoudas *et al.* [57] and compares them with numerical simulations of a SMA oscillator where the behavior of the SMA elements where described by a modified version of the constitutive model proposed by Machado and Lagoudas [58]. This modified version of the constitutive model predicts the strong thermomechanical coupling behavior of the SMAs caused by the presence of the latent heat of transformation. The thermomechanical coupling leads to a time-dependent behavior of the SMA device, even though the constitutive model is rate-independent, where the temperature variations caused by stress-induced phase transformation were also predicted. Machado and Lagoudas [73] evaluated the dynamical response of an S-DOF SMA oscillator using the same simplified model proposed by Khan *et al.* [71] to simulate the SMA behavior. As a consequence of the nonlinearities exhibited by the

SMA, the oscillator response was shown to be complex, where chaotic behavior is also observed.

D. Outline of the Present Research

The research effort presented in this work can be divided into two major parts. The first part of this work evaluates the nonlinear dynamics of a passive vibration isolation and damping (PVID) device through numerical simulations and experimental correlations. The device, a mass connected to a frame through two pre-strained pseudoelastic SMA wires, is subjected to a series of continuous acceleration functions in the form of a sine sweep. Frequency responses and transmissibility of the device as well as temperature variations of the SMA wires are analyzed. Numerical simulations of a one-degree of freedom (1-DOF) SMA oscillator are also conducted to corroborate the experimental results. The configuration of the SMA oscillator is based on the PVID device. A modified version of the constitutive model proposed by Boyd and Lagoudas [24] is used to predict the behavior of the SMA elements of the oscillator. This modified model considers the thermomechanical coupling through the integration of the heat equation. The constitutive model is numerical implemented by a return mapping algorithm. The phenomenon of stress-relaxation phenomenon caused by phase transformation is numerically and experimentally investigated.

The second part of this work numerically evaluates chaotic responses of a one-degree of freedom SMA oscillator composed of a mass and a SMA element. The restitution force of the oscillator is provided by an SMA element described by a rate-independent, hysteretic, thermomechanical constitutive model that allows smooth transitions between the austenitic and the martensitic phases. Experimental thermomechanical and calorimetric results are compared to the model's prediction, with a very good agreement. Chaotic responses of the SMA oscillator are evaluated through the estimation of the Lyapunov exponents. The Lyapunov exponent estimation of the nonlinear hysteretic SMA system is done by adapting the classical algorithm by Wolf and co-workers. The main issue of using this algorithm for nonlinear, rate-independent, hysteretic systems is related to the procedure of linearization of the equations of motion. The present work establishes a procedure of linearization that allows the use of the classical algorithm by Wolf and co-workers. Two different modeling cases are considered for isothermal and non-isothermal heat transfer conditions, and numerical simulations are performed for both cases. The evaluation of the Lyapunov exponents shows that the proposed procedure is capable of quantifying chaos in rate-independent, hysteretic dynamical systems.

The present research is organized as follows: Chapter II presents a brief review on continuous mechanics, where the conservation relations and the first and second law of thermodynamics are derived. A procedure to obtain constitutive relations for SMAs is also briefly described. Chapter III introduces the constitutive model for polycrystalline shape memory alloys proposed by Boyd and Lagoudas [24]. The theoretical derivations of how to integrate the heat equation into the constitutive model are presented in Chapter IV, while chapter V presents the numerical implementation of the constitutive model for SMAs, also considering the integration of the heat equation. The implementation follows the same guidelines of previous work by Qidwai and Lagoudas[27]. Chapter VI presents the numerical and experimental investigation of the dynamics of a PVID device where the main elements of the device are pseudoelastic SMA wires. Experimental results of vibration tests on the device are compared to the numerical simulations of a SMA oscillator.

Chapter VII presents a new development in the field of thermomechanical constitutive modeling of shape memory alloys (SMAs). The proposed constitutive model is a modification of earlier work of Boyd and Lagoudas [24] and it allows for smooth transitions between the martensitic and austenitic phases. Due to the smoothness on phase transitions, the present model better simulates the behavior of trained polycrystalline pseudoelastic SMAs. Experimental results are compared to the predictions of the model, with a very good agreement. In addition, the model's description of the latent heat associated with phase transformation is compared with calorimetry results and found to be in good agreement. Chapter VIII discusses the Lyapunov exponent estimation of nonlinear hysteretic systems by adapting the classical algorithm by Wolf and coworkers. The dynamical response of a single-degree of freedom pseudoelastic shape memory alloy (SMA) oscillator is discussed as an application of the proposed algorithm. The evaluation of the Lyapunov exponents shows that the proposed procedure is capable of quantifying chaos in rate-independent, hysteretic dynamical systems. Finally, conclusions and future work are presented in Chapter IX.

CHAPTER II

CONTINUUM DESCRIPTION OF SHAPE MEMORY ALLOYS

In the current chapter, we will discuss the thermomechanical modeling of shape memory alloys. A brief review of the conservation laws as applied to continuum mechanics is also presented in the beginning of this chapter. A methodology for obtaining the thermomechanical constitutive equations for SMAs by enforcing the conversation laws and basic principles of continuum thermodynamics will then be discussed.

The three basic components of continuum mechanics are kinematics, conservation (balance) laws and constitutive equations. The kinematics component describes the geometry of motion and deformation of a continuum body, without considering the cause of motion or deformation. The conservation laws express how external effects influence the motion of a continuum body. Finally, constitutive equations mathematically describe the main characteristics of material behavior that can only be understood and/or predicted through an understanding of experimental observations.

A. Kinematics of SMAs

Assume that the SMA body in its deformed or current configuration occupies a region Ω, at time t, with boundary surface $\partial\Omega$. The notion of choosing a reference configuration for SMAs is more complicated than for other conventional materials, because there are two natural reference configurations to choose from, *i.e.*, the austenitic and martensitic. There are researchers [30, 31] who have selected both austenite and martensite as reference configurations for the constitutive modeling of SMAs. However, in this work, we will select the austenitic parent phase as the reference configuration and the transition from austenite to martensite will be accounted for by an internal state variable to be introduced in Section 1.

The position of a material point in the deformed configuration in relation to the position of the material point in the reference configuration is given by the displacement vector $\mathbf{u}$. One can define a measure of deformation of neighboring material points that is invariant under rigid body rotation and translation in terms of the symmetric second-order Green-Lagrange strain tensor as

$$\mathbf{E} = \frac{1}{2}\left[(\boldsymbol{\nabla}\mathbf{u}) + (\boldsymbol{\nabla}\mathbf{u})^T + \Big((\boldsymbol{\nabla}\mathbf{u})^T(\boldsymbol{\nabla}\mathbf{u})\Big)\right], \tag{2.1}$$

where $\boldsymbol{\nabla}\mathbf{u}$ is the gradient of the displacement field [74].

For infinitesimal displacement gradients, the quadratic term in Eqn. 2.1 above can be neglected and also the difference between the reference and the current configuration becomes negligible. The actual choice of the reference configuration is not essential. This assumption, which is realistic for most applications of SMAs, leads to an infinitesimal strain tensor of the following form:

$$\boldsymbol{\varepsilon} = \frac{1}{2}\Big((\boldsymbol{\nabla}\mathbf{u}) + (\boldsymbol{\nabla}\mathbf{u})^T\Big), \tag{2.2}$$

where the displacement gradient can be evaluated in either the austenitic or martensitic phases. The infinitesimal strain tensor $\boldsymbol{\varepsilon}$ will be used in this chapter and the remainder of the work.

B. Conservation (Balance) Laws

The basic conservation laws of continuum mechanics are [75, 76]:

1. Conservation of mass
2. Conservation of linear momentum
3. Conservation of angular momentum

4. Conservation of energy

In continuum thermodynamics, the conservation of energy is also called the first law of thermodynamics, while the second law is the entropy inequality principle.

Before the derivation of the conservation laws, and first and second law of thermodynamics, we introduce, without proof, two theorems that will be useful during the derivations: the divergence theorem and the Reynolds transport theorem. The divergence theorem states that if Ω is a closed bounded region with piecewise smooth boundary $\partial\Omega$, and a unit normal $\mathbf{n}$, for any smooth vector $\mathbf{a}$ field in the Euclidean space we have:

$$\int_{\partial\Omega} \mathbf{a}(\mathbf{x},t)\cdot\mathbf{n}\mathrm{d}s = \int_{\Omega} \mathrm{div}\mathbf{a}(\mathbf{x},t)\mathrm{d}v. \tag{2.3}$$

The Reynolds transport theorem states that the time rate of change of the integral of the scalar field $\varphi(\mathbf{x},t)$ over the region Ω is equal to the rate of transport (or the outward normal flux) of $\varphi\mathbf{v}$ across the surface $\partial\Omega$ out of region Ω, plus the local time rate of change of the spatial scalar field φ within region Ω.

$$\frac{D}{Dt}\left(\int_{\Omega} \varphi(\mathbf{x},t)\mathrm{d}v\right) = \int_{\partial\Omega} \varphi\mathbf{v}\cdot\mathbf{n}\mathrm{d}s + \int_{\Omega} \frac{\partial\varphi}{\partial t}\mathrm{d}v, \tag{2.4}$$

where $\mathbf{v}$ is the velocity of a material point [74]. Next, we present the derivations of the conservation laws and the first and second laws of thermodynamics.

1. Conservation of Mass

The law of conservation of mass states that the total mass of a continuum body cannot change with time or deformation. Considering the mass of an SMA body to be related to the density, ρ, by

$$M = \int_{\Omega} \rho \mathrm{dv}, \tag{2.5}$$

the law of conservation of mass can be written as

$$\frac{DM}{Dt} = \frac{D}{Dt}\left(\int_{\Omega} \rho \mathrm{dv}\right) = 0, \tag{2.6}$$

where $\frac{D}{Dt}$ is the material time derivative [76].

By applying the Reynolds transport theorem, Eqn. 2.4, on the equation above we get

$$\int_{\partial\Omega} \rho \mathbf{v} \cdot \mathbf{n} \mathrm{d}s + \int_{\Omega} \frac{\partial \rho}{\partial t} \mathrm{d}v = 0. \tag{2.7}$$

Next, we use the divergence theorem on the first term of the left-hand side of Eqn. 2.7 to obtain:

$$\int_{\Omega} \left[\mathrm{div} \rho \mathbf{v} + \frac{\partial \rho}{\partial t}\right] \mathrm{d}v = 0. \tag{2.8}$$

Therefore, the local form of the conservation of mass is defined as

$$\frac{\partial \rho}{\partial t} + \mathrm{div}\left(\rho \mathbf{v}\right) = 0, \tag{2.9}$$

2. Conservation of Linear Momentum

The law of conservation of linear momentum states that the rate of change of linear momentum of a continuum body is equal to the total sum of surface and body forces applied to it. The integral form of the conservation of linear momentum is given by:

$$\frac{D}{Dt}\left(\int_{\Omega} \rho \mathbf{v} \mathrm{dv}\right) = \int_{\partial\Omega} \mathbf{t} \mathrm{ds} + \int_{\Omega} \mathbf{b} \mathrm{dv}, \tag{2.10}$$

where $\mathbf{t}$ is the surface traction vector, and $\mathbf{b}$ is the body force vector.

Using the Reynolds Transport theorem, the Cauchy formula, $\mathbf{t} = \boldsymbol{\sigma}^T \cdot \mathbf{n}$, with $\boldsymbol{\sigma}$ denoting the Cauchy stress tensor and the divergence theorem on the equation above we obtain

$$\int_{\Omega} \left[\rho \frac{D\mathbf{v}}{Dt} - \mathrm{div} \boldsymbol{\sigma}^T - \mathbf{b}\right] \mathrm{dv} = 0. \tag{2.11}$$

The local form of the conservation of linear momentum can be written as

$$\mathrm{div}\boldsymbol{\sigma}^T + \mathbf{b} = \rho\dot{\mathbf{v}}. \tag{2.12}$$

3. Conservation of Angular Momentum

The law of conservation of angular momentum states that the rate of change of angular momentum of a continuum body is equal to the sum of the moments applied by the surface and body forces in addition to distributed body couples. In the absence of distributed body couples, the integral form of the conservation of angular momentum is given by

$$\frac{D}{Dt}\left(\int_\Omega \mathbf{r} \times \rho\mathbf{v}\right)\mathrm{dv} = \int_{\partial\Omega} \mathbf{r} \times \mathbf{t}\mathrm{ds} + \int_\Omega \mathbf{r} \times \mathbf{b}\mathrm{dv}. \tag{2.13}$$

where $\mathbf{r}$ is the position vector of a material point.

The local form of the conservation of angular momentum states that the Cauchy stress tensor is symmetric

$$\boldsymbol{\sigma} = \boldsymbol{\sigma}^T. \tag{2.14}$$

4. Conservation of Energy

The law of conservation of energy states that the time rate of change of the total energy (kinetic plus internal energy) of a continuum body is equal to the rate at which external mechanical work is done to that body by surface tractions and body forces plus the rate at which thermal energy is added by heat flux, $\mathbf{q}$ and heat sources, r. The integral form of the conservation of energy is given by the following equation

$$\begin{aligned}\frac{D}{Dt}\left(\int_\Omega \frac{1}{2}\rho\mathbf{v}\cdot\mathbf{v}\mathrm{dv} + \int_\Omega \rho u\mathrm{dv}\right) = \int_{\partial\Omega} \mathbf{t}\cdot\mathbf{v}\mathrm{ds} + \int_\Omega \mathbf{b}\cdot\mathbf{v}\mathrm{dv} + \\ \int_{\partial\Omega} -\mathbf{q}\cdot\mathbf{n}\mathrm{ds} + \int_\Omega \rho r\mathrm{dv},\end{aligned} \tag{2.15}$$

where u is the internal energy per unit mass. Using again the Reynolds Transport theorem, the Cauchy formula, the divergence theorem, the conservation relations of mass, Eqn. 2.9, linear momentum, Eqn. 2.11, and angular momentum, Eqn. 2.14, on the above equation, we obtain

$$\int_{\Omega}\left[\rho\frac{Du}{Dt}-\boldsymbol{\sigma}:\dot{\boldsymbol{\varepsilon}}+\mathrm{div}\mathbf{q}-\rho r\right]\mathrm{dv}=0. \tag{2.16}$$

The local form of conservation of energy is defined as:

$$\rho\dot{u}=\boldsymbol{\sigma}:\dot{\boldsymbol{\varepsilon}}-\mathrm{div}\mathbf{q}+\rho r. \tag{2.17}$$

5. Entropy Inequality - Second Law of Thermodynamics

The entropy inequality principle, or second law of thermodynamics, states that the internal entropy production is always greater than or equal to zero. The second law of thermodynamics can be expressed by the Clausius-Duhem inequality as

$$\frac{D}{Dt}\left(\int_{\Omega}\rho s\mathrm{dv}\right)+\int_{\partial\Omega}\frac{\mathbf{q}}{T}\cdot\mathbf{n}\mathrm{ds}-\int_{\Omega}\frac{\rho r}{T}\mathrm{dv}\geq 0. \tag{2.18}$$

where s is the specific entropy per unit mass. By following the same standard procedure used above we obtain the following integral form of the second law of thermodynamics

$$\int_{\Omega}\left[\rho\frac{Ds}{Dt}+\mathrm{div}\left(\frac{\mathbf{q}}{T}\right)-\frac{\rho r}{T}\right]\mathrm{dv}\geq 0. \tag{2.19}$$

Therefore, the local form of the Clausius-Duhem inequality is defined as,

$$\rho\dot{s}+\frac{1}{T}\mathrm{div}\left(\mathbf{q}\right)-\frac{1}{T^2}\mathbf{q}\cdot\mathbf{g}-\frac{\rho r}{T}\geq 0, \tag{2.20}$$

where $\mathbf{g}=\boldsymbol{\nabla}T$ is the thermal gradient. Assuming that the term $-\frac{1}{T^2}\mathbf{q}\cdot\mathbf{g}$ is always greater than or equal to zero, based on the experimental observation that heat only flows spontaneously from a hotter material point to a colder one, the strong form of the second law reduces to:

$$\rho\dot{s} + \frac{1}{T}\mathrm{div}\,(\mathbf{q}) - \frac{\rho r}{T} \geq 0, \tag{2.21}$$

which is also known as Clausius-Planck inequality [77].

C. Need for Constitutive Equations

Now that the conservation laws of mass, linear momentum, and angular momentum, as well as the first and second laws of thermodynamics have been presented, it is instructive to count the number of unknowns and equations to verify that we have a well-posed system with the same number of equations and unknowns. Thus, starting at the stress and strain tensors, we have six unknown components from the stress tensor, $\boldsymbol{\sigma}$, and six from the symmetric strain tensor, $\boldsymbol{\varepsilon}$. We also have three unknowns from the components of the displacement vector $\mathbf{u}$, three from the heat flux vector $\mathbf{q}$, and three additional unknowns from temperature, density and internal energy. Therefore, we have a total of 21 unknowns.

The number of equations we have available is 11: one equation from the conservation of mass, Eqn. 2.9, three equations from the conservation of linear momentum, Eqn. 2.12, and one equation from the conservation of energy. In addition, we have six equations from kinematics Eqn. 2.2. Notice that we have already used the equations from the conservation of angular momentum to define that the stress tensor has only six unknowns. Therefore, we have a total of 21 unknowns, but only 11 equations, as summarized in Table I. Consequently, we need 10 more equations, which can be found by introducing constitutive equations.

Table I. Need for constitutive equations

Quantities			Independent Equations	
Name	Symbol	Unknowns	Name	Equations
Displacement vector	$\mathbf{u}$	3	Linear Momentum	3
Strain tensor	$\boldsymbol{\varepsilon}$	6	Kinematics	6
Stress tensor	$\boldsymbol{\sigma}$	6		
Density	ρ	1	Conservation of Mass	1
Internal Energy	u	1	Conservation of Energy	1
Temperature	T	1		
Heat Flux	$\mathbf{q}$	3		
Total of Unknowns:		21	Total of Equations	11

D. Constitutive Equations

Constitutive equations are mathematical models intended to describe the principal features of a material behavior in an idealized form. In reality, a material can behave in a intricate way, making it very difficult for one to construct a constitutive model that considers all the possibilities of the material behavior. Therefore, a key point in developing constitutive models is to define what aspects of the behavior of the material can be regarded as essential. This process of idealization is very important because it limits the possibilities of the material's behavior, disregarding effects that are less important. SMAs are materials that undergo a phase transformation and therefore are characterized by a sequence of thermodynamic states that can described by only the introduction of additional internal state variables such as the martensitic volume fraction. In this section we present a procedure of obtaining constitutive equations in the presence of internal state variables. *Thermodynamic state variables* are those that represent all quantities that characterize a material body at a certain state. If these variables can be measured and controlled, they are called *external state variables*, otherwise they are called *internal state variables.* The thermodynamic state of an SMA can be fully determined by a combination of external and internal state variables.

A *thermodynamic potential* is a function that characterizes a certain thermodynamic state of a material and it depends on state variables, both external and internal. Four thermodynamic potentials are commonly defined, according to a certain choice of the independent state variables. These four thermodynamic potentials are the internal energy, u, the Helmholtz free energy, ψ, the enthalpy, $\hbar$, and the Gibbs free energy, G, as specific quantities all defined per unit mass. The internal energy, u can be defined as a measure of kinetic and potential energy of the material points within the material system. The Helmholtz free energy, ψ, is defined to be the portion of the internal energy available for doing work at constant temperature, whereas enthalpy, $\hbar$, is the portion of internal energy that can be released as heat at constant applied stress. The Gibbs free energy, G, is finally the portion of enthalpy available for doing work at constant temperature.[1].

The first natural choice for a thermodynamic potential when deriving constitutive equations can be the internal energy. However, the internal energy is not often used because it depends on the entropy, which is a difficult quantity to measure. For the same reason, enthalpy is not commonly used either. The two remaining choices for thermodynamic potentials, most commonly used when deriving constitutive equations are the Helmholtz and the Gibbs free energies. The choice between Gibbs and Helmholtz free energies is based on the state variable one can control during experiments, such as stress or strain, and temperature. SMA experimentation is based on prescribing either stress and temperature, or strain and temperature, where the remaining quantity is measured. For example, if one prescribes temperature and stress, strain is measured.

---

[1] All specific quantities defined per unit mass, such as internal energy, enthalpy and Helmholtz free energy, are represented by lower case letters. The only exception is the Gibbs free energy that is represented by the capital letter G, following the notation used since the earlier papers by Lagoudas and coworkers.

Table II presents the four thermodynamic potentials and their relation to the internal energy, obtained through a Legendre transformation. The set of internal state variables is denoted by $\boldsymbol{\zeta}$.

Table II. Thermodynamic potentials

Thermodynamic Potentials	Symbol	Relation to u (Legendre Transformation)	Independent Variables
Internal energy	u	u	s, $\boldsymbol{\varepsilon}$, $\boldsymbol{\zeta}$
Enthalpy	$\hbar$	$\hbar = u - \frac{1}{\rho}\boldsymbol{\sigma} : \boldsymbol{\varepsilon}$	s, $\boldsymbol{\sigma}$, $\boldsymbol{\zeta}$
Helmholtz free energy	ψ	$\psi = u - sT$	T, $\boldsymbol{\varepsilon}$, $\boldsymbol{\zeta}$
Gibbs free energy	G	$G = u - \dfrac{1}{\rho}\boldsymbol{\sigma} : \boldsymbol{\varepsilon} - sT$	T, $\boldsymbol{\sigma}$, $\boldsymbol{\zeta}$

1. Constitutive Assumptions for SMAs

The first step in developing constitutive equations for a SMA is to properly select the independent and dependent state variables that will characterize the behavior of the material. Next, we discuss how to obtain constitutive equations by utilizing the Gibbs free energy as the thermodynamic potential. The constitutive behavior of a material point is characterized by five response functions, $\hat{G}$, $\hat{\boldsymbol{\varepsilon}}$, $\hat{s}$ and $\hat{\mathbf{q}}$, which give G, $\boldsymbol{\varepsilon}$, s, and $\mathbf{q}$, when $\boldsymbol{\sigma}$, T and $\mathbf{g}$ are known:

$$\boldsymbol{\varepsilon} = \hat{\boldsymbol{\varepsilon}}\left(\boldsymbol{\sigma}, T, \mathbf{g}, \boldsymbol{\zeta}\right) \tag{2.22}$$

$$\mathbf{q} = \hat{\mathbf{q}}\left(\boldsymbol{\sigma}, T, \mathbf{g}, \boldsymbol{\zeta}\right) \tag{2.23}$$

$$s = \hat{s}\left(\boldsymbol{\sigma}, T, \mathbf{g}, \boldsymbol{\zeta}\right) \tag{2.24}$$

$$G = \hat{G}\left(\boldsymbol{\sigma}, T, \mathbf{g}, \boldsymbol{\zeta}\right) \tag{2.25}$$

The key point in the process of obtaining constitutive equations is to consider that every admissible thermodynamic process in the body must obey the entropy inequality at each time t and for all material points in the body [78]. Also it is assumed that, for a fixed material point at a given time t, the variables $\boldsymbol{\sigma}$, $\dot{\boldsymbol{\sigma}}$, T, $\dot{T}$, $\mathbf{g}$, $\dot{\mathbf{g}}$, $\boldsymbol{\zeta}$ and $\dot{\boldsymbol{\zeta}}$ can all be varied independently, and $\dot{T}$, $\dot{\mathbf{g}}$ and $\dot{\boldsymbol{\zeta}}$ are not arguments in the response functions. Substituting the first law of thermodynamics 2.17,

$$\rho\dot{u} = \boldsymbol{\sigma} : \dot{\boldsymbol{\varepsilon}} - \operatorname{div}\left(\mathbf{q}\right) + \rho r,$$

and the time derivative of the Legendre transformation as expressed in terms of the Gibbs free energy, given by Table II,

$$\dot{G} = \dot{u} - \frac{1}{\rho}\dot{\boldsymbol{\sigma}} : \boldsymbol{\varepsilon} - \frac{1}{\rho}\boldsymbol{\sigma} : \dot{\boldsymbol{\varepsilon}} - \dot{s}T - s\dot{T} \tag{2.26}$$

into the second law of thermodynamics, 2.21,

$$\rho\dot{s} + \frac{1}{T}\mathrm{div}\,(\mathbf{q}) - \frac{\rho r}{T} \geq 0,$$

we obtain

$$-\rho\dot{G} - \boldsymbol{\varepsilon} : \dot{\boldsymbol{\sigma}} - \rho s\dot{T} \geq 0. \tag{2.27}$$

Next, we differentiate the Gibbs free energy with respect to time. Assuming that $\hat{G}$ is a continuous function, we can use the chain rule of differentiation to obtain the time derivative of the Gibbs free energy as

$$\dot{G} = \frac{\partial\hat{G}}{\partial\boldsymbol{\sigma}} : \dot{\boldsymbol{\sigma}} + \frac{\partial\hat{G}}{\partial T}\dot{T} + \frac{\partial\hat{G}}{\partial\mathbf{g}} \cdot \dot{\mathbf{g}} + \frac{\partial\hat{G}}{\partial\boldsymbol{\zeta}} \cdot \dot{\boldsymbol{\zeta}}. \tag{2.28}$$

After substituting (2.28) into (2.27) we obtain:

$$-\boldsymbol{\varepsilon} : \dot{\boldsymbol{\sigma}} - \rho\left[\frac{\partial\hat{G}}{\partial\boldsymbol{\sigma}} : \dot{\boldsymbol{\sigma}} + \frac{\partial\hat{G}}{\partial T}\dot{T} + \frac{\partial\hat{G}}{\partial\mathbf{g}} \cdot \dot{\mathbf{g}} + \frac{\partial\hat{G}}{\partial\boldsymbol{\zeta}} \cdot \dot{\boldsymbol{\zeta}}\right] - \rho s\dot{T} \geq 0. \tag{2.29}$$

We can now fix all variables, *i.e.*, $\boldsymbol{\sigma}$, $\dot{\boldsymbol{\sigma}}$, T, $\dot{T}$, $\mathbf{g}$, $\boldsymbol{\zeta}$, $\dot{\boldsymbol{\zeta}}$, but let $\dot{\mathbf{g}}$ vary arbitrarily. Since $\dot{\mathbf{g}}$ can assume either positive or negative values, 2.29 can only be satisfied through the requirement that $\partial\hat{G}/\partial\mathbf{g} \equiv 0$. Thus, the Gibbs free energy is not a function of $\mathbf{g}$, and consequently, no other state variable depends on $\mathbf{g}$.

Next, we fix all variables, except for $\dot{T}$, which results in the requirement that

$$s = -\frac{\partial\hat{G}}{\partial T}. \tag{2.30}$$

Following the same idea, the constitutive equation for strain can be obtained as follows:

$$\boldsymbol{\varepsilon} = -\rho\frac{\partial\hat{G}}{\partial\boldsymbol{\sigma}}. \tag{2.31}$$

After defining the above two constitutive equations for entropy and stress, the Clausius-

Planck inequality has the remaining form:

$$-\rho\frac{\partial\hat{\psi}}{\partial\boldsymbol{\zeta}}\cdot\dot{\boldsymbol{\zeta}}\geq 0 \tag{2.32}$$

Depending on the form of the Gibbs free energy, the expression for stress and entropy can be determined through (2.31) and (2.30), respectively. Next chapter, we will present a specific form of the Gibbs free energy that is considered by the constitutive model proposed by Boyd and Lagoudas [24].

CHAPTER III

THERMOMECHANICAL CONSTITUTIVE MODEL FOR SMAS

The basic thermodynamic framework for the constitutive model for SMAs was presented in the previous chapter. In this chapter we present the derivation of the constitutive model for polycrystalline shape memory alloys proposed by Boyd and Lagoudas [24]. The constitutive equations will be determined by following the procedure of thermodynamics considering interval state variables, which was presented in the Chapter II. The approach is to propose a specific form of the Gibbs free energy that contains terms that are relevant for the description of the constitutive behavior of the SMAs.

A. Choice of Internal State Variables

The first step towards obtaining constitutive equations for SMAs is the selection of the internal variables that will best represent the SMA behaviors of interest. We have seen in Chapter I that the martensitic phase itself can exist in two different forms: the twinned martensite M^t, and the detwinned martensite M^d. Recall that twinned martensite is induced by temperature variation, *i.e.* cooling. It is formed by different variants of martensite configured in an energetically favorable manner such that no macroscopic deformation is observed during transformation. Detwinned martensite, on the other hand, is induced by stress only and it is formed predominantly by a single variant of martensite. We also saw in Chapter I that the martensitic phase transformation into detwinned martensite leads to a macroscopic shape change. This strain generated by the martensitic phase transformation is called transformation strain $\boldsymbol{\varepsilon}^t$.

Our constitutive model considers the martensitic volume fraction ξ and the transformation strain $\boldsymbol{\varepsilon}^t$ to be the internal state variables. The martensitic volume fraction is assumed to be a scalar quantity, and it incorporates the volume fraction of all variants presented in the material.

B. Kinematic Assumptions

Experimental observations have shown that polycrystalline SMAs can achieve transformation strains of about 6%. Therefore, we can use infinitesimal strains, as mentioned earlier, to describe their deformations. With the assumption of infinitesimal strains, there is no longer a meaningful distinction between reference and current configurations. As a consequence, the total strain tensor can be decomposed additively into two components, a thermoelastic $\boldsymbol{\varepsilon}^{th}$, and an inelastic $\boldsymbol{\varepsilon}^{in}$ part as follows:

$$\boldsymbol{\varepsilon} = \boldsymbol{\varepsilon}^{th} + \boldsymbol{\varepsilon}^{in}. \tag{3.1}$$

The inelastic strain component could further be decomposed into additional components to account for various phenomena, including the generalization of transformation strain, $\boldsymbol{\varepsilon}^t$, the formation of plastic strains, $\boldsymbol{\varepsilon}^p$, and strain generated during the detwinning process $\boldsymbol{\varepsilon}^d$. However, since in this work we are neither interested in modeling plastic processes nor re-orientation processes, we assume that the inelastic component of strain is associated with only the transformation strain

$$\boldsymbol{\varepsilon}^{in} = \boldsymbol{\varepsilon}^t. \tag{3.2}$$

C. Constitutive Assumptions for the SMA Material

Now that we have selected the internal state variables, ξ and $\boldsymbol{\varepsilon}^t$, and also defined the applicable kinematics of the SMA material we want to model, the next step is to define the thermodynamic potential that will be used. In this model, the Gibbs energy is selected to be the thermodynamic potential, instead of the Helmholtz free energy. Notice that the Gibbs free energy, G, is a function of the independent state variables stress, $\boldsymbol{\sigma}$, and temperature, T, which can be more suitable when comparing numerical with experimental results.

The total Gibbs free energy is given by [24, 79]:

$$\begin{aligned} G\left(\boldsymbol{\sigma}, T, \xi, \boldsymbol{\varepsilon}^t\right) = &-\frac{1}{2\rho}\boldsymbol{\sigma} : \boldsymbol{\mathcal{S}} : \boldsymbol{\sigma} - \frac{1}{\rho}\boldsymbol{\sigma} : \left[\boldsymbol{\alpha}\left(T - T_0\right) + \boldsymbol{\varepsilon}^t\right] + \\ &c\left[\left(T - T_0\right) - T\ln\left(\frac{T}{T_0}\right)\right] - s_0 T + u_0 + f(\xi) \end{aligned} \tag{3.3}$$

where T_0 is a reference temperature, and ρ is the mass density. The effective material parameters S, $\boldsymbol{\alpha}$, c, s_0, and u_0 are the 4^{th} order effective compliance tensor, and the 2^{th} order effective thermal expansion tensor, the effective specific heat coefficient, the effective specific entropy at the reference state, and the effective specific internal energy at the reference state, respectively. The function $f(\xi)$ is the hardening function and will be defined in the following sections.

The effective material properties can be defined in terms of the martensitic volume fraction, ξ, by the rule of mixtures

$$\boldsymbol{\mathcal{S}}\left(\xi\right) = \boldsymbol{\mathcal{S}}^A + \xi\left(\boldsymbol{\mathcal{S}}^M - \boldsymbol{\mathcal{S}}^A\right) = \boldsymbol{\mathcal{S}}^A + \xi\Delta\boldsymbol{\mathcal{S}} \tag{3.4}$$

$$\boldsymbol{\alpha}\left(\xi\right) = \boldsymbol{\alpha}^A + \xi\left(\boldsymbol{\alpha}^M - \boldsymbol{\alpha}^A\right) = \boldsymbol{\alpha}^A + \xi\Delta\boldsymbol{\alpha} \tag{3.5}$$

$$c\left(\xi\right) = c^A + \xi\left(c^M - c^A\right) = c^A + \xi\Delta c \tag{3.6}$$

$$s_0\left(\xi\right) = s_0^A + \xi\left(s_0^M - s_0^A\right) = s_0^A + \xi\Delta s_0 \tag{3.7}$$

$$u_0\left(\xi\right) = u_0^A + \xi\left(u_0^M - u_0^A\right) = u_0^A + \xi\Delta u_0 \tag{3.8}$$

where the superscripts A and M represent the austenitic and martensitic phase, respectively.

Constitutive relations are obtained following a similar procedure presented in Chapter II, Section D. The Gibbs free energy, G, and the internal energy, u, which are related to each other through the Legendre transformation, are substituted into the first and second law of thermodynamics as expressed in the Clausius-Planck inequality [78]. After imposing restrictions to the behavior of the material in the Clausius-Planck inequality, the total infinitesimal strain tensor and the entropy are defined as

$$\boldsymbol{\varepsilon} = -\rho \frac{\partial G}{\partial \boldsymbol{\sigma}} = \boldsymbol{\mathcal{S}} : \boldsymbol{\sigma} + \boldsymbol{\alpha} \left(T - T_0 \right) + \boldsymbol{\varepsilon}^t, \tag{3.9}$$

$$s = -\frac{\partial G}{\partial T} = \frac{1}{\rho} \boldsymbol{\sigma} : \boldsymbol{\alpha} + c \ln \left(\frac{T}{T_0} \right) + s_0. \tag{3.10}$$

After defining the expressions for strain tensor and entropy, we have the remainder of the Clausius-Planck inequality, also known as the local dissipation inequality:

$$\left(-\rho \frac{\partial G}{\partial \boldsymbol{\varepsilon}^t} \right) : \dot{\boldsymbol{\varepsilon}}^t + \left(-\rho \frac{\partial G}{\partial \xi} \right) \dot{\xi} \geq 0. \tag{3.11}$$

Next, we must propose evolution equations for the internal state variables, ξ, and $\boldsymbol{\varepsilon}^t$.

1. Evolution of Internal State Variables and Kuhn-Tucker Conditions

Now that the expressions for the total strain, entropy and the local form of the dissipation inequality have been defined, we need to determine the evolution equations for the internal variables $\boldsymbol{\varepsilon}^t$ and ξ. One key assumption made about martensitic phase transformation without the possibility of reorientation is that any change in the current state of the system is only with a change in the martensitic volume fraction, and that any other internal state variable evolves with it [79]. Given this, a relation between the evolution of the transformation strain and the evolution of the martensitic volume fraction during forward and reverse transformation (flow rule) can be expressed by

$$\dot{\boldsymbol{\varepsilon}}^t = \boldsymbol{\Lambda}\dot{\xi}, \tag{3.12}$$

where $\boldsymbol{\Lambda}$ is the transformation tensor, [1] which determines the transformation strain direction, and is assumed to have the following form:

$$\boldsymbol{\Lambda} = \begin{cases} \dfrac{3}{2}H(\sigma)\dfrac{\boldsymbol{\sigma}'}{\overline{\boldsymbol{\sigma}}} \quad ; \qquad \dot{\xi} > 0 \\ H(\sigma)\dfrac{\varepsilon^{t-r}}{\overline{\varepsilon}^{t-r}} \quad ; \qquad \dot{\xi} < 0 \end{cases} \tag{3.13}$$

where H is the maximum uniaxial transformation strain.

The deviatoric stress tensor $\boldsymbol{\sigma}'$ and the transformation strain at the reversal of phase transformation $\boldsymbol{\varepsilon}^{t-r}$, are defined by

$$\overline{\sigma} = \sqrt{\frac{3}{2}||\boldsymbol{\sigma}'||^2} \quad ; \quad \boldsymbol{\sigma}' = \boldsymbol{\sigma} - \frac{1}{3}\left(\mathrm{tr}\boldsymbol{\sigma}\right)\mathbf{1} \quad ; \quad \overline{\varepsilon}^{t-r} = \sqrt{\frac{2}{3}||\varepsilon^{t-r}||^2} \tag{3.14}$$

where $||\cdot||^2 = (\cdot : \cdot)$ is the inner product of the enclosed quantity.

By substituting the flow rule, (3.12) into (3.11), the local dissipation inequality, can be rewritten as:

$$\left(\boldsymbol{\sigma} : \boldsymbol{\Lambda} - \rho\frac{\partial G}{\partial \xi}\right)\dot{\xi} = \pi\dot{\xi} \geq 0 \tag{3.15}$$

where π is defined as a thermodynamic force conjugated to ξ and has the form

$$\begin{aligned} \pi =& \boldsymbol{\sigma} : \boldsymbol{\Lambda} + \frac{1}{2}\boldsymbol{\sigma} : \Delta\boldsymbol{\mathcal{S}} : \boldsymbol{\sigma} + \boldsymbol{\sigma} : \Delta\alpha\left(T - T_0\right) + \\ & - \rho\Delta c\left[\left(T - T_0\right) - T\ln\left(\frac{T}{T_0}\right)\right] + \rho\Delta s_0 T - \rho\Delta u_0 - \frac{\partial f}{\partial \xi} \end{aligned} \tag{3.16}$$

Equation 3.12 connects the evolution equation of the transformation strain with the evolution of the martensitic volume fraction. As a result, the transformation strain is not an independent state variable anymore. Therefore, it is sufficient to define an evolution equation for only the martensitic volume fraction, namely, to define an expression for $\dot{\xi}$. And this is connected to the conditions imposed for the martensitic phase transformation's onset.

---

[1] The current form of the transformation tensor, $\boldsymbol{\Lambda}$, can be associated to J_2 plasticity. This is discussed in the previous work of [79], which also proposes different forms of the transformation tensor, in the context of large strain formulations, so that the cases of $J_2 - J_3$ and $J_2 - J_3 - I_1$ plasticity can also be contemplated.

The conditions for the occurrence of the martensitic phase transformations, forward and reverse, need to be defined now. The current constitutive model assumes that the martensitic phase transformation will take place whenever the thermodynamic force π reaches a threshold value. This criterion, assumed to be valid for both the onset of the forward and the reverse phase transformation, must be implemented in such a way that the second law of thermodynamics, in the form of the Clausius-Planck inequality, is satisfied at all times, as discussed next:

1. When the forward martensitic transformation is taking place, $\dot{\xi}$ assumes positive values since austenite is being transformed into martensite. Therefore, the only way that the Clausius-Planck inequality, Eqn. 3.15, can be satisfied is for π to assume a positive value. Consequently, for the forward martensitic transformation, $\dot{\xi} > 0$, the function π assumes the value of $\pi = Y^*$.

2. However, when the reverse martensitic transformation is taking place, $\dot{\xi}$ assumes negative values since martensite is transforming back into austenite. Therefore, the only way that the Clausius-Planck inequality, Eqn. 3.15, can be satisfied is for π to assume a negative threshold value. Consequently, for the reverse martensitic transformation, $\dot{\xi} < 0$, the function π assumes the value of $\pi = -Y^*$.

3. Finally, when the state of stress and temperature of the SMA is such that no phase transformation is taking place, $\dot{\xi} = 0$. Therefore, the second law of thermodynamics is satisfied regardless of the value of π, because $\pi\dot{\xi} = 0$. In

fact, in that case the Clausius-Planck inequality turns into an equality, which indicates the SMA is not dissipating any energy in the elastic regime.

The above relations for the forward and the reverse martensitic transformation can be defined in an implicit way by introducing a transformation function, Φ, such that:

$$\Phi = \begin{cases} \pi - Y^* & ; \quad \dot{\xi} > 0 \\ \\ -\pi - Y^* & ; \quad \dot{\xi} < 0 \end{cases} \tag{3.17}$$

Thus, the transformation function, Φ, must satisfy the condition of $\Phi = 0$ during both forward and reverse phase transformations. The transformation function represents a transformation surface for a given set of internal state variables, and the two surfaces for $\xi = 0$ and $\xi = 1$ represent the upper and lower boundaries of the transformation surfaces. Any stress and state that do not belong on the surfaces is considered to be elastic. The constraints on the evolution of the martensitic volume fraction presented above can be expressed in terms of the so-called Kuhn-Tucker conditions:

$$\dot{\xi} \geq 0; \qquad \Phi\left(\sigma, T, \xi\right) \leq 0; \qquad \Phi\dot{\xi} = 0 \tag{3.18}$$

$$\dot{\xi} \leq 0; \qquad \Phi\left(\sigma, T, \xi\right) \leq 0; \qquad \Phi\dot{\xi} = 0$$

where all the relations should hold simultaneously along any loading path. During phase transformation, the stress state should remain on the transformation surface [27, 80, 81]. This condition is mathematically expressed by the so-called consistency condition. Following the Kuhn-Tucker condition, and assuming that martensitic transformation is rate independent, the consistency condition is defined by $\dot{\Phi} = 0$, or in other words:

$$\dot{\Phi} = \frac{\partial \Phi}{\partial \sigma} : \dot{\sigma} + \frac{\partial \Phi}{\partial T}\dot{T} + \frac{\partial \Phi}{\partial \xi}\dot{\xi} = 0, \tag{3.19}$$

where the partial derivatives of the transformation function, for forward transformation ($\dot{\xi} > 0$) are given by

$$\frac{\partial \Phi}{\partial \boldsymbol{\sigma}} = \boldsymbol{\Lambda} + \Delta \boldsymbol{\mathcal{S}} : \boldsymbol{\sigma} + \Delta \boldsymbol{\alpha} \left(T - T_0\right) \tag{3.20}$$

$$\frac{\partial \Phi}{\partial T} = \Delta \boldsymbol{\alpha} : \boldsymbol{\sigma} + \rho \Delta c \ln \left(\frac{T}{T_0}\right) + \rho \Delta s_0 \tag{3.21}$$

$$\frac{\partial \Phi}{\partial \xi} = -\frac{\partial^2 f}{\partial \xi^2}. \tag{3.22}$$

the partial derivatives of the transformation function, for reverse phase transformation, ($\dot{\xi} < 0$), are given by

$$\frac{\partial \Phi}{\partial \boldsymbol{\sigma}} = -\boldsymbol{\Lambda} - \Delta \boldsymbol{\mathcal{S}} : \boldsymbol{\sigma} - \Delta \boldsymbol{\alpha} \left(T - T_0\right) \tag{3.23}$$

$$\frac{\partial \Phi}{\partial T} = -\Delta \boldsymbol{\alpha} : \boldsymbol{\sigma} - \rho \Delta c \ln \left(\frac{T}{T_0}\right) - \rho \Delta s_0 \tag{3.24}$$

$$\frac{\partial \Phi}{\partial \xi} = \frac{\partial^2 f}{\partial \xi^2} \tag{3.25}$$

The above formulation is consistent with the assumption of rate-independent behavior of SMAs. As we have seen in Chapter I experimental observations have shown that the martensitic transformation is a rate-independent phenomenon, due to its diffusionless nature.

The final step in the constitutive formulation is to select a hardening function, $f(\xi)$. The hardening function is used to account for the interactions between the austenitic phase and the martensitic phase, and also among the martensitic variants themselves. So far, we have not considered any particular form of the hardening function, which appears in Eqn. 3.3 and is fundamental to the construction of Eqn. 3.16. Here we consider a second order polynomial representation of the transformation-hardening function. The hardening function $f\left(\xi\right)$ assumes the following form during

Table III. Definitions of the model parameters of Boyd and Lagoudas model

$$\boxed{\begin{gathered} \rho b^A = -\rho\Delta s_0\left(A_f - A_s\right) \\ \rho b^M = -\rho\Delta s_0\left(M_s - M_f\right) \\ Y^* = \tfrac{1}{4}\rho\Delta s_0\left(M_s + M_f - A_f - A_s\right) \\ \mu_1 = \tfrac{1}{2}\rho\Delta s_0\left(M_s + A_f\right) - \rho\Delta u_0 \\ \mu_2 = \tfrac{1}{4}\rho\Delta s_0\left(A_s - A_f - M_f + M_s\right) \end{gathered}}$$

the forward and reverse phase transformation:

$$f\left(\xi\right) = \begin{cases} \frac{1}{2}\rho b^M \xi^2 + \left(\mu_1 + \mu_2\right)\xi; & \dot{\xi} > 0 \\ \\ \frac{1}{2}\rho b^A \xi^2 + \left(\mu_1 - \mu_2\right)\xi; & \dot{\xi} < 0 \end{cases} \tag{3.26}$$

where ρb^M, ρb^A, μ_1, μ_2 are transformation model parameters. These model parameters of the hardening function can be calculated as a function of the material constants obtained from experimental tests. Table III shows the model parameters.

Next section presents a one-dimensional reduction of the constitutive model and the procedure to identify material parameters from experimental results that are needed for the model's calibrations.

D. One-dimensional Reduction and Identification of the Material Parameters

Since a great number of SMA applications can be reduced to a one-dimensional representation, it is convenient to reduce the model from its three dimensional form to a one-dimensional one. Moreover, the reduction of the model to a one-dimensional form helps the identification of the material parameters through experimental results. The reduction can be accomplished by assuming uniaxial loading of an SMA specimen, *e.g.* a wire, in the x_1-direction. This loading state leads to the condition at which the stress tensor has only one non-zero component

$$\sigma_{11} = \sigma \neq 0 \tag{3.27}$$

where σ is the applied uniaxial stress.

The transformation strain tensor components are given by

$$\varepsilon^t_{11} = \varepsilon^t; \quad \varepsilon^t_{22} = \varepsilon^t_{33} = -\frac{1}{2}\varepsilon^t; \quad \varepsilon_{ij} = 0; \qquad \mathrm{i,j} = 1,...,3 \tag{3.28}$$

where ε^t is the uniaxial transformation strain assuming that it results in isochoric deformations.

Due to the fact that the stress tensor has one non-zero component and the transformation strain tensor is of the form presented above, the double dot product between tensor quantities of the equations presented in this chapter will be reduced to a simple scalar multiplication. As a result, the fourth-order compliance tensors $\boldsymbol{\mathcal{S}}^A$ and $\boldsymbol{\mathcal{S}}^M$ reduce to the scalar components $S^A_{1111} = S^A$ and $S^M_{1111} = S^M$, respectively. The compliance coefficients S^A and S^M are given by $S^A = \frac{1}{E^A}$ and $S^M = \frac{1}{E^M}$, in terms of the elastic stiffness coefficients. The second-order thermal expansion tensors $\boldsymbol{\alpha}^A$ and $\boldsymbol{\alpha}^M$ reduce to the scalar components $\alpha^A_{11} = \alpha^A$ and $\alpha^M_{11} = \alpha^M$, whereas the transformation tensor $\boldsymbol{\Lambda}$ reduces to $H(\sigma)$ in the one-dimensional case. The effective compliance and thermal expansion coefficients, S, and α, are defined by the reduced form of Eqns. 3.4 and 3.5 , respectively:

$$S\left(\xi\right) = S^A + \xi\left(S^M - S^A\right) = S^A + \xi\Delta S \tag{3.29}$$

$$\alpha\left(\xi\right) = \alpha^A + \xi\left(\alpha^M - \alpha^A\right) = \alpha^A + \xi\Delta\alpha \tag{3.30}$$

The evolution equation of the transformation strain given by Eq. 3.12 becomes

$$\dot{\varepsilon^t} = H\operatorname{sgn}(\sigma)\dot{\xi}, \tag{3.31}$$

while the one-dimensional form of the total strain is given by

$$\varepsilon = S\sigma + \alpha\left(T - T_0\right) + \varepsilon^t. \tag{3.32}$$

The one-dimensional form of the transformation function is given by

$$\begin{aligned} \Phi = \left|\sigma\right| H + \frac{1}{2}\sigma^2\Delta S + \sigma\Delta\alpha\left(T - T_0\right) - \rho\Delta c\left[\left(T - T_0\right) - T\ln\left(\frac{T}{T_0}\right)\right] \\ + \rho\Delta s_0 T - \rho\Delta u_0 - \frac{\partial f}{\partial\xi} \mp Y^* = 0. \end{aligned} \tag{3.33}$$

The consistency condition, Eq. 3.19, reduces to the following form:

$$\dot{\Phi} = \frac{\partial\Phi}{\partial\sigma}\dot{\sigma} + \frac{\partial\Phi}{\partial T}\dot{T} + \frac{\partial\Phi}{\partial\xi}{}_{\xi}\,\Phi = 0. \tag{3.34}$$

For forward transformation, $\dot{\xi} > 0$, we have:

$$\frac{\partial\Phi}{\partial\sigma} = H\operatorname{sgn}(\sigma) + \Delta S\sigma + \Delta\alpha\left(T - T_0\right) \tag{3.35}$$

$$\frac{\partial\Phi}{\partial T} = \Delta\alpha\sigma + \rho\Delta c\ln\left(\frac{T}{T_0}\right) + \rho\Delta s_0 \tag{3.36}$$

$$\frac{\partial\Phi}{\partial\xi} = -\frac{\partial^2 f}{\partial\xi^2}. \tag{3.37}$$

For reverse phase transformation, $\dot{\xi} < 0$, we have

$$\frac{\partial\Phi}{\partial\sigma} = -H\operatorname{sgn}(\sigma) - \Delta S\sigma - \Delta\boldsymbol{\alpha}\left(T - T_0\right) \tag{3.38}$$

$$\frac{\partial\Phi}{\partial T} = -\Delta\alpha\sigma - \rho\Delta c\ln\left(\frac{T}{T_0}\right) - \rho\Delta s_0 \tag{3.39}$$

$$\frac{\partial\Phi}{\partial\xi} = \frac{\partial^2 f}{\partial\xi^2} \tag{3.40}$$

The calibration of the constitutive model with experimentally obtained material parameters is presented next. The material parameters that need to be determined are the elastic stiffness coefficients of austenitic and martensitic phases, E^A, and E^M, respectively; the thermal expansion coefficients of both phases, α_A, α_M; the heat capacity coefficient per unit volume, $\rho\Delta c$, which expresses the difference between the heat capacity coefficients of martensite and austenite; the maximum uniaxial transformation strain, H; the difference in internal energy per unit of volume between martensite and austenite at reference state, $\rho\Delta u_0$; the difference in the entropy per unit volume between martensite and austenite at the reference state, Δs_0; and finally the transformation temperatures at zero stress that define the start and finish of the forward and reverse martensitic phase transformation, *i.e.*, M_s, M_f, A_s, and A_f.

From a uniaxial pseudoelastic test at isothermal conditions one can determine the material parameters E^A, E^M, and H. As an example, Fig. 8 shows two tensile loading - unloading tests of an SMA wire performed at the temperatures of 308K, and 328K, under isothermal conditions. The elastic stiffness of austenite is determined by computing the initial slope of the stress-strain curve, while the elastic stiffness of martensite is determined as the slope at the end of the phase transformation. The maximum uniaxial transformation strain H is estimated by extending the unloading part of the stress-strain curve using the elastic stiffness of the martensitic phase E^M, until it reaches the x-axis, as shown in Fig. 8.

The thermal expansion coefficient α^A, and α^M can be obtained by measuring the slopes of the strain-temperature curve under constant stress, at high temperature for austenite and low temperature for martensite, while the the heat capacity coefficient per unit volume, $\rho\Delta c$ is obtained from calorimetric tests. The slope of the stress-temperature curves can be computed by defining the stress values for which the martensitic phase transformations (forward and reverse) start and end, *i.e.*, σ^{Ms}, σ^{Mf},

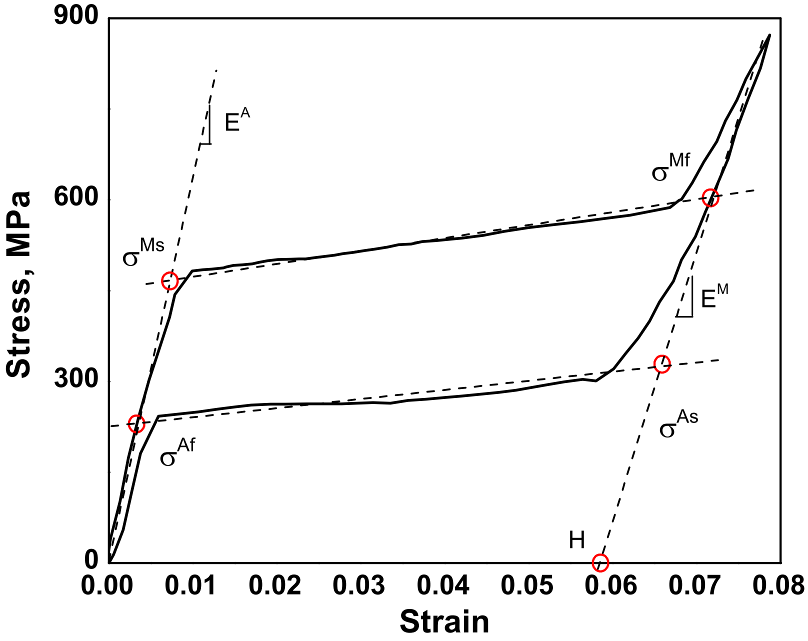

(a) Stress *vs.* strain for $T = 308$K

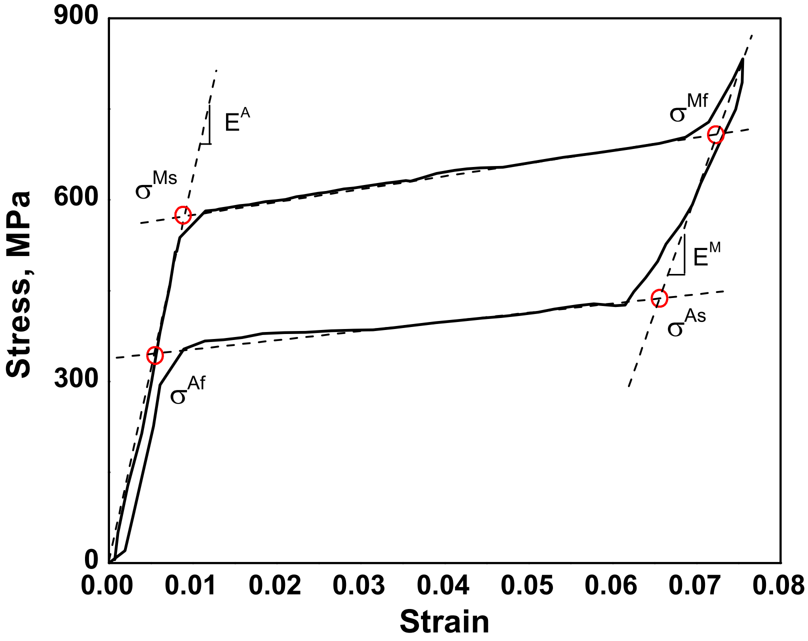

(b) Stress *vs.* strain $T = 328$K

Fig. 8. Experimental stress *vs.* strain curves for different temperatures (Lagoudas *et al.* [1]).

σ^{As}, and σ^{Af}, from the temperature tests of 303K, and 313K (Fig. 8). Then, with these two sets of stress values, four different straight lines can be extrapolated in the stress-temperature space, leading to the determination of transformation temperature curves and their slopes. The transformation temperatures at zero-stress, *i.e.*, M_f, M_s, A_s, and A_f, can be approximately obtained by computing the intersection points of the stress-temperature curves with the temperature axis, or can be obtained from a calorimetric test. In fact, the transformation temperatures calculated are not the same as those obtained by a differential calorimetry test, as will be shown later. However, since the temperature range of this work for pseudoelastic loading paths is for temperatures higher than austenitic finish temperature, this is a valid assumption.

The entropy difference $\rho\Delta s_0$ per unit of volume between the phases can be determined by the slopes of the stress-temperature transformation curves. With the aid of the one-dimensional forms of the the transformation function, Eqn. 3.33, and consistency condition, Eqn. 3.19, the slopes of the transformation curves can be analytically determined as follows:

$$\begin{aligned}&\left(\Delta S\sigma + \Delta\alpha\left(T - T_0\right) + H\mathrm{sgn}(\sigma)\right)\dot{\sigma} + \left(\Delta\alpha\sigma - \rho\Delta c\ln\left(\frac{T}{T_0}\right) + \rho\Delta s_0\right)\dot{T} + \\ &\quad - \frac{\partial^2 f}{\partial\xi^2}\dot{\xi} = 0\end{aligned} \tag{3.41}$$

Now, by substituting zero stress, neglecting the Δc and $\Delta\alpha$ terms (a common assumption for SMA materials), and assuming $\dot{\xi} = 0$ in the above equation, the slope $\frac{d\sigma}{dT}$ of these curves at zero stress is [25] :

$$\frac{d\sigma}{dT} = -\frac{\rho\Delta s_0}{H} \tag{3.42}$$

E. Closed-Form Solutions

For the case of a one-dimensional proportional loading path, Eqn. 3.31, Eqn. 3.32 and Eqn. 3.33 can be used to define closed-form solutions for either isothermal or isobaric loading paths when there is no reorienation phenomenon occurring. An expression for ξ can be obtained by solving (3.33) for both forward as well as reverse phase transformation. For the case of *Forward Phase Transformation*, and assuming $\Delta c = 0$ and $\Delta\alpha = 0$, the thermodynamic force π is given by:

$$\pi = |\sigma|\, H + \frac{1}{2}\Delta\mathcal{S}\sigma^2 + \rho\Delta s_0 T - \rho\Delta u_0 - \left(\rho b^M\xi + (\mu 1 + \mu 2)\right) = Y^* \tag{3.43}$$

Solving (3.43) for ξ, we obtain

$$\xi = \frac{1}{\rho b^M}\left(|\sigma|\, H + \frac{1}{2}\Delta\mathcal{S}\sigma^2 + \rho\Delta s_0\left(T - M_s\right)\right). \tag{3.44}$$

Substituting (3.43) into (3.32) for the case of forward martensitic transformation, the total strain becomes,

$$\varepsilon = \mathcal{S}\sigma + \alpha\left(T - T_0\right) + \frac{H\mathrm{sgn}\left(\sigma\right)}{\rho b^M}\left(|\sigma|\, H + \frac{1}{2}\Delta\mathcal{S}\sigma^2 + \rho\Delta s_0\left(T - M_s\right)\right), \tag{3.45}$$

where

$$S = S^A + \xi\left(S^M - S^A\right) \quad ; \qquad \alpha = \alpha^A + \xi\left(\alpha^M - \alpha^A\right).$$

Next, consider the case for *Reverse Phase Transformation.* The thermodynamic force π is given by:

$$\pi = |\sigma|\, H + \frac{1}{2}\Delta\mathcal{S}\sigma^2 + \rho\Delta s_0 T - \rho\Delta u_0 - \left(\rho b^A\xi + (\mu 1 - \mu 2)\right) = -Y^*, \tag{3.46}$$

which leads to

$$\xi = \frac{1}{\rho b^A}\left(Y^* + |\sigma| H + \frac{1}{2}\Delta\mathcal{S}\sigma^2 + \rho\Delta s_0 (T - A_f)\right). \qquad (3.47)$$

Substituting (3.46) into (3.32) we get an expression for the total strain for the case of reverse martensitic transformation.

$$\varepsilon = \mathcal{S}\sigma + \alpha (T - T_0) + \frac{H \mathrm{sgn}(\sigma)}{\rho b^A}\left(|\sigma| H + \frac{1}{2}\Delta\mathcal{S}\sigma^2 + \rho\Delta s_0 (T - A_f)\right) \qquad (3.48)$$

Finally, for the cases where neither forward nor reverse transformation occur, the total strain is given by:

$$\varepsilon = \mathcal{S}^\gamma \sigma + \alpha^\gamma (T - T_0) \qquad (3.49)$$

where γ is either austenite or martensite

Next, we present different examples that utilize the closed-form solutions discussed above to predict the behavior of an SMA wire under different thermomechanical loading paths. The value of the material parameters are presented in Table IV. These values were evaluated from experimental results of the alloy presented in Fig. 8.

Firstly, we consider isothermal pseudoelastic loading paths. The stress *vs.* temperature and stress *vs.* strain plots with different initial temperatures. The selected temperatures are $T_1 = 328$K, $T_2 = 308$K, $T_3 = 276$K, and $T_4 = 260$K. Figure 9 shows the stress *vs.* temperature plot of these four temperatures, while the stress *vs.* strain curves are presented in Fig. 10.

We consider now isobaric loading paths. Specifically, three isobaric paths for the stress levels of $\sigma = 100$ MPa, $\sigma = 150$ MPa and $\sigma = 200$ MPa are considered. Figure 11 shows the stress *vs.* temperature plots with the isobaric loading paths,

Table IV. Values of the material parameters of a typical SMA wire

$E^A = 55.0 \cdot 10^9 Pa$	$E^M = 46.0 \cdot 10^9 Pa$
$\Delta\alpha^A = 0.0\mathrm{K}$	$\Delta c = 0.0\mathrm{J/(kgK)}$
$M_f = 230\mathrm{K}$	$M_s = 245\mathrm{K}$
$A_s = 270\mathrm{K}$	$A^{0f} = 280\mathrm{K}$
$H = 0.056$	$\dfrac{d\sigma}{dT} = 7.4\ \mathrm{MPa/K}$
$T_0 = 298\mathrm{K}$	

while Fig. 12 shows the strain *vs.* temperature plots, for the different stress levels.

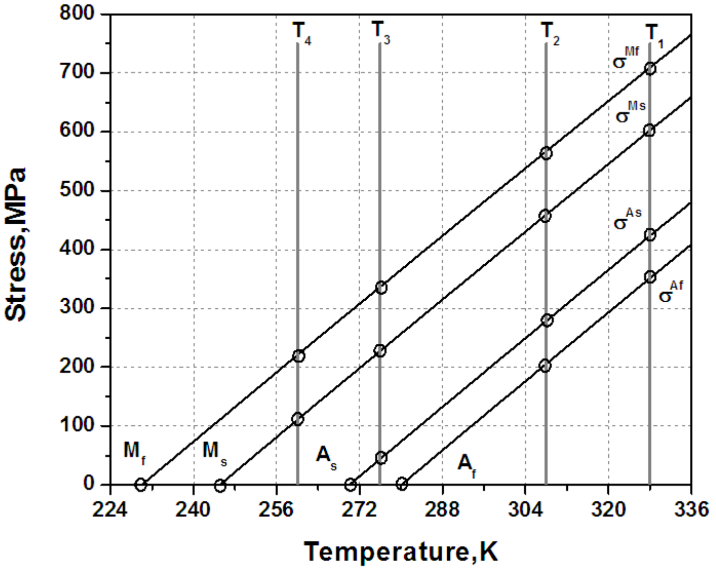

Fig. 9. Isothermal pseudoelastic loading paths. Stress *vs.* temperature.

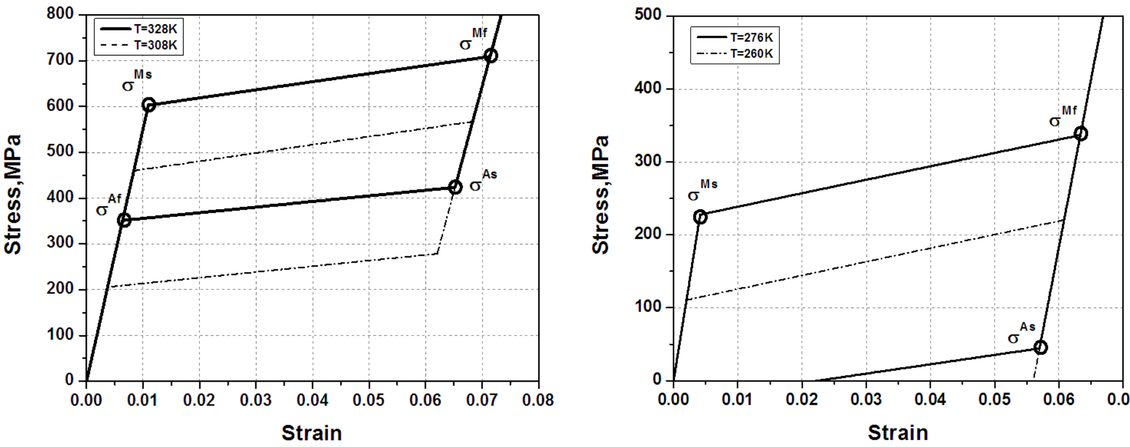

(a) Stress *vs.* strain curves for $T = 328$K and $T = 308$K

(b) Stress *vs.* strain curves for $T = 276$K and $T = 260$K

Fig. 10. Isothermal pseudoelastic stress *vs.* strain curves for different temperatures (Lagoudas *et al.* [1]).

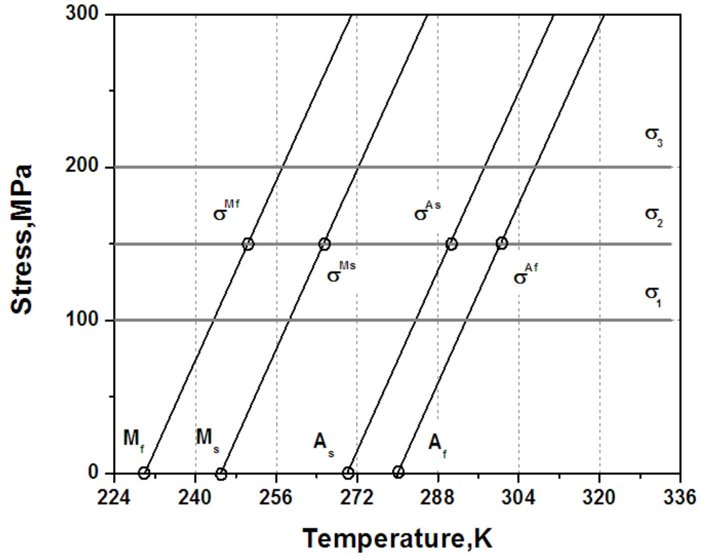

Fig. 11. Stress *vs.* temperature plot of isobaric loading paths (Lagoudas *et al.* [1]).

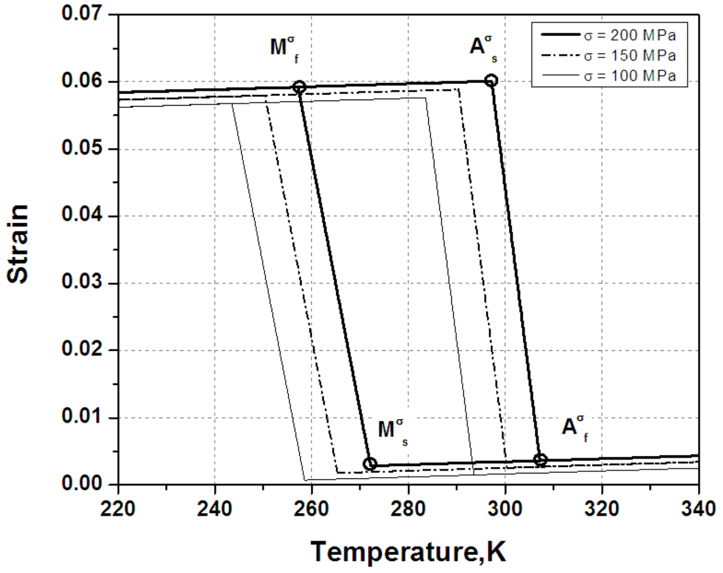

Fig. 12. Strain *vs.* temperature plot of isobaric loading paths (Lagoudas *et al.* [1]).

CHAPTER IV

THERMOMECHANICAL COUPLING IN SHAPE MEMORY ALLOYS

The previous chapters have introduced the basic thermodynamic framework and the constitutive model for polycrystalline SMAs. This chapter considers the thermomechanical coupling that occurs on SMAs. It has been experimentally observed that the thermomechanical coupling is very strong in SMAs. Since latent heat is produced/absorbed during the stress-induced martensitic phase transformations, temperature variations can occur in the material, altering its behavior. The amount of latent heat produced is strongly related to the amount of martensitic phase transformation. Therefore, the thermomechanical coupling is a key factor to be considered in the modeling of SMA.

The thermomechanical coupling induces the time-dependent behavior due to the latent heat production during phase transformation, and also due to the interaction of the SMA with the heat transfer medium. This time-dependent behavior leads to the appearance of phenomena such as transformation induced stress relaxation and transformation induced creep. Therefore, it can be said that the time rate of change of martensitic phase transformation is controlled by the time rate of the heat transfer. As a result, it is important to consider different forms of heat conditions, such as adiabatic, isothermal and non-isothermal heat convection cases. For the sake of simplicity, we define non-isothermal conditions as heat conditions that are in-between the isothermal and adiabatic cases, which are extreme cases.

The first step in modeling the thermomechanical coupling is to consider the local form of the first law of thermodynamics

$$\rho \dot{u} = \boldsymbol{\sigma} : \dot{\boldsymbol{\varepsilon}} - \operatorname{div}(\mathbf{q}) + \rho r.$$

We can rewrite the first law of thermodynamics, Eqn. 2.17, after combining it with the second law of thermodynamics, (2.21), and the Legendre transformation, Table II, as follows:

$$\rho T\dot{s} = \pi\dot{\xi} - \mathrm{div}\,(\mathbf{q}) + \rho r \tag{4.1}$$

where $\pi\dot{\xi}$ should be always ≥ 0, according to (3.15).

Next, we need to define an expression for the time derivative of entropy, $\dot{s}$. This expression can be found by computing the derivative of entropy with respect to time from (3.10), as:

$$\dot{s} = -\frac{\partial\dot{G}}{\partial T} = -\frac{\partial^2 G}{\partial T\partial\boldsymbol{\sigma}} : \dot{\boldsymbol{\sigma}} - \frac{\partial^2 G}{\partial T^2}\dot{T} + \frac{1}{\rho}\frac{\partial\pi}{\partial T}\dot{\xi}, \tag{4.2}$$

where the thermal expansion coefficient, $\boldsymbol{\alpha}$, and the heat capacity, c, can be defined in terms of the Gibbs free energy as:

$$\boldsymbol{\alpha} = -\rho\frac{\partial^2 G}{\partial\boldsymbol{\sigma}\partial T} \tag{4.3}$$

$$c = -T\frac{\partial^2 G}{\partial T^2}, \tag{4.4}$$

and the partial derivative of π with respect to the temperature, derived from (3.16), is given by

$$\frac{\partial\pi}{\partial T} = \boldsymbol{\Delta\alpha} : \boldsymbol{\sigma} - \rho\Delta c\ln\left(\frac{T}{T_0}\right) + \rho\Delta s_0 \tag{4.5}$$

Thus, Eqn. 4.2 can be rewritten as

$$\dot{s} = \frac{1}{\rho}\boldsymbol{\alpha} : \dot{\boldsymbol{\sigma}} + \frac{c}{T}\dot{T} + \left(\frac{1}{\rho}\boldsymbol{\Delta\alpha\sigma} - \Delta c\ln\left(\frac{T}{T_0}\right) + \Delta s_0\right)\dot{\xi}. \tag{4.6}$$

Now, by substituting Eqn. 4.6 into Eqn. 4.1, we obtain the relation:

$$\begin{aligned} T\boldsymbol{\alpha} : \dot{\boldsymbol{\sigma}} + \rho c\dot{T} + \left(-\pi + T\boldsymbol{\Delta\alpha} : \boldsymbol{\sigma} - \rho\Delta cT\ln\left(\frac{T}{T_0}\right) + \rho\Delta s_0 T\right)\dot{\xi} = \\ = \left(-\mathrm{div}\,(\mathbf{q}) + \rho r\right), \end{aligned} \tag{4.7}$$

which is the 3D form of the fully thermomechanical coupled heat equation for shape memory alloys. The first term of the left-hand side of Eqn. 4.7 expresses how the temperature changes due to a change in the stress state of the system, while the second term of the left-hand side is related to the amount of energy necessary to increase/decrease the temperature of the system by one degree. The third term of the left-hand side expresses how the temperature of the SMA changes due to a variation of the martensitic volume fraction, where the term in the big parenthesis is related to the latent heat due to phase transformation. Therefore, one can think about the martensitic phase transformation as being an internal heat source (or sink), which increases(or decreases) the temperature of the SMA. The first and second terms of the right-hand side of Eqn. 4.7 are related to the heat transfer processes that are occurring. The cases of heat transfer by conduction, convection, and/or resistive heating are considered based on the choice of **q**, and ρr, and will be discussed later.

1. Adiabatic Conditions

Different heat conditions can be contemplated by considering the energy balanced heat equation, Eqn. 4.7, derived previously. Adiabatic conditions, for example, can be simulated by vanishing the right-hand side of the heat equation, Eqn. 4.7, that is, $(-\mathrm{div}\,(\mathbf{q}) + \rho r) = 0$. Thus, the heat equation assumes the form:

$$T\boldsymbol{\alpha} : \dot{\boldsymbol{\sigma}} + \rho c\dot{T} + \left(-\pi + T\Delta\boldsymbol{\alpha} : \boldsymbol{\sigma} - \rho\Delta c T \ln\left(\frac{T}{T_0}\right) + \rho\Delta s_0 T\right)\dot{\xi} = 0 \tag{4.8}$$

The consistency condition, Eqn. 3.19 can be inserted in the heat equation for the adiabatic case, Eqn. 4.8, so that the heat equation can be determined as a function of the increment of stress (known) only. The increment of martensitic volume fraction can be derived from the consistency condition as:

$$\dot{\xi} = \frac{-\partial_{\boldsymbol{\sigma}}\Phi : \dot{\boldsymbol{\sigma}} - \partial_T \Phi \dot{T}}{\partial_\xi \Phi} \tag{4.9}$$

The increment of temperature can be easily derived by substituting Eqn. 4.9 into the heat equation, Eqn. 4.8. After some algebraic manipulations, we get:

$$\dot{T} = -\frac{\left[T\boldsymbol{\alpha} - \left(-\pi + T\Delta\boldsymbol{\alpha} : \boldsymbol{\sigma} - \rho\Delta c T \ln\left(\frac{T}{T_0}\right) + \rho\Delta s_0 T\right)\frac{\partial_{\boldsymbol{\sigma}}\Phi}{\partial_\xi\Phi}\right] : \dot{\boldsymbol{\sigma}}}{\left[\rho c - \left(-\pi + T\Delta\boldsymbol{\alpha} : \boldsymbol{\sigma} - \rho\Delta c T \ln\left(\frac{T}{T_0}\right) + \rho\Delta s_0 T\right)\frac{\partial_T\Phi}{\partial_\xi\Phi}\right]} \tag{4.10}$$

For the case of forward martensitic transformation, the increment of temperature can be found by substituting Eqn. 3.20, Eqn. 3.21, Eqn. 3.22 into Eqn. 4.10, and replacing π by Y^*. Similarly, we obtain the increment of temperature for the case of reserve transformation by substituting Eqn. 3.23, Eqn. 3.24, Eqn. 3.25 into Eqn. 4.10, and replacing π by $-Y^*$.

2. Non-isothermal Conditions

Next we derive the increment of temperature for non-isothermal conditions. The derivation of the increment of temperature follows the same procedure as the adiabatic conditions. Recall that the heat equation is given by

$$T\boldsymbol{\alpha} : \dot{\boldsymbol{\sigma}} + \rho c\dot{T} + \left(-\pi + T\Delta\boldsymbol{\alpha} : \boldsymbol{\sigma} - \rho\Delta c T \ln\left(\frac{T}{T_0}\right) + \rho\Delta s_0 T\right)\dot{\xi} = -\mathrm{div}\mathbf{q} + \rho r.$$

Therefore, by substituting the consistency condition, Eqn. 3.19, into the above equation, and after some algebraic manipulations, we obtain:

$$\dot{T} = \frac{-\left[T\boldsymbol{\alpha} - \left(-\pi + T\Delta\boldsymbol{\alpha} : \boldsymbol{\sigma} - \rho\Delta c T \ln\left(\frac{T}{T_0}\right) + \rho\Delta s_0 T\right)\frac{\partial_{\boldsymbol{\sigma}}\Phi}{\partial_\xi\Phi}\right] : \dot{\boldsymbol{\sigma}} + (-\mathrm{div}\mathbf{q} + \rho r)}{\left[\rho c - \left(-\pi + T\Delta\boldsymbol{\alpha} : \boldsymbol{\sigma} - \rho\Delta c T \ln\left(\frac{T}{T_0}\right) + \rho\Delta s_0 T\right)\frac{\partial_T\Phi}{\partial_\xi\Phi}\right]} \tag{4.11}$$

Similarly to the adiabatic adiabatic conditions, the increment of temperature for the case of forward martensitic transformation can be found by substituting Eqn. 3.20, Eqn. 3.21, Eqn. 3.22 into Eqn. 4.11, and also replacing π by Y^*. The increment of temperature for the case of reserve transformation can be found by substituting Eqn. 3.23, Eqn. 3.24, Eqn. 3.25 into Eqn. 4.11, and also replacing π by $-Y^*$.

Note that the increment of temperature, Eqn. 4.11 is a function of the increment of stress. However, it is often useful to obtain an expression of the increment of temperature as a function of the increment of strain. For this purpose, we can differentiate the constitutive relation of strain, Eq. 3.9, with respect of time and obtain an expression that relates the increment of stress with the increment of strain. The increment of Eqn. 2.22 has the form:

$$\dot{\boldsymbol{\varepsilon}} = -\rho \frac{\partial^2 G}{\partial \boldsymbol{\sigma}^2} : \dot{\boldsymbol{\sigma}} - \rho \frac{\partial^2 G}{\partial \boldsymbol{\sigma} \partial T} \dot{T} + \frac{\partial \pi}{\partial \boldsymbol{\sigma}} \dot{\xi} \tag{4.12}$$

After some algebraic manipulation, we obtain the increment of stress as

$$\dot{\boldsymbol{\sigma}} = \boldsymbol{\mathcal{S}}^{-1} : \left(\dot{\boldsymbol{\varepsilon}} - \boldsymbol{\alpha} \dot{T} - \left\{ \begin{array}{l} \partial_{\boldsymbol{\sigma}} \Phi (\dot{\xi} > 0) \\ \\ -\partial_{\boldsymbol{\sigma}} \Phi (\dot{\xi} < 0) \end{array} \right. \dot{\xi} \right). \tag{4.13}$$

Next, we substitute the increment of stress, Eqn. 4.13, into the consistency condition, Eqn. 3.19, and into the increment of temperature, Eqn. 4.11. After some algebraic manipulations we obtain the increment of martensitic volume fraction as a function of the increments of strain and temperature is given by:

$$\dot{\xi} = \frac{\left(\partial_{\boldsymbol{\sigma}} \Phi : \mathcal{S}^{-1} \right) : \dot{\boldsymbol{\varepsilon}} + \left(\partial_T \Phi - \partial_{\boldsymbol{\sigma}} \Phi : \mathcal{S}^{-1} : \alpha \right) \dot{T}}{\left(\partial_{\boldsymbol{\sigma}} \Phi : \mathcal{S}^{-1} : \partial_{\boldsymbol{\sigma}} \Phi - \partial_{\xi} \Phi \right)} \tag{4.14}$$

The final form of the heat equation for forward phase transformation is obtained by substituting the expressions for the increment of martensitic volume fraction, Eqn. 4.14, and the increment of stress for the forward transformation, Eqn. 4.13a, into Eqn. 4.11.

$$\begin{aligned}\mathcal{C}\dot{T} =& -\Big[T\boldsymbol{\alpha} : \mathcal{S}^{-1} + (-\pi + T\Delta\boldsymbol{\alpha} : \boldsymbol{\sigma} - \rho\Delta c T \ln\left(\frac{T}{T_0}\right) + \\ & \rho\Delta s_0 T - T\boldsymbol{\alpha} : \mathcal{S}^{-1} : \partial_{\boldsymbol{\sigma}}\Phi)\frac{(\partial_{\boldsymbol{\sigma}}\Phi : \mathcal{S}^{-1})}{(\partial_{\boldsymbol{\sigma}}\Phi : \mathcal{S}^{-1} : \partial_{\boldsymbol{\sigma}}\Phi - \partial_{\xi}\Phi)}\Big] : \dot{\boldsymbol{\varepsilon}} + \\ & -\boldsymbol{\nabla}\cdot\mathbf{q} + \rho r\end{aligned} \tag{4.15}$$

where $\mathcal{C}$ has the following form:

$$\begin{aligned}\mathcal{C} =& \rho c - T\boldsymbol{\alpha} : \mathcal{S}^{-1} : \boldsymbol{\alpha} + \\ & (-\pi + T\Delta\boldsymbol{\alpha} : \boldsymbol{\sigma} - \rho\Delta c T \ln\left(\frac{T}{T_0}\right) + \\ & \rho\Delta s_0 T - T\boldsymbol{\alpha} : \mathcal{S}^{-1} : \partial_{\boldsymbol{\sigma}}\Phi)\frac{(\partial_T\Phi - \partial_{\boldsymbol{\sigma}}\Phi : \mathcal{S}^{-1} : \boldsymbol{\alpha})}{(\partial_{\boldsymbol{\sigma}}\Phi : \mathcal{S}^{-1} : \partial_{\boldsymbol{\sigma}}\Phi - \partial_{\xi}\Phi)}\end{aligned} \tag{4.16}$$

Likewise forward martensitic phase transformation, an expression for $\dot{\xi}(t)$ as a function of $\dot{T}$ and $\dot{\varepsilon}(t)$ for reverse phase transformation can be found by substituting the increment of stress, Eqn. 4.13b into the consistency condition, Eqn. 3.19. After some algebraic manipulations, we obtain the increment of martensitic volume fraction for the case of reverse transformation as:

$$\dot{\xi} = \frac{-(\partial_{\boldsymbol{\sigma}}\Phi : \mathcal{S}^{-1}) : \dot{\boldsymbol{\varepsilon}} - (\partial_T\Phi - \partial_{\boldsymbol{\sigma}}\Phi : \mathcal{S}^{-1} : \boldsymbol{\alpha})\,\dot{T}}{(\partial_{\boldsymbol{\sigma}}\Phi : \mathcal{S}^{-1} : \partial_{\boldsymbol{\sigma}}\Phi + \partial_{\xi}\Phi)} \tag{4.17}$$

Therefore, by substituting the expressions for $\dot{\xi}$ and $\dot{\sigma}$, Eq. 4.17 and Eq. 4.13, into Eq. 4.11 we obtain the final form of the heat equation for the reverse martensitic phase transformation as

$$\begin{aligned}\mathcal{C}\dot{T} =& -\Big[T\boldsymbol{\alpha} : \mathcal{S}^{-1} + (-\pi + T\Delta\boldsymbol{\alpha} : \boldsymbol{\sigma} - \rho\Delta c T \ln\left(\frac{T}{T_0}\right) + \\ & \rho\Delta s_0 T + T\boldsymbol{\alpha} : \mathcal{S}^{-1} : \partial_{\boldsymbol{\sigma}}\Phi)\frac{(-\partial_{\boldsymbol{\sigma}}\Phi : \mathcal{S}^{-1})}{(\partial_{\boldsymbol{\sigma}}\Phi : \mathcal{S}^{-1} : \partial_{\boldsymbol{\sigma}}\Phi + \partial_{\xi}\Phi)}\Big] : \dot{\boldsymbol{\varepsilon}} + \\ & -\boldsymbol{\nabla}\cdot\mathbf{q} + \rho r,\end{aligned} \tag{4.18}$$

where $\mathcal{C}$

$$\begin{aligned}\mathcal{C} =& \rho c - T\boldsymbol{\alpha} : \mathcal{S}^{-1} : \boldsymbol{\alpha} + \\ & [-\pi + T\Delta\boldsymbol{\alpha} : \boldsymbol{\sigma} - \rho\Delta c T \ln\left(\frac{T}{T_0}\right) + \\ & \rho\Delta s_0 T + T\boldsymbol{\alpha} : \mathcal{S}^{-1} : \partial_{\boldsymbol{\sigma}}\Phi]\frac{(-\partial_T\Phi + \partial_{\boldsymbol{\sigma}}\Phi : \mathcal{S}^{-1} : \boldsymbol{\alpha})}{(\partial_{\boldsymbol{\sigma}}\Phi : \mathcal{S}^{-1} : \partial_{\boldsymbol{\sigma}}\Phi + \partial_{\xi}\Phi)}\end{aligned} \tag{4.19}$$

Finally, if no phase transformation is taking place, and assuming the term $T\boldsymbol{\alpha} : \dot{\boldsymbol{\sigma}}$ is very small for SMAs, the heat equation can be reduced to

$$\rho c\dot{T} = -\boldsymbol{\nabla} \cdot \mathbf{q} + \rho r \tag{4.20}$$

A. Characterization of SMA Elements for Different Heat Transfer Processes and One-dimensional Reduction of the Model

Since this work is concerned to the investigation of the thermomechanical coupling on one-dimensional SMA elements, such as wires, some assumptions should be made in order to reduce the energy balance heat equation to the one-dimensional case. The first assumption about the heat transfer on the boundaries of the SMA is that there is no heat flux either entering or leaving through the boundaries as heat conduction. In addition, the effect of radial heat conduction is disregarded. Therefore, we assume that there is no gradient of temperature inside the material. As a consequence, by assuming $\boldsymbol{\nabla} \cdot \mathbf{q} = 0$, all the spatial derivatives of the problem are eliminated. Thus, the only form of heat transfer considered in this work is under the assumption that heat input supply can describe the case of heat exchange with the environment due to convection, assuming Newton's law of cooling.

$$\rho r = h\left(T - T_{\infty}\right) \tag{4.21}$$

where h is the heat convection coefficient, T_∞ is the surrounding environment temperature.

The case of resistive heating could also be considered by including the term of $\rho^e J$ on the right-hand side of Eq. 4.21, where ρ^e stands for the electrical resistivity, and J is the magnitude of the current density.

1. 1-D Reduction of the Model

Since we have reduced the constitutive model to a one-dimensional form in the previous chapter, we also need to reduce the heat equation to a one-dimensional form. The reduction of the heat equation follows the same assumptions of Chapter III, in Section D. Thus, the one-dimensional form of the heat equation, Eq. 4.11, is given by

$$\dot{T} = \frac{-\left[T\alpha - \left(-\pi + T\Delta\alpha\sigma - \rho\Delta c T\ln\left(\frac{T}{T_0}\right) + \rho\Delta s_0 T\right)\frac{\partial_\sigma\Phi}{\partial_\xi\Phi}\right]\dot{\sigma} + h\left(T - T_\infty\right)}{\left[\rho c - \left(-\pi + T\Delta\alpha\sigma - \rho\Delta c T\ln\left(\frac{T}{T_0}\right) + \rho\Delta s_0 T\right)\frac{\partial_T\Phi}{\partial_\xi\Phi}\right]} \tag{4.22}$$

Considering the 1D form of the Heat equation as a function of the increment of strain, Eq. 4.15, for the case of forward martensitic phase transformation is given as follows:

$$\begin{aligned} C\dot{T} = &-[T\alpha S^{-1} + (-\pi + T\Delta\alpha\sigma - \rho\Delta c T\ln\left(\frac{T}{T_0}\right) + \\ &\rho\Delta s_0 T - T\alpha\mathcal{S}^{-1}\partial_\sigma\Phi)\frac{(\partial_\sigma\Phi\mathcal{S}^{-1})}{(\partial_\sigma\Phi\mathcal{S}^{-1}\partial_\sigma\Phi - \partial_\xi\Phi)}]\dot{\varepsilon} + h\left(T - T_\infty\right) \end{aligned} \tag{4.23}$$

where the 1D form of C is given by

$$\begin{aligned} C =& \rho c - T S^{-1} \alpha^2 + \\ & (-\pi + T\Delta\alpha\sigma - \rho\Delta c T \ln\left(\frac{T}{T_0}\right) + \\ & \rho\Delta s_0 T - T\alpha S^{-1}\partial_\sigma\Phi)\frac{(\partial_T\Phi - \partial_\sigma\Phi S^{-1}\alpha)}{(\partial_\sigma\Phi S^{-1}\partial_\sigma\Phi - \partial_\xi\Phi)} \end{aligned} \tag{4.24}$$

Now, for the case of reserve phase transformation, the 1D form of the Heat equation is given by:

$$\begin{aligned} \mathcal{C}\dot{T} =& -[T\alpha S^{-1} + (-\pi + T\Delta\alpha\sigma - \rho\Delta c T \ln\left(\frac{T}{T_0}\right) + \\ & \rho\Delta s_0 T + T\alpha S^{-1}\partial_\sigma\Phi)\frac{(-\partial_\sigma\Phi S^{-1})}{(\partial_\sigma\Phi S^{-1}\partial_\sigma\Phi + \partial_\xi\Phi)}]\dot{\varepsilon} + h\left(T - T_\infty\right) \end{aligned} \tag{4.25}$$

and the effective Heat Capacity for the case of reverse phase transformation is given by:

$$\begin{aligned} \mathcal{C} =& \rho c - T\alpha S^{-1}\alpha + \\ & [-\pi + T\Delta\alpha\sigma - \rho\Delta c T \ln\left(\frac{T}{T_0}\right) + \\ & \rho\Delta s_0 T + T\alpha S^{-1}\partial_\sigma\Phi]\frac{(-\partial_T\Phi + \partial_\sigma\Phi S^{-1}\alpha)}{(\partial_\sigma\Phi S^{-1}\partial_\sigma\Phi + \partial_\xi\Phi)} \end{aligned} \tag{4.26}$$

2. Material Parameter Characterization and Model Parameter Calibration

In the previous chapter, we have presented the procedure to identify the material parameters of the SMA and the calibrate the constitutive model. However, we consider in this chapter the thermomechanical coupling. Thus, the only material parameter of the constitutive model that needs to be determined is the heat convection coefficient, h. The heat convection coefficient can be determined by performing an experiment with a pseudoelastic SMA wire. The experiment consists of heating the wire through resistive heating up to a certain temperature, and then allowing the wire to cool down. As an example, Fig. 13 shows the plot of the measured temperature during the cooling process with respect to time. After the experimental test, several numerical simulation cases were performed for different values of the heat convection coefficient to get the best curve-fitting of the cooling temperature curve.

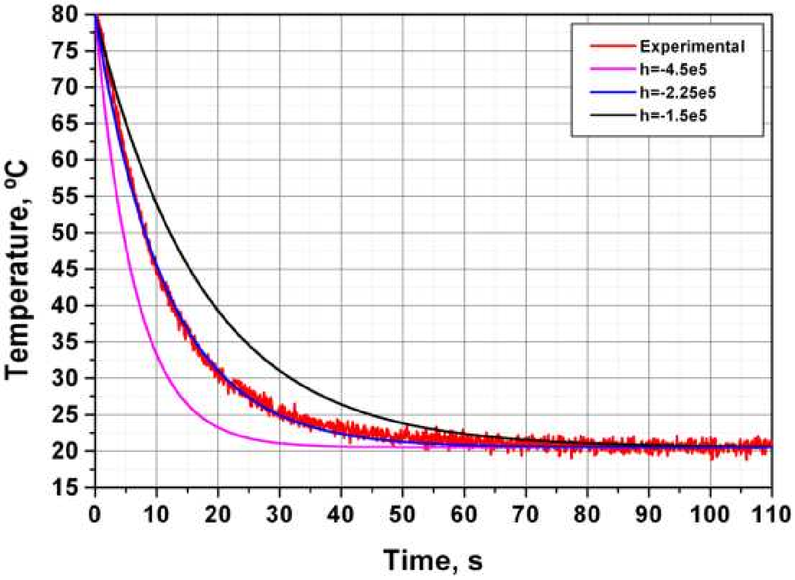

Fig. 13. Determination of the heat convection coefficient.

3. Closed-Form Solutions for Adiabatic and Non-Isothermal Conditions

Closed-form solutions can also be determined for adiabatic and non-isothermal heat conditions. Equation 4.22 can be used along with the closed-form solutions presented in Chapter III, in Sect. E, to simulate the behavior of the SMA under adiabatic and non-isothermal conditions. Recall that adiabatic conditions can be simulated if the value of the heat convection coefficient, h, is selected to be zero. On the other hand, if the value of h is selected to be infinite, isothermal conditions are recovered, and any value of h between zero and infinite is considered non-isothermal heat conditions. As

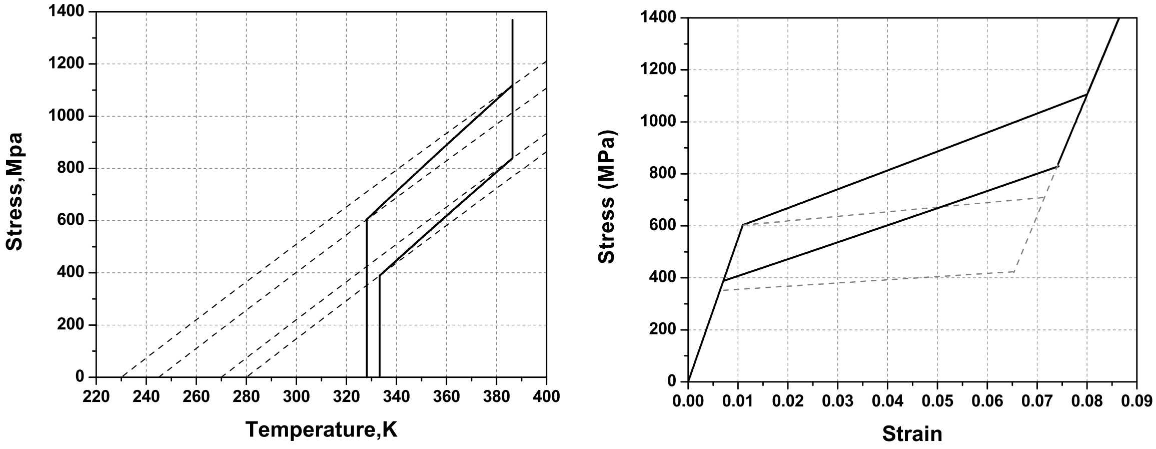

(a) Stress *vs.* temperature plot for adiabatic conditions

(b) Stress *vs.* strain curves for isothermal and adiabatic conditions

Fig. 14. Strain *vs.* temperature and stress *vs.* plots - comparison of isothermal and adiabatic conditions (Lagoudas *et al.* [1]).

an example, Fig. 14 compares SMA behavior under isothermal and adiabatic loading conditions.

CHAPTER V

NUMERICAL IMPLEMENTATION OF THE CONSTITUTIVE MODEL

This chapter is divided into two parts. The first part introduces the numerical implementation of the constitutive model for SMAs presented in the previous chapters using return mapping algorithm, while the second part investigate the thermomechanical coupling and stress-relaxation phenomenon on SMAs by comparing experimental results with numerical results.

Since the constitutive model has a structure very similar to rate-independent plasticity models, the same methods utilized to integrate constitutive equations describing plasticity(Ortiz and Popov [82], Ortiz and Simo [83], Simo and Hughes [81]) can be applied for SMAs. Qidwai and Lagoudas [27] have shown that return mapping algorithms can be successfully employed to integrate constitutive equations that describe the SMA behavior.

Return mapping algorithms are two steps predictor-corrector algorithms. At first, a thermoelastic trial loading (predictor) is attempted. If the stress state after the predictor step violates the transformation conditions (for the case of SMAs) the corrector step is applied to restore the consistency. Return mapping algorithms may differ based on the type of discretization method employed to numerically integrate the evolution differential equations of the flow rule and the iterative procedure adopted to solve the resultant set of non-linear algebraic equations in the corrector part [33]. A comprehensive review of different types of return mapping algorithms can be found in Simo and Hughes [81].

In this chapter we implement a return mapping algorithm to integrate the constitutive model for SMAs presented in the previous chapters. The implementation of this algorithm follows very closely the implementation described in Qidwai and

Lagoudas [27]. The main difference between both implementations is that the return mapping algorithm presented in this work integrates the constitutive equations and the heat equation, allowing the description of the thermomechanical coupling, while the implementation described in Qidwai and Lagoudas [27] applies to isothermal loading cases only. We present two different ways of implementing the heat equation with the return mapping algorithm. The first method discretizes the flow rule using the general trapezoidal rule for the case of implicit Euler integration scheme. During the integration of the constitutive model the temperature is kept constant until the values of stress and martensitic volume fraction reach convergency. These converged values of stress and martensitic volume fraction are substitute into the heat equation, which is then solved using the fourth-order Runge-Kutta integration scheme. With the new value of temperature, the return mapping algorithm is run again and the new values of stress and martensitic volume fraction are computed. This process continues until the values of stress, martensitic volume fraction and temperature converge, within a specified tolerance. The second method discretizes the flow rule and the heat equation using the implicit Euler integration scheme. Thus, the values of stress, martensitic volume fraction and temperature reach convergence at the same time. For the sake of completeness the derivation of the return mapping algorithm is conducted for the three-dimensional model. However, the numerical implementation was performed for the one-dimensional form of the model.

The second part of this chapter compares the numerical results provided by the two implementations, and investigates the effects of the thermomechanical coupling on the SMA behavior, such as the stress relaxation phenomenon. Experimental results are presented, and numerical simulations are conducted to corroborate the experimental results.

A. Review of Important Equations

Before discussing the implementation of the model, we revisit some equations presented in Chapter III and Chapter IV that will be utilized during the implementation of the return mapping algorithm. The stress-strain relation is given by:

$$\boldsymbol{\sigma} = \mathcal{S}^{-1} : \left[\boldsymbol{\varepsilon} - \boldsymbol{\alpha}\left(T - T_0\right) - \boldsymbol{\varepsilon}^t\right] \tag{5.1}$$

The evolution equation of the transformation strain (flow rule) is given by

$$\dot{\boldsymbol{\varepsilon}}^t = \boldsymbol{\Lambda}\dot{\xi}, \tag{5.2}$$

The Kuhn Tucker conditions, which specify the conditions for the occurrence of the martensitic phase transformation, are given by

$$\begin{aligned} &\dot{\xi} \geq 0; \qquad \Phi\left(\sigma, T, \xi\right) \leq 0; \qquad \Phi\dot{\xi} = 0 \\ &\dot{\xi} \leq 0; \qquad \Phi\left(\sigma, T, \xi\right) \leq 0; \qquad \Phi\dot{\xi} = 0. \end{aligned} \tag{5.3}$$

The rate independent aspect of the constitutive model is enforced by the consistency condition, which has the form

$$\dot{\Phi} = \partial_{\boldsymbol{\sigma}}\Phi : \dot{\boldsymbol{\sigma}} + \partial_T\Phi\dot{T} + \partial_\xi\Phi\dot{\xi} = 0 \tag{5.4}$$

The fully coupled heat equation introduced in Chapter IV has the form

$$T\boldsymbol{\alpha} : \dot{\boldsymbol{\sigma}} + \rho c\dot{T} + \left(-\pi + T\Delta\boldsymbol{\alpha} : \boldsymbol{\sigma} - \rho\Delta cT\ln\left(\frac{T}{T_0}\right) + \rho\Delta s_0 T\right)\dot{\xi} = h\left(T - T_\infty\right), \tag{5.5}$$

We can rewrite Eqn. 5.5 by substituting the consistency condition, Eqn. 3.19, the time derivative of martensitic volume fraction, Eq. 4.14, and the time derivative of the stress tensor, Eqn. 4.13, into it. After some algebraic manipulations, we obtain for forward phase transformation:

$$\begin{aligned}\mathcal{C}\dot{T} =& -\left[T\boldsymbol{\alpha} : \boldsymbol{\mathcal{S}}^{-1} + (-\pi + T\Delta\boldsymbol{\alpha} : \boldsymbol{\sigma} - \rho\Delta c T \ln\left(\frac{T}{T_0}\right) + \right.\\ & \left.\rho\Delta s_0 T - T\boldsymbol{\alpha} : \boldsymbol{\mathcal{S}}^{-1} : \partial_{\boldsymbol{\sigma}}\Phi)\frac{(\partial_{\boldsymbol{\sigma}}\Phi : \boldsymbol{\mathcal{S}}^{-1})}{(\partial_{\boldsymbol{\sigma}}\Phi : \boldsymbol{\mathcal{S}}^{-1} : \partial_{\boldsymbol{\sigma}}\Phi - \partial_{\xi}\Phi)}\right] : \dot{\boldsymbol{\varepsilon}} + \\ & h\left(T - T_{\infty}\right)\end{aligned} \tag{5.6}$$

where $\mathcal{C}$ has the following form:

$$\begin{aligned}\mathcal{C} =& \rho c - T\boldsymbol{\alpha} : \mathcal{S}^{-1} : \boldsymbol{\alpha} + \\ & (-\pi + T\Delta\boldsymbol{\alpha} : \boldsymbol{\sigma} - \rho\Delta c T \ln\left(\frac{T}{T_0}\right) + \\ & \rho\Delta s_0 T - T\boldsymbol{\alpha} : \mathcal{S}^{-1} : \partial_{\boldsymbol{\sigma}}\Phi)\frac{(\partial_T\Phi - \partial_{\boldsymbol{\sigma}}\Phi : \mathcal{S}^{-1} : \boldsymbol{\alpha})}{(\partial_{\boldsymbol{\sigma}}\Phi : \mathcal{S}^{-1} : \partial_{\boldsymbol{\sigma}}\Phi - \partial_{\xi}\Phi)}.\end{aligned} \tag{5.7}$$

The final form of the heat equation for the case of reverse phase transformation is given by

$$\begin{aligned}\mathcal{C}\dot{T} =& -\left[T\boldsymbol{\alpha} : \boldsymbol{\mathcal{S}}^{-1} + (-\pi + T\Delta\boldsymbol{\alpha} : \boldsymbol{\sigma} - \rho\Delta c T \ln\left(\frac{T}{T_0}\right) + \right.\\ & \left.\rho\Delta s_0 T + T\boldsymbol{\alpha} : \boldsymbol{\mathcal{S}}^{-1} : \partial_{\boldsymbol{\sigma}}\Phi)\frac{(-\partial_{\boldsymbol{\sigma}}\Phi : \boldsymbol{\mathcal{S}}^{-1})}{(\partial_{\boldsymbol{\sigma}}\Phi : \boldsymbol{\mathcal{S}}^{-1} : \partial_{\boldsymbol{\sigma}}\Phi + \partial_{\xi}\Phi)}\right] : \dot{\boldsymbol{\varepsilon}} + \\ & h\left(T - T_{\infty}\right),\end{aligned} \tag{5.8}$$

where $\mathcal{C}$ is given by

$$\begin{aligned}\mathcal{C} =& \rho c - T\boldsymbol{\alpha} : \mathcal{S}^{-1} : \boldsymbol{\alpha} + \\ & [-\pi + T\Delta\boldsymbol{\alpha} : \boldsymbol{\sigma} - \rho\Delta c T \ln\left(\frac{T}{T_0}\right) + \\ & \rho\Delta s_0 T + T\boldsymbol{\alpha} : \mathcal{S}^{-1} : \partial_{\boldsymbol{\sigma}}\Phi]\frac{(-\partial_T\Phi + \partial_{\boldsymbol{\sigma}}\Phi : \mathcal{S}^{-1} : \boldsymbol{\alpha})}{(\partial_{\boldsymbol{\sigma}}\Phi : \mathcal{S}^{-1} : \partial_{\boldsymbol{\sigma}}\Phi + \partial_{\xi}\Phi)}\end{aligned} \tag{5.9}$$

If no phase transformation is taking place the heat equation can be reduced to

$$\rho c\dot{T} = h\left(T - T_{\infty}\right) \tag{5.10}$$

B. Return Mapping Algorithm

The return mapping algorithm solves the thermoelastic-transformation problem defined by the stress-strain relation, Eq. 5.1, flow rule, Eq. 5.2 and the heat equation, Eqn. 5.5 or Eqn. 5.6 and Eqn. 5.8 by dividing it into two problems using an additive split[27, 84]: a trial problem and a correction problem. At first, a thermoelastic prediction problem is tried, assuming that the increment of the transformation strain is zero. If the predicted thermoelastic state violates the consistency condition, or in other words, if it lies outside the transformation surface ($\Phi > 0$), a transformation correction problem takes place to restore the consistency condition. This work uses the closest point projection return mapping algorithm as the corrector algorithm. The algorithm is explained next.

1. Closest Point Projection Return Mapping Algorithm - I

The main idea of the closest point projection return mapping algorithm is that it integrates the transformation correction equations in an implicit manner, using the backward Euler rule of integration (Qidwai and Lagoudas [27]). The Newton's method is then applied to compute the solution of the equations of the corrector problem in an iterative way.

The thermoelastic predictor problem considers that the increments of strain and temperature at time t are known, and that the increment of transformation strain is zero, that is

$$\begin{aligned} \dot{\boldsymbol{\varepsilon}} &= \dot{\boldsymbol{\varepsilon}}(t) \\ \dot{T} &= \dot{T} \\ \dot{\boldsymbol{\varepsilon}}^t &= 0 \end{aligned} \tag{5.11}$$

The transformation corrector problem is applied if the thermoelastic predictor lies outside the transformation surface. In this corrector step, the increments of strain and temperature are assumed to be zero and the increment of transformation strain is computed according to the flow rule.

$$\begin{aligned} \dot{\boldsymbol{\varepsilon}} &= 0 \\ \dot{T} &= 0 \\ \dot{\boldsymbol{\varepsilon}}^t &= \boldsymbol{\Lambda}\dot{\xi} \end{aligned} \tag{5.12}$$

The initial conditions of the corrector problem are provided by the solution of the thermoelastic predictor problem. During the transformation correction step, the evolution equations of the transformation strain (flow rule) are discretized according to the general trapezoidal rule

$$\boldsymbol{\varepsilon}^t_{n+1} = \boldsymbol{\varepsilon}^t_n + (\xi_{n+1} - \xi_n)\left[\beta\boldsymbol{\Lambda}_{n+1} + (1-\beta)\,\boldsymbol{\Lambda}_n\right]. \tag{5.13}$$

The parameter β, in Eqn. 5.13, varies within the interval from $[0, 1]$ and the subscripts n and $n+1$ indicate function evaluations at times t_n and t_{n+1}, respectively. Depending on the value of β, different integration schemes can be contemplated (Qidwai and Lagoudas [27]). If the value of β is selected to be equal to one, for example, the implicit (backward) Euler integration rule is obtained. However, if the value of β is equal to zero, the explicit (forward) Euler integration rule is recovered. This work assumes that the value $\beta = 1$.

Thus, by applying the trapezoidal rule with $\beta = 1$, the discretized form of the flow rule and stress-strain relation are given by

$$\boldsymbol{\varepsilon}^t_{n+1} = \boldsymbol{\varepsilon}^t_n + (\xi_{n+1} - \xi_n)\,\boldsymbol{\Lambda}_{n+1}, \tag{5.14}$$

and

$$\boldsymbol{\sigma}_{n+1} = \boldsymbol{\mathcal{S}}_{n+1}^{-1} : \left[\boldsymbol{\varepsilon}_{n+1} - \boldsymbol{\alpha}_{n+1}\left(T_{n+1} - T_0\right) - \boldsymbol{\varepsilon}_{n+1}^{t}\right] \tag{5.15}$$

In addition, the discretized form of the Kuhn-Tucker conditions are given by

$$\begin{aligned} \left(\xi_{n+1} - \xi_n\right) > 0; \quad & \Phi_{n+1}\left(\boldsymbol{\sigma}_{n+1}, T_{n+1}, \xi_{n+1}\right) \leq 0; \\ & \left(\xi_{n+1} - \xi_n\right)\Phi_{n+1}\left(\boldsymbol{\sigma}_{n+1}, T_{n+1}, \xi_{n+1}\right) = 0 \\ \left(\xi_{n+1} - \xi_n\right) < 0; \quad & \Phi_{n+1}\left(\boldsymbol{\sigma}_{n+1}, T_{n+1}, \xi_{n+1}\right) \leq 0; \\ & \left(\xi_{n+1} - \xi_n\right)\Phi_{n+1}\left(\boldsymbol{\sigma}_{n+1}, T_{n+1}, \xi_{n+1}\right) = 0 \end{aligned} \tag{5.16}$$

a. Thermoelastic Prediction

The transformation prediction problem is given by

$$\boldsymbol{\varepsilon}_{n+1} = \boldsymbol{\varepsilon}_n + \Delta\boldsymbol{\varepsilon}_{n+1} \tag{5.17}$$

$$T_{n+1} = T_n + \Delta T_{n+1} \tag{5.18}$$

$$\boldsymbol{\varepsilon}_{n+1}^{t(0)} = \boldsymbol{\varepsilon}_n^{t} \tag{5.19}$$

$$\xi_{n+1}^{(0)} = \xi^{n} \tag{5.20}$$

where $\Delta\boldsymbol{\varepsilon}_{n+1}$ and ΔT_{n+1} are the increments of strain and temperature, which are specified over the time step $\Delta t = t_{n+1} - t_n$. The superscript (0) denotes the values obtained in the prediction step. Thus, with the values of Eqn. 5.17-Eqn. 5.20, we can compute the stress tensor and the transformation function for the trial step, given by

$$\boldsymbol{\sigma}_{n+1}^{(0)} = \boldsymbol{\mathcal{S}}_{n+1}^{-1} : \left[\boldsymbol{\varepsilon}_{n+1} - \boldsymbol{\alpha}_{n+1}\left(T_{n+1} - T_0\right) - \boldsymbol{\varepsilon}_{n+1}^{t}\right]. \tag{5.21}$$

$$\Phi_{n+1}^{(0)} = \Phi\left[\boldsymbol{\sigma}_{n+1}^{(0)}, T_{n+1}, \xi_n\right] \tag{5.22}$$

After computing the trial values of $\boldsymbol{\sigma}_{n+1}^{(0)}$ and $\Phi_{n+1}^{(0)}$, the transformation criterion needs to be checked. If the transformation criterion is satisfied, that is, $\Phi_{n+1}^{(0)} \leq 0$ then this trial thermoelastic state is the final state. Otherwise, the corrector step takes place.

b. Transformation Correction

If the converged values of the trial step violates the consistency condition, *i.e.*, if $\Phi_{n+1}^{(0)} > 0$, the correction step is applied to solve the system of algebraic equations defined by Eqn. 5.14 and Eqn. 5.15. The converged solution $(\boldsymbol{\sigma}_{n+1}^{(0)}, \boldsymbol{\varepsilon}_n^t, \xi_n)$ of the trial step is taken as the initial condition for the corrector step.

The nonlinear system of the algebraic equations is solved by defining the transformation condition valid for the transformation corrector phase, a residual transformation strain function based on implicit backward Euler integration for the k^{th} iteration (Qidwai and Lagoudas [27]). So, we obtain

$$\Phi_{n+1}^{(k)} := \Phi_{n+1}\left(\boldsymbol{\sigma}_{n+1}, T_{n+1}, \xi_{n+1}\right) \tag{5.23}$$

and

$$\mathbf{R}_{n+1}^{t(k)} := -\boldsymbol{\varepsilon}_{n+1}^{t(k)} + \boldsymbol{\varepsilon}_{n}^{t(k)} + \boldsymbol{\Lambda}_{n+1}^{(k)}\left(\xi_{n+1}^{k} - \xi_n\right). \tag{5.24}$$

Note that $\Phi_{n+1}^{(k)}$ and $\mathbf{R}_{n+1}^{t(k)}$ should converge to zero at the end of each iteration process. Next step in the derivation of the transformation correction problem is to linearize Eqn. 5.23, and Eqn. 5.24, using the Newton-Raphson iteration method (Simo and Hughes [81]). Therefore, Eqn. 5.23 is linearized as follows:

$$\Phi_{n+1}^{(k)} + \partial_{\boldsymbol{\sigma}}\Phi_{n+1}^{(k)} : \Delta\sigma_{n+1}^{(k)} + \partial_{\xi}\Phi_{n+1}^{(k)} : \Delta\xi_{n+1}^{(k)} = 0 \tag{5.25}$$

where the partial derivatives of the transformation function, for forward transformation ($\dot{\xi} > 0$) are given by

$$\partial_{\boldsymbol{\sigma}} \Phi^{(k)}_{n+1} = \boldsymbol{\Lambda}^{(k)}_{n+1} + \Delta\boldsymbol{\mathcal{S}}^{(k)}_{n+1} : \boldsymbol{\sigma}^{(k)}_{n+1} + \Delta\boldsymbol{\alpha}^{(k)}_{n+1} \left(T^{(k)}_{n+1} - T_0\right) \tag{5.26}$$

$$\partial_{\xi} \Phi^{(k)}_{n+1} = -\frac{\partial^2 f^{(k)}_{n+1}}{\partial \xi^2}. \tag{5.27}$$

the partial derivatives of the transformation function, for reverse phase transformation, ($\dot{\xi} < 0$), are given by

$$\partial_{\boldsymbol{\sigma}} \Phi^{(k)}_{n+1} = -\boldsymbol{\Lambda}^{(k)}_{n+1} - \Delta\boldsymbol{\mathcal{S}}^{(k)}_{n+1} : \boldsymbol{\sigma}^{(k)}_{n+1} - \Delta\boldsymbol{\alpha}^{(k)}_{n+1} \left(T^{(k)}_{n+1} - T_0\right) \tag{5.28}$$

$$\partial_{\xi} \Phi^{(k)}_{n+1} = \frac{\partial^2 f^{(k)}_{n+1}}{\partial \xi^2} \tag{5.29}$$

Using a similar procedure, Eqn. 5.24 can be linearized as

$$\mathbf{R}^{t(k)}_{n+1} - \Delta\boldsymbol{\varepsilon}^{t(k)}_{n+1} + \boldsymbol{\Lambda}^{(k)}_{n+1} \Delta\xi^{k}_{n+1} + \begin{cases} \left(\xi^{k}_{n+1} - \xi_n\right) \partial_{\boldsymbol{\sigma}} \Lambda^{(k)}_{n+1} : \Delta\sigma^{(k)}_{n+1}, & \dot{\xi} > 0 \\ \mathbf{0}, & \dot{\xi} < 0 \end{cases} = 0 \tag{5.30}$$

Note that the term $\partial_{\boldsymbol{\sigma}} \Lambda^{(k)}_{n+1}$ is equal to zero during reverse transformation. The reason for this is because $\Lambda^{(k)}_{n+1}$ remains constant during the reverse transformation (Eqn. 3.13). Its components are determined at the end of the previous forward transformation (Qidwai and Lagoudas [27]). Then, for forward phase transformation the term $\partial_{\boldsymbol{\sigma}} \Lambda^{(k)}_{n+1}$ can be derived as follows: [1]

$$\partial_{\boldsymbol{\sigma}} \Lambda^{(k)}_{n+1} = \sqrt{\frac{3}{2}} \frac{H}{\parallel \boldsymbol{\sigma}' \parallel} \left[\mathbf{I} - \frac{1}{3} \mathbf{1} \otimes \mathbf{1} - \frac{\boldsymbol{\sigma}'}{\parallel \boldsymbol{\sigma}' \parallel} \otimes \frac{\boldsymbol{\sigma}'}{\parallel \boldsymbol{\sigma}' \parallel} \right] \tag{5.31}$$

where $\mathbf{I}$ the fourth-order identity tensor given by

$$\mathbf{I} = \frac{1}{2} \left[\delta_{ik}\delta_{jl} + \delta_{il}\delta_{jk}\right] \mathbf{e}_i \otimes \mathbf{e}_j \otimes \mathbf{e}_k \otimes \mathbf{e}_l, \tag{5.32}$$

---

[1] It is important to mention that in the one-dimensional implementation of the return mapping algorithm the term $\partial_{\boldsymbol{\sigma}} \Lambda^{(k)}_{n+1}$ is equal to zero.

and the second-order identity tensor is given by

$$\mathbf{1} = \delta_{ij}\mathbf{e}_i \otimes \mathbf{e}_j. \tag{5.33}$$

Next, we need to define the expressions for $\Delta\sigma^{(k)}_{n+1}$, $\Delta\xi^{(k)}_{n+1}$ and $\Delta\boldsymbol{\varepsilon}^{t(k)}_{n+1}$. We start by expressing Eqn. 5.15 in its incremental form:

$$\Delta\boldsymbol{\varepsilon}_{n+1} = \Delta\boldsymbol{\mathcal{S}}_{n+1} : \boldsymbol{\sigma}_{n+1} + \boldsymbol{\mathcal{S}}_{n+1} : \Delta\boldsymbol{\sigma}_{n+1} + \Delta\boldsymbol{\alpha}_{n+1}\left(T_{n+1} - T_0\right) + \boldsymbol{\alpha}_{n+1}\Delta T_{n+1} + \Delta\boldsymbol{\varepsilon}^{t}_{n+1} \tag{5.34}$$

where $\Delta\boldsymbol{\mathcal{S}}_{n+1}$ and $\Delta\boldsymbol{\alpha}_{n+1}$ are given by

$$\Delta\boldsymbol{\mathcal{S}}_{n+1} = \Delta\boldsymbol{\mathcal{S}}\Delta\xi_{n+1} \tag{5.35}$$

$$\Delta\boldsymbol{\alpha}_{n+1} = \Delta\boldsymbol{\alpha}\Delta\xi_{n+1}, \tag{5.36}$$

and $\Delta\boldsymbol{\mathcal{S}}$ and $\Delta\boldsymbol{\alpha}$ are determined by Eqn. 3.4 and Eqn. 3.5, respectively.

Recall that the increments of total strain, $\Delta\boldsymbol{\varepsilon}_{n+1}$ and temperature, ΔT_{n+1}, are equal to zero during the corrector problem. Therefore, we can solve Eqn. 5.34 for $\Delta\boldsymbol{\varepsilon}^{t(k)}_{n+1}$ and find the expression for the increment of the transformation strain, as follows:

$$\Delta\boldsymbol{\varepsilon}^{t(k)}_{n+1} = -\boldsymbol{\mathcal{S}}^{(k)}_{n+1} : \Delta\boldsymbol{\sigma}^{(k)}_{n+1} - \left[\Delta\boldsymbol{\mathcal{S}} : \boldsymbol{\sigma}^{(k)}_{n+1} + \Delta\boldsymbol{\alpha}\left(T^{(k)}_{n+1} - T_0\right)\right]\Delta\xi^{(k)}_{n+1} \tag{5.37}$$

The increment of stress can be obtained by substituting the increment of transformation strain, Eqn. 5.37, into the linearized residual equation of the transformation strain, Eqn. 5.30. After some algebraic manipulations, we obtain

$$\Delta\boldsymbol{\sigma}^{(k)}_{n+1} = \boldsymbol{\mathcal{E}}^{(k)}_{n+1} : \left[-\mathbf{R}^{t(k)}_{n+1} - \partial_{\boldsymbol{\sigma}}\Phi^{(k)}_{n+1}\Delta\xi^{(k)}_{n+1}\right] \tag{5.38}$$

where $\boldsymbol{\mathcal{E}}^{k}_{n+1}$ is defined to be

$$\boldsymbol{\mathcal{E}}^{k}_{n+1} := \left[\boldsymbol{\mathcal{S}}^{k}_{n+1} + \left(\xi^{k}_{n+1} - \xi_{n}\right) \partial_{\boldsymbol{\sigma}} \Lambda^{(k)}_{n+1}\right]^{-1}. \tag{5.39}$$

In order to derive the increment of martensitic volume fraction we need to substitute the increment of stress, Eqn. 5.38, into the linearized equation of the transformation function, Eqn. 5.25. After some algebraic manipulations we obtain

$$\Delta\xi^{(k)}_{n+1} = \frac{\Phi^{(k)}_{n+1} - \partial_{\boldsymbol{\sigma}} \Phi^{(k)}_{n+1} : \boldsymbol{\mathcal{E}}^{(k)}_{n+1} : \mathbf{R}^{t(k)}_{n+1}}{\partial_{\boldsymbol{\sigma}} \Phi^{(k)}_{n+1} : \boldsymbol{\mathcal{E}}^{k}_{n+1} : \partial_{\boldsymbol{\sigma}} \Phi^{(k)}_{n+1} - \partial_{\xi} \Phi^{(k)}_{n+1}} \tag{5.40}$$

Following the same procedure used for the forward transformation, the expressions for the increment of stress, $\Delta\boldsymbol{\sigma}^{(k)}_{n+1}$, and martensitic volume fraction, $\Delta\xi^{(k)}_{n+1}$ for the reverse phase transformation are given by

$$\Delta\boldsymbol{\sigma}^{(k)}_{n+1} = \left[\boldsymbol{\mathcal{S}}^{(k)}_{n+1}\right]^{-1} : \left[-\mathbf{R}^{t(k)}_{n+1} + \partial_{\boldsymbol{\sigma}} \Phi^{(k)}_{n+1} \Delta\xi^{(k)}_{n+1}\right] \tag{5.41}$$

and

$$\Delta\xi^{(k)}_{n+1} = \frac{\Phi^{(k)}_{n+1} - \partial_{\boldsymbol{\sigma}} \Phi^{(k)}_{n+1} : \left[\boldsymbol{\mathcal{S}}^{(k)}_{n+1}\right]^{-1} : \mathbf{R}^{t(k)}_{n+1}}{-\partial_{\boldsymbol{\sigma}} \Phi^{(k)}_{n+1} : \boldsymbol{\mathcal{E}}^{k}_{n+1} : \partial_{\boldsymbol{\sigma}} \Phi^{(k)}_{n+1} - \partial_{\xi} \Phi^{(k)}_{n+1}} \tag{5.42}$$

Since that the expressions for the increments of transformation strain, martensitic volume fraction were defined for forward and reverse martensitic phase transformation, the next step is to update the values of the transformation strain and martensitic volume fraction as:

$$\boldsymbol{\varepsilon}^{t(k+1)}_{n+1} = \boldsymbol{\varepsilon}^{t(k)}_{n+1} + \Delta\boldsymbol{\varepsilon}^{t(k+1)}_{n+1} \tag{5.43}$$

$$\xi^{(k+1)}_{n+1} = \xi^{(k)}_{n+1} + \Delta\xi^{(k+1)}_{n+1}. \tag{5.44}$$

Moreover, we update the values of the material parameters as:

$$\boldsymbol{\mathcal{S}}_{n+1}^{(k)} = \boldsymbol{\mathcal{S}}^{A} + \xi_{n+1}^{(k)} \left(\boldsymbol{\mathcal{S}}^{M} - \boldsymbol{\mathcal{S}}^{A}\right) \tag{5.45}$$

$$\boldsymbol{\alpha}_{n+1}^{(k)} = \boldsymbol{\alpha}^{A} + \xi_{n+1}^{(k)} \left(\boldsymbol{\alpha}^{M} - \boldsymbol{\alpha}^{A}\right) \tag{5.46}$$

$$c_{n+1}^{(k)} = c^{A} + \xi_{n+1}^{(k)} \left(c^{M} - c^{A}\right) \tag{5.47}$$

$$s_{0(n+1)}^{(k)} = s_0^{A} + \xi_{n+1}^{(k)} \left(s_0^{M} - s_0^{A}\right) \tag{5.48}$$

$$u_{0(n+1)}^{(k)} = u_0^{A} + \xi_{n+1}^{(k)} \left(u_0^{M} - u_0^{A}\right) \tag{5.49}$$

The final step is to update the stress tensor is updated, as follows:

$$\boldsymbol{\sigma}_{n+1}^{(k)} = \left[\boldsymbol{\mathcal{S}}_{n+1}^{(k)}\right]^{-1} : \left[\boldsymbol{\varepsilon}_{n+1} - \boldsymbol{\alpha}_{n+1}^{(k)} \left(T_{n+1}^{(k)} - T_0\right) - \boldsymbol{\varepsilon}_{n+1}^{t(k)}\right]. \tag{5.50}$$

It is important to mention that, so far, we have not considered the thermomechanical coupling, since the return mapping algorithm presented above is similar to the algorithm presented in Qidwai and Lagoudas [27]. The strategy that we have used to implement the thermomechanical coupling is now explained. At first, the thermoelastic prediction step uses the converged value of temperature from the previous time step. This value of temperature is also passed to the corrector step, if phase transformation occurs. At the end of the corrector step we obtain the converged value of the stress and martensitic volume fraction. Next, these converged values of stress and martensitic volume fraction are substituted in the heat equation, Eqn. 5.6 or Eqn. 5.8 depending on the direction of the transformation. A new value of temperature is directly obtained by integrating the heat equation using the fourth-order Runge-Kutta scheme. With the updated value of temperature, the return mapping algorithm subroutine is run again, and a new value of stress and martensitic volume fraction are computed. Then a new value of temperature is computed with the updated values of stress and martensitic volume fraction. This process continues until the convergency of the values of stress, martensitic volume fraction and temperature is achieved within a tolerance. A schematic representation of the return mapping algorithm scheme is shown in Table V.

2. Closest Point Projection Return Mapping Algorithm - II

The second implementation of the return mapping algorithm is presented in this section. This second method still uses the closest point projection return mapping algorithm as the integration scheme. However, the difference between this new implementation of the return mapping algorithm and the one presented before is that besides the flow rule, the heat equation, Eqn. 5.5, is discretized in an implicit manner using the backward Euler rule of integration. The Newton's method is then applied to calculate the increments of stress, martensitic volume fraction and temperature in a iterative way.

The thermoelastic predictor problem considers that the increment of strain at time t is known, and that the increments of transformation strain and temperature are zero, that is

$$\begin{aligned} \dot{\boldsymbol{\varepsilon}} &= \dot{\boldsymbol{\varepsilon}}(t) \\ \dot{T} &= 0 \\ \dot{\boldsymbol{\varepsilon}}^t &= 0 \end{aligned} \tag{5.51}$$

Similarly to the previous method, the transformation corrector problem is applied if the thermoelastic predictor lies outside the transformation surface. However, in this method, during the corrector problem the increment of strain is assumed to be zero

Table V. Closest point projection implicit return mapping algorithm-I

Thermoelastic Prediction:

$$\boldsymbol{\varepsilon}_{n+1} = \boldsymbol{\varepsilon}_n + \Delta\boldsymbol{\varepsilon}_{n+1}; \quad T_{n+1} = T_n + \Delta T_{n+1}; \quad \boldsymbol{\varepsilon}^t_{n+1} = \boldsymbol{\varepsilon}^t_n; \quad \xi_{n+1} = \xi_n$$

Compute stress tensor and Transformation function

$$\boldsymbol{\sigma}^{(0)}_{n+1} = \boldsymbol{\mathcal{S}}^{-1}_{n+1} : \left[\boldsymbol{\varepsilon}_{n+1} - \boldsymbol{\alpha}_{n+1}\left(T_{n+1} - T_0\right) - \boldsymbol{\varepsilon}^t_{n+1}\right];$$

$$\Phi^{(0)}_{n+1} = \Phi\left[\boldsymbol{\sigma}^{(0)}_{n+1}, T_{n+1}, \xi_n\right]$$

Check Kuhn-Tucker Condition:

$$\left(\xi_{n+1} - \xi_n\right) > 0 \text{ or } < 0; \quad \Phi_{n+1}\left(\boldsymbol{\sigma}_{n+1}, T_{n+1}, \xi_{n+1}\right) \leq 0;$$

$$\left(\xi_{n+1} - \xi_n\right)\Phi_{n+1}\left(\boldsymbol{\sigma}_{n+1}, T_{n+1}, \xi_{n+1}\right) = 0$$

Transformation Correction:

If $(\Phi^{(0)}_{n+1} > 0)$ & $(0 \leq \xi_{n+1} \leq 1)$ do

Compute $\boldsymbol{\mathcal{E}}^k_{n+1} := \left[\boldsymbol{\mathcal{S}}^k_{n+1} + \left(\xi^k_{n+1} - \xi_n\right)\partial_{\boldsymbol{\sigma}}\Lambda^{(k)}_{n+1}\right]^{-1}$ and $\left[\boldsymbol{\mathcal{S}}^k_{n+1}\right]^{-1}$

Compute increments of ξ and $\boldsymbol{\sigma}$:

For forward phase transformation:

$$\Delta\xi^{(k)}_{n+1} = \frac{\Phi^{(k)}_{n+1} - \partial_{\boldsymbol{\sigma}}\Phi^{(k)}_{n+1} : \boldsymbol{\mathcal{E}}^{(k)}_{n+1} : \mathbf{R}^{t(k)}_{n+1}}{\partial_{\boldsymbol{\sigma}}\Phi^{(k)}_{n+1} : \boldsymbol{\mathcal{E}}^k_{n+1} : \partial_{\boldsymbol{\sigma}}\Phi^{(k)}_{n+1} - \partial_\xi\Phi^{(k)}_{n+1}}$$

$$\Delta\boldsymbol{\sigma}^{(k)}_{n+1} = \boldsymbol{\mathcal{E}}^{(k)}_{n+1} : \left[-\mathbf{R}^{t(k)}_{n+1} - \partial_{\boldsymbol{\sigma}}\Phi^{(k)}_{n+1}\Delta\xi^{(k)}_{n+1}\right]$$

For reverse phase transformation:

$$\Delta\xi^{(k)}_{n+1} = \frac{\Phi^{(k)}_{n+1} - \partial_{\boldsymbol{\sigma}}\Phi^{(k)}_{n+1} : \left[\boldsymbol{\mathcal{S}}^{(k)}_{n+1}\right]^{-1} : \mathbf{R}^{t(k)}_{n+1}}{-\partial_{\boldsymbol{\sigma}}\Phi^{(k)}_{n+1} : \boldsymbol{\mathcal{E}}^k_{n+1} : \partial_{\boldsymbol{\sigma}}\Phi^{(k)}_{n+1} - \partial_\xi\Phi^{(k)}_{n+1}}$$

$$\Delta\boldsymbol{\sigma}^{(k)}_{n+1} = \left[\boldsymbol{\mathcal{S}}^{(k)}_{n+1}\right]^{-1} : \left[-\mathbf{R}^{t(k)}_{n+1} + \partial_{\boldsymbol{\sigma}}\Phi^{(k)}_{n+1}\Delta\xi^{(k)}_{n+1}\right]$$

Table V continued

```
Compute increment of $\boldsymbol{\varepsilon}^t$
    $\Delta\boldsymbol{\varepsilon}^{t(k)}_{n+1} = -\boldsymbol{\mathcal{S}}^{(k)}_{n+1} : \Delta\boldsymbol{\sigma}^{(k)}_{n+1} - \left[\Delta\boldsymbol{\mathcal{S}} : \boldsymbol{\sigma}^{(k)}_{n+1} + \Delta\boldsymbol{\alpha}\left(T^{(k)}_{n+1} - T_0\right)\right]\Delta\xi^{(k)}_{n+1}$
Update martensitic volume fraction $\xi$, and transformation strain tensor $\varepsilon^t$
    $\xi^{(k+1)}_{n+1} = \xi^{(k)}_{n+1} + \Delta\xi^{(k+1)}_{n+1}$
    $\boldsymbol{\varepsilon}^{t(k+1)}_{n+1} = \boldsymbol{\varepsilon}^{t(k)}_{n+1} + \Delta\boldsymbol{\varepsilon}^{t(k+1)}_{n+1}$
Update the effective material parameters
    $\boldsymbol{\mathcal{S}}^{(k)}_{n+1} = \boldsymbol{\mathcal{S}}^{A} + \xi^{(k)}_{n+1}\left(\boldsymbol{\mathcal{S}}^{M} - \boldsymbol{\mathcal{S}}^{A}\right)$
    $\boldsymbol{\alpha}^{(k)}_{n+1} = \boldsymbol{\alpha}^{A} + \xi^{(k)}_{n+1}\left(\boldsymbol{\alpha}^{M} - \boldsymbol{\alpha}^{A}\right)$
    $c^{(k)}_{n+1} = c^{A} + \xi^{(k)}_{n+1}\left(c^{M} - c^{A}\right)$
    $s^{(k)}_{0(n+1)} = s^{A}_{0} + \xi^{(k)}_{n+1}\left(s^{M}_{0} - s^{A}_{0}\right)$
    $u^{(k)}_{0(n+1)} = u^{A}_{0} + \xi^{(k)}_{n+1}\left(u^{M}_{0} - u^{A}_{0}\right)$
    $k = k + 1$
Update stress tensor, transformation function and residual tensor
    $\boldsymbol{\sigma}^{(k)}_{n+1} = \left[\boldsymbol{\mathcal{S}}^{(k)}_{n+1}\right]^{-1} : \left[\boldsymbol{\varepsilon}_{n+1} - \boldsymbol{\alpha}^{(k)}_{n+1}\left(T^{(k)}_{n+1} - T_0\right) - \boldsymbol{\varepsilon}^{t(k)}_{n+1}\right]$
    $\Phi_{n+1} = \Phi\left[\boldsymbol{\sigma}_{n+1}, T_{n+1}, \xi_{n+1}\right]$
    $\mathbf{R}^{t(k)}_{n+1} := -\boldsymbol{\varepsilon}^{t(k)}_{n+1} + \boldsymbol{\varepsilon}^{t(k)}_{n} + \boldsymbol{\Lambda}^{(k)}_{n+1}\left(\xi^{k}_{n+1} - \xi_n\right)$
    while $\Phi^{t(k)}_{n+1} > tol$, $\mathbf{R}^{t(k)}_{n+1} > tol$
Compute Temperature (Eqn. 5.6) or (Eqn. 5.8) using Runge-Kutta scheme
Check Temperature Tolerance
```

and the increments of transformation strain and temperature are computed.

$$\begin{aligned}\dot{\boldsymbol{\varepsilon}} &= 0\\ \dot{T} &= \dot{T}(t)\\ \dot{\boldsymbol{\varepsilon}}^t &= \boldsymbol{\Lambda}\dot{\xi}\end{aligned} \tag{5.52}$$

During the transformation correction step, the flow rule and the heat equation, Eqm. 5.5 are discretized according to the general trapezoidal rule. Since both return algorithm schemes presented in this chapter use the implicit Euler rule, the discretized flow rule has the same form of Eqn. 5.14, as well as the stress-strain relation and the discretized form of the Kuhn-Tucker conditions have the same form given by Eqn. 5.15 and Eqn. 5.16, respectively. The discretized form of the heat equation, Eqn. 5.5, is given by

$$\begin{aligned}&T_{n+1}\boldsymbol{\alpha}_{n+1} : (\boldsymbol{\sigma}_{n+1} - \boldsymbol{\sigma}_n) + \rho c_{n+1}(T_{n+1} - T_n) +\\ &\left[-\pi + T_{n+1}\Delta\boldsymbol{\alpha} : \boldsymbol{\sigma}_{n+1} + \rho T_{n+1}\Delta s_0 + \rho\Delta c T_{n+1}\ln\left(\frac{T_{n+1}}{T_0}\right)\right](\xi_{n+1} - \xi_n)\\ &= (t_{n+1} - t_n)\, h\,(T_{n+1} - T_\infty)\end{aligned} \tag{5.53}$$

a. Thermoelastic Prediction

The transformation prediction problem is given by

$$\boldsymbol{\varepsilon}_{n+1} = \boldsymbol{\varepsilon}_n + \Delta\boldsymbol{\varepsilon}_{n+1} \tag{5.54}$$

$$\boldsymbol{\varepsilon}^{t(0)}_{n+1} = \boldsymbol{\varepsilon}^t_n \tag{5.55}$$

$$\xi^{(0)}_{n+1} = \xi^n \tag{5.56}$$

$$T^{(0)}_{n+1} = T_n \tag{5.57}$$

where $\Delta\boldsymbol{\varepsilon}_{n+1}$ is the given strain increment, which is specified over the time step $\Delta t = t_{n+1} - t_n$. The superscript (0) denotes the values obtained in the prediction step. Thus, with the values of Eqn. 5.54-Eqn. 5.57, we can compute the stress tensor and the transformation function for the trial step, given by

$$\boldsymbol{\sigma}^{(0)}_{n+1} = \boldsymbol{\mathcal{S}}^{-1}_{n+1} : \left[\boldsymbol{\varepsilon}_{n+1} - \boldsymbol{\alpha}_{n+1}\left(T_{n+1} - T_0\right) - \boldsymbol{\varepsilon}^{t}_{n+1}\right]. \tag{5.58}$$

$$\Phi^{(0)}_{n+1} = \Phi\left[\boldsymbol{\sigma}^{(0)}_{n+1}, T^{(0)}_{n+1}, \xi_n\right] \tag{5.59}$$

Next, we need to check the transformation criterion, with the new values of the trial values of $\boldsymbol{\sigma}^{(0)}_{n+1}$ and $\Phi^{(0)}_{n+1}$. If the transformation criterion is satisfied, then this trial thermoelastic state is the final state. Otherwise, the corrector step needs to be applied.

b. Transformation Correction

If the converged values of the trial step violates the consistency condition, *i.e.*, if $\Phi^{(0)}_{n+1} > 0$, the correction step is applied at the $(n+1)^{th}$ loading increment for the solution of system of algebraic equations defined by Eqn. 5.14 and Eqn. 5.53. The converged solution $(\boldsymbol{\sigma}^{(0)}_{n+1}, \boldsymbol{\varepsilon}^{t}_{n}, \xi_n, T_n)$ of the trial step is taken as the initial condition for the corrector step, and the constraints for the corrector step are given by Eqn. 5.16.

The nonlinear system of the algebraic equations is solved by defining the transformation condition valid for the transformation corrector phase, the transformation strain residual and the heat residual functions based on implicit backward Euler integration for the k^{th} iteration (Qidwai and Lagoudas [27]). So, we obtain

$$\Phi^{(k)}_{n+1} := \Phi_{n+1}\left(\boldsymbol{\sigma}_{n+1}, T_{n+1}, \xi_{n+1}\right), \tag{5.60}$$

$$\mathbf{R}^{t(k)}_{n+1} := -\boldsymbol{\varepsilon}^{t(k)}_{n+1} + \boldsymbol{\varepsilon}^{t(k)}_{n} + \boldsymbol{\Lambda}^{(k)}_{n+1}\left(\xi^{k}_{n+1} - \xi_n\right) \tag{5.61}$$

and

$$\begin{aligned} L^{(k)}_{n+1} :=& T^{(k)}_{n+1}\boldsymbol{\alpha}^{(k)}_{n+1} : \left(\boldsymbol{\sigma}^{(k)}_{n+1} - \boldsymbol{\sigma}_n\right) + \rho c^{(k)}_{n+1}\left(T^{(k)}_{n+1} - T_n\right) + \\ & \left[-\pi + T^{(k)}_{n+1}\Delta\boldsymbol{\alpha} : \boldsymbol{\sigma}^{(k)}_{n+1} + \rho T^{(k)}_{n+1}\Delta s_0 + \rho\Delta c T^{(k)}_{n+1}\ln\left(\frac{T^{(k)}_{n+1}}{T_0}\right)\right]\left(\xi^{k}_{n+1} - \xi_n\right) \\ & - \left(t_{n+1} - t_n\right) h\left(T^{(k)}_{n+1} - T_{\infty}\right). \end{aligned} \tag{5.62}$$

The system of equations defined by Eqn. 5.60, Eqn. 5.61 and Eqn. 5.62 (Simo and Hughes [81]) are solved iteratively by the Newton-Raphson method, where $\Phi^{(k)}_{n+1}$, $\mathbf{R}^{t(k)}_{n+1}$ and $L^{(k)}_{n+1}$ should converge to zero at the end of each iteration process. In order to applied the Newton-Raphson method, we need to linearized Eqn. 5.60, Eqn. 5.61 and Eqn. 5.62. The linearized residual equation of the transformation strain used in the current return mapping algorithm implementation is the same as in Eqn. 5.30. However, the linearized form of Eqn. 5.60 is not the same as in Eq. 5.25 because it has an extra term related to the increment of temperature. The linearized form of Eqn. 5.60 is given by

$$\Phi^{(k)}_{n+1} + \partial_{\boldsymbol{\sigma}}\Phi^{(k)}_{n+1} : \Delta\sigma^{(k)}_{n+1} + \partial_T\Phi^{(k)}_{n+1}\Delta T^{(k)}_{n+1} + \partial_{\xi}\Phi^{(k)}_{n+1}\Delta\xi^{(k)}_{n+1} = 0. \tag{5.63}$$

The partial derivatives of the transformation function, for forward transformation

$(\dot{\xi} > 0)$ are given by

$$\partial_{\boldsymbol{\sigma}}\Phi^{(k)}_{n+1} = \boldsymbol{\Lambda}^{(k)}_{n+1} + \Delta\boldsymbol{\mathcal{S}}^{(k)}_{n+1} : \boldsymbol{\sigma}^{(k)}_{n+1} + \Delta\boldsymbol{\alpha}^{(k)}_{n+1}\left(T^{(k)}_{n+1} - T_0\right) \tag{5.64}$$

$$\partial_{T}\Phi^{(k)}_{n+1} = \Delta\boldsymbol{\alpha}^{(k)}_{n+1} : \boldsymbol{\sigma}^{(k)}_{n+1} + \rho\Delta c \ln\left(\frac{T^{(k)}_{n+1}}{T_0}\right) + \rho\Delta s_0 \tag{5.65}$$

$$\partial_{\xi}\Phi^{(k)}_{n+1} = -\frac{\partial^2 f^{(k)}_{n+1}}{\partial\xi^2}. \tag{5.66}$$

the partial derivatives of the transformation function, for reverse phase transformation, $(\dot{\xi} < 0)$, are given by

$$\partial_{\boldsymbol{\sigma}}\Phi^{(k)}_{n+1} = -\boldsymbol{\Lambda}^{(k)}_{n+1} - \Delta\boldsymbol{\mathcal{S}}^{(k)}_{n+1} : \boldsymbol{\sigma}^{(k)}_{n+1} - \Delta\boldsymbol{\alpha}^{(k)}_{n+1}\left(T^{(k)}_{n+1} - T_0\right) \tag{5.67}$$

$$\partial_{T}\Phi^{(k)}_{n+1} = -\Delta\boldsymbol{\alpha}^{(k)}_{n+1} : \boldsymbol{\sigma}^{(k)}_{n+1} - \rho\Delta c \ln\left(\frac{T^{(k)}_{n+1}}{T_0}\right) - \rho\Delta s_0 \tag{5.68}$$

$$\partial_{\xi}\Phi^{(k)}_{n+1} = \frac{\partial^2 f^{(k)}_{n+1}}{\partial\xi^2} \tag{5.69}$$

The next step is to define the expressions for $\Delta\sigma^{(k)}_{n+1}$, $\Delta\xi^{(k)}_{n+1}$, $\Delta\boldsymbol{\varepsilon}^{t(k)}_{n+1}$ and $\Delta T^{(k)}_{n+1}$. The increment of martensitic volume fraction can also be derived from the incremental form of Eqn. 5.15. However, in this implementation only the increment of strain, $\Delta\boldsymbol{\varepsilon}_{n+1}$, during the corrector problem that is equal to zero. Therefore, the increment of martensitic volume fraction, $\Delta\boldsymbol{\varepsilon}^{t(k)}_{n+1}$ is given by

$$\Delta\boldsymbol{\varepsilon}^{t(k)}_{n+1} = -\boldsymbol{\mathcal{S}}^{(k)}_{n+1} : \Delta\boldsymbol{\sigma}^{(k)}_{n+1} - \boldsymbol{\alpha}^{(k)}_{n+1}\Delta T^{(k)}_{n+1} - \left[\Delta\boldsymbol{\mathcal{S}} : \boldsymbol{\sigma}^{(k)}_{n+1} + \Delta\boldsymbol{\alpha}\left(T^{(k)}_{n+1} - T_0\right)\right]\Delta\xi^{(k)}_{n+1} \tag{5.70}$$

The increment of stress can be obtained by substituting the increment of transformation strain, Eqn. 5.70, into the linearized residual equation of the transformation strain, Eqn. 5.30. Thus, after some algebraic manipulations, we obtain

$$\Delta\boldsymbol{\sigma}^{(k)}_{n+1} = \boldsymbol{\mathcal{E}}^{(k)}_{n+1} : \left[-\mathbf{R}^{t(k)}_{n+1} - \partial_{\boldsymbol{\sigma}}\Phi^{(k)}_{n+1}\Delta\xi^{(k)}_{n+1} - \boldsymbol{\alpha}^{(k)}_{n+1}\Delta T^{(k)}_{n+1}\right] \tag{5.71}$$

where $\boldsymbol{\mathcal{E}}^{k}_{n+1}$ is defined to be

$$\boldsymbol{\mathcal{E}}^{k}_{n+1} := \left[\boldsymbol{\mathcal{S}}^{k}_{n+1} + \left(\xi^{k}_{n+1} - \xi_n\right) \partial_{\boldsymbol{\sigma}} \Lambda^{(k)}_{n+1}\right]^{-1}. \tag{5.72}$$

Next, we need to define the increment of martensitic volume fraction. For this purpose, we can substitute the increment of stress, Eqn. 5.71, into the linearized equation of the transformation function, Eqn. 5.63. Thus, after some algebraic manipulation we obtain

$$\Delta\xi^{(k)}_{n+1} = \frac{\Phi^{(k)}_{n+1} - \partial_{\boldsymbol{\sigma}}\Phi^{(k)}_{n+1} : \boldsymbol{\mathcal{E}}^{(k)}_{n+1} : \mathbf{R}^{t(k)}_{n+1} - \left[\partial_{\boldsymbol{\sigma}}\Phi^{(k)}_{n+1} : \boldsymbol{\mathcal{E}}^{(k)}_{n+1} : \boldsymbol{\alpha}^{(k)}_{n+1} - \partial_{T}\Phi^{(k)}_{n+1}\right] \Delta T^{(k)}_{n+1}}{\partial_{\boldsymbol{\sigma}}\Phi^{(k)}_{n+1} : \boldsymbol{\mathcal{E}}^{k}_{n+1} : \partial_{\boldsymbol{\sigma}}\Phi^{(k)}_{n+1} - \partial_{\xi}\Phi^{(k)}_{n+1}} \tag{5.73}$$

The only increment that still needs to be defined is the increment of temperature. So, we need to linearize the residual form heat equation, Eqn. 5.62. Following the same procedure of linearization used previously, we obtain

$$L^{(k)}_{n+1} + \partial_{\boldsymbol{\sigma}} L^{(k)}_{n+1} : \Delta\boldsymbol{\sigma}^{(k)}_{n+1} + \partial_{T} L^{(k)}_{n+1}\Delta T^{(k)}_{n+1} + \partial_{\xi} L^{(k)}_{n+1}\Delta\xi^{(k)}_{n+1} \tag{5.74}$$

We can obtain the increment of temperature by substituting the increment of stress, Eqn. 5.38, the increment of martensitic volume fraction, Eqn. 5.40, into the Eqn. 5.74. After some algebraic manipulations, we obtain

$$\begin{aligned}\Delta T^{(k)}_{n+1} =& \frac{1}{G^{(k)}_{n+1}}[-L^{(k)}_{n+1} + \mathbf{B}^{(k)}_{n+1} : \boldsymbol{\mathcal{E}} : R^{t(k)}_{n+1} + \\ & \left(\mathbf{B}^{(k)}_{n+1} : \boldsymbol{\mathcal{E}} : \partial_{\boldsymbol{\sigma}}\Phi_{n+1} - F^{(k)}_{n+1} + A^{(k)}_{n+1}\right)\left(\frac{\Phi^{(k)}_{n+1} - I^{(k)}_{n+1}}{D^{(k)}_{n+1}}\right)]\end{aligned} \tag{5.75}$$

where

$$A_{n+1}^{(k)} = -\pi + T_{n+1}^{(k)} \Delta \boldsymbol{\alpha} : \boldsymbol{\sigma}_{n+1}^{(k)} + \rho T_{n+1}^{(k)} \Delta s_0 + \rho \Delta c T_{n+1}^{(k)} \ln \left(\frac{T_{n+1}^{(k)}}{T_0} \right) \tag{5.76}$$

$$\mathbf{B}_{n+1}^{(k)} = T_{n+1}^{(k)} \boldsymbol{\alpha}_{n+1}^{(k)} + T_{n+1}^{(k)} \Delta \boldsymbol{\alpha} \left(\xi_{n+1}^{k} - \xi_n \right) \tag{5.77}$$

$$C_{n+1}^{(k)} = \partial_{\boldsymbol{\sigma}} \Phi_{n+1}^{(k)} : \boldsymbol{\mathcal{E}}_{n+1}^{k} : \Delta \boldsymbol{\alpha}_{n+1}^{(k)} - \partial_T \Phi_{n+1}^{(k)} \tag{5.78}$$

$$D_{n+1}^{(k)} = \partial_{\boldsymbol{\sigma}} \Phi_{n+1}^{(k)} : \boldsymbol{\mathcal{E}}_{n+1}^{k} : \partial_{\boldsymbol{\sigma}} \Phi_{n+1}^{(k)} - \partial_{\xi} \Phi_{n+1}^{(k)} \tag{5.79}$$

$$\begin{aligned} E_{n+1}^{(k)} &= \boldsymbol{\alpha}_{n+1}^{(k)} : \left(\boldsymbol{\sigma}_{n+1}^{(k)} - \boldsymbol{\sigma}_n \right) + \rho c_{n+1} \\ &+ \left[\Delta \boldsymbol{\alpha} : \boldsymbol{\sigma}_{n+1}^{(k)} + \rho \Delta c \ln \left(\frac{T_{n+1}^{(k)}}{T_0} \right) + \rho \Delta c + \rho \Delta s_0 \right] \left(\xi_{n+1}^{k} - \xi_n \right) \end{aligned} \tag{5.80}$$

$$F_{n+1}^{(k)} = T_{n+1}^{(k)} \Delta \boldsymbol{\alpha} : \left(\boldsymbol{\sigma}_{n+1}^{(k)} - \boldsymbol{\sigma}_n \right) + \rho c_{n+1}^{(k)} \left(T_{n+1}^{(k)} - T_0 \right) \tag{5.81}$$

$$\begin{aligned} G_{n+1}^{(k)} &= \left[\mathbf{B}_{n+1}^{(k)} : \boldsymbol{\mathcal{E}}_{n+1}^{k} : \partial_{\boldsymbol{\sigma}} \Phi_{n+1}^{(k)} + F_{n+1}^{(k)} + A_{n+1}^{(k)} \right] \left(\frac{C_{n+1}^{(k)}}{D_{n+1}^{(k)}} \right) + \\ &- \left(\mathbf{B}_{n+1}^{(k)} : \boldsymbol{\mathcal{E}}_{n+1}^{k} : \alpha_{n+1}^{k} \right) + E_{n+1}^{(k)} \end{aligned} \tag{5.82}$$

$$\mathbf{H}_{n+1}^{(k)} = \Delta \boldsymbol{\mathcal{S}} : \boldsymbol{\sigma}_{n+1}^{(k)} + \Delta \boldsymbol{\alpha} \left(T_{n+1}^{(k)} - T_0 \right) \tag{5.83}$$

$$I_{n+1}^{(k)} = \partial_{\boldsymbol{\sigma}} \Phi_{n+1}^{(k)} : \boldsymbol{\mathcal{E}}_{n+1}^{k} : R_{n+1}^{t(k)} \tag{5.84}$$

Next, we need to compute the increment of stress, $\Delta \boldsymbol{\sigma}_{n+1}^{(k)}$, the increment of martensitic volume fraction, $\Delta \xi_{n+1}^{(k)}$, and the increment of temperature, $\Delta T_{n+1}^{(k)}$, for the reverse transformation. Thus, by following similar procedure used before, we obtain:

$$\Delta \boldsymbol{\sigma}_{n+1}^{(k)} = \left[\boldsymbol{\mathcal{S}}_{n+1}^{(k)} \right]^{-1} : \left[-\mathbf{R}_{n+1}^{t(k)} + \partial_{\boldsymbol{\sigma}} \Phi_{n+1}^{(k)} \Delta \xi_{n+1}^{(k)} - \boldsymbol{\alpha}_{n+1}^{(k)} \Delta T_{n+1}^{(k)} \right] \tag{5.85}$$

$$
\begin{aligned}
\Delta\xi^{(k)}_{n+1} = {} & \frac{\Phi^{(k)}_{n+1}}{-\partial_{\boldsymbol{\sigma}}\Phi^{(k)}_{n+1} : [\boldsymbol{\mathcal{S}}^{(k)}_{n+1}]^{-1} : \partial_{\boldsymbol{\sigma}}\Phi^{(k)}_{n+1} - \partial_{\xi}\Phi^{(k)}_{n+1}} + \\
& \frac{-\partial_{\boldsymbol{\sigma}}\Phi^{(k)}_{n+1} : [\boldsymbol{\mathcal{S}}^{(k)}_{n+1}]^{-1} : \mathbf{R}^{t(k)}_{n+1} - \left[\partial_{\boldsymbol{\sigma}}\Phi^{(k)}_{n+1} : [\boldsymbol{\mathcal{S}}^{(k)}_{n+1}]^{-1} : \boldsymbol{\alpha}^{(k)}_{n+1} - \partial_{T}\Phi^{(k)}_{n+1}\right] \Delta T^{(k)}_{n+1}}{-\partial_{\boldsymbol{\sigma}}\Phi^{(k)}_{n+1} : [\boldsymbol{\mathcal{S}}^{(k)}_{n+1}]^{-1} : \partial_{\boldsymbol{\sigma}}\Phi^{(k)}_{n+1} - \partial_{\xi}\Phi^{(k)}_{n+1}}
\end{aligned}
\tag{5.86}
$$

$$
\begin{aligned}
\Delta T^{(k)}_{n+1} = {} & \frac{1}{G^{(k)}_{n+1}}[-L^{(k)}_{n+1} + \mathbf{B}^{(k)}_{n+1} : \left[\boldsymbol{\mathcal{S}}^{(k)}_{n+1}\right]^{-1} : R^{t(k)}_{n+1} \\
& - \left(\mathbf{B}^{(k)}_{n+1} : \left[\boldsymbol{\mathcal{S}}^{(k)}_{n+1}\right]^{-1} : \partial_{\boldsymbol{\sigma}}\Phi_{n+1} + F^{(k)}_{n+1} + A^{(k)}_{n+1}\right)\left(\frac{\Phi^{(k)}_{n+1} - I^{(k)}_{n+1}}{D^{(k)}_{n+1}}\right)]
\end{aligned}
\tag{5.87}
$$

where

$$
A^{(k)}_{n+1} = -\pi + T^{(k)}_{n+1}\Delta\boldsymbol{\alpha} : \boldsymbol{\sigma}^{(k)}_{n+1} + \rho T^{(k)}_{n+1}\Delta s_0 + \rho\Delta c T^{(k)}_{n+1}\ln\left(\frac{T^{(k)}_{n+1}}{T_0}\right) \tag{5.88}
$$

$$
\mathbf{B}^{(k)}_{n+1} = T^{(k)}_{n+1}\boldsymbol{\alpha}^{(k)}_{n+1} + T^{(k)}_{n+1}\Delta\boldsymbol{\alpha}\left(\xi^{k}_{n+1} - \xi_n\right) \tag{5.89}
$$

$$
C^{(k)}_{n+1} = \partial_{\boldsymbol{\sigma}}\Phi^{(k)}_{n+1} : \left[\boldsymbol{\mathcal{S}}^{(k)}_{n+1}\right]^{-1} : \Delta\boldsymbol{\alpha}^{(k)}_{n+1} - \partial_{T}\Phi^{(k)}_{n+1} \tag{5.90}
$$

$$
D^{(k)}_{n+1} = \partial_{\boldsymbol{\sigma}}\Phi^{(k)}_{n+1} : \left[\boldsymbol{\mathcal{S}}^{(k)}_{n+1}\right]^{-1} : \partial_{\boldsymbol{\sigma}}\Phi^{(k)}_{n+1} - \partial_{\xi}\Phi^{(k)}_{n+1} \tag{5.91}
$$

$$
\begin{aligned}
E^{(k)}_{n+1} = {} & \boldsymbol{\alpha}^{(k)}_{n+1} : \left(\boldsymbol{\sigma}^{(k)}_{n+1} - \boldsymbol{\sigma}_n\right) + \rho c_{n+1} \\
& + \left[\Delta\boldsymbol{\alpha} : \boldsymbol{\sigma}^{(k)}_{n+1} + \rho\Delta c\ln\left(\frac{T^{(k)}_{n+1}}{T_0}\right) + \rho\Delta c + \rho\Delta s_0\right]\left(\xi^{k}_{n+1} - \xi_n\right)
\end{aligned}
\tag{5.92}
$$

(5.93)

$$F_{n+1}^{(k)} = T_{n+1}^{(k)} \Delta \boldsymbol{\alpha} : \left(\boldsymbol{\sigma}_{n+1}^{(k)} - \boldsymbol{\sigma}_n \right) + \rho c_{n+1}^{(k)} \left(T_{n+1}^{(k)} - T_0 \right) \tag{5.94}$$

$$\begin{aligned} G_{n+1}^{(k)} = & \left[\mathbf{B}_{n+1}^{(k)} : \left[\boldsymbol{\mathcal{S}}_{n+1}^{(k)} \right]^{-1} : \partial_{\boldsymbol{\sigma}} \Phi_{n+1}^{(k)} + F_{n+1}^{(k)} + A_{n+1}^{(k)} \right] \left(\frac{C_{n+1}^{(k)}}{D_{n+1}^{(k)}} \right) + \\ & - \left(\mathbf{B}_{n+1}^{(k)} : \left[\boldsymbol{\mathcal{S}}_{n+1}^{(k)} \right]^{-1} : \alpha_{n+1}^{k} \right) + E_{n+1}^{(k)} \end{aligned} \tag{5.95}$$

$$\mathbf{H}_{n+1}^{(k)} = \Delta \boldsymbol{\mathcal{S}} : \boldsymbol{\sigma}_{n+1}^{(k)} + \Delta \boldsymbol{\alpha} \left(T_{n+1}^{(k)} - T_0 \right) \tag{5.96}$$

$$I_{n+1}^{(k)} = \partial_{\boldsymbol{\sigma}} \Phi_{n+1}^{(k)} : \left[\boldsymbol{\mathcal{S}}_{n+1}^{(k)} \right]^{-1} : R_{n+1}^{t(k)} \tag{5.97}$$

Now that the expressions for the increments of transformation strain, martensitic volume fraction and temperature were derived for forward and reverse martensitic phase transformation, we need to update the values of the transformation strain, martensitic volume fraction and temperature as follows:

$$\boldsymbol{\varepsilon}_{n+1}^{t(k+1)} = \boldsymbol{\varepsilon}_{n+1}^{t(k)} + \Delta \boldsymbol{\varepsilon}_{n+1}^{t(k+1)} \tag{5.98}$$

$$\xi_{n+1}^{(k+1)} = \xi_{n+1}^{(k)} + \Delta \xi_{n+1}^{(k+1)} \tag{5.99}$$

$$T_{n+1}^{t(k+1)} = T_{n+1}^{(k)} + \Delta T_{n+1}^{(k+1)}. \tag{5.100}$$

Afterwards, we update the values of the material parameters as follows:

$$\boldsymbol{\mathcal{S}}_{n+1}^{(k)} = \boldsymbol{\mathcal{S}}^{A} + \xi_{n+1}^{(k)} \left(\boldsymbol{\mathcal{S}}^{M} - \boldsymbol{\mathcal{S}}^{A} \right) \tag{5.101}$$

$$\boldsymbol{\alpha}_{n+1}^{(k)} = \boldsymbol{\alpha}^{A} + \xi_{n+1}^{(k)} \left(\boldsymbol{\alpha}^{M} - \boldsymbol{\alpha}^{A} \right) \tag{5.102}$$

$$c_{n+1}^{(k)} = c^{A} + \xi_{n+1}^{(k)} \left(c^{M} - c^{A} \right) \tag{5.103}$$

$$s_{0(n+1)}^{(k)} = s_0^{A} + \xi_{n+1}^{(k)} \left(s_0^{M} - s_0^{A} \right) \tag{5.104}$$

$$u_{0(n+1)}^{(k)} = u_0^{A} + \xi_{n+1}^{(k)} \left(u_0^{M} - u_0^{A} \right) \tag{5.105}$$

Finally, the stress tensor is updated, as follows:

$$\boldsymbol{\sigma}_{n+1}^{(k)} = \left[\boldsymbol{\mathcal{S}}_{n+1}^{(k)}\right]^{-1} : \left[\boldsymbol{\varepsilon}_{n+1} - \boldsymbol{\alpha}_{n+1}^{(k)}\left(T_{n+1}^{(k)} - T_0\right) - \boldsymbol{\varepsilon}_{n+1}^{t(k)}\right] \tag{5.106}$$

A schematic representation of the return mapping algorithm scheme is shown in Table b.

C. Numerical Simulations of the Constitutive Model Using Return Mapping Algorithm

In order to evaluate the thermomechanical coupling on SMAs, this section compares experimental results of an SMA wire with numerical simulations. First, the two implementations of the return mapping algorithm presented in the previous section are compared. Afterwards, numerical simulations of the constitutive model are correlated with results of two experimental tests. The first test investigates the variation of temperature of a SMA wire due to stress-induced martensitic phase transformation. The second experimental test was conducted to evaluate the transformation-induced stress relaxation phenomenon on SMAs. In this test, an SMA wire was subjected to a specific strain-driven loading-unloading path, where certain levels of strains were selected to be kept constant for a given period of time. The temperature of the SMA was also recorded throughout the test. The same loading-unloading paths were given as input of the numerical simulations of the constitutive model.

1. Comparison of Return Mapping Algorithm Implementations

This section compares both return mapping algorithms predictions. Thus, consider a one-dimensional SMA element, *e.g.* a wire, subjected to a triangular strain-driven loading-unloading input. The total time of the loading-unloading path was selected

Table VI. Closest point projection implicit return mapping algorithm-II

Thermoelastic Prediction:

$$\boldsymbol{\varepsilon}_{n+1} = \boldsymbol{\varepsilon}_n + \Delta\boldsymbol{\varepsilon}_{n+1}; \qquad T_{n+1} = T_n; \qquad \boldsymbol{\varepsilon}^t_{n+1} = \boldsymbol{\varepsilon}^t_n; \qquad \xi_{n+1} = \xi_n$$

Compute stress tensor and Transformation function

$$\boldsymbol{\sigma}^{(0)}_{n+1} = \boldsymbol{\mathcal{S}}^{-1}_{n+1} : \left[\boldsymbol{\varepsilon}_{n+1} - \boldsymbol{\alpha}_{n+1}\left(T_{n+1} - T_0\right) - \boldsymbol{\varepsilon}^t_{n+1}\right];$$
$$\Phi^{(0)}_{n+1} = \Phi\left[\boldsymbol{\sigma}^{(0)}_{n+1}, T_{n+1}, \xi_n\right]$$

Check Kuhn-Tucker Condition:

$$\left(\xi_{n+1} - \xi_n\right) > 0 \text{ or } < 0; \quad \Phi_{n+1}\left(\boldsymbol{\sigma}_{n+1}, T_{n+1}, \xi_{n+1}\right) \leq 0;$$
$$\left(\xi_{n+1} - \xi_n\right)\Phi_{n+1}\left(\boldsymbol{\sigma}_{n+1}, T_{n+1}, \xi_{n+1}\right) = 0$$

Transformation Correction:

If $(\Phi^{(0)}_{n+1} > 0)$ & $(0 \leq \xi_{n+1} \leq 1)$ do

Compute $\boldsymbol{\mathcal{E}}^k_{n+1} := \left[\boldsymbol{\mathcal{S}}^k_{n+1} + \left(\xi^k_{n+1} - \xi_n\right)\partial_{\boldsymbol{\sigma}}\Lambda^{(k)}_{n+1}\right]^{-1}$ and $\left[\boldsymbol{\mathcal{S}}^k_{n+1}\right]^{-1}$

Compute increments of ξ, T and $\boldsymbol{\sigma}$:

For forward phase transformation

$$\Delta\xi^{(k)}_{n+1} = \frac{\Phi^{(k)}_{n+1} - \partial_{\boldsymbol{\sigma}}\Phi^{(k)}_{n+1} : \boldsymbol{\mathcal{E}}^{(k)}_{n+1} : \mathbf{R}^{t(k)}_{n+1} - \left[\partial_{\boldsymbol{\sigma}}\Phi^{(k)}_{n+1} : \boldsymbol{\mathcal{E}}^{(k)}_{n+1} : \boldsymbol{\alpha}^{(k)}_{n+1} - \partial_T\Phi^{(k)}_{n+1}\right]\Delta T^{(k)}_{n+1}}{\partial_{\boldsymbol{\sigma}}\Phi^{(k)}_{n+1} : \boldsymbol{\mathcal{E}}^k_{n+1} : \partial_{\boldsymbol{\sigma}}\Phi^{(k)}_{n+1} - \partial_\xi\Phi^{(k)}_{n+1}}$$

$$\Delta\boldsymbol{\sigma}^{(k)}_{n+1} = \boldsymbol{\mathcal{E}}^{(k)}_{n+1} : \left[-\mathbf{R}^{t(k)}_{n+1} - \partial_{\boldsymbol{\sigma}}\Phi^{(k)}_{n+1}\Delta\xi^{(k)}_{n+1} - \boldsymbol{\alpha}^{(k)}_{n+1}\Delta T^{(k)}_{n+1}\right]$$

$$\Delta T^{(k)}_{n+1} = \frac{1}{G^{(k)}_{n+1}}[-L^{(k)}_{n+1} + \mathbf{B}^{(k)}_{n+1} : \boldsymbol{\mathcal{E}} : R^{t(k)}_{n+1} +$$
$$\left(\mathbf{B}^{(k)}_{n+1} : \boldsymbol{\mathcal{E}} : \partial_{\boldsymbol{\sigma}}\Phi_{n+1} - F^{(k)}_{n+1} + A^{(k)}_{n+1}\right)\left(\frac{\Phi^{(k)}_{n+1} - I^{(k)}_{n+1}}{D^{(k)}_{n+1}}\right)]$$

For reverse phase transformation

$$\Delta\xi^{(k)}_{n+1} = \frac{\Phi^{(k)}_{n+1} - \partial_{\boldsymbol{\sigma}}\Phi^{(k)}_{n+1} : \left[\boldsymbol{\mathcal{S}}^{(k)}_{n+1}\right]^{-1} : \mathbf{R}^{t(k)}_{n+1} - \left[\partial_{\boldsymbol{\sigma}}\Phi^{(k)}_{n+1} : \left[\boldsymbol{\mathcal{S}}^{(k)}_{n+1}\right]^{-1} : \boldsymbol{\alpha}^{(k)}_{n+1} - \partial_T\Phi^{(k)}_{n+1}\right]\Delta T^{(k)}_{n+1}}{-\partial_{\boldsymbol{\sigma}}\Phi^{(k)}_{n+1} : \left[\boldsymbol{\mathcal{S}}^{(k)}_{n+1}\right]^{-1} : \partial_{\boldsymbol{\sigma}}\Phi^{(k)}_{n+1} - \partial_\xi\Phi^{(k)}_{n+1}}$$

Table VI continued

$$\Delta\boldsymbol{\sigma}^{(k)}_{n+1} = \left[\boldsymbol{\mathcal{S}}^{(k)}_{n+1}\right]^{-1} : \left[-\mathbf{R}^{t(k)}_{n+1} + \partial_{\boldsymbol{\sigma}}\Phi^{(k)}_{n+1}\Delta\xi^{(k)}_{n+1} - \boldsymbol{\alpha}^{(k)}_{n+1}\Delta T^{(k)}_{n+1}\right]$$

$$\begin{aligned}\Delta T^{(k)}_{n+1} = \frac{1}{G^{(k)}_{n+1}}[&-L^{(k)}_{n+1} + \mathbf{B}^{(k)}_{n+1} : \left[\boldsymbol{\mathcal{S}}^{(k)}_{n+1}\right]^{-1} : R^{t(k)}_{n+1} \\ &- \left(\mathbf{B}^{(k)}_{n+1} : \left[\boldsymbol{\mathcal{S}}^{(k)}_{n+1}\right]^{-1} : \partial_{\boldsymbol{\sigma}}\Phi_{n+1} + F^{(k)}_{n+1} + A^{(k)}_{n+1}\right)\left(\frac{\Phi^{(k)}_{n+1} - I^{(k)}_{n+1}}{D^{(k)}_{n+1}}\right)]\end{aligned}$$

Compute increment of $\boldsymbol{\varepsilon}^{t(k)}_{n+1}$:

$$\begin{aligned}\Delta\boldsymbol{\varepsilon}^{t(k)}_{n+1} = -\boldsymbol{\mathcal{S}}^{(k)}_{n+1} : \Delta\boldsymbol{\sigma}^{(k)}_{n+1} - \boldsymbol{\alpha}^{(k)}_{n+1}\Delta T^{(k)}_{n+1} + \\ - \left[\Delta\boldsymbol{\mathcal{S}} : \boldsymbol{\sigma}^{(k)}_{n+1} + \Delta\boldsymbol{\alpha}\left(T^{(k)}_{n+1} - T_0\right)\right]\Delta\xi^{(k)}_{n+1}\end{aligned}$$

Update ξ, T and ε^t

$$\boldsymbol{\varepsilon}^{t(k+1)}_{n+1} = \boldsymbol{\varepsilon}^{t(k)}_{n+1} + \Delta\boldsymbol{\varepsilon}^{t(k+1)}_{n+1}$$

$$\xi^{(k+1)}_{n+1} = \xi^{(k)}_{n+1} + \Delta\xi^{(k+1)}_{n+1}$$

$$T^{t(k+1)}_{n+1} = T^{(k)}_{n+1} + \Delta T^{(k+1)}_{n+1}$$

Update the effective material properties

$$\boldsymbol{\mathcal{S}}^{(k)}_{n+1} = \boldsymbol{\mathcal{S}}^{A} + \xi^{(k)}_{n+1}\left(\boldsymbol{\mathcal{S}}^{M} - \boldsymbol{\mathcal{S}}^{A}\right)$$

$$\boldsymbol{\alpha}^{(k)}_{n+1} = \boldsymbol{\alpha}^{A} + \xi^{(k)}_{n+1}\left(\boldsymbol{\alpha}^{M} - \boldsymbol{\alpha}^{A}\right)$$

$$c^{(k)}_{n+1} = c^{A} + \xi^{(k)}_{n+1}\left(c^{M} - c^{A}\right)$$

$$s^{(k)}_{0(n+1)} = s^{A}_{0} + \xi^{(k)}_{n+1}\left(s^{M}_{0} - s^{A}_{0}\right)$$

$$u^{(k)}_{0(n+1)} = u^{A}_{0} + \xi^{(k)}_{n+1}\left(u^{M}_{0} - u^{A}_{0}\right)$$

$$k = k + 1$$

Update stress tensor, transformation function and residual tensor

$$\boldsymbol{\sigma}^{(k)}_{n+1} = \left[\boldsymbol{\mathcal{S}}^{(k)}_{n+1}\right]^{-1} : \left[\boldsymbol{\varepsilon}_{n+1} - \boldsymbol{\alpha}^{(k)}_{n+1}\left(T^{(k)}_{n+1} - T_0\right) - \boldsymbol{\varepsilon}^{t(k)}_{n+1}\right]$$

Table VI continued

$$\Phi_{n+1} = \Phi\left[\boldsymbol{\sigma}_{n+1}, T_{n+1}, \xi_{n+1}\right]$$

$$\mathbf{R}^{t(k)}_{n+1} := -\boldsymbol{\varepsilon}^{t(k)}_{n+1} + \boldsymbol{\varepsilon}^{t(k)}_{n} + \boldsymbol{\Lambda}^{(k)}_{n+1}\left(\xi^{k}_{n+1} - \xi_{n}\right)$$

$$\begin{aligned} L^{(k)}_{n+1} := {} & T^{(k)}_{n+1}\boldsymbol{\alpha}^{(k)}_{n+1} : \left(\boldsymbol{\sigma}^{(k)}_{n+1} - \boldsymbol{\sigma}_{n}\right) + \rho c^{(k)}_{n+1}\left(T^{(k)}_{n+1} - T_{n}\right) + \\ & \left[-\pi + T^{(k)}_{n+1}\Delta\boldsymbol{\alpha} : \boldsymbol{\sigma}^{(k)}_{n+1} + \rho T^{(k)}_{n+1}\Delta s_{0} + \rho\Delta c T^{(k)}_{n+1}\ln\left(\frac{T^{(k)}_{n+1}}{T_{0}}\right)\right]\left(\xi^{k}_{n+1} - \xi_{n}\right) + \\ & -\left(t_{n+1} - t_{n}\right) h\left(T^{(k)}_{n+1} - T_{\infty}\right) \end{aligned}$$

while $\Phi^{t(k)}_{n+1} > tol$, $\mathbf{R}^{t(k)}_{n+1} > tol$ and $\mathbf{L}^{t(k)}_{n+1} > tol$

to be 100s, with a time increment of $1.0 \cdot 10^{-3}$s. In addition, the maximum strain reached during the loading step was selected to be 0.05. The values of the SMA material paramenters used in this simulation are given in Table VII.

The results of this simulation are presented in Fig. 15. The stress *vs.* time plot is shown in Figure 15a, while Fig. 15b presents the temperature *vs.* time plot. The stress *vs.* strain and temperature *vs.* strain plots are presented in Fig. 15c and Fig. 15d, respectively. The return mapping algorithm implementation that integrates the heat equation using the Runge-Kutta scheme is identified in Fig. 15 as $RMA-1$, whereas the return mapping algorithm implementation that discretizes the heat equation using the implicit Euler rule is identified as $RMA-2$.

From the analyzes of Fig. 15 we can conclude that both implementations provide the same result. Even though the solution provided by both implementations converges fast, $RMA-2$ needs more iterations to converge than $RMA-1$, specifically during the reverse phase transformation.

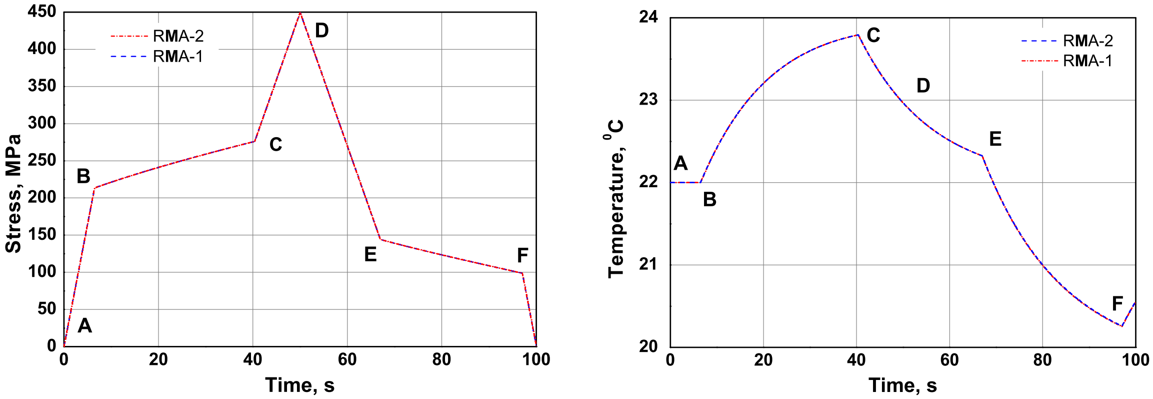

(a) Stress *vs.* time plot (b) Temperature *vs.* time plot

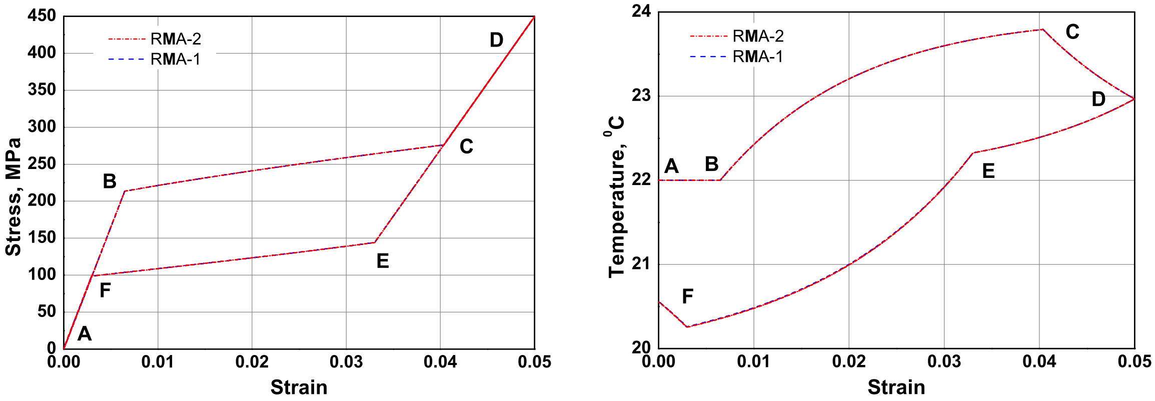

(c) Stress *vs.* strain plot (d) Temperature *vs.* strain plot

Fig. 15. Comparison of return mapping algorithm implementations.

Table VII. Values of a SMA material parameters used on the comparison of the return mapping algorithms

$E^A = 33.0 \cdot 10^9 Pa$	$E^M = 18.0 \cdot 10^9 Pa$
$\Delta\alpha = 0.0\mathrm{K}^{-1}$	$\Delta c = 0.0\mathrm{kJ/(kgK)}$
$M_f = -46\,^\circ\mathrm{C} = 227\mathrm{K}$	$M_s = -30\,^\circ\mathrm{C} = 243\mathrm{K}$
$A_s = -12\,^\circ\mathrm{C} = 261\mathrm{K}$	$A_f = -3\,^\circ\mathrm{C} = 270\mathrm{K}$
$H = 0.025$	$h = -5.0 \cdot 10^5\mathrm{W/m^3K}$
$T_0 = 22\,^\circ\mathrm{C} = 295\mathrm{K}$	$\dfrac{\mathrm{d}\sigma}{\mathrm{d}T} = 4.5\mathrm{Pa/K}$

Different points were placed in Fig. 15a-d to facilitate the understanding of the SMA behavior. These points are explained now. The loading step starts at point A. At this point the SMA is completely in the austenitic phase and its temperature is assumed to be in equilibrium with the environment, *i.e.*, $T = T_\infty$. During the interval from A to B, the SMA behaves as a linear elastic material, and no change in temperature is observed. The forward phase transformation occurs in the interval from point B to C. Since latent heat is produced during the forward phase transformation, the temperature of the SMA increases in this interval, until point C is reached. A further loading from point C to D will not increase the SMA temperature, but rather decrease, since the temperature of the SMA is higher than T_∞. The SMA behaves in a elastic manner during this interval. The same behavior can be observed during the elastic unloading in the interval from point D to E. The reverse phase transformation starts at point E. Since latent heat is absorbed during reverse phase transformation, the temperature of the SMA decreases even more. When the reverse phase transformation finishes at point F the temperature of the SMA is lower than the environment temperature. Therefore, during the final elastic unloading the SMA temperature increases, trying to equilibrate with the environment.

2. Comparison of Tensile Test on a SMA Wire with Numerical Simulations

Let us now compare experimental results of a tensile test of a SMA wire with numerical results predicted by the constitutive model. The experimental test consisted of loading and unloading an SMA wire in a MTS frame. In this test, strain is prescribed as input and stress and temperature are the recorded outputs. The loading and unloading steps have the same strain rate of $\dot{\varepsilon} = 0.0013$ s^{-1}. The initial temperature of the SMA wire was selected to be 49.5°C. The stress is measured by a load cell that is attached to the MTS frame and connected to the grips that hold the SMA wire, while the temperature is measured by a thermocouple connected to the midpoint length of the wire.

The same input of the experimental test was used as input for the numerical simulation of the constitutive model, and the value of the material constants utilized by the model is given by Table VII. Figure 16 presents the comparison of the experimental results with the numerical results. The strain history input is shown in Fig. 16a, while Fig. 16b and Fig. 16c present the stress *vs.* strain curve and temperature *vs.* time curve, respectively.

It can be noted that the models prediction of the stress *vs.* strain and temperature *vs.* time curves are in very good agreement with the experimental results. We should mention that the constitutive model predicts a lower SMA temperature in the interval from 40s to 70s (Fig. 16c) than the measured value of the temperature during the experiment. The reason for this is that the model predicts that the forward martensitic transformation ends around the strain level of 0.05, while

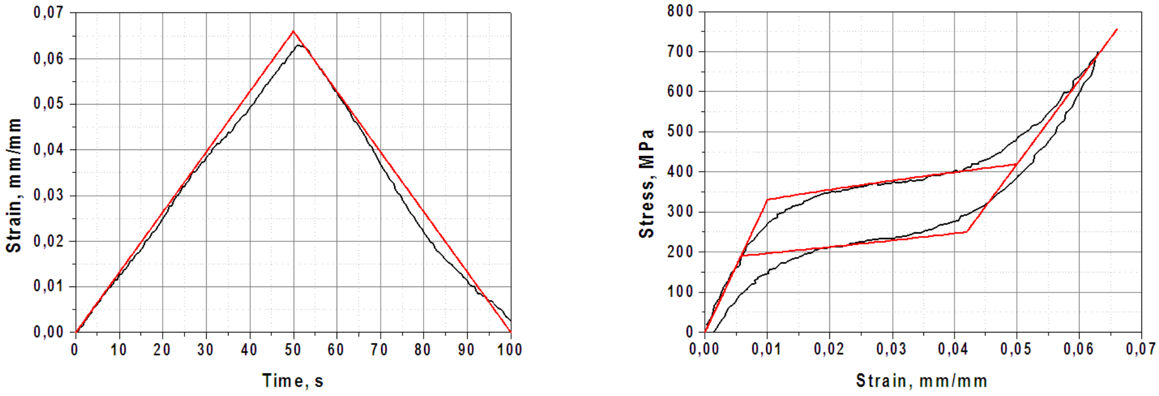

(a) Strain x Time

(b) Stress x Strain Curve

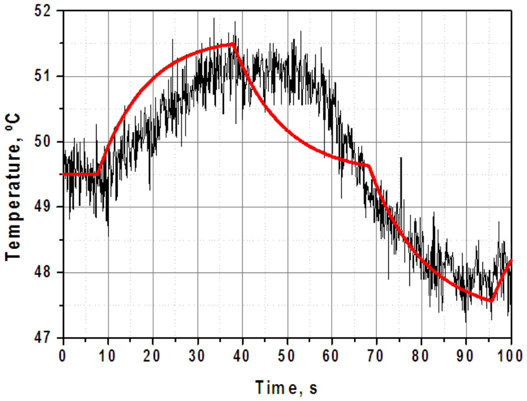

(c) Temperature x Time Curves

Fig. 16. Comparison of an experimental tensile test performed with numerical simulations.

in the actual material the transformation still continues after that point (Fig. 16b). Therefore, from the point that the forward transformation finishes to the point where the reverse phase transformation starts, the model predicts an elastic behavior, while in the experimental result, the forward transformation ends a little further and the reverse transformation starts a little earlier. As a result, the latent heat due to phase transformation is not considered, which leads to a decrease in the temperature value.

3. Investigation of the Stress-Relaxation Phenomenon on SMAs

Next, we investigate the stress-relaxation phenomenon induced by phase transformation. For this purpose, an experimental test was conducted on a previous cycled pseudoelastic SMA wire. The experiment consisted of the subjecting the SMA wire to a loading / unloading cycle with the strain rate of 0.00136/s. During the loading and unloading path, four different level of strains were selected to remain constant for a period of 300s. The strain levels are: 0.03 (point A) and 0.04 (point B) during loading, and 0.03 (point C) and 0.018 (point D) during unloading. The total time of the experiment was approximately 1300s.

Figure 17 presents the comparison of the stress-relaxation test with numerical simulations. The strain history input with respect to time for both experimental and numerical cases is presented in Fig. 17a, while temperature and stress with respect to time are presented in Fig. 17b and Fig. 17c, respectively. Figure 17d presents an enlargement of point A in the stress *vs.* strain plot of Fig. 17a.

Figure 17b shows that the temperature of the SMA increases during the forward martensitic phase transformation, until the strain level reaches the first holding point A. When the strain level reaches the value of 0.03 it stays constant for 300s , giving enough time for the wire to cool down. While the temperature reduces, the stress level also reduces (Fig. 17c), until the temperature of the wire reaches the environment temperature. When the temperature of the wire and the temperature of the environment are in equilibrium again, there is no more drop in the stress level, and it remains constant until the loading restarts again. Then, after 300s of holding, the loading restarts leading to another increase in the temperature, and consequently, in the level of stress, until the strain reach the value of 0.04. Likewise the first holding point, strain remains constant for 300s, leading to a new drop in the temperature and

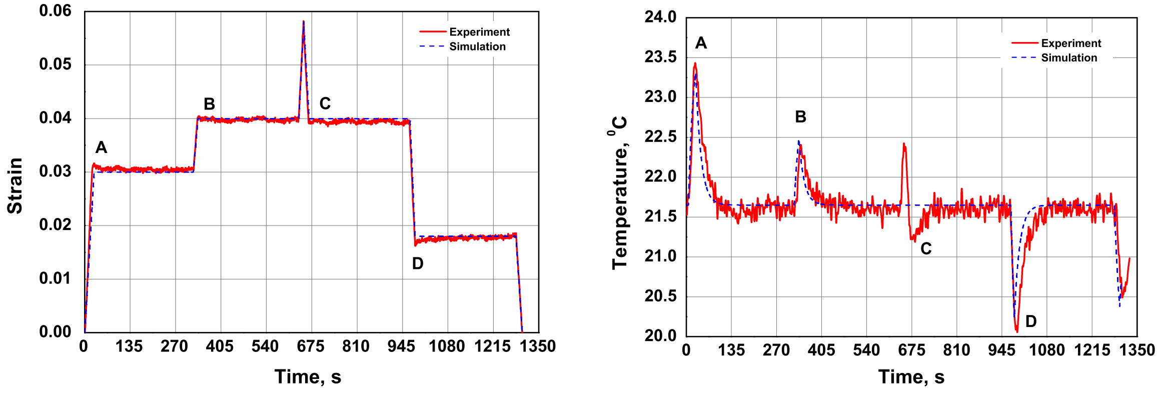

(a) Strain *vs.* Time

(b) Temperature *vs.* Time Curves

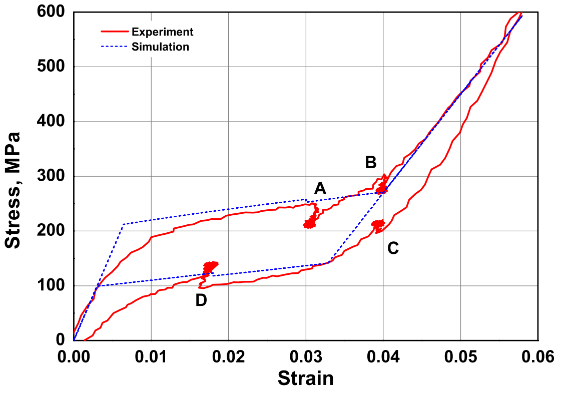

(c) Stress *vs.* Strain Curve

Fig. 17. Comparison of stress-relaxation test at room temperature with numerical simulations.

in the stress. After the completion of the 300s, the loading take places again up to 0.05 of strain. The same behavior can be observed during the unloading step. However, the temperature and the stress level increase, instead of decreasing as observed in the loading step.

It can be notice that there exist a small difference between the experimental results and the results predicted by the model, with respect to the value of the drop in stress levels, and peaks of temperature, at the holding points. This difference may be caused due to a small inaccuracy in the temperature measurement by the thermocouple, and also in the stress measurement by the load cell. The selected strain rate is fast, the holding points were reached very fast. Therefore, even though the thermocouple used to measure the temperature was very thin and light, it may take some time until the temperature of the thermocouple equilibrates with the wire's temperature. However, it should be emphasized that the model was able to predict the same temperature variation profile measured from the experiment.

A comparison of the stress-strain curve with both numerical and experimental simulation is presented in Fig. 17c. It can be observed that the second holding point barely appears in the numerical result, whereas the third holding point does not appear at all. The reason for this fact is that the constitutive model does not predict a smooth transition between the martensitic and austenitic phases, as observed in the experimental result. Thus, the holding points B and C represent the end of the forward transformation, and the beginning of the reverse phase transformation, respectively. At those points there is no phase transformation taking place, and the latent heat of transformation is neither generated or absorbed. Therefore, the effect of stress relaxation is not captured by the model in these two points.

Finally, Fig. 18 compares experimental results of different loading-unloading paths, under isothermal and non-isothermal conditions. Figure 18a compares two isothermal loading-unloading paths. The first test was conducted without any holding points. The second test was also conducted under isothermal conditions, however, the level of strain of 0.028 was selected to remain constant for 300s as the previous analysis. Since there is no temperature variation under isothermal loading conditions, the fact that a specific strain level was selected to remain constant for some time does not produce any change in the SMA behavior. Therefore, the two experimental results coincide. On the other hand, Fig. 18b compares the experimental result of the isothermal loading path without holding points with the non-isothermal loading path with holding points that was presented before. It can be observed that during the drop of stress, when the temperature of the non-isothermal loading path equilibrates with the environment, the stress level reaches the value of the stress for the isothermal loading path. The stress level will remain there until the loading starts again. A new increase in the SMA temperature separates the stress level of both curves again, until the next holding point, where the temperature of the SMA equilibrates again with the environment. This effect shows that the apparent stress-relaxation effect on the SMA behavior is only caused by the thermomechanical coupling, having no relation with viscous effects. This effect is not so evident for the reverse phase transformation because the reversal points of loading for the isothermal and non-isothermal conditions do not coincide. Also, the temperature variation under reverse transformation is lower than during forward transformation. Figure 18c shows the numerical result that compares the stress *vs.* strain plot for isothermal and non-isothermal conditions

4. Numerical Simulations: Different Strain Rates and Stress Relaxation Test

The forthcoming analysis is related to numerical simulations of the model with three different strain rates. The strain profile of all cases was chosen so that the maximum value of strain reached was 0.05, while the strain rate-1, -2 and -3 were selected to be equal to 0.0005/s, 0.001/s and 0.002/s, respectively. The initial temperature of the SMA, as well as the reference temperature and the environment temperature were selected to be 22 °C.

Figure 19a shows how the stress evolves with respect to time for the strain rates case, whereas The temperature plots of the SMA wire with respect to time for the different strain rate tests are presented in Fig. 19b. It can be notice that faster strain rates produce larger temperature variations, meaning that more latent heat due to phase transformation. The model's prediction of stress and temperature with respect to a given strain input is presented in Fig. 19c and 19d, respectively. By analyzing Fig. 19c one can notice that the loop of hysteresis not only enlarges, but also rotates with the increase of the strain rate. Therefore, the effect of temperature variation of the SMA material due to the thermomechanical coupling increases the dissipation provided by the loop of hysteresis.

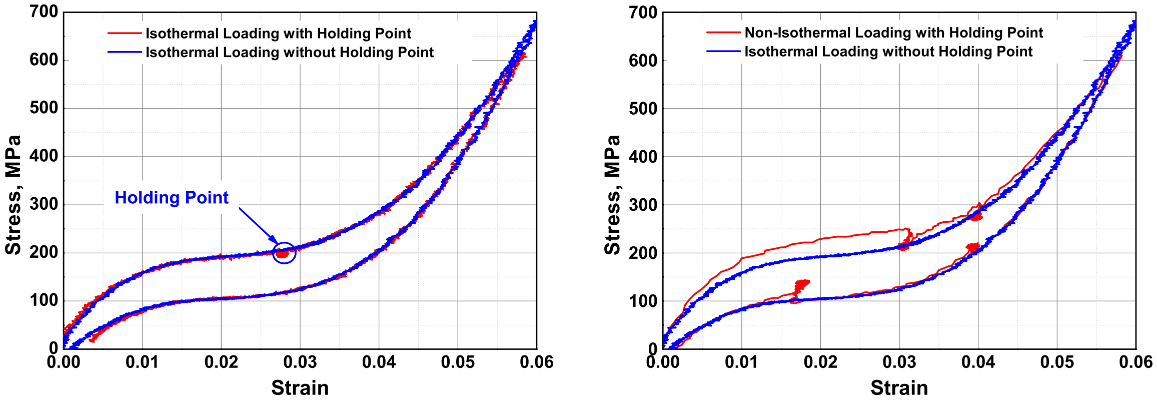

(a) Stress *vs.* strain curve - isothermal loading paths

(b) Stress *vs.* strain curve - isothermal and non-isothermal loading paths

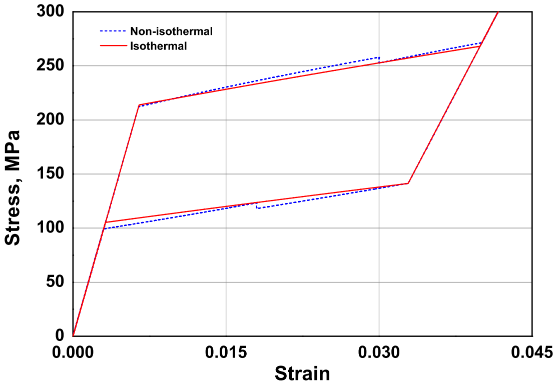

(c) Numerical simulation of the stress *vs.* strain curve - isothermal and non-isothermal loading paths

Fig. 18. Comparison of stress-relaxation test at room temperature - isothermal and non-isothermal loading paths.

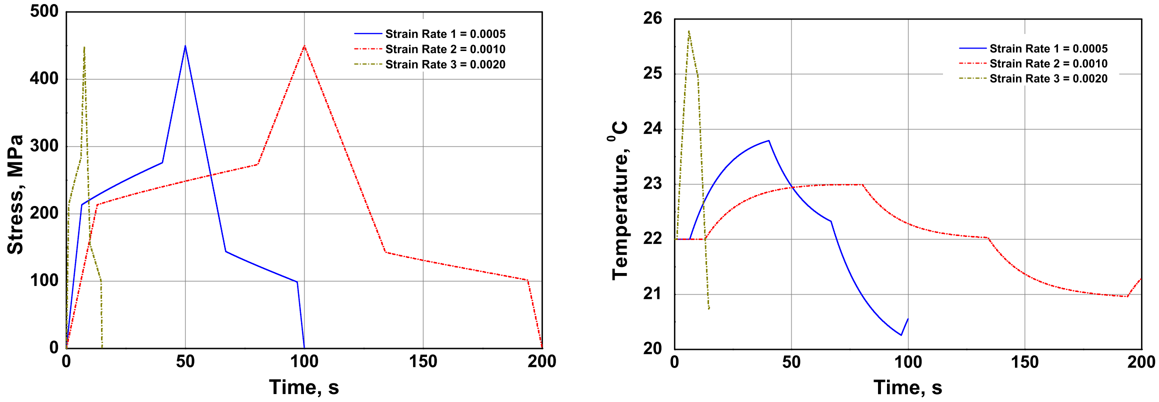

(a) Stress *vs.* time plot (b) Temperature *vs.* time plot

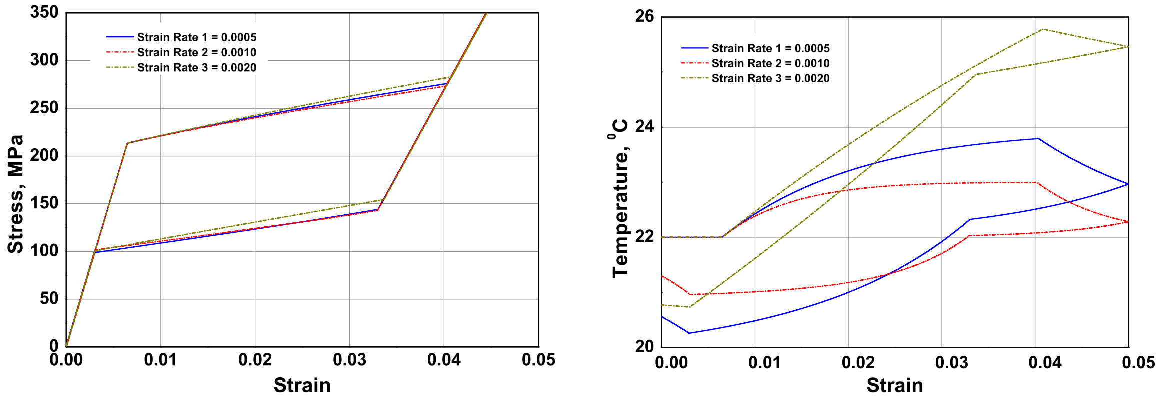

(c) Stress *vs.* strain plot (d) Temperature *vs.* strain plot

Fig. 19. Simulation of uniaxial loading / unloading tests of a SMA wire for different strain rate inputs.

CHAPTER VI

NONLINEAR DYNAMICS OF A PASSIVE VIBRATION ISOLATION AND DAMPING DEVICE

This chapter investigates the nonlinear dynamics of a passive damping vibration isolation and damping (PVID) device, where the main elements are SMA wires. The device is subjected to a series of continuous sinusoidal acceleration functions in the form of a sine sweep. Frequency responses and transmissibility of the device are analyzed for the case where the SMA wires were pre-strained 4% of their original length. In addition, the temperature of the wires was recorded during the dynamical tests, where a large variation was observed caused by stress induced martensitic phase transformation.

Numerical simulations of a one-degree of freedom (1-DOF) SMA oscillator were conducted to corroborate the experimental results. The configuration of the oscillator was based on the SMA passive vibration isolation and damping device, where a mass is balanced by two one-dimensional SMA elements. The constitutive model with the thermomechanical coupling presented in the previous chapters is used to simulate the constitutive pseudoelastic response of the SMA elements.

A. Experimental Investigation

Motivated by the unique properties of SMAs, an experimental setup was designed to investigate the passive vibration isolation and damping capabilities of these materials. The SMA passive vibration isolation and damping device (Fig. 20) is composed of a robust frame, two low-friction ball bearings, a mass (0.6kg), and two pseudoelastic SMA wires of equal length (76mm) and diameter (0.5mm) connecting the mass to the frame (both top and bottom). The ball bearings, which travel connected to vertical circular shafts, are attached to the mass in order to prevent any lateral displacement or rotation of the mass. In addition, since wires do not support compressive loads, each SMA wire was pre-strained at 4% of their original length to assure that they remain in tension throughout the tests. A screw assembled on the top plate of the frame provides the pre-tension of the wires.

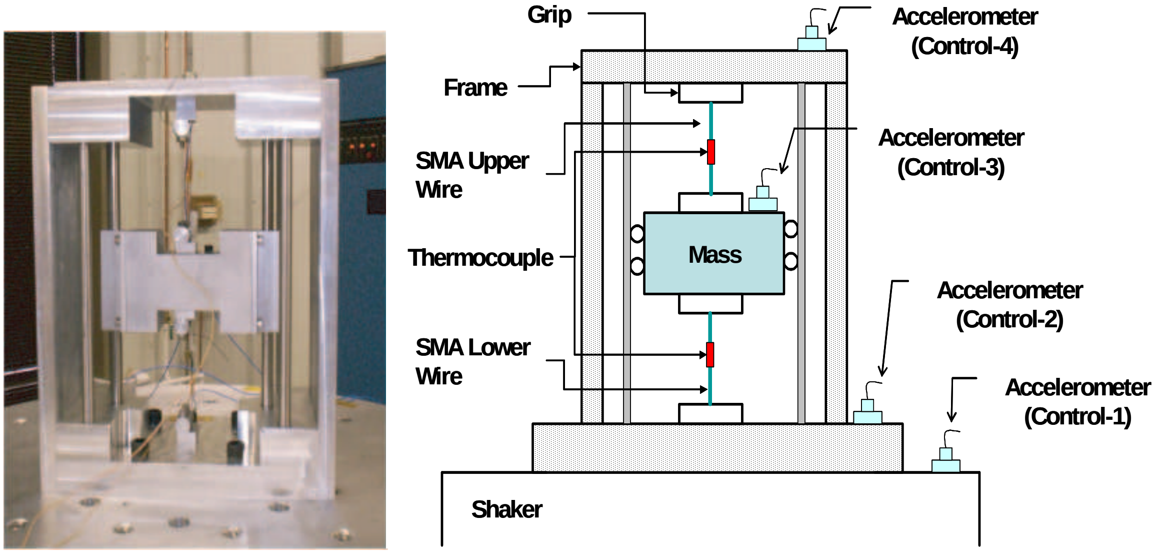
Grip
Accelerometer (Control-4)
Frame
SMA Upper Wire
Accelerometer (Control-3)
Thermocouple
Mass
Accelerometer (Control-2)
SMA Lower Wire
Accelerometer (Control-1)
Shaker

(a) SMA PVID device (b) Schematic of the SMA PVID device

Fig. 20. SMA passive vibration isolation and damping device.

The frame was designed to be of high stiffness in order to avoid any resonance or structural mode of vibration that could contaminate the analysis of the SMA response within the frequency range of the experiment. For this reason, a dynamic analysis of the frame was performed in *ABAQUS* 6.4, where the eigenfrequencies and modes of vibrations of the frame were estimated. Figure 21 presents the shape of the first four modes of vibration of the frame. The first mode of vibration of the structure happens at the frequency of 308Hz, while the second, the third and the fourth modes of vibration occur at the frequencies of 415Hz, 450Hz and 612Hz, respectively.

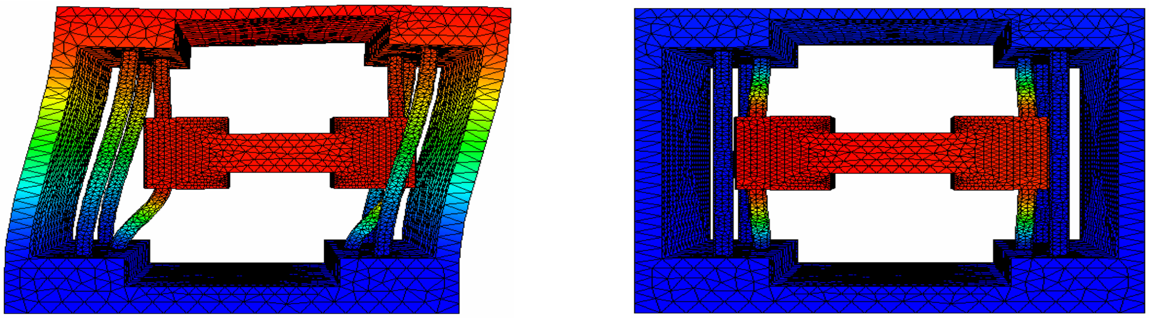

(a) $1^{st} mode - 308$Hz (b) $2^{nd} mode - 415$Hz

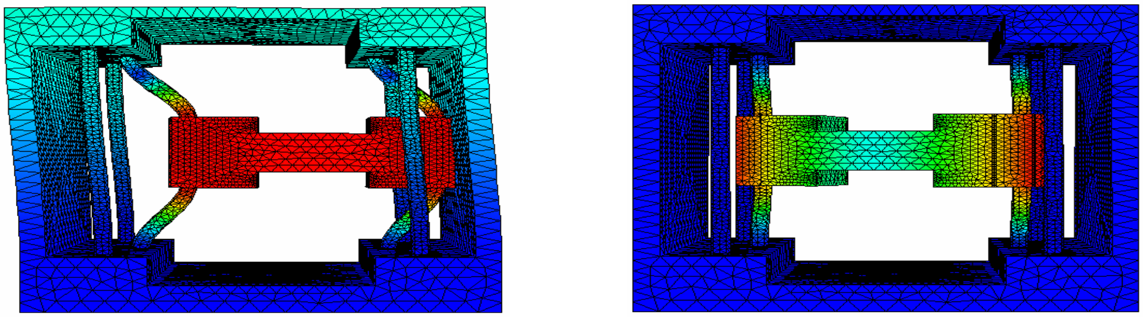

(c) $3^{rd} mode - 450$Hz (d) $4^{th} mode - 612$Hz

Fig. 21. Modes of vibration of the device.

1. Material Parameter Characterization

The material selected for the calibration of the model was a pseudoelastic NiTi wire, with 0.5mm of diameter. The basic requirement for the selection of the material was to exhibit pseudoelastic behavior at room temperature. Several thermomechanical tests were conducted with the purpose of characterizing and preparing the SMA wires for the vibration tests. At first, a sequence of thirty loading/unloading cycles was performed at constant temperature of 50°C (323.0 K), at the rate of 0.0003/s. The objective of this sequence of loading/unloading cycles was to stabilize the loop of hysteresis. Figure 22 a presents the stress-strain curve of theses cycles. After the thirty loading/unloading cycles, the SMA wire was cooled to room temperature, and then three single loading-unloading paths were performed at 25°C, 30°C, and 40°C, (Fig. 22b). These three single loading-unloading cycles were conducted to identify the value of the material parameters of the SMA wires used in the PVID device.

It is important to mention that, even though the model couples the thermal and mechanical problems, the sequence of loading/unloading cycle to stabilize the loop of hysteresis and the further loading and unloading cycles at different temperature were conducted by enforcing isothermal conditions. The reason for this is that the isothermal condition represents the actual behavior of the material. The effect of temperature variation caused by different loading/unloading rates is considered through the thermomechanical coupling effect, when the heat equation is incorporated into the constitutive modeling. If the latent heat generated due to the phase transformation is rapidly removed or added, then the same material response would be obtained for different loading/unloading strain rates [85]. The Newton cooling law will be used to consider the case of heat transfer by convection.

The identification of the values of the material parameters were performed according to the procedure presented in Chapter III, based on the experimental results presented in Fig. 22. Table VIII presents the values of the material parameters of the SMA wires used on the PVID device.

2. Experimental Vibration Test

Next, we introduce the vibration test of the PVID device. The experiment consisted of exciting the SMA PVID device (Fig. 20a) over a given frequency range by a series of continuous sinusoidal acceleration functions, in the form of a sine sweep. The amplitude of all sinusoidal acceleration functions was chosen to be a multiple of the

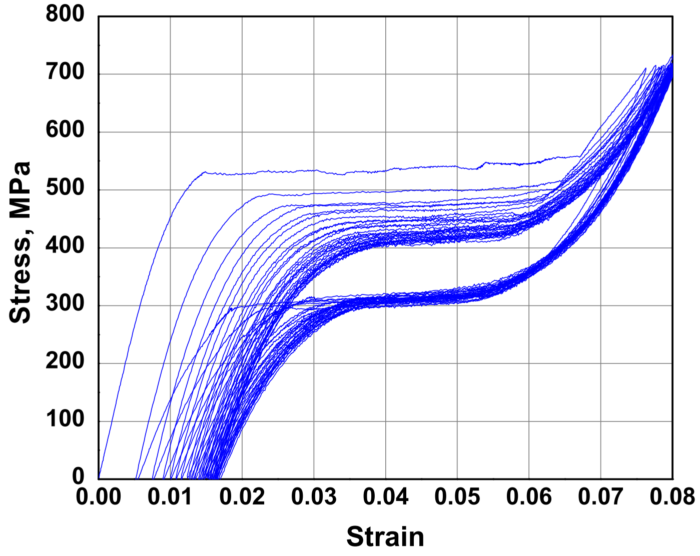

(a) Sequence of 30 loading/unloading cycles at 50°C

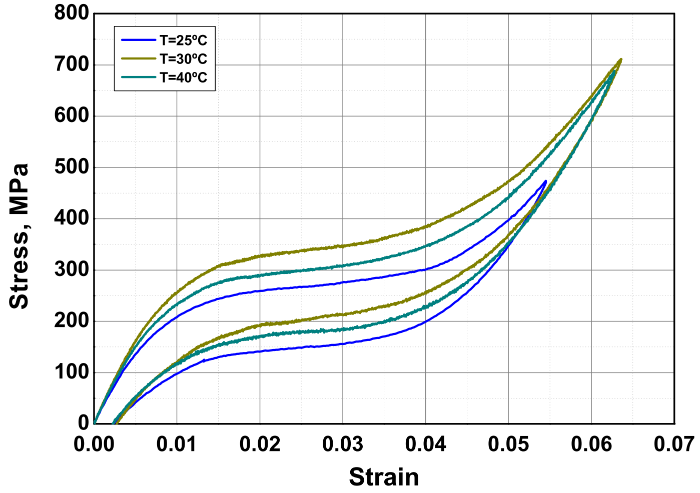

(b) Stress-Strain curves at 25°C, 30°C and 40°C

Fig. 22. Stress-Strain curves of the pseudoelastic SMA wires used on the experimental vibration test.

Table VIII. Values of the material parameters of the SMA wires used on the passive vibration isolation and damping device

$E^A = 33.0 \cdot 10^9 Pa$	$E^M = 15.0 \cdot 10^9 Pa$
$\Delta\alpha = 0.0\text{K}$	$\Delta c = 0.0\text{J}/(\text{kgK})$
$M_f = -46\,^\circ\text{C} = 227\text{K}$	$M_s = -30\,^\circ\text{C} = 243\text{K}$
$A_s = -12\,^\circ\text{C} = 261\text{K}$	$A_{0f} = -3\,^\circ\text{C} = 270\text{K}$
$H = 0.023$	$T_0 = 25\,^\circ\text{C} = 298\text{K}$

gravitational acceleration, g. Four tests were performed within the frequency interval from 32Hz to 256Hz, here defined as up sine sweep, with acceleration amplitudes of 0.5g, 1g, 2g, and 4g. Then, two tests were conducted for frequency interval from 256Hz to 32Hz, here defined as down sine sweep, with acceleration amplitudes of 1g and 2g. The sweep rate of all vibration tests was selected to be equal to 1.2Hz/sec, which resulted in total test time of approximately 180s. The initial temperature of all tests was measured to be 25 °C (298K). All vibration tests were conducted using a $C126$ shaker with a PUMA vibration control system by Spectral Dynamics.

Four accelerometers were used to record accelerations at different locations of the frame and on the shaker plate (Fig. 20b). The first accelerometer (#1) was placed on the shaker's plate, while the three others were positioned on different parts of the frame, *i.e.*, on the base plate (accelerometer #2), mass (accelerometer #3) and top plate (accelerometer #4). The accelerometers of the base and top plate of the frame measured the vibration of the frame and its possible influence on the mass dynamics, while the accelerometer on the mass captured the effects of the SMA wires. Temperature variations of the wires were also measured throughout the dynamical tests. One thermocouple was attached to the midpoint length of the SMA wire (see Fig. 20b), where a Labview program was used to record the temperatures during the dynamical tests.

Although acceleration constitutes the output for the experimental sine sweep tests, the experimental results are presented here in the form of transmissibility curves. Transmissibility was computed as the ratio of the mass acceleration measured by accelerometer #3 and the acceleration provided by the shaker measured by accelerometer #1. The condition of vibration isolation is achieved whenever the value of transmissibility is less than one.

The transmissibility responses of the up sine sweep tests for the input acceleration amplitudes of 1g, 2g, and 4g, are presented in Fig. 23a. Figure 23b shows the transmissibility responses for the down sine sweep tests with 1g and 2g of input acceleration amplitudes. It can be seen in both cases that, as the amplitude of the input acceleration increases, the value of the transmissibility peak and frequency, at which the peak occurs, decrease. Moreover, a discontinuity (jump) in the system dynamic response can be observed for the cases of 2g and 4g in the up and down sine sweep tests. The reduction of the resonance frequency of the system occurs as a consequence of the martensitic phase transformation that the SMA wires undergo during the test. The stress-induced martensitic phase transformation that takes place in the SMA wires during the dynamical tests results in lower tangent stiffness, which reduces the frequency of resonance of the device. The reduction in the peak of the transmissibility curves is related to the hysteretic damping provided by the SMA wires. Higher amplitudes of the input acceleration result in higher hysteretic damping.

The maximum value of the transmissibility curve in Fig. 23a, for the acceleration amplitude of 1.0g, was measured to be 8.4 and it occurs at the frequency of 54.5Hz. With an increase of the acceleration amplitude for 2.0g, the value of the transmis-

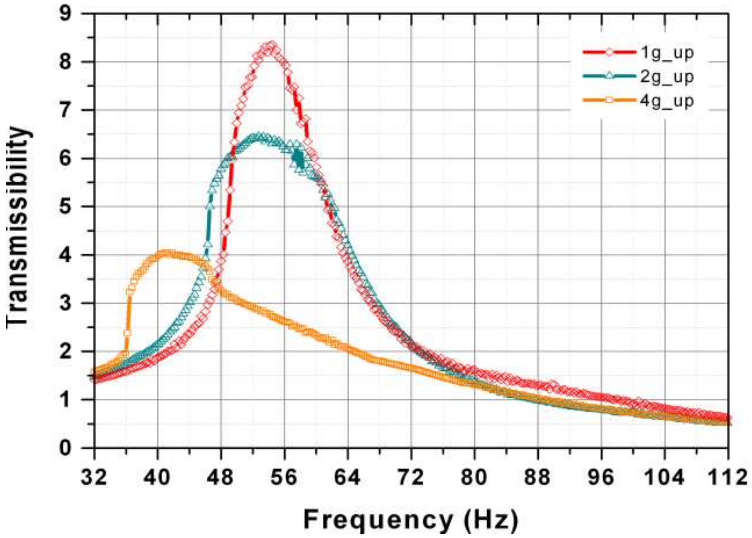

(a) Transmissibility curve for up sine sweep tests

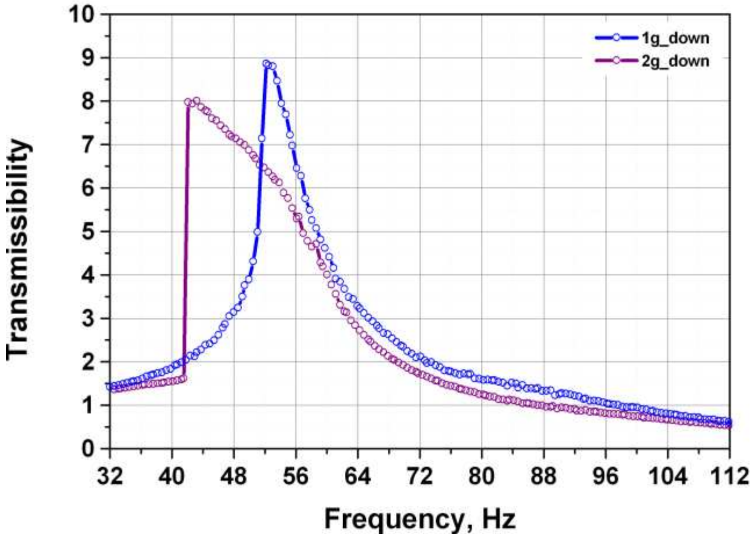

(b) Transmissibility curve for down sine sweep tests

Fig. 23. Transmissibility curves for the up and down sine sweep tests at the temperature of T=25 °C.

sibility peak reduces to 6.45 as well as the frequency that it occurs, reduce to *i.e.*, 53.0Hz. Following the same trend, the value of the transmissibility peak for 4.0g of acceleration amplitude reduces to 4.04, occurring at the frequency of 41Hz. The discontinuity in the transmissibility curve of the SMA PVID device is more evident for the acceleration amplitudes of 2g and 4g. The discontinuity always happens before the frequency that the transmissibility peak occurs, as shown in Figure 23. This fact happens as a result of the nonlinear softening behavior of the SMA wires during the dynamical tests, which is related to the nonlinear damping introduced by the SMA loop of hysteresis. For the 2.0g case, the transmissibility response jumps from 4.2 to 5.0, while for 4.0g it jumps from 1.9 to 3.2. It can be also noticed that the minimum frequency for vibration isolation decreases from to 98.4Hz for 1.0g, to 88.0Hz for 2.0g, and stays at 89.0Hz for 4.0g.

Figure 23b presents the vibration tests that were conducted with decreasing excitation frequencies (down sine sweep tests), with input acceleration amplitudes of 1.0g, and 2.0g. It was observed that the martensitic phase transformation and hysteresis of the SMA wires produced similar effects on the dynamics of the system as before in the up sine sweep tests. As the value of the input acceleration amplitude increased, the value of the transmissibility peak and frequency decreased. The value of the transmissibility peak for the acceleration amplitude of 1.0g was measured to be 8.9 and it happened at the frequency of 52Hz, whereas the peak for the amplitude of 2.0g was measured to be 8.0 and it happened at 42.0Hz. Furthermore, the discontinuities in the frequency response are more evident than the up sine sweep tests. For the case of 1.0g, the transmissibility value changes from 8.9 to 5.0, while for the case of 2.0g the transmissibility peak is largely reduced from 8.0 to 1.6.

For the sake of comparison, Fig. 24 combined in the same plot the results of the sine sweep tests for acceleration amplitudes 1g and 2g up (Fig. 24a), and 1g and 2g

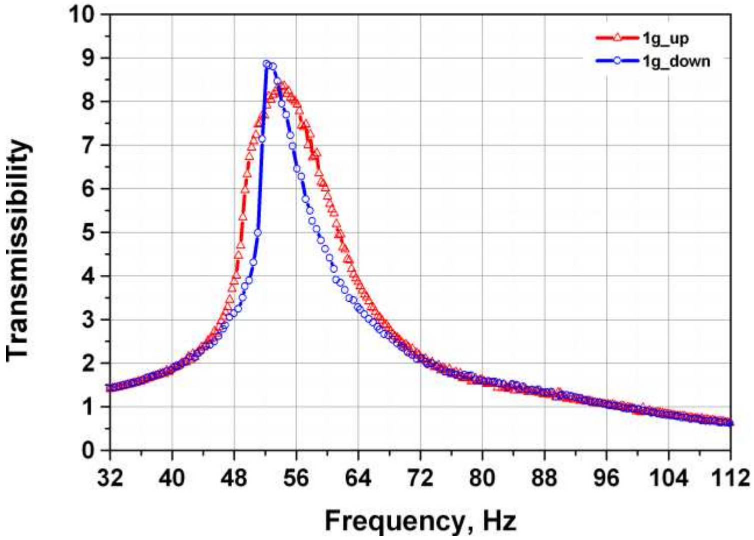

(a) Transmissibility curve for 1g up and down

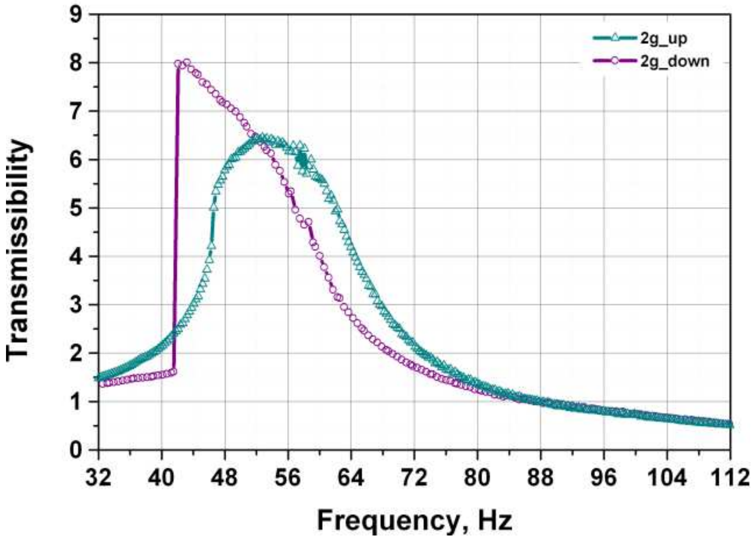

(b) Transmissibility curve for 2g up and down

Fig. 24. Transmissibility curve for 1g and 2g up and down sine sweep test at the temperature of T=25 °C.

down(Fig. 24b). It can be seen in both cases that the transmissibility peaks for the down sine sweep tests have a higher value than the up sine sweep tests. In addition, the frequency for vibration isolation of the 1g up and down (Fig. 24a), and 2g up and down (Fig. 24b) happened at the same value, that is 96Hz for 1g and 88Hz for 2g.

The temperature variations of the SMA wires during the vibration experiment are presented in Fig. 25. Figure 25a presents the temperature variation of the SMA wires for the case of up sine sweep tests, while Fig. 25b shows the case of down sine sweep test. The increase in the temperature that the SMA wires experience are caused by the stress induced martensitic phase transformation that the wires undergo during the vibration tests. The higher amplitude of acceleration input, the higher is the temperature variation of the wires, denoting a very strong thermomechanical coupling. In addition, the highest values of temperature for all sine sweep tests occurred when the device was excited around the system's resonance frequency. During up sine sweep tests, the maximum temperature variation for the acceleration amplitude of 1g was measured to be approximately 13.5 °C, which resulted in the total temperature of the SMA wires to be 38.5 °C. For the acceleration amplitude of 2g the temperature variation was measured to be 25 °C, while for the acceleration amplitude of 4g the temperature variation was measured to be 28 °C. Therefore, the maximum temperature of the SMA wires during the sine sweep test with acceleration amplitude of 2g was measured to be 50 °C, whereas for 4g the temperature of the SMA wires reached 53 °C. The temperature variation of the SMA wires during the down sine sweep tests were measured to be 11 °C for the acceleration amplitude of 1g and 27 °C for the amplitude of 2g. Then, the maximum temperature of the SMA wires during the test with amplitude 1g was measured to be 36 °C, while for 2g the temperature reached the value of 52 °C. Therefore, the down sine sweep tests generated higher temperature variations on the SMA wires, than the up sine sweep tests.

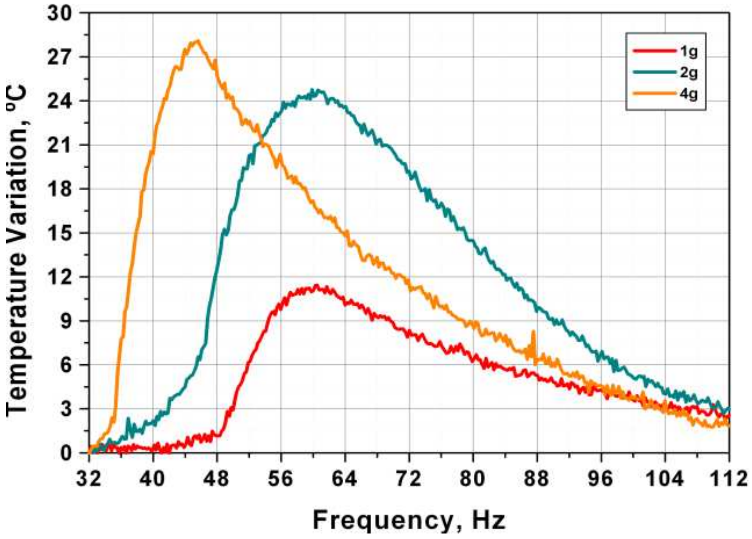

(a) Temperature variation for up sine sweep test

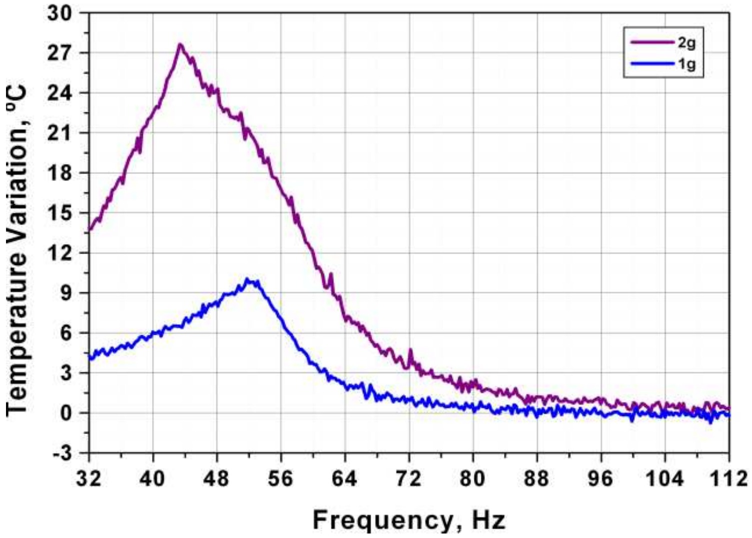

(b) Temperature variation for down sine sweep test

Fig. 25. Temperature variation of the SMA wires for up and down sine sweep tests.

At this point, it is important to compare some features related to the transmissibility of vibration isolation systems with linear stiffness and linear viscous damping, with the transmissibility of a vibration system composed with SMA wires. First of all, the transmissibility of a linear system is a single-valued curve, where there is no discontinuity (jump) present, and higher damping results in lower transmissibility values. However, the damping has no effect on the frequency at which the effective isolation happens[86]. Also, there is no change in the temperature of the isolation system. The analysis of the experimental results of the passive SMA damping device has shown that the transmissibility curves present a discontinuity related to the hysteretic behavior of the SMA wires. The damping effect on the SMA system is variable, and it is a function of the area of the loop of hysteresis. Also, the stress-induced martensitic transformation that the SMA wires undergo reduces the resonance frequency of the system, and largely increases the temperature of the SMA wires.

B. Numerical Simulations of a Passive Vibration Isolation SMA Device

This section presents the numerical simulation of a one-degree of freedom (1-DOF) SMA oscillator. The configuration of the oscillator was based on the SMA passive vibration isolation and damping device presented in Section A. The constitutive model for SMAs presented in the previous chapters this work is used to describe the constitutive behavior pseudoelastic SMA elements of the oscillator. The comparisons between numerical and experimental results are presented in Section C.

1. One-Degree of Freedom Shape Memory Alloy Oscillator

Consider a one-degree of freedom oscillator (Fig. 26) composed of a mass balanced by two pseudoelastic SMA elements, which are also pre-strained at 4% of their original length. The oscillator parameters were chosen to be the same as the SMA PVID device, and the material properties of the SMA elements are the same presented in Table VIII.

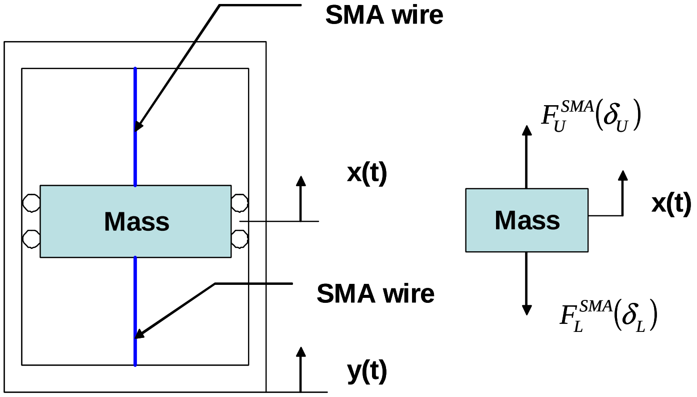

Fig. 26. One-degree of freedom SMA oscillator.

The governing equation of motion of the oscillator is given by Eq. 6.1, below:

$$m\ddot{x} = F_U^{SMA} - F_L^{SMA} \tag{6.1}$$

where m is the mass of the oscillator, $\ddot{x}$ is the acceleration of the mass, F_U^{SMA} is the force exerted by the SMA wire above the mass, and F_L^{SMA} is the force exerted by the SMA wire below the mass.

It is important to mention that the only dissipation considered in the SMA oscillator is provided by the loop of hysteresis, which is loading/unloading path dependent. Therefore, Eq. 6.1 does not consider any velocity dependent term due to rate dependent dissipation, such as in viscoelastic materials. Furthermore, the forces exerted by the SMA wires are dependent on the history of the displacement. Consequently, F_U^{SMA} and F_L^{SMA} have, in general, different magnitudes, since the upper and the lower displacements have opposite histories[73] and there is a pre-strain that is imposed on the wires at static equilibrium. The change in length of the SMA wires as a function of the mass and base displacements is described by Eq. 6.2, as follows:

$$\delta_L = -\delta_U = x(t) - z(t) \tag{6.2}$$

where δ_U is the upper wire displacement, and δ_L is the lower wire displacement, while $x(t)$ is the mass displacement, and $z(t)$ is the base displacement. The system is harmonically excited by a base displacement in a sinusoidal form, as given by:

$$z(t) = \bar{z}\sin(\omega t) \tag{6.3}$$

$$\bar{z} = \frac{ag}{\omega^2} \tag{6.4}$$

where ω is the excitation circular frequency, and $\bar{z}$ (given by Eq. 6.4) is the amplitude of the imposed displacement, given in terms of a, which is a fraction of the gravitational acceleration, g.

The constitutive model for SMA is presented in the next section. Since the model was constructed based on stress and strain, and the equation of motion is defined in terms of force and displacement, we correlate stress with force by the expression $\sigma = F/A$, and strain with displacement by the expression $\varepsilon = x/L$.

2. Constitutive Model for SMAs

The constitutive model used to describe the behavior of the SMA elements is the same model presented in the previous chapters. Since the model was already introduced in detail we just present here the basic equations. Moreover, the basic equations are presented in the one-dimensional form because the SMA element is a one-dimensional element.

The one-dimensional form of the stress-strain relation is given by

$$\sigma = S^{-1}\left[\varepsilon - \alpha\left(T - T_0\right) - \varepsilon^t\right]. \tag{6.5}$$

where the one-dimensional form of the effective material properties are given by

$$S\left(\xi\right) = S^A + \xi\left(S^M - S^A\right) = S^A + \xi\Delta S \tag{6.6}$$

$$\alpha\left(\xi\right) = \alpha^A + \xi\left(\alpha^M - \alpha^A\right) = \alpha^A + \xi\Delta\alpha \tag{6.7}$$

The one-dimensional form of the flow rule is given by:

$$\dot{\varepsilon^t} = H\text{sgn}(\sigma)\dot{\xi}, \tag{6.8}$$

The one-dimensional form of the transformation function for forward phase transformation is given by

$$\begin{aligned}&\left|\sigma\right|H + \frac{1}{2}\sigma^2\Delta S + \sigma\Delta\alpha\left(T - T_0\right) - \rho\Delta c\left[\left(T - T_0\right) - T\ln\left(\frac{T}{T_0}\right)\right]\\&+ \rho\Delta s_0 T - \rho\Delta u_0 - \frac{\partial f}{\partial\xi} - Y^* = 0,\end{aligned} \tag{6.9}$$

while the one-dimensional form of the transformation function for the reverse phase transformation is given by

$$\begin{aligned}&\left|\sigma\right|H + \frac{1}{2}\sigma^2\Delta S + \sigma\Delta\alpha\left(T - T_0\right) - \rho\Delta c\left[\left(T - T_0\right) - T\ln\left(\frac{T}{T_0}\right)\right]\\&+ \rho\Delta s_0 T - \rho\Delta u_0 - \frac{\partial f}{\partial\xi} + Y^* = 0.\end{aligned} \tag{6.10}$$

Finally, the one-dimensional form of the heat equation is given by

$$T\alpha\dot{\sigma} + \rho c\dot{T} + \left(-\pi + T\Delta\alpha\sigma - \rho\Delta cT\ln\left(\frac{T}{T_0}\right) + \rho\Delta s_0 T\right)\dot{\xi} = h\left(T - T_\infty\right). \tag{6.11}$$

The definition of the model parameters are given by Table III.

3. Material Characterization and Numerical Implementation of the Model

The material selected for the calibration of the model was the same used in the vibration test, where the basic requirement was to exhibit pseudoelastic behavior at room temperature. Since the thermomechanical tests that are used to identify the value of the material parameters were already described in Chapter III, we presented the values of the material parameters in Table XIV.

The implementation of the constitutive model follows the same procedure described in Chapter V. Basically, given an increment of strain, the incremental form of the SMA constitutive model provides increments of stress and temperature as outcomes. The increments of stress and temperature are calculated by implementing the Return Mapping Algorithm.

Now that the equation of motion of the SMA oscillator and the thermomechanical constitutive model for the SMA wires have already been defined, we proceed by integrating numerically Eq. 6.1, and thereby predicting the dynamical response of the oscillator. Since the response of the SMA oscillator is highly nonlinear, an efficient and reliable numerical method should be employed to assure stability and convergence of the solution. For this reason, Newmark integration scheme is used to compute the time response of the system.

Originally, Newmark proposed as an unconditional stable scheme, the case where the weight parameters α, and γ are equal to 0.25 and 0.5, respectively [87]. However, in this work, time integration is performed by Galerkin Method, a variant of the Newmark scheme[88], where α and γ are defined to be equal to 0.5 and 1.6, respectively. Time step and weighting parameters are chosen in order to ensure the stability and convergence of the solution. According to the Newmark scheme, the function and its derivatives are approximated as follows[87]:

$$\begin{aligned} x_{n+1} &= x_n + \Delta t \dot{x}_n + \frac{1}{2}\Delta t^2 \ddot{x}_{n+\gamma} \\ \dot{x}_{n+1} &= \dot{x}_n + \ddot{x}_{n+\alpha}\Delta t \\ \ddot{x}_{n+\gamma} &= (1-\gamma)\,\dot{x}_n + \gamma \ddot{x}_{n+1} \\ \ddot{x}_{n+\alpha} &= (1-\alpha)\,\dot{x}_n + \alpha \ddot{x}_{n+1} \end{aligned} \tag{6.12}$$

After re-arranging some terms of Eq. 6.12, one can easily show that:

$$\ddot{x}_{n+1} = a_3 x_{n+1} - G_n \tag{6.13}$$

where:

$$G_n = a_3 x_n - a_4 \dot{x}_n - a_5 \ddot{x}_n \tag{6.14}$$

$$a_3 = \frac{2}{\gamma \Delta t^2}; \qquad a_4 = \frac{2}{\gamma \Delta t}; \qquad a_5 = \frac{(1-\gamma)}{\gamma} \tag{6.15}$$

Substituting Eq. 6.13 into Eq. 6.1, we can easily find the relation

$$x_{n+1} = \frac{\tilde{F} + mG_n}{a_3 m} \tag{6.16}$$

where

$$\tilde{F} = F_U^{SMA} - F_L^{SMA} \tag{6.17}$$

The expression for acceleration can be obtained from Eq. 6.13, while the expression for velocity is given by:

$$\dot{x}_{n+1} = x_n + a_2 \dot{x}_n + a_1 \ddot{x}_{n+1} \tag{6.18}$$

where

$$a_1 = \alpha \Delta t; \qquad a_2 = (1 - \alpha)\, \Delta t \tag{6.19}$$

Notice that $\tilde{F}$ is function of the forces exerted by the upper and lower wires. These forces are functions of the variable tangent stiffness of the SMA wires that are displacement history dependent. Therefore, the actual solution of Eq. 6.16 is computed through an iterative scheme. For each time interval the displacement of both SMA wires is calculated. Then, the displacement history is used as input for the return mapping algorithm, which resolves the nonlinear behavior of the material and updates the value of the tangent stiffness and the value of the forces exerted by the SMA wires. The displacement of the previous converged time step, x_n, is used as a initial condition for the actual time step $x_{n+1}^{k=0} = x_n$. Eq. 6.20 is computed until convergence is reached $\left(\left|x_{n+1}^{(k+1)} - x_n\right| < tol = 1.0e - 6\right)$.

$$x_{n+1}^{(k+1)} = \frac{\tilde{F}\left(x_{n+1}^{(k)}\right) + mG_n}{a_3 m} \tag{6.20}$$

C. Comparison of Experimental Results with Numerical Simulations

This section compares the experimental results obtained from sine-sweep vibration tests presented in section A with numerical simulation of the SMA oscillator for the isothermal and non-isothermal conditions. The comparisons between numerical and experimental up sine sweep tests are presented in Fig. 27 and Fig. 28, while Fig. 29 and Fig. 30 show the comparison of the down sine sweep tests.

Figure 27a compares the transmissibility curve obtained from the up sine sweep test of the PVID device with the transmissibility curves predicted by the numerical simulations of the SMA oscillator, for the cases of isothermal and non-isothermal conditions, with the input acceleration amplitude of 1g. The frequencies of resonance

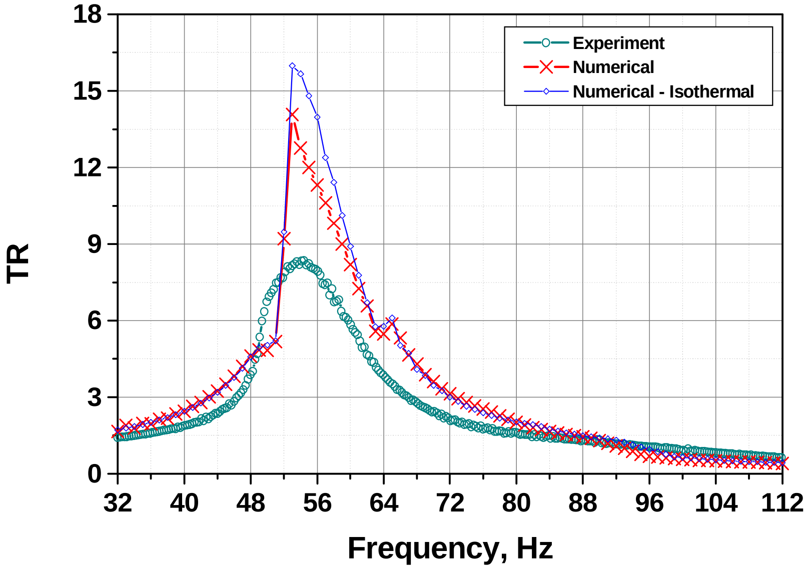

(a) Comparison of experimental and numerical transmissibility curve for up sine sweep test with acceleration amplitude of 1.0g

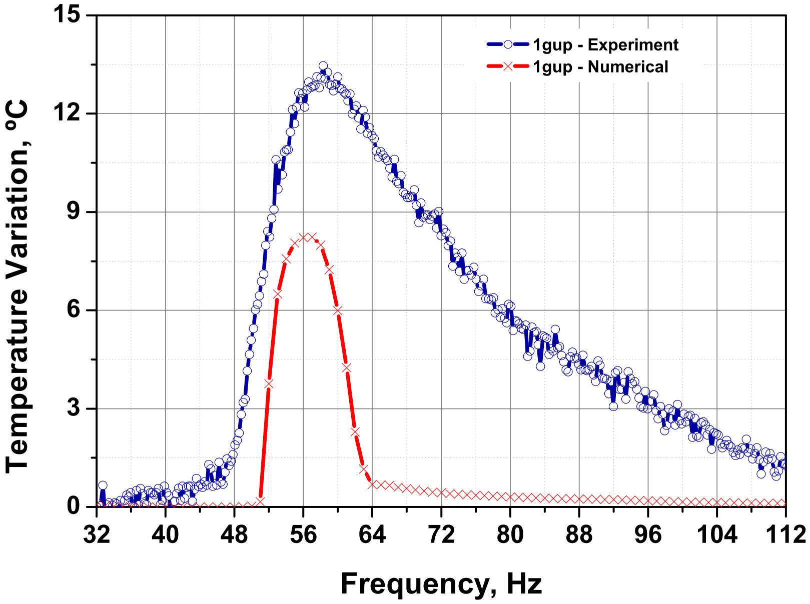

(b) Comparison of experimental and numerical temperature response for up sine sweep test with acceleration amplitude of 1.0g

Fig. 27. Comparison of experimental and numerical transmissibility curve and temperature variation for up sine sweep test with acceleration amplitude of 1.0g.

obtained from the simulations are equivalent to the frequency of resonance measured from the experimental test, that is 54.4Hz. However, the peak of transmissibility predicted by the numerical simulation for both isothermal and non-isothermal conditions is higher than the peak measured from the experimental test. Moreover, the value of the transmissibility peak obtained from the simulation with non-isothermal conditions is lower than the transmissibility peak for simulations with isothermal conditions. This fact indicates that the temperature variation of the SMA wires caused by the stress-induced phase transformation increases the amount of energy dissipated, when compared to the isothermal case.

The comparison of temperature variation of the SMA wires measured in the experimental test with temperature variation predicted by the numerical simulations with non-isothermal conditions is presented in Fig. 27b. It can be observed that the peak of the experimental curve is higher than the peak predicted by the numerical simulations. Even though the peak of the experimental temperature variation curve was measured to be 13.5 °C, and the numerical simulations predicted the temperature variation peak to be 8.5 °C, the simulation was able to predict the interval of frequency that the temperature peak occurred.

Figure 28 compares the experimental transmissibility and temperature variation curves with the results predicted by the numerical simulations, for input acceleration amplitude of 2.0g in the up sine sweep. Once more the peak of the transmissibility curve for the simulation with non-isothermal conditions is lower than the peak predicted by the isothermal condition. Moreover, the simulations predicted a discontinuous transmissibility curve as observed by the experimental result. The frequency at which the discontinuity occurred in the numerical simulations coincide with the experimental result. The transmissibility peak predicted by the simulation with non-isothermal conditions is closer to the value obtained experimentally than the previous simulation of acceleration amplitude of 1g. The numerical simulation was also able to predict a reduction on the value of the transmissibility peak with an increase of the input acceleration amplitude, from 1g to 2g. It is important to mention that the numerical simulations show an small bump in the frequency interval from 69Hz to 72Hz. However, this bump is not related to a second frequency of resonance.

The comparison of the temperature variation of the SMA wires for the up sine sweep with acceleration amplitude of 2g predicted by the non-isothermal simulation with the experimental result is presented in Fig. 28b. The temperature variation curve predicted by the simulation has the same profile as the experimental curve. The main difference is in the peak of the temperature curve, where the simulation predicted a lower peak than the experimental one.

Figure 29 and Fig. 30 present the comparison of numerical simulation with experimental results for the case of down sine sweep tests with acceleration amplitudes of 1g and 2g. The transmissibility responses are presented in Fig. 29a and Fig. 30a, while the temperature variation curves for 1g and 2g are shown in Fig. 29b and Fig. 30b, respectively. Basically, the same comments that were made for the case of 1.0g and 2.0g up sine sweeps apply to the case of 1.0g and 2.0g down sine sweeps, where it can be seen a reduction of the transmissibility peak and frequency of resonance, for an increase of the amplitude of acceleration input. Also, there is an increase in the temperature variation of the SMA wires with an increase of the amplitude of acceleration input.

The comparison of numerical and experimental transmissibility response for the case of 2.0g down is presented in Fig. 30a. For this case, one can see that the numerical and experimental curves show good agreement. The value of the peak of transmissibility was measured to be 7.7 at the frequency of 43Hz, and 8.0 at the frequency of 42Hz, for the numerical and experimental tests, respectively. Moreover, likewise the case for up sine sweeps, the temperature of the wires largely increases at the resonance. However, for the case of 1.0g and 2.0 down sine sweeps, the frequency at maximum temperature variation presents better agreement, compared to the 1.0g and 2.0g up sine sweep. Even though there is still some discrepancies with respect to the value of temperature variation between the numerical and experimental vibration tests, the model was able to predict the frequency range where the temperature variation is more pronounced.

The transmissibility curve for down sine sweep test with the acceleration amplitude 2g is revisit in Fig. 31. However, the stress *vs.* strain plot of the SMA elements for selected values of frequency is also plotted in the figure. The idea is to analyze the SMA behavior for each value of frequency. At the frequency of 39Hz, for example, the SMA behaves as a undamped linear elastic material in the martensitic phase, since the stress *vs.* strain curve at this value of frequency is a straight line. However, at the transmissibility peak, at the frequency of 42Hz, the SMA response oscillates within the loop of hysteresis. Therefore, the discontinuity of the transmissibility curve is related to the sudden appearance of an hysteretic damping caused by the SMA behavior. In addition, we should emphasize that the SMA response at the frequency of 42Hz utilizes the largest area of the loop, leading to the maximum hysteretic damping. For frequencies higher than 42hz the loop of hysteresis progressively shrinks until the SMA response returns to the linear elastic material, without any damping.

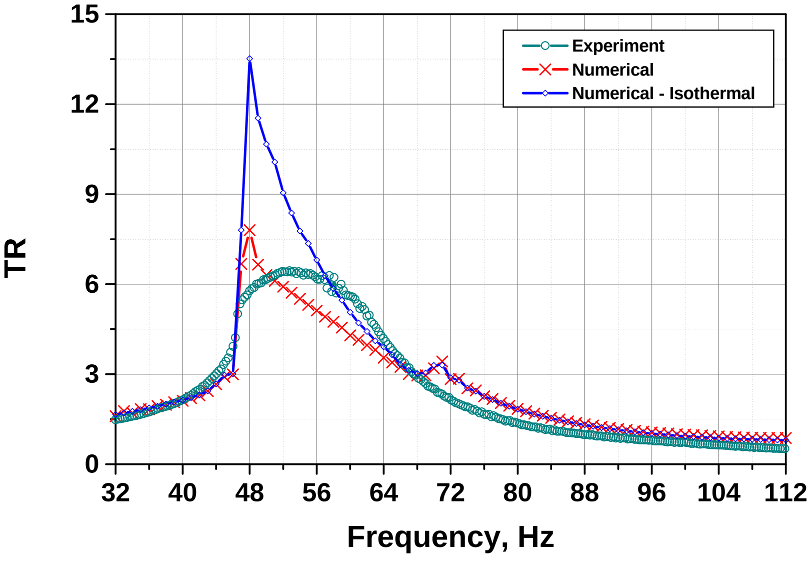

(a) Comparison of experimental and numerical transmissibility curve for up sine sweep test with acceleration amplitude of 2.0g

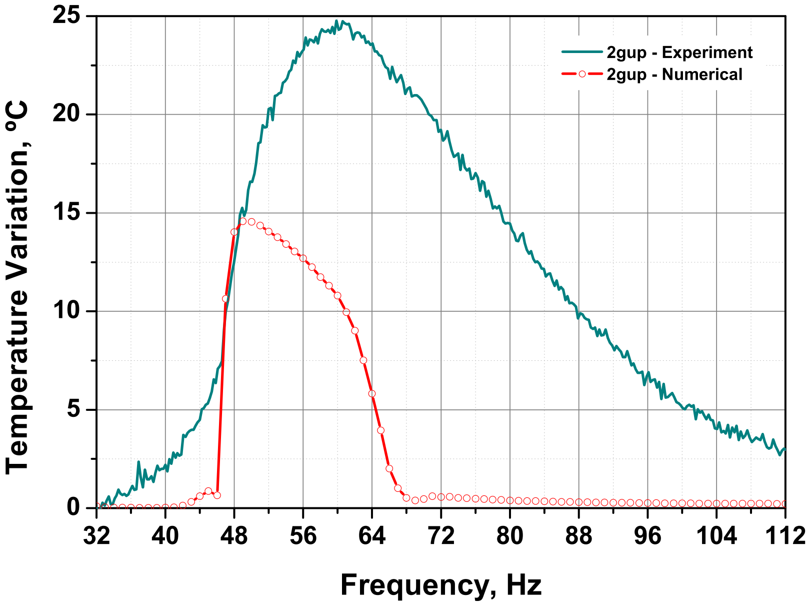

(b) Comparison of experimental and numerical temperature variation for up sine sweep test with acceleration amplitude of 2.0g

Fig. 28. Comparison of experimental and numerical transmissibility curve and temperature variation for up sine sweep test with acceleration amplitude of 2.0g.

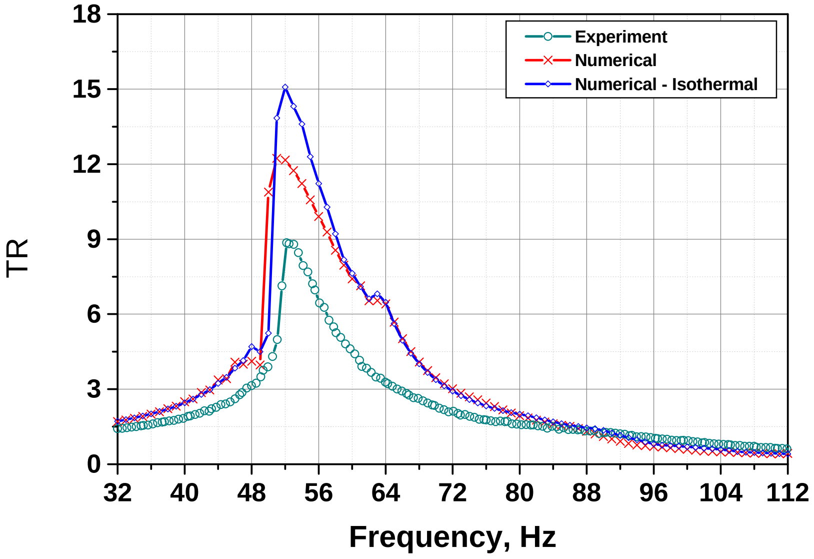

(a) Comparison of experimental and numerical transmissibility curve for down sine sweep test with acceleration amplitude of 1.0g

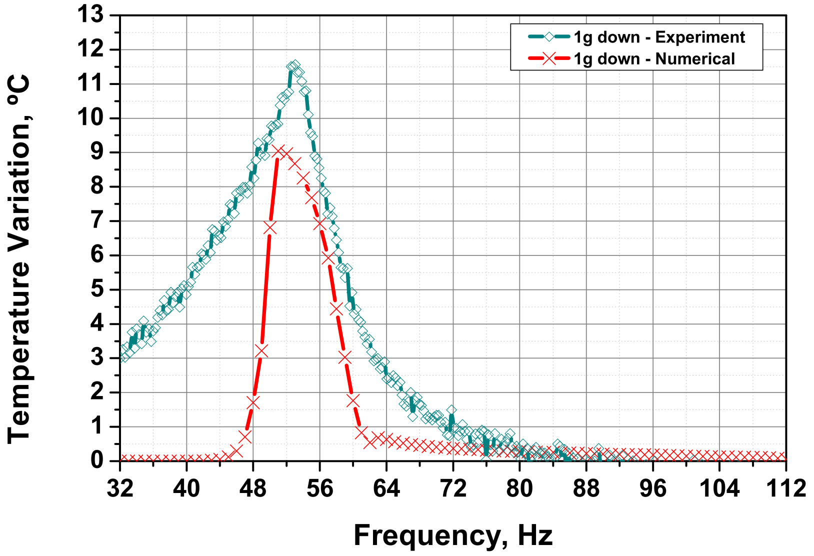

(b) Comparison of experimental and numerical temperature variation for down sine sweep test with acceleration amplitude of 1.0g

Fig. 29. Comparison of experimental and numerical transmissibility curve and temperature variation, for down sine sweep test with acceleration amplitude of 1.0g.

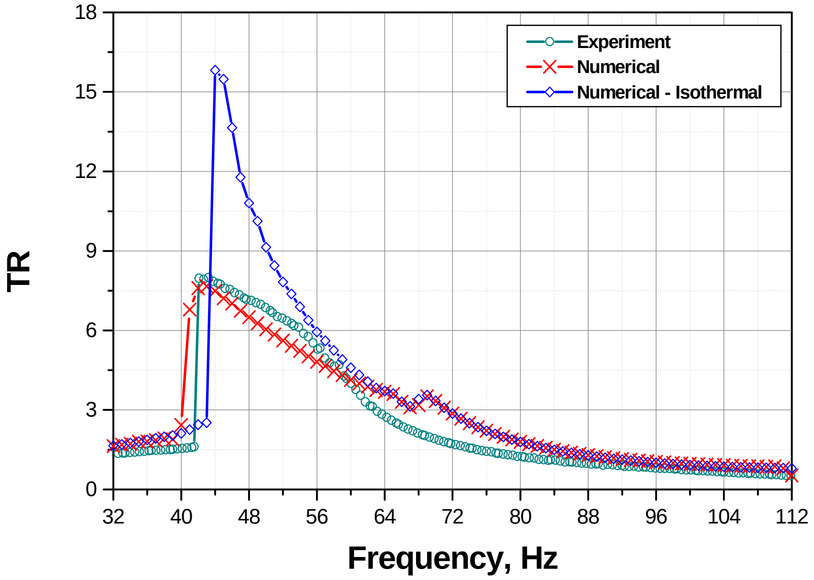

(a) Comparison of experimental and numerical transmissibility curve for down sine sweep test with acceleration amplitude of 2.0g

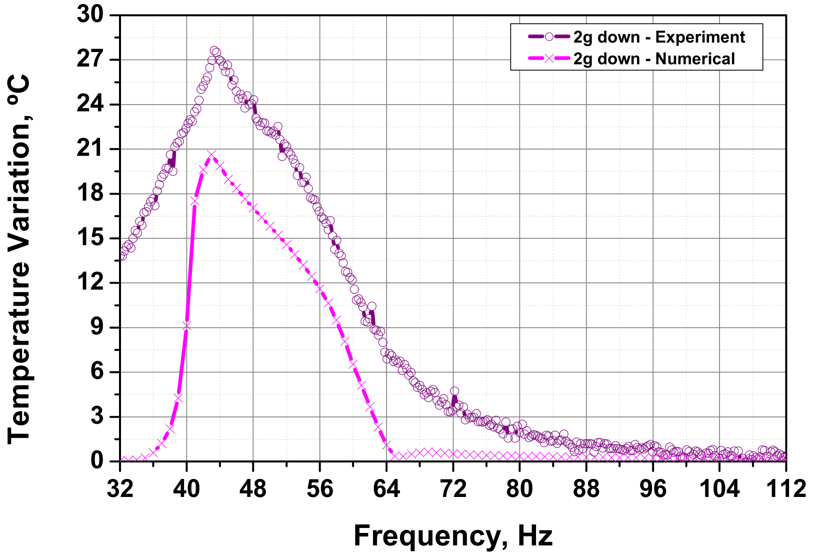

(b) Comparison of experimental and numerical temperature variation for down sine sweep test with acceleration amplitude of 1.0g

Fig. 30. Comparison of experimental and numerical transmissibility curve and temperature variation for down sine sweep test with acceleration amplitude of 2.0g.

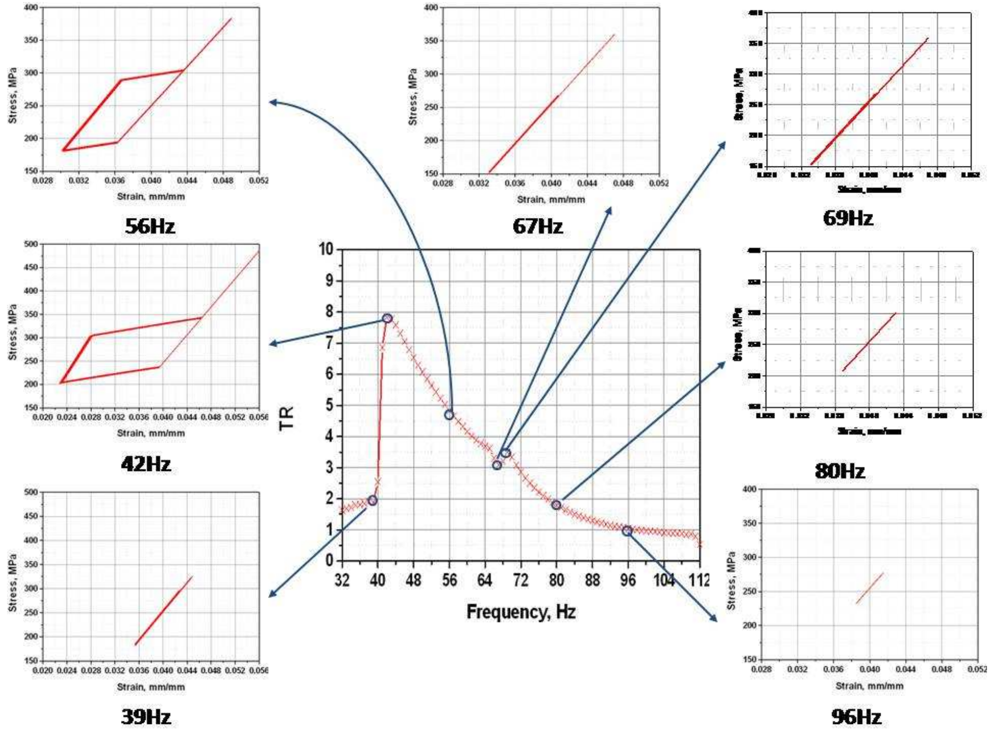

Fig. 31. Analysis of the numerical transmissibility curve for down sine sweep test with acceleration amplitude of 2.0g.

CHAPTER VII

CONSTITUTIVE MODEL FOR POLYCRYSTALLINE SHAPE MEMORY ALLOYS WITH SMOOTH TRANSFORMATION HARDENING

One of the characteristics of the phenomenological models is that a great number of them predict nonsmooth transitions between the martensitic and the austenitic phases. These discontinuous transitions can be experimentally verified in *singlecrystalline* SMAs (Patoor *et al.* [3]), and also in the loading-unloading cycles of untrained *polycrystalline* SMAs. However, experimental observations of trained polycrystalline SMAs have shown that the martensitic transformations start and finish in a smooth and gradual manner (Lagoudas *et al.* [33]). This gradual phase transformation is due to different crystallographic orientations of microstructural grains combined with transformation induced plasticity, and appears in the stress *vs.* strain curves as a smooth transition, without the presence of kinks.

Boyd and Lagoudas [24] developed a constitutive model based on a free energy function and dissipation potentials as in rate-independent plasticity, where for a given strain and temperature loading/unloading path input, stress output is provided. Later, Lagoudas and coworkers ([25, 27]) proposed a unified model, which unifies the models of Boyd and Lagoudas, Tanaka and coworkers ([18, 19]), and Liang and Rogers [20] under the same thermodynamical framework. Even though the unified model combines different constitutive models, it still considers hardening functions which result in continuous stress-strain curves but with discontinuous derivatives between phase transitions.

The current chapter discusses a new development of a phenomenological constitutive model for shape memory alloys. The model is developed under the same thermomechanical framework proposed by Boyd and Lagoudas [24]. The main difference between the model by Boyd and Lagoudas and the model presented here is the hardening function utilized to describe the transformation hardening behavior of SMAs. This new hardening function allows continuous and smooth transitions between the martensitic and austenitic phases. The model exhibits smooth material response in both thermomechanical tests and calorimetric measurements.

A. Thermomechanical Constitutive Model for SMA

This section revisits the thermodynamical framework of the model proposed by Boyd and Lagoudas [24], which is also the framework under which the present, smooth, constitutive model is developed.

1. Basic Equations

The current model considers the Gibbs free energy of a SMA polycrystalline material as a function of the independent state variables stress $\boldsymbol{\sigma}$, and temperature T, and also as a function of internal state variables, such as martensitic volume fraction ξ, and transformation strain $\boldsymbol{\varepsilon}^t$. The form of the total Gibbs free energy is given by (Lagoudas and coworkers[24, 25, 27]):

$$\begin{aligned} G\left(\boldsymbol{\sigma}, T, \xi, \boldsymbol{\varepsilon}^t\right) = & -\frac{1}{2\rho}\boldsymbol{\sigma} : \mathcal{S} : \boldsymbol{\sigma} - \frac{1}{\rho}\boldsymbol{\sigma} : \left[\boldsymbol{\alpha}\left(T - T_0\right) + \boldsymbol{\varepsilon}^t\right] + \\ & c\left[\left(T - T_0\right) - T\ln\left(\frac{T}{T_0}\right)\right] - s_0 T + u_0 + \frac{1}{\rho}f(\xi) \end{aligned} \tag{7.1}$$

where T and T_0 are the temperature and the reference temperature, respectively, and ρ is the mass density. The effective material parameters S, $\boldsymbol{\alpha}$, c, s_0 , and u_0 are the 4^{th} order effective compliance tensor, 2^{nd} order effective thermal expansion tensor, effective specific heat coefficient, effective specific entropy at the reference state, and the effective specific internal energy at the reference state, respectively. They are defined, based on micromechanics considerations (Lagoudas *et al.* [25]), in terms of the martensitic volume fraction, ξ, by the rule of mixtures, as follows:

$$\boldsymbol{\mathcal{S}}(\xi) = \boldsymbol{\mathcal{S}}^A + \xi\left(\boldsymbol{\mathcal{S}}^M - \boldsymbol{\mathcal{S}}^A\right) = \boldsymbol{\mathcal{S}}^A + \xi\Delta\boldsymbol{\mathcal{S}} \tag{7.2}$$

$$\boldsymbol{\alpha}(\xi) = \boldsymbol{\alpha}^A + \xi\left(\boldsymbol{\alpha}^M - \boldsymbol{\alpha}^A\right) = \boldsymbol{\alpha}^A + \xi\Delta\boldsymbol{\alpha} \tag{7.3}$$

$$c(\xi) = c^A + \xi\left(c^M - c^A\right) = c^A + \xi\Delta c \tag{7.4}$$

$$s_0(\xi) = s_0^A + \xi\left(s_0^M - s_0^A\right) = s_0^A + \xi\Delta s_0 \tag{7.5}$$

$$u_0(\xi) = u_0^A + \xi\left(u_0^M - u_0^A\right) = u_0^A + \xi\Delta u_0 \tag{7.6}$$

where S^i, $\boldsymbol{\alpha}^i$, C^i, s_0^i, and u_0^i, for $i = A, M$, are the corresponding material constants for the pure austenitic and martensitic phase, respectively. The function, $f(\xi)$, is the transformation hardening function, and it will be presented later.

The constitutive relations for the strain tensor and entropy are obtained through the thermodynamical procedure of combining the first and second laws of thermodynamics, as expressed in the Clausius-Duhem inequality, with a thermomechanical potential (in our case the Gibbs free energy) and the Legendre transformation (Coleman and Gurtin [78]). Restrictions on the Clausius-Duhem inequality can be applied in such way that the second law is not violated at any time. These restrictions lead to the determination of the constitutive relations for strain and entropy as

$$\boldsymbol{\varepsilon} = -\rho\frac{\partial G}{\partial\boldsymbol{\sigma}} = \boldsymbol{\mathcal{S}} : \boldsymbol{\sigma} + \boldsymbol{\alpha}(T - T_0) + \boldsymbol{\varepsilon}^t, \tag{7.7}$$

$$s = -\frac{\partial G}{\partial T} = \frac{1}{\rho}\boldsymbol{\alpha} : \boldsymbol{\sigma} + c\ln\left(\frac{T}{T_0}\right) + s_0. \tag{7.8}$$

As a result of the two constitutive relations above, the Clausius-Duhem (dissipation) inequality reduces to the following form (Lagoudas and coworkers [25, 27]:

$$\left(-\rho\frac{\partial G}{\partial \boldsymbol{\varepsilon}^t}\right) : \dot{\boldsymbol{\varepsilon}}^t + \left(-\rho\frac{\partial G}{\partial \xi}\right)\dot{\xi} \geq 0. \tag{7.9}$$

The next step on the model's development is the determination of evolution equations for the internal variables $\boldsymbol{\varepsilon}^t$ and ξ. One assumption that can be made for the case of martensitic phase transformation without reorientation is that any change in the current state of the system is only possible due to a change in the martensitic volume fraction, and that any other internal state variable evolves with it (Qidwai and Lagoudas [79]). Consequently, a relationship between the evolution of the transformation strain and the evolution of the martensitic volume fraction during forward and reverse transformation can be defined as:

$$\dot{\boldsymbol{\varepsilon}}^t = \boldsymbol{\Lambda}\dot{\xi}, \tag{7.10}$$

$\boldsymbol{\Lambda}$ is the transformation tensor, which determines the transformation strain direction, and is assumed to have the following form:

$$\boldsymbol{\Lambda} = \begin{cases} \dfrac{3}{2}H\dfrac{\boldsymbol{\sigma}'}{\overline{\boldsymbol{\sigma}}} \quad ; \quad \dot{\xi} > 0 \\ H\dfrac{\varepsilon^{t-r}}{\overline{\varepsilon}^{t-r}} \quad ; \quad \dot{\xi} < 0 \end{cases} \tag{7.11}$$

The deviatoric stress tensor $\boldsymbol{\sigma}'$ and the transformation strain at the reversal of phase transformation $\boldsymbol{\varepsilon}^{t-r}$, are defined as in Qidwai and Lagoudas [27]:

$$\overline{\sigma} = \sqrt{\frac{3}{2}}||\boldsymbol{\sigma}'|| \quad ; \quad \boldsymbol{\sigma}' = \boldsymbol{\sigma} - \frac{1}{3}\left(tr\boldsymbol{\sigma}\right)\mathbf{1} \quad ; \quad \overline{\varepsilon}^{t-r} = \sqrt{\frac{2}{3}}||\varepsilon^{t-r}|| \tag{7.12}$$

where $||\cdot||^2 = (\cdot : \cdot)$ is the inner product of the enclosed quantity. The reader is referred to the work of Qidwai and Lagoudas [79] and Rajagopal and Srinivasa [31]) for additional insights into other possible choices of transformation flow rules and surfaces, as well as the implications of the principle of maximum transformation dissipation on the flow rule. The present choice is made for the sake of simplicity as the main focus of this paper is the choice for the hardening function (Section 2).

Substituting the flow rule, Eqn. 7.10, into the dissipation inequality, Eqn. 7.9, one can obtain:

$$\left(\boldsymbol{\sigma} : \boldsymbol{\Lambda} - \rho\frac{\partial G}{\partial \xi}\right)\dot{\xi} = \pi\dot{\xi} \geq 0, \tag{7.13}$$

where π is defined as a thermodynamic force conjugated to ξ and has the form:

$$\begin{aligned}\pi =& \boldsymbol{\sigma} : \boldsymbol{\Lambda} + \frac{1}{2}\boldsymbol{\sigma} : \Delta\mathcal{S} : \boldsymbol{\sigma} + \boldsymbol{\sigma} : \Delta\boldsymbol{\alpha}\,(T - T_0) + \\ & - \rho\Delta c\left[(T - T_0) - T\ln\left(\frac{T}{T_0}\right)\right] + \rho\Delta s_0 T - \rho\Delta u_0 - \frac{\partial f}{\partial \xi},\end{aligned} \tag{7.14}$$

where the terms defined with the prefix Δ in Eqn. 3.16 represents the difference between the martensitic and austenitic phases of the given quantity.

In this constitutive model, the martensitic volume fraction, ξ, is considered to be a scalar. It combines all the martensitic volume fractions of the different variants of martensite that can occur (Qidwai and Lagoudas [27]). Therefore, instead of prescribing an evolution equation for ξ one can use Eqn. 3.16 to directly obtain the value of ξ, for a given temperature and stress level.

The martensitic phase transformation will take place whenever the function π satisfies a certain criterion that does not violate the second law of thermodynamics. It is assumed that phase transformation starts whenever the thermodynamic force π reaches the critical value of $\pi = \pm Y^*$, where the positive value is related to the forward transformation, while the negative value is for reverse transformation. Another way of expressing this criterion is to define a transformation function, Φ, in terms of π, such that:

$$\Phi = \begin{cases} \pi - Y^* & ; \quad \dot{\xi} > 0 \\ -\pi - Y^* & ; \quad \dot{\xi} < 0 \end{cases} \tag{7.15}$$

Essentially, the transformation function, Φ, represents a transformation surface for a given set of internal state variables, where the two surfaces for $\xi = 0$ and $\xi = 1$ are the upper and lower boundaries of the transformation surfaces, respectively. Any stress state that is not on these surfaces is considered to be an elastic state.

The constraints on the evolution of the martensitic volume fraction can be expressed in terms of the Kuhn-Tucker conditions, given by:

$$\dot{\xi} \geq 0 \quad \text{or} \quad \dot{\xi} \leq 0; \qquad \Phi\left(\boldsymbol{\sigma}, T, \xi\right) \leq 0; \qquad \Phi\dot{\xi} = 0, \tag{7.16}$$

where all the relations should hold simultaneously along any loading path.

Following the Kuhn-Tucker conditions, and assuming that martensitic transformation is rate-independent, the consistency condition is defined by:

$$\dot{\Phi} = \partial_{\boldsymbol{\sigma}}\Phi : \dot{\boldsymbol{\sigma}} + \partial_T\Phi\dot{T} + \partial_\xi\Phi\dot{\xi} = 0. \tag{7.17}$$

2. Hardening Function

Next, we introduce the hardening function that is used to describe the interaction between the austenitic and martensitic phases. The new hardening function proposed in this work is a general power law function in terms of ξ with fractional exponents. It allows for (continuous and) smooth transitions between the elastic and transformation regimes. The proposed hardening function has the following form:

$$f\left(\xi\right) = \begin{cases} \frac{1}{2}a_1\left(\xi + \frac{\xi^{n_1+1}}{(n_1+1)} + \frac{(1-\xi)^{n_2+1}}{(n_2+1)}\right) & ; \qquad \dot{\xi} > 0 \\ \frac{1}{2}a_2\left(\xi + \frac{\xi^{n_3+1}}{(n_3+1)} + \frac{(1-\xi)^{n_4+1}}{(n_4+1)}\right) & ; \qquad \dot{\xi} < 0, \end{cases} \tag{7.18}$$

The exponents n_1, n_2, n_3 and n_4 can assume real number values in the interval $(0, 1]$. In general, these exponents should be considered material parameters, whose values are determined from experimental measurements. If n_1 and/or n_3 take values strictly less than 1, the forward and/or reverse phase transformations respectively, are initiated in a smooth fashion. Similarly, if n_2 and/or n_4 take values strictly less than 1, the forward and/or reverse phase transformations respectively, are completed in a smooth fashion. If all the exponents are equal to 1, the original model of ([24]) is recovered. Note also that f takes two different values depending on the type of transformation (forward or reverse). This in fact makes G an implicit function of $\dot{\xi}$ (Eqn. 3.3), however, it can be shown that this does not violate continuum thermodynamics (Popov and Lagoudas [26]).

Kiefer *et al.* [89] have also proposed a polynomial hardening function with rational exponents. The constitutive modeling presented in their work predicts the magnetic field-induced strain hysteresis curves observed in magnetic shape memory alloys. The hardening function, in that context, reflects the physical observation that the movement of twin boundaries becomes increasingly difficult with the progression of the reorientation process, while the hardening function of this work describes the interaction between the austenitic and martensitic phases, without considering reorientation processes.

Let us now demonstrate that this model exhibits smooth evolution of the stress $\boldsymbol{\sigma}$ during an arbitrary thermomechanical path which does not involve minor loops. Our goal is to obtain an expression for $\partial_{\boldsymbol{\varepsilon}}\boldsymbol{\sigma}$ and $\partial_T\boldsymbol{\sigma}$ and demonstrate that each of these partial derivatives is smooth.

To this end, let us first compute the derivative of f with respect to ξ, which enters the thermodynamic force (Eqn. 3.16) and, consequently, the transformation surface (Eqn. 3.17). It is obtained by straightforward differentiation of Eqn. 7.18:

$$\frac{\partial f(\xi)}{\partial \xi} = \begin{cases} \frac{1}{2}a_1\left(1+\xi^{n_1}-(1-\xi)^{n_2}\right) \quad ; \qquad \dot{\xi} > 0 \\ \\ \frac{1}{2}a_2\left(1+\xi^{n_3}-(1-\xi)^{n_4}\right) \quad ; \qquad \dot{\xi} < 0, \end{cases} \tag{7.19}$$

We also will need the second derivative, which is:

$$\frac{\partial^2 f(\xi)}{\partial \xi^2} = \begin{cases} \frac{1}{2} a_1 \left(n_1 \xi^{n_1 - 1} + n_2 (1-\xi)^{n_2 - 1} \right) \quad ; & \dot{\xi} > 0 \\ \\ \frac{1}{2} a_2 \left(n_3 \xi^{n_3 - 1} + n_4 (1-\xi)^{n_4 - 1} \right) \quad ; & \dot{\xi} < 0, \end{cases} \tag{7.20}$$

Observe, that for $n_1 < 1$ and $\dot{\xi} > 0$, or $n_3 < 1$ and $\dot{\xi} < 0$ one has

$$\lim_{\xi \to 0} \frac{\partial^2 f}{\partial \xi^2} = \infty, \tag{7.21}$$

and for $n_2 < 1$ and $\dot{\xi} > 0$, or $n_4 < 1$ and $\dot{\xi} < 0$ one has

$$\lim_{\xi \to 1} \frac{\partial^2 f}{\partial \xi^2} = \infty. \tag{7.22}$$

Now we are ready to demonstrate that partial derivative $\partial_{\boldsymbol{\varepsilon}} \boldsymbol{\sigma}$ is smooth. Indeed, consider a material point in an isothermal loading path. Further, assume that at a given instance of time, the material is undergoing, without loss of generality, forward phase transformation. By applying the chain rule to Eqn. 7.10 one obtains:

$$\frac{\partial \boldsymbol{\varepsilon}^t}{\partial \xi} = \boldsymbol{\Lambda}(\boldsymbol{\sigma}). \tag{7.23}$$

Next, we formally differentiate Eqn. 7.7 with respect to $\boldsymbol{\varepsilon}$, applying the chain rule and combining with Eqn. 7.2, Eqn. 7.3 and 7.23 to obtain:

$$\begin{aligned} \mathbf{1} &= \frac{\partial \mathcal{S}(\xi)}{\partial \boldsymbol{\varepsilon}} : \boldsymbol{\sigma} + \mathcal{S}(\xi) : \frac{\partial \boldsymbol{\sigma}}{\partial \boldsymbol{\varepsilon}} + (T - T_0) \frac{\partial \boldsymbol{\alpha}(\xi)}{\partial \boldsymbol{\varepsilon}} + \frac{\partial \boldsymbol{\varepsilon}^t}{\partial \boldsymbol{\varepsilon}} \\ &= \left(\frac{\partial \mathcal{S}(\xi)}{\partial \xi} : \boldsymbol{\sigma} \right) \frac{\partial \xi}{\partial \boldsymbol{\varepsilon}} + \mathcal{S}(\xi) : \frac{\partial \boldsymbol{\sigma}}{\partial \boldsymbol{\varepsilon}} + (T - T_0) \frac{\partial \boldsymbol{\alpha}(\xi)}{\partial \xi} \frac{\partial \xi}{\partial \boldsymbol{\varepsilon}} + \frac{\partial \boldsymbol{\varepsilon}^t}{\partial \xi} \frac{\partial \xi}{\partial \boldsymbol{\varepsilon}} \\ &= \mathcal{S}(\xi) : \frac{\partial \boldsymbol{\sigma}}{\partial \boldsymbol{\varepsilon}} + \left(\Delta \mathcal{S} : \boldsymbol{\sigma} + \Delta \boldsymbol{\alpha} \, (T - T_0) + \boldsymbol{\Lambda}(\boldsymbol{\sigma}) \right) \frac{\partial \xi}{\partial \boldsymbol{\varepsilon}}. \end{aligned} \tag{7.24}$$

Since phase transformation is taking place ($\dot{\xi} \neq 0$), the constraints in Eqn. 7.16 imply:

$$\Phi(\boldsymbol{\sigma}, T, \xi) = 0.$$

During isothermal phase transformation, the temperature is constant, hence differentiating this last equation with respect to $\boldsymbol{\varepsilon}$ yields:

$$\frac{\partial \Phi}{\partial \boldsymbol{\sigma}} : \frac{\partial \boldsymbol{\sigma}}{\partial \boldsymbol{\varepsilon}} + \frac{\partial \Phi}{\partial \xi} \frac{\partial \xi}{\partial \boldsymbol{\varepsilon}} = 0, \tag{7.25}$$

and therefore:

$$\frac{\partial \xi}{\partial \boldsymbol{\varepsilon}} = -\frac{\dfrac{\partial \Phi}{\partial \boldsymbol{\sigma}} : \dfrac{\partial \boldsymbol{\sigma}}{\partial \boldsymbol{\varepsilon}}}{\dfrac{\partial \Phi}{\partial \xi}} \tag{7.26}$$

Substituting the equation above into Eqn. 7.24 and rearranging terms, one obtains:

$$\frac{\partial \boldsymbol{\sigma}}{\partial \boldsymbol{\varepsilon}} = \left(\mathcal{S}(\xi) - \left(\Delta \mathcal{S} : \boldsymbol{\sigma} + \Delta \boldsymbol{\alpha} \, (T - T_0) + \boldsymbol{\Lambda}(\boldsymbol{\sigma}) \right) \frac{\partial \Phi}{\partial \boldsymbol{\sigma}} / \frac{\partial \Phi}{\partial \xi} \right)^{-1} \tag{7.27}$$

Finally, the partial derivatives $\partial_{\boldsymbol{\sigma}} \Phi$ and $\partial_\xi \Phi$ are obtained by direct differentiation of Eqn. 7.14, which together with equation Eqn. 7.15 gives:

$$\frac{\partial \Phi}{\partial \boldsymbol{\sigma}} = \boldsymbol{\Lambda}(\boldsymbol{\sigma}) + \Delta \mathcal{S} : \boldsymbol{\sigma} + \Delta \boldsymbol{\alpha} \, (T - T_0) \qquad \text{and} \qquad \frac{\partial \Phi}{\partial \xi} = -\frac{\partial^2 f}{\partial \xi^2}. \tag{7.28}$$

Therefore, Eqn. 7.27 can be written in its final form:

$$\frac{\partial \boldsymbol{\sigma}}{\partial \boldsymbol{\varepsilon}} = \left(\mathcal{S}(\xi) + \frac{\left(\boldsymbol{\Lambda}(\boldsymbol{\sigma}) + \Delta \mathcal{S} : \boldsymbol{\sigma} + \Delta \boldsymbol{\alpha} \, (T - T_0) \right) \left(\boldsymbol{\Lambda}(\boldsymbol{\sigma}) + \Delta \mathcal{S} : \boldsymbol{\sigma} + \Delta \boldsymbol{\alpha} \, (T - T_0) \right)}{\dfrac{\partial^2 f}{\partial \xi^2}} \right)^{-1} \tag{7.29}$$

Now, since $\dot{\xi} > 0$ and by using Eqn 7.21 and Eqn. 7.22 for $0 < n_1, n_2 < 1$ we obtain:

$$\lim_{\xi \to 0} \frac{\partial \boldsymbol{\sigma}}{\partial \boldsymbol{\varepsilon}} = \left[\mathcal{S}(0) \right]^{-1}, \tag{7.30}$$

$$\lim_{\xi \to 1} \frac{\partial \boldsymbol{\sigma}}{\partial \boldsymbol{\varepsilon}} = \left[\mathcal{S}(1) \right]^{-1}. \tag{7.31}$$

On the other hand, in the thermoelastic region ($\dot{\xi} = 0$), one simply has:

$$\frac{\partial \boldsymbol{\sigma}}{\partial \boldsymbol{\varepsilon}} = \mathcal{S}(\xi)^{-1}, \tag{7.32}$$

hence, at the start ($\xi = 0$) and finish ($\xi = 1$) of a major loop isothermal path, the derivative $\partial_{\boldsymbol{\varepsilon}} \boldsymbol{\sigma}$ is continuous, since S is continuous. The derivation for reverse transformation is equivalent and will not be repeated. Note that if $n_1 \geq 1$ then $\partial^2_\xi f < \infty$ and the limit in Eqn. 7.30 no longer holds. Similarly, if $n_2 \geq 1$ the limit in Eqn. 7.31 no longer holds.

Figure 32 presents an enlargement of the regions at the beginning and end of the forward and reverse martensitic transformations predicted by the current model. It can be observed that the model predicts smooth transitions between the elastic and transformation regimes.

Using similar techniques as shown above one can also show that $\partial_T \boldsymbol{\sigma}$ is continuous at the start and finish of a major loop isobaric transformation. Thus, by considering the internal variables $\boldsymbol{\varepsilon}^t$ and ξ to be implicit functions of the $\boldsymbol{\varepsilon}$ and T (as is physically reasonable for strain/temperature driven problems) and by observing that:

$$\dot{\boldsymbol{\sigma}} = \frac{\partial \boldsymbol{\sigma}}{\partial \boldsymbol{\varepsilon}} \dot{\boldsymbol{\varepsilon}} + \frac{\partial \boldsymbol{\sigma}}{\partial T} \dot{T}$$

it is now clear that the stress (as a function of time) is a smooth function at the start and finish of an arbitrary major loop thermomechanical loading path.

B. One-dimensional Reduction and Identification of the Material Parameters

Since a great number of SMA applications can be reduced to a one-dimensional representation, it is convenient to reduce the model from its three dimensional form to a one-dimensional one. Moreover, the reduction of the model to a one-dimensional form

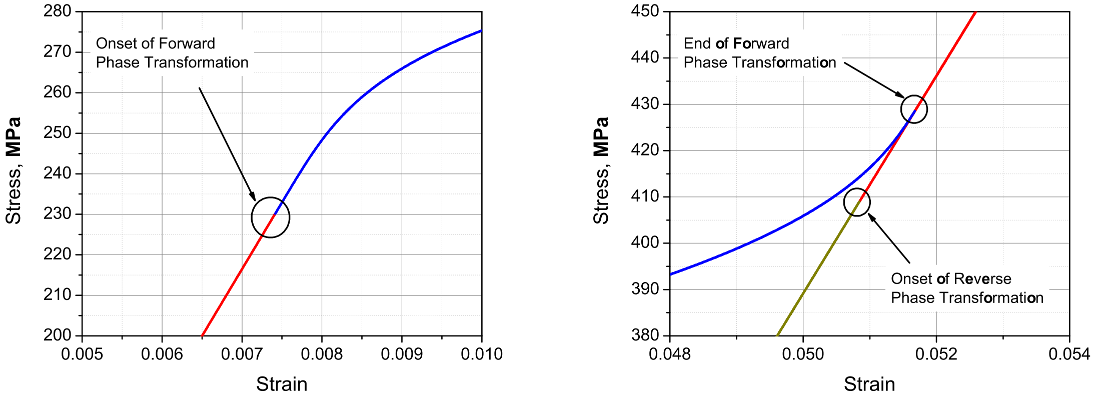

(a) Begin of forward phase transformation (b) End of forward and begin of reverse phase transformation

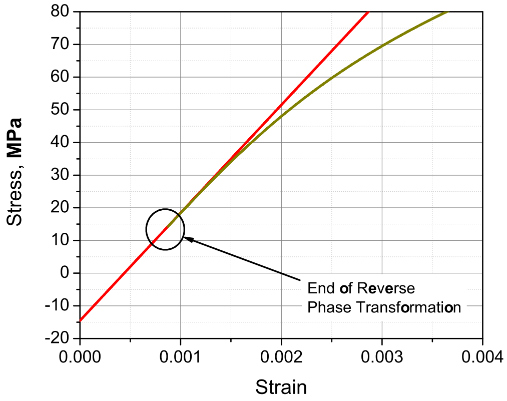

(c) End of reverse phase transformation

Fig. 32. Stress-strain curves of the current model: smooth transitions between the phases.

helps the identification of the material parameters through experimental results. The reduction can be accomplished by assuming uniaxial loading of an SMA specimen, *e.g.* a wire, in the x_1-direction. This loading state leads to the condition at which the stress tensor has only one non-zero component

$$\sigma_{11} = \sigma \neq 0 \tag{7.33}$$

where σ is the applied uniaxial stress.

The transformation strain tensor components are given by

$$\varepsilon^t_{11} = \varepsilon^t; \quad \varepsilon^t_{22} = \varepsilon^t_{33} = -\frac{1}{2}\varepsilon^t; \quad \varepsilon_{ij} = 0; \qquad \mathrm{i, j} = 1, ..., 3 \tag{7.34}$$

where ε^t is the uniaxial transformation strain assuming that it results in isochoric deformations.

Due to the fact that the stress tensor has one non-zero component and the transformation strain tensor is of the form presented above, the double dot product between tensor quantities of the equations presented in Section 1 will be reduced to a simple scalar multiplication. As a result, the fourth order compliance tensors $\boldsymbol{\mathcal{S}}^A$ and $\boldsymbol{\mathcal{S}}^M$ reduce to the scalar components $S^A_{1111} = S^A$ and $S^M_{1111} = S^M$, respectively. Note that the compliance coefficients S^A and S^M are given by $S^A = \frac{1}{E^A}$ and $S^M = \frac{1}{E^M}$, in terms of the elastic stiffness coefficients. The second order thermal expansion tensors $\boldsymbol{\alpha}^A$ and $\boldsymbol{\alpha}^M$ reduce to the scalar components $\alpha^A_{11} = \alpha^A$ and $\alpha^M_{11} = \alpha^M$, whereas the transformation tensor $\boldsymbol{\Lambda}$ reduces to $H(\sigma)$ in the one-dimensional case. The effective compliance and thermal expansion coefficients, S, and α, are defined by the reduced form of Eqns. 3.4 and 3.5 , respectively:

$$S(\xi) = S^A + \xi\left(S^M - S^A\right) = S^A + \xi\Delta S \tag{7.35}$$

$$\alpha(\xi) = \alpha^A + \xi\left(\alpha^M - \alpha^A\right) = \alpha^A + \xi\Delta\alpha \tag{7.36}$$

$$\tag{7.37}$$

The evolution equation of the transformation strain given by Eq. 7.10 becomes

$$\dot{\varepsilon^t} = H\mathrm{sgn}(\sigma)\dot{\xi}, \tag{7.38}$$

while the one-dimensional form of the total strain is given by

$$\varepsilon = S\sigma + \alpha(T - T_0) + \varepsilon^t. \tag{7.39}$$

The one-dimensional form of the transformation function is given by

$$\begin{aligned}\Phi = |\sigma| H + \frac{1}{2}\sigma^2\Delta S + \sigma\Delta\alpha(T - T_0) - \rho\Delta c\left[(T - T_0) - T\ln\left(\frac{T}{T_0}\right)\right]\\ + \rho\Delta s_0 T - \rho\Delta u_0 - \frac{\partial f}{\partial \xi} \mp Y^* = 0.\end{aligned} \tag{7.40}$$

The calibration of the constitutive model with experimentally obtained material parameters is presented next. The material parameters that need to be determined are the elastic stiffness coefficients of austenitic and martensitic phases, E^A, and E^M, respectively; the thermal expansion coefficients of both phases, α_A, α_M; the heat capacity coefficient per unit volume, $\rho\Delta c$, which expresses the difference between the heat capacity coefficients of martensite and austenite; the maximum uniaxial transformation strain, H; the difference in internal energy per unit of volume between martensite and austenite at reference state, $\rho\Delta u_0$; the difference in the entropy per unit volume between martensite and austenite at the reference state, Δs_0; and finally the transformation temperatures at zero stress that define the start and finish of the forward and reverse martensitic phase transformation, *i.e.*, M_s, M_f, A_s, and A_f.

From a uniaxial pseudoelastic test at isothermal conditions one can determine the material parameters E^A, E^M, and H. For this purpose, two tensile loading - unloading tests were performed at the temperatures of 303K, and 313K(Fig. 33). The elastic stiffness of austenite is determined by computing the initial slope of the stress-strain curve, while the elastic stiffness of martensite is determined as the slope at the end of the phase transformation. The maximum uniaxial transformation strain H is estimated by extending the unloading part of the stress-strain curve using the elastic stiffness of the martensitic phase E^M, until it reaches the x-axis, as shown in Fig. 33.

The thermal expansion coefficient α^A, and α^M can be obtained by measuring the slopes of the strain-temperature curve under constant stress, at high temperature for austenite and low temperature for martensite, while the the heat capacity coefficient per unit volume, $\rho\Delta c$ is obtained from calorimetric tests. The slope of the stress-temperature curves can be computed by defining the stress values for which the martensitic phase transformations (forward and reverse) start and end, *i.e.*, σ^{Ms}, σ^{Mf}, σ^{As}, and σ^{Af}, from the temperature tests of 303K, and 313K (Fig. 33). Then, with these two sets of stress values, four different straight lines can be extrapolated in the stress-temperature space, leading to the determination of transformation temperature curves and their slopes. The transformation temperatures at zero-stress, *i.e.*, M_f, M_s, A_s, and A_f, can be approximately obtained by computing the intersection points of the stress-temperature curves with the temperature axis, or can be obtained from a calorimetric test. In fact, the transformation temperatures calculated are not the same as those obtained by a differential calorimetry test, as will be shown later. However, since the temperature range of this paper for pseudoelastic loading paths is for temperatures higher than austenitic finish temperature, this is a valid assumption.

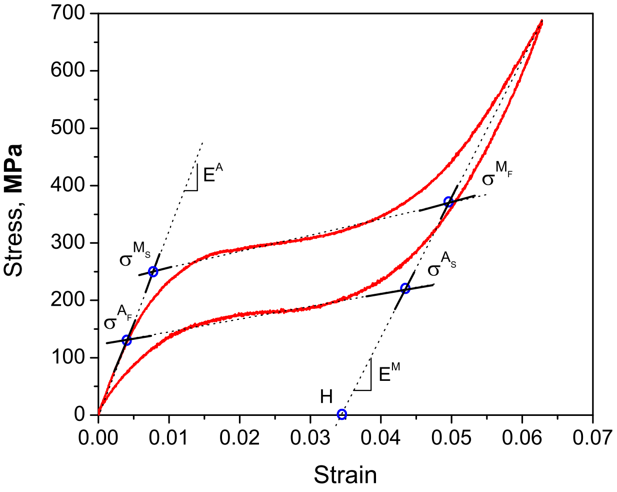

(a) $T = 303\text{K}$

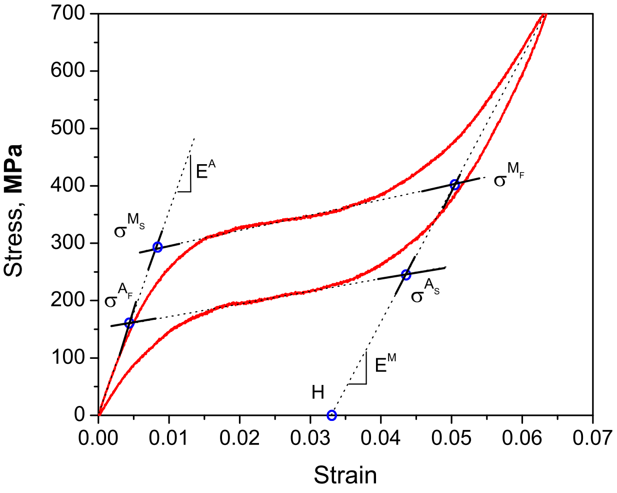

(b) $T = 313\text{K}$

Fig. 33. Stress-strain curves of current model, at different temperatures.

The entropy difference $\rho\Delta s_0$ per unit of volume between the phases can be determined by the slopes of the stress-temperature transformation curves. With the aid of the one-dimensional forms of the the transformation function,Eqn. 7.40, and consistency condition, Eqn. 7.17, the slopes of the transformation curves can be analytically determined as follows:

$$\begin{aligned}&\left(\Delta S\sigma + \Delta\alpha\left(T - T_0\right) + H\mathrm{sgn}(\sigma)\right)\dot{\sigma} + \left(\Delta\alpha\sigma - \rho\Delta c\ln\left(\frac{T}{T_0}\right) + \rho\Delta s_0\right)\dot{T} + \\ &\quad - \frac{\partial^2 f}{\partial\xi^2}\dot{\xi} = 0\end{aligned} \tag{7.41}$$

Now, by substituting zero stress, neglecting the Δc and$\Delta\alpha$ terms, and assuming $\dot{\xi} = 0$ in the above equation, the slope $\frac{d\sigma}{dT}$ of these curves at zero stress is [25] :

$$\frac{d\sigma}{dT} = -\frac{\rho\Delta s_0}{H} \tag{7.42}$$

Next, we need to calibrate the parameters of the model, a_1, a_2, c_1, c_2, n_1, n_2, n_3, and n_4, Y^*, and the last material parameter $\rho\Delta u_0$. The parameters a_1, a_2, Y^*, and $\rho\Delta u_0$ are defined as a function of the material parameters, such as, transformation temperatures and the entropy difference per unit volume between the phases. Note that the exponents n_1, n_2, n_3, and n_4 are not defined as functions of the material parameters, such as Y^*, a_1, and a_2. Recall that when the coefficients are defined in the interval $0 < n_1, n_2, n_3, n_4 < 1$ smooth responses are obtained. The material parameter $\rho\Delta u_0$ is defined to be:

$$\rho\Delta u_0 := \frac{1}{2}\rho\Delta s_0\left(A_f + M_s\right). \tag{7.43}$$

Table IX presents the material parameters correspondent to the experimental tests from Fig. 33, while Table X presents the expressions describing the model parameters.

Table IX. Values of material parameters typical of the SMA wire used to calibrate the constitutive model with smooth hardening transitions

$E^A = 32.5 \cdot 10^9 \text{Pa}$	$E^M = 23.0 \cdot 10^9 \text{Pa}$
$\Delta\alpha^A = 0.0\text{K}$	$\Delta c = 0.0 \text{J}/(\text{kgK})$
$H = 0.033$	$\rho = 6500 \frac{\text{kg}}{\text{m}^3}$
$T_0 = 303\text{K}$	$\rho\Delta s_0 = -115.5 \frac{\text{kJ}}{\text{m}^3\text{K}}$
$A_s = 217\text{K}$	$M_s = 264\text{K}$
$A_f = 290\text{K}$	$M_f = 160\text{K}$

Table X. Definition of the model parameters of the constitutive model with smooth hardening transitions

$Y^* = \frac{1}{2}\rho\Delta s_0 \left(M_s - A_f\right)$
$a_1 = \rho\Delta s_0 \left(M_f - M_s\right)$
$a_2 = \rho\Delta s_0 \left(A_s - A_f\right)$

C. Numerical Implementation and Numerical Evaluation of the Transformation Hardening Function

The implementation of the constitutive model follows the same procedure described in [27]. Given an increment of strain, ε, and temperature, T, the incremental form of the SMA constitutive model provides an increment of stress, σ as an outcome. The increment of stress is calculated by implementing a Return Mapping Algorithm.

A return mapping algorithm is used to solve the thermoelastic-transformation problem defined by the total strain relation (7.39), the flow rule (7.38), and the transformation function (7.40), by dividing it into two problems [27]. At first, a thermoelastic prediction problem assuming that the increment of the transformation strain vanishes is tried. If the predicted thermoelastic state violates the consistency condition, in other words, if it lies outside the transformation surface ($\Phi > 0$), a transformation correction problem takes place to restore the consistency condition. The present work uses the closest point projection algorithm as the corrector algorithm. The algorithm is based on the backward Euler integration rule of the transformation strain flow rule, which results in a set of non-linear algebraic equations solved using Newtons iteration method [27].

It has been previously shown that the condition at which the smooth hardening function goes to infinity as the martensitic volume fraction, ξ approaches to 0 or 1 is an essential condition ensuring the smoothness of the hardening function. While this condition works very well for the analytical solutions, it can bring some computational problems depending on the platform and its precision at which the model is implemented. The source of the problem is that in order to compute the value of the transformation surfaces, given by Eqn. 7.15, one needs to compute the value of the martensitic volume fraction, ξ, which is subjected to the power of rational exponents. This can be a very difficult operation computationally; where problems to loss of precision during arithmetic operations can occur

One solution to the precision problem is to use arbitrary precision arithmetics via some software library, *e.g.* gnu math precision, when computing the value of the transformation surfaces (Φ). While this approach can greatly improve the precision, and consequently solve the problem, it can be very computationally expensive.

Another approach would be to introduce a modification into the hardening function, just for the purpose of computational issues. Therefore, considering a constant

δ, such that $\delta \ll \xi$, one can use the following derivative of the hardening function to compute the transformation surfaces Φ.

$$\frac{\partial f}{\partial \xi} = \begin{cases} \frac{1}{2} a_1 \left(1 + \left(\frac{\xi^{\left(\frac{1}{n_1}\right)}}{(\xi+\delta)^{\left(\frac{1}{n_1}-1\right)}} \right)^{n_1} - \left(\frac{(1-\xi)^{\left(\frac{1}{n_2}\right)}}{(1-\xi+\delta)^{\left(\frac{1}{n_2}-1\right)}} \right)^{n_2} \right) & ; \qquad \dot{\xi} > 0 \\ \frac{1}{2} a_2 \left(1 + \left(\frac{\xi^{\left(\frac{1}{n_3}\right)}}{(\xi+\delta)^{\left(\frac{1}{n_3}-1\right)}} \right)^{n_3} - \left(\frac{(1-\xi)^{\left(\frac{1}{n_4}\right)}}{(1-\xi+\delta)^{\left(\frac{1}{n_4}-1\right)}} \right)^{n_4} \right) & ; \qquad \dot{\xi} < 0 \end{cases} \tag{7.44}$$

This "numerical" hardening function is not smooth anymore, since its limits do not go to infinity when ξ tends to zero and/or one. However, for values of δ very small, *e.g.*, $\delta = 1.0 \cdot 10^{-4}$, Eqn. 7.44 will produce very similar results as the first derivative of the hardening function from Eqn. 7.18. For the value of δ equal to 0, we recover Eqn. 7.19.

D. Comparison with Experimental Tests

This section compares numerical simulations of the current model with experimental results. The first simulation results of the current model is compared with the same set of experimental tensile tests at different temperatures used to calibrate the constitutive model. The material parameters used in the simulations are given by Table IX, and the current model exponents were selected to be: $n_1 = 0.17$, $n_2 = 0.27$, $n_3 = 0.25$, and $n_4 = 0.35$.

Figure 34 shows the comparison of the numerical with experimental results, for the temperatures of $T = 293$K, $T = 303$K, and $T = 313$K, respectively. Figures 34a and 34b compare the predictions of the current model with experimental results for the temperatures of $T = 313$K, and $T = 303$K, respectively. Recall that these temperature were used to calibrate the model, in Section B. Figure 34c compares the experimental results with numerical simulations for the temperature of $T = 298$K. Specifically, this stress *vs.* strain curve at this level of temperature was not used for the determination of the material properties, or to calibrate the model. The results show a good agreement between the model's prediction and the experimental curve.

Next, Fig. 35 shows the comparison of Boyd and Lagoudas model and experimental results, for the temperature of $T = 303$K. It can be observed that the current model predicts a stress *vs.* much closer to experimental results than the previous model by Boyd and Lagoudas. Also, it should be mentioned that the material parameters used in the simulations of both models were slightly different. Specifically, the transformation temperatures for the Boyd and Lagoudas model were selected to be $M_f = 194\text{K}; M_f = 226\text{K}; A_s = 241\text{K}; A_f = 290\text{K}$. All the other parameters are selected to be the same for both constitutive models, as presented in Table IX

E. Comparison of the Current Model's Predictions with Calorimetric Results

In this section we compare the results from the constitutive model with experimental DSC results. Differential Scanning Calorimetry, or DSC, is a technique that measures the amount of heat rate transfer, or thermal energy, of a material's sample at a stress free state, as it is subjected to a controlled change in temperature. The temperature and heat rate measured is related to a reference material of well defined thermal properties, that is subjected to the same change in temperature. DSC measurements are very useful to determine the temperatures at which phase transformations occur at a stress free SMA sample, as well as the latent heat of transformation.

The fully thermomechanical coupled heat equation for shape memory alloys can be obtained by substituting Eqn. 7.7, Eqn. 7.8, into the first law of thermodynamics

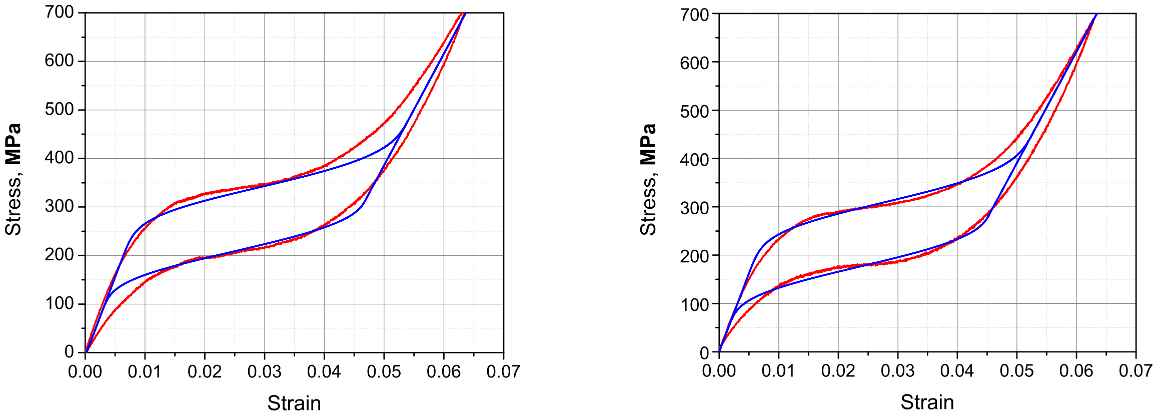

(a) T=313K (b) T=303K

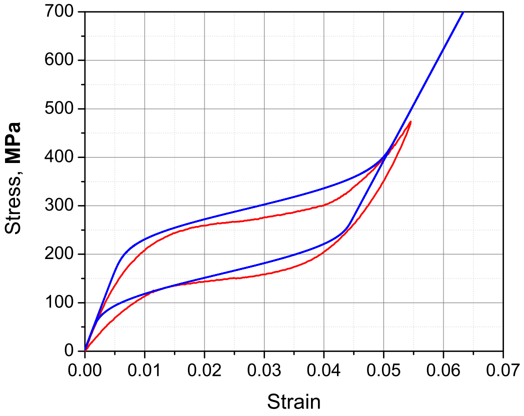

(c) T=298K

Fig. 34. Comparison of current model (dark lines) with experimental results (light lines). Stress *vs.* strain curves at temperatures of T=313K, T=303K, and T=298K.

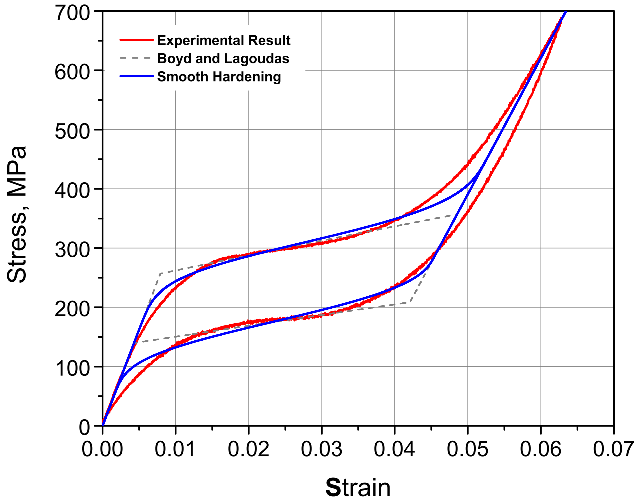

Fig. 35. Comparison of experimental results with Boyd and Lagoudas and current model.

(2.17). After some algebraic manipulations, the heat equation is given by:

$$\rho\dot{Q} = \left(-\pi + \Delta\boldsymbol{\alpha} : \boldsymbol{\sigma} T + \rho\Delta c T \ln\left(\frac{T}{T_0}\right) + \rho\Delta s_0 T\right)\dot{\xi} + T\boldsymbol{\alpha} : \dot{\boldsymbol{\sigma}} + \rho c\dot{T}. \qquad (7.45)$$

The collection of terms that multiplies $\dot{\xi}$ on the right-hand side of Eqn. 7.45 expresses how the temperature of a SMA changes due to a variation of the martensitic volume fraction. It is related to the latent heat of transformation. The second term of the right-hand side is related to the changes in the material's temperature due to a change in the stress state of the material, while the last term accounts for the amount of energy associated with the heat capacity of the material due to temperature variations. On the other hand, the term of the left-hand is related to the rate of heat transfer per unit volume.

Since the DSC test is performed upon a stress free sample of SMA, Eqn. 7.45

can be reduced to

$$\rho\dot{Q} = \left(-\pi + \rho\Delta cT\ln\left(\frac{T}{T_0}\right) + \rho\Delta s_0 T\right)\dot{\xi} + \rho c\dot{T}, \tag{7.46}$$

were $\dot{Q}$ is the heat flux per unit mass. Also, by using the consistency condition, one can compute the rate of martensitic volume fraction, $\dot{\xi}$ as

$$\dot{\xi} = -\left(\frac{\frac{\partial\Phi}{\partial T}}{\frac{\partial\Phi}{\partial\xi}}\right)\dot{T}. \tag{7.47}$$

Therefore, by substituting Eqn. 7.47 into Eqn. 7.46, one can arrive in the following expression for the heat equation:

$$\dot{Q} = \left(\rho c + \frac{g}{\rho}\right)\dot{T}. \tag{7.48}$$

where the function $g\left(\xi, T\right)$ is the excess of specific heat during phase transformation, given by:

$$g = \left(-\pi + \rho\Delta cT\ln\left(\frac{T}{T_0}\right) + \rho\Delta s_0 T\right)\left(-\frac{\frac{\partial\Phi}{\partial T}}{\frac{\partial\Phi}{\partial\xi}}\right) \tag{7.49}$$

For the forward phase transformation the function g is given by

$$g = \left(-Y^* + \rho\Delta cT\ln\left(\frac{T}{T_0}\right) + \rho\Delta s_0 T\right)\left(\frac{-\rho\Delta c\ln\left(\frac{T}{T_0}\right) + \rho\Delta s_0}{\frac{1}{2}a_1\left(n_1\xi^{n_1-1} + n_2\left(1-\xi\right)^{n_2-1}\right)}\right). \tag{7.50}$$

A similar expression for g can be found for the case of reverse phase transformation.

$$g = \left(Y^* + \rho\Delta cT\ln\left(\frac{T}{T_0}\right) + \rho\Delta s_0 T\right)\left(\frac{-\rho\Delta c\ln\left(\frac{T}{T_0}\right) + \rho\Delta s_0}{\frac{1}{2}a_2\left(n_3\xi^{n_3-1} + n_4\left(1-\xi\right)^{n_4-1}\right)}\right). \tag{7.51}$$

The heat equation as expressed in Eqn. 7.48 will be used to compare the theoretical results with experimental results given by DSC tests. An important observation to be made is that the rate of heat, $\dot{Q}$, expressed in Eqn. 7.48 is normalized by mass, that is, it has unit of W/kg. On the other hand, the heat rate measured by the DSC is not normalized, and it has unit of W. Therefore, we need to multiple the right-hand side of Eqn. 7.48 by the value of the mass of the specimen for which the DSC test was conducted, in order to be able to compare the experiment with theoretical results. Specifically, for the DSC results that will be presented below, the mass of the SMA specimen was measured to be 14g, and the temperature rate, $\dot{T}$, was selected to be 10K/min.

Figures 36 and 37 compare the heat rate of a SMA specimen during reverse phase transformation with the predictions of the Boyd and Lagoudas model and the current constitutive model. As it can be observed in the picture, the current model's predictions are closer to experimental results than the previous model by Boyd-Lagoudas. Another key point is that due to the shape of the calorimetric results the current model uses a different way of determining the transformation temperatures. In fact, the standard procedure of obtaining transformation temperatures from calorimetric tests, *i.e.*, from DSC, is to draw tangent lines from the start and finish regions of the transformation peak and baseline for the heating and cooling rate curves. However, since the current model predicts smooth transitions between the austenitic and martensitic phases, better results are obtained when the transformation temperatures are selected closer to the point where the heat rate curve begins to deviate from the baseline. The values of the material parameters used in the current model were taken from typical DSC data for NiTi and are given in Table XI. The values of the exponents in the current model were selected to match the experimental data and they have the following values: $n_1 = 0.2$, $n_2 = 0.25$, $n_3 = 0.2$, and $n_4 = 0.25$.

The values of the material parameters used in the Boyd and Lagoudas model are given in Table XII.

Note that the value of the material constants, *i.e.*, $\rho\Delta s_0$, the reference temperature T_0, and the transformation temperatures M_s, M_f, A_s, and A_f presented in

Table XI. Values of material parameters of the SMA specimen used to calibrate the constitutive model with hardening smooth transitions for calorimetric tests

$c^A = 377.0\frac{\mathrm{J}}{\mathrm{kgK}}$	$c^M = 400.0\frac{\mathrm{J}}{\mathrm{kgK}}$
$T_0 = 285\mathrm{K}$	$\rho\Delta s_0 = -44.0\frac{\mathrm{kJ}}{\mathrm{m^3K}}$
$A_s = 262\mathrm{K}$	$M_s = 302\mathrm{K}$
$A_f = 308\mathrm{K}$	$M_f = 259\mathrm{K}$

Table XII. Values of material parameters of the SMA specimen used to calibrate the Boyd and Lagoudas model for calorimetric tests

$c^A = 377.0\frac{\mathrm{J}}{\mathrm{kgK}}$	$c^M = 400.0\frac{\mathrm{J}}{\mathrm{kgK}}$
$T_0 = 285\mathrm{K}$	$\rho\Delta s_0 = -44.0\frac{\mathrm{kJ}}{\mathrm{m^3K}}$
$A_s = 270\mathrm{K}$	$M_s = 298\mathrm{K}$
$A_f = 300\mathrm{K}$	$M_f = 267\mathrm{K}$

Table IX are different from the values of material constants presented in Table XI and Table XII. The reason for this difference is that the SMA specimen used in Sec. C to calibrate the model for pseudoelastic loading paths is different from the SMA used in Sec. E to calibrate the model based on calorimetric results. In addition, the way that the transformation temperatures were determined for the pseudoelastic loading path and calorimetric results was different. Recall that, for the case of pseudoelastic paths, the transformation temperatures at zero stress were determined through an extrapolation of transformation surfaces in the stress-temperature space. The constant $\rho\Delta s_0$, in the context of pseudoelastic loading paths, is related to the slope of the transformation surfaces at zero stress level, as shown in Eq. 7.42. On the other hand, the transformation temperatures for the case of calorimetric results were directly obtained from the DSC measurements. The constant $\rho\Delta s_0$ is related to the area under the transformation peak of the heat rate curves, and consequently, related to the latent heat of transformation. We finally mention that the temperature T_0 was selected to be equal to $0.5\,(A_s + A_f)$, which generated better results than the value of T_0 selected by [25], which was equal to $0.5\,(M_s + A_f)$.

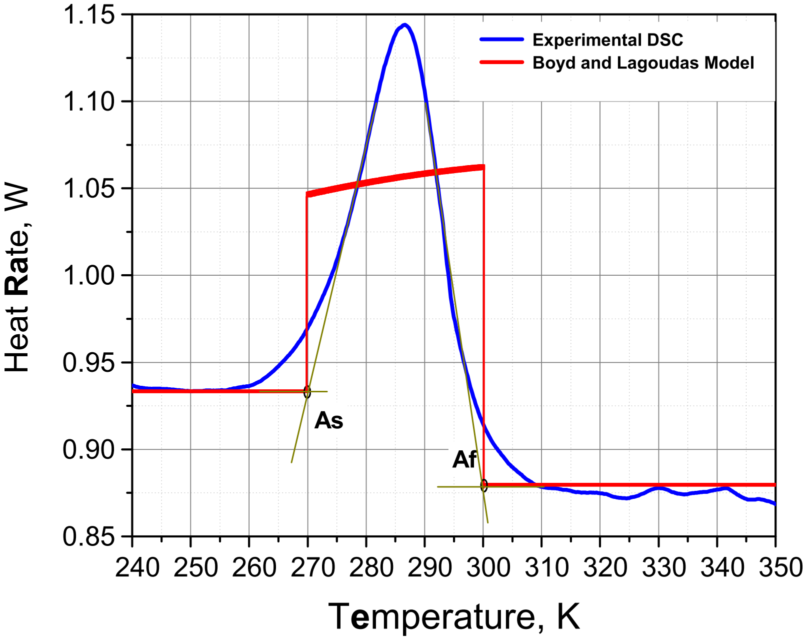

Fig. 36. Comparison of the quadratic polynomial model with experimental DSC results.

Similarly comparisons between experimental calorimetric results and model simulations that have been shown in Figs. 36 and 37, have also been obtained for the forward transformation from austenite to martensite.

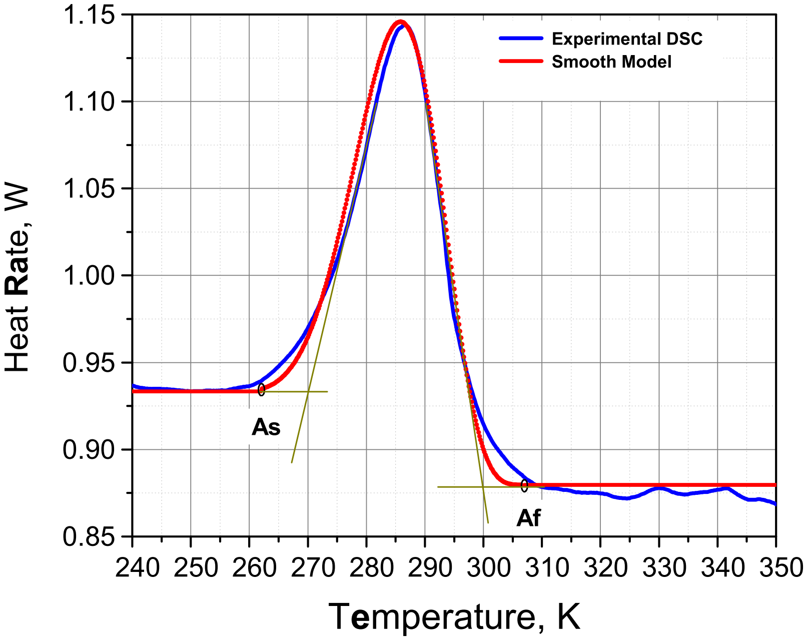

Fig. 37. Comparison of current model with experimental DSC results.

CHAPTER VIII

CHAOTIC VIBRATION OF A ONE-DEGREE OF FREEDOM SHAPE MEMORY OSCILLATOR

The current chapter discusses the Lyapunov exponents estimation by using an adapted version of the algorithm by [65] for hysteretic systems. Lyapunov exponents have proven to be the most useful dynamical diagnostic tool for chaotic behavior (Wolf *et al.* [65]). These exponents evaluate the sensitive dependence on initial conditions by estimating the exponential divergence of nearby orbits (Wolf *et al.* [65],Nayfeh and Balachandran [90]). The signs of the Lyapunov exponents provide a qualitative picture of the system's dynamics and any system containing at least one positive exponent presents chaotic behavior. The determination of Lyapunov exponents of dynamical system with an explicitly mathematical model that can be linearized is well-established. The algorithm proposed by Wolf *et al.* [65] is a well-known algorithm to compute the spectrum of Lyapunov exponents that evaluates the divergence of nearby orbits monitoring a reference trajectory, evaluated from the equations of motion, and a perturbed trajectory integrated by a linearized system. The main issue of implementing the original algorithm for hysteretic systems is related to the linearization process, where information about the rate-independent hysteretic damping may be lost during the linearization process. Therefore, a procedure to linearize the equations of motion is proposed by defining equivalent stiffness and also an equivalent viscous damping. As an application of the proposed procedure, the dynamical response of a single-degree of freedom pseudoelastic SMA oscillator is discussed. The oscillator's restitution force is provided by a pseudoelastic SMA element described by a rate-independent thermomechanical constitutive model (Machado *et al.* [91]). The model is developed under the same thermomechanical framework introduced by Boyd and Lagoudas [24] but with a new hardening function that guarantees continuous and smooth transitions between elastic and transformation regimes(Machado *et al.* [91]). Due to the continuity and smoothness of the phase transitions, the model is suitable to simulate the behavior of trained polycrystalline pseudoelastic SMAs (Machado *et al.* [91]). Numerical simulations of the SMA oscillator are carried out for free and forced vibrations, where two different analyzes are of concern: isothermal and non-isothermal conditions. Non-isothermal conditions are performed by considering the thermomechanical coupling in the constitutive model. Special attention is given to chaotic responses of the oscillator, where the proposed procedure of Lyapunov exponent estimation is employed to quantify chaos.

A. Single-Degree of Freedom Hysteretic Oscillator

The hysteretic system analyzed in this article is a single-degree of freedom oscillator (Fig. 38), which consists of a mass m attached to a hysteretic element, assumed to be a prismatic bar of length L and cross-section area A. The system is harmonically excited by a force $F \sin(\omega t)$.

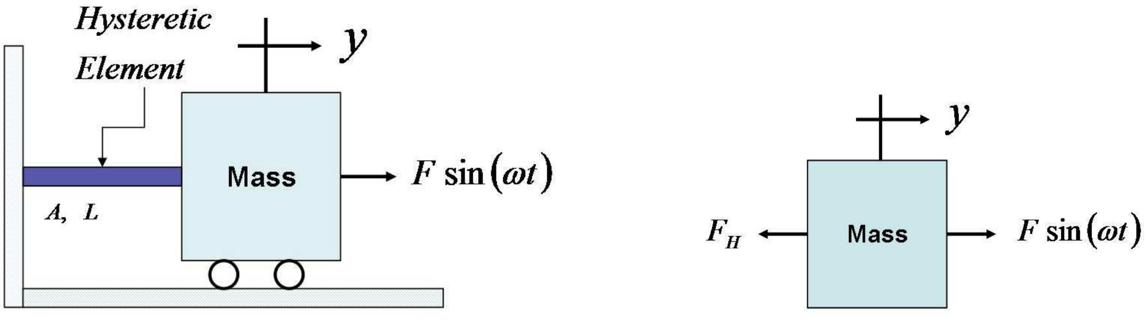

(a) Hysteretic oscillator

(b) Free body diagram

Fig. 38. Single-degree of freedom hysteretic oscillator.

The equation of motion of the oscillator is given by

$$m\ddot{y} + F_H = F \sin(\omega t) \tag{8.1}$$

where y is the mass displacement from its reference position, relative to an inertial frame, ω is the forcing frequency, F is the amplitude of the excitation force and F_H is the force exerted by the hysteretic element on the mass.

A non-dimensional version of Eqn. 8.1, can be obtained by assuming that the hysteretic element restitution force is equally distributed at all points of the SMA element. We can then define $\sigma := F_H/A$, where σ represents the nominal uniaxial stress in the hysteretic element, and $\varepsilon := y/L$, where ε is a non-dimensional displacement of the mass, also corresponding to the axial strain of the hysteretic element. The equation of motion of the oscillator, Eqn. 8.1 then results in the following form:

$$\ddot{\varepsilon} + \frac{\sigma A}{mL} = \frac{F}{mL} \sin(\omega t) . \tag{8.2}$$

In addition to the normalized displacement, the following non-dimensional variables are introduced:

$$\begin{gathered} \omega_0 := \sqrt{\frac{E^A A}{mL}}; \qquad \hat{F} := \frac{F}{mL\omega_0^2}; \\ \hat{t} := \omega_0 t; \qquad \hat{\omega} := \frac{\omega}{\omega_0}; \qquad \hat{\sigma} := \frac{\sigma}{E^A} \end{gathered} \tag{8.3}$$

where E^A represents a general modulus with units of stress (it could be identified with the elastic Young's modulus of the hysteretic element, *e.g.*, in the case of an SMA , the elastic modulus of austenite) and ω_0 is related to the natural frequency of the system (it could be identified as the natural frequency of the system, when the SMA element is in fully austenitic phase). With the above definitions, and after introducing the derivative with respect to non-dimensional time, $\varepsilon' := \partial\varepsilon/\partial\hat{t}$, the equation of motion, Eqn. 8.2, can be re-written in a non-dimensional form as:

$$\varepsilon'' + \hat{\sigma} = \hat{F} \sin\left(\hat{\omega}\hat{t}\right) \tag{8.4}$$

A state vector can now be introduced as:

$$\mathbf{x} := \left(x_1, x_2\right)^T := \left(\varepsilon, \varepsilon'\right)^T, \tag{8.5}$$

which will reduce Eqn. 8.4 from a second-order ordinary differential equation form to a first order system as follows:

$$\begin{aligned} x_1' &= x_2 \\ x_2' &= \hat{F} \sin\left(\hat{\omega}\hat{t}\right) - \hat{\sigma} \end{aligned} \tag{8.6}$$

The specific expression for $\hat{\sigma}$ depends on the constitutive modeling of the hysteretic material. As a specific application of hysteretic behavior, an SMA material system is considered, described by a rate-independent thermomechanical constitutive model presented in the next section.

1. Constitutive Model for Polycrystalline SMAs with Smooth Transformation Hardening

This section presents the constitutive model used in this work to simulate the SMA hysteretic behavior. The model is developed under the same thermomechanical framework proposed by Boyd and Lagoudas [24]. The main difference between the model by Boyd and Lagoudas [24] and the model presented here is the hardening function employed to describe the transformation hardening behavior of SMAs. This new hardening function allows smooth transitions between the martensitic and austenitic phases.

Since the SMA element is a one-dimensional element, we present here only the one-dimensional one form of the constitutive model. Moreover, we present the Gibbs free energy in a non-dimensional form. The constitutive model introduces a non-dimensional Gibbs free energy, $\hat{G}$, of a polycrystalline SMA, as a function of the independent state variables: stress $\hat{\sigma}$, and temperature $\hat{T}$, and also of the internal state variables: martensitic volume fraction ξ, and transformation strain ε^t. Note that in this constitutive model the martensitic volume fraction is assumed to be a scalar quantity, and it includes the volume fractions of all martensitic variants. The non-dimensional quantities are defined as follows:

$$\begin{aligned}
&\hat{G} := \frac{\rho G}{E^A}; \qquad && \hat{S}^A := S^A E^A; \qquad && \hat{S}^M := S^M E^A; \qquad && \hat{\alpha}^A := \alpha^A A_s;\\
&\hat{\alpha}^M := \alpha^M A_s; && \hat{T} := \frac{T}{A_s}; && \hat{T}_0 := \frac{T_0}{A_s}; && \hat{c}^A := \frac{\rho}{E^A} A_s c^A;\\
&\hat{c}^M := \frac{\rho}{E^A} A_s c^M; && \hat{s}_0^A := \frac{\rho}{E^A} A_s s_0^A; && \hat{s}_0^M := \frac{\rho}{E^A} A_s s_0^M; && \hat{u}_0^A := \frac{\rho}{E^A} u_0^A;\\
&\hat{u}_0^M := \frac{\rho}{E^A} u_0^M; && \hat{f} := \frac{f}{E^A}.
\end{aligned} \tag{8.7}$$

The one-dimensional form of the normalized Gibbs free energy ([27]) has following form:

$$\begin{aligned}
\hat{G}\left(\hat{\sigma}, \hat{T}, \xi, \varepsilon^t\right) = & -\frac{1}{2}\hat{\mathcal{S}}\hat{\sigma}^2 - \hat{\sigma}\left[\hat{\alpha}\left(\hat{T} - \hat{T}_0\right) + \varepsilon^t\right] + \\
& \hat{c}\left[\left(\hat{T} - \hat{T}_0\right) - \hat{T}\ln\left(\frac{\hat{T}}{\hat{T}_0}\right)\right] - \hat{s}_0\hat{T} + \hat{u}_0 + \hat{f}(\xi)
\end{aligned} \tag{8.8}$$

In the above equation $\hat{T}_0$ is the non-dimensional reference state temperature. The function $\hat{f}(\xi)$ is the non-dimensional hardening function that defines the interaction between the austenitic and martensitic phases, and will be discussed later. The non-dimensional material constants $\hat{S}$, $\hat{\alpha}$, $\hat{c}$, $\hat{s}_0$, $\hat{u}_0$ are, respectively, the non-dimensional effective compliance coefficient, non-dimensional effective thermal expansion coefficient, non-dimensional effective heat capacity coefficient, non-dimensional effective specific entropy at the reference state, and the non-dimensional effective specific internal energy at the reference state. These non-dimensional effective material properties can be defined in terms of the martensitic volume fraction, ξ, by the rule of mixtures, as follows

$$\hat{S} = \hat{S}^A + \xi\left(\hat{S}^M - \hat{S}^A\right) \tag{8.9}$$

$$\hat{\alpha} = \hat{\alpha}^A + \xi\left(\hat{\alpha}^M - \hat{\alpha}^A\right) \tag{8.10}$$

$$\hat{c} = \hat{c}^A + \xi\left(\hat{c}^M - \hat{c}^A\right) \tag{8.11}$$

$$\hat{s}_0 = \hat{s}_0^A + \xi\left(\hat{s}_0^M - \hat{s}_0^A\right) \tag{8.12}$$

$$\hat{u}_0 = \hat{u}_0^A + \xi\left(\hat{u}_0^M - \hat{u}_0^A\right) \tag{8.13}$$

where the superscript A stands for the austenitic phase, and the superscript M stands for the martensitic phase.

Constitutive relations are obtained by following a standard thermodynamic procedure, where the Gibbs free energy and the internal energy, which are related through the Legendre transformation, are substituted into the first and second law of thermodynamics as expressed in the Clausius-Duhem inequality (Coleman and Gurtin [78]). The total infinitesimal strain tensor, entropy are derived as follows:

$$\varepsilon = -\frac{\partial \hat{G}}{\partial \hat{\sigma}} = \hat{S}\hat{\sigma} + \hat{\alpha}\left(\hat{T} - \hat{T}_0\right) + \varepsilon^t, \tag{8.14}$$

$$\hat{s} = -\frac{\partial \hat{G}}{\partial \hat{T}} = \hat{\sigma}\hat{\alpha} + \hat{c}\ln\left(\frac{\hat{T}}{\hat{T}_0}\right) + \hat{s}_0. \tag{8.15}$$

After defining the expressions for the strain and non-dimensional entropy, we have as the remaining of the local dissipation inequality the following expression:

$$\left(-\frac{\partial \hat{G}}{\partial \varepsilon^t}\right)\left(\varepsilon^t\right)' + \left(-\frac{\partial \hat{G}}{\partial \xi}\right)\xi' \geq 0 \tag{8.16}$$

The evolution of the martensitic volume fraction during forward and reverse transformation (flow rule) can be expressed by:

$$\left(\varepsilon^t\right)' = H\text{sgn}(\hat{\sigma})\xi' \tag{8.17}$$

H is the maximum uniaxial transformation strain.

Substituting the flow rule, Eqn. 8.17 into the local dissipation inequality, Eqn. 8.16 we obtain

$$\left(-\frac{\partial \hat{G}}{\partial \varepsilon^t}H\text{sgn}(\hat{\sigma}) - \frac{\partial \hat{G}}{\partial \xi}\right)\xi' = \hat{\Pi}\xi' \geq 0 \tag{8.18}$$

where $\hat{\Pi}$ is the thermodynamic force conjugated to ξ, and it has the following form:

$$\begin{aligned}\hat{\Pi} =& |\hat{\sigma}|H + \frac{1}{2}\Delta\hat{S}\hat{\sigma}^2 + \hat{\sigma}\Delta\hat{\alpha}\left(\hat{T} - \hat{T}_0\right) + \\ &- \Delta\hat{c}\left[\left(\hat{T} - \hat{T}_0\right) - \hat{T}\ln\left(\frac{\hat{T}}{\hat{T}_0}\right)\right] + \Delta\hat{s}_0\hat{T} + \Delta\hat{u}_0 - \frac{\partial \hat{f}}{\partial \xi}\end{aligned} \tag{8.19}$$

Next, we introduce the hardening function that is used to describe the interaction between the austenitic and martensitic phases and martensitic variant themselves. The new hardening function is a general polynomial hardening function, which allows smooth transitions between the elastic and transformation regimes. The new hardening function is constructed in such a way that it has continuous derivatives and it has the following form:

$$\hat{f}(\xi) = \begin{cases} \frac{1}{2}\hat{a}_1\left(\xi + \frac{\xi^{n_1+1}}{(n_1+1)} + \frac{(1-\xi)^{n_2+1}}{(n_2+1)}\right) \quad ; & \xi' > 0 \\ \frac{1}{2}\hat{a}_2\left(\xi + \frac{\xi^{n_3+1}}{(n_3+1)} + \frac{(1-\xi)^{n_4+1}}{(n_4+1)}\right) \quad ; & \xi' < 0 \end{cases} \tag{8.20}$$

where $\hat{a}_1$ and $\hat{a}_2$ are model parameters that are defined as functions of the material parameters. The exponents n_1, n_2, n_3 and n_4 can assume values as either integers or rational numbers. [91] has shown that for $0 \leq n_1, n_2, n_3, n_4 \leq 1$ the hardening function is smooth and has continuous derivatives.

Since the constitutive model is constructed under a rate-independent formulation, instead of prescribing an evolution equation for $\dot{\xi}$ one can use Eqn. 8.19 to directly obtain the value of ξ. In the original Boyd and Lagoudas model this computation was straightforward. However, for the current hardening function, one needs to use an iterative scheme to find the value of ξ. Equation 8.21 and Eqn. 8.22 show the form of the transformation function during forward and reverse phase transformation, respectively

$$\begin{aligned}&\left|\hat{\sigma}\right| H + \frac{1}{2}\Delta\hat{S}\hat{\sigma}^2 + \hat{\sigma}\Delta\hat{\alpha}\left(\hat{T}-\hat{T}_0\right) - \Delta\hat{c}\left[\left(\hat{T}-\hat{T}_0\right) - \hat{T}\ln\left(\frac{\hat{T}}{\hat{T}_0}\right)\right] + \\ &\Delta\hat{s}_0\hat{T} + \Delta\hat{u}_0 - \frac{1}{2}\hat{a}_1\left(1+\xi^{n_1} - \left(1-\xi\right)^{n_2}\right) = \hat{Y}^*; \qquad \xi' > 0\end{aligned} \tag{8.21}$$

$$\begin{aligned}&\left|\hat{\sigma}\right| H + \frac{1}{2}\Delta\hat{S}\hat{\sigma}^2 + \hat{\sigma}\Delta\hat{\alpha}\left(\hat{T}-\hat{T}_0\right) - \Delta\hat{c}\left[\left(\hat{T}-\hat{T}_0\right) - \hat{T}\ln\left(\frac{\hat{T}}{\hat{T}_0}\right)\right] + \\ &\Delta\hat{s}_0\hat{T} + \Delta\hat{u}_0 - \frac{1}{2}\hat{a}_2\left(1+\xi^{n_3} - \left(1-\xi\right)^{n_4}\right) = -\hat{Y}^*; \qquad \xi' < 0\end{aligned} \tag{8.22}$$

It has been experimentally observed that the SMAs have a strong thermomechanical coupling, due to generation of latent heat during phase transformation. The thermomechanical coupling can cause the self-heating and self-cooling of the material during phase transformation, altering the material's behavior. Therefore, it is fundamental that the constitutive model be able to capture temperature variations of the SMA due to phase transformation. It is even more important to consider the thermomechanical coupling when the SMA is subjected to dynamical loadings, because it can lead to consecutive phase transitions, and consequently to large temperature variations.

The thermomechanical coupling is incorporated in the constitutive model through the heat equation. The fully thermomechanical coupled heat equation can be derived, by combining the total strain (Eqn. 8.14), entropy (Eqn. 8.15) and the first law of thermodynamics with the time derivative of the entropy, where the dissipation inequality is satisfied at all times. The only form of heat transfer considered in the current work is due to heat convection. It is assumed that no heat flux occurs within the SMA element, and that there is no heat transfer due to radiation. Therefore, after some algebraic manipulation, the one-dimensional form of the heat equation is given by:

$$\hat{T}\hat{\alpha}\hat{\sigma}' + \hat{c}\hat{T}' + \left(\hat{T}\hat{\sigma}\Delta\hat{\alpha} - \Delta\hat{c}\hat{T}\ln\left(\frac{\hat{T}}{\hat{T}_0}\right) + \Delta\hat{s}_0\hat{T}\right)\xi' = \hat{h}\left(\hat{T} - \hat{T}_\infty\right) \tag{8.23}$$

where the first term on the left-hand side, which is related to the thermoelastic coupling, expresses how the temperature changes due to a variation of the stress level. The second term is related to the thermal energy, while the third term of the left-hand side expresses how the SMA temperature changes due to phase transformation. The term of the right-hand side is related to the heat transfer condition due to convection, where $\hat{T}_\infty$ is the non-dimensional surrounding environment temperature, and $\hat{h}$ is the non-dimensional heat convection coefficient. Isothermal conditions can be simulated by assuming an infinite heat convection coefficient $\hat{h}$ in Eqn. 4.7, whereas adiabatic conditions can be achieved by assuming $\hat{h}$ equal to zero. Any value of the $\hat{h}$ between zero and infinity is considered, in the present work, as non-isothermal heat transfer conditions. The non-dimensional form of $\hat{h}$ is defined by $\hat{h} := \frac{A_s}{VE^A\omega_0}h$, where V is the volume of the SMA element.

Now that the constitutive model with the thermomechanical coupling has already been presented, we can substitute the expression for the non-dimensional stress from

Eq. 3.9, *i.e.*,

$$\hat{\sigma} = \frac{1}{\hat{S}}\left[\varepsilon - \hat{\alpha}\left(\hat{T} - \hat{T}_0\right) - \varepsilon^t\right], \tag{8.24}$$

into Eqn. 8.6 to get the new form of the non-dimensional system of equations of motion, as:

$$\begin{aligned} x_1' &= x_2 \\ x_2' &= \hat{F}\sin\left(\hat{\theta}\right) - \frac{1}{\hat{S}}\left[x_1 - \hat{\alpha}\left(\hat{T} - \hat{T}_0\right) - \varepsilon^t\right] \end{aligned} \tag{8.25}$$

where $\hat{S}$ and $\hat{\alpha}$ can be calculated from Eqns. 8.9 and 8.10, respectively. The state variables $\mathbf{x}$ and $\hat{T}$ are found by solving the above equations of motion, Eqn. 8.25, and heat equation, Eqn. 8.23; while the internal state variables ξ and ε^t are found by integrating the evolution equation, Eqn. 8.17, together with the transformation function, Eqn. 8.21 or 8.22 using a return mapping algorithm that will briefly be described in the next section.

B. Numerical Implementation of the Constitutive Model and Integration of the Equations of Motion

In order to deal with nonlinearities of the equations of motion, an iterative procedure based on the operator split technique (Ortiz *et al.* [92]) is employed. A predictor step is obtained by assuming that no phase transformation has occurred. Under this assumption, the value of the variables ε^t, and $\hat{T}$ assume a trial value that is equal to the values of these variables at the previous time instant. Therefore, equations of motion may be integrated by some classical integrator, as the Newmark method, for example.

Afterwards, the displacement is used as an input for the constitutive model equations. The implementation of the constitutive model follows the same procedure described in Qidwai and Lagoudas [27]. In general, given an increment of strain and temperature, the incremental form of the SMA constitutive model provides an increment of stress as an outcome. The increment of stress is calculated by implementing a return mapping algorithm. The return mapping algorithm solves the thermoelastic-transformation problem defined by the total strain relation, Eqn. 3.9, the flow rule, Eqn. 3.12 and the Eqns. 8.21 or 8.22, by dividing it into two problems using an additive split (Qidwai and Lagoudas [27]). At first, a thermoelastic prediction problem, assuming that the increment of the transformation strain vanishes, is attempted. If the predicted thermoelastic state violates the condition that $\hat{\pi} = \pm\hat{Y}^{*}$, during forward or reverse transformation, a transformation correction problem takes place to restore the condition. The present work uses the closest point projection algorithm as the corrector algorithm. The algorithm is based on the backward Euler integration rule of the transformation strain flow rule, which results in a set of non-linear algebraic equations solved using Newtons iteration method (Qidwai and Lagoudas [27]).

After the constitutive calculation, the equations of motion need to be reevaluated with the updated values of the ε^{t}, and $\hat{T}$. Notice that under these assumptions, the coupled equations of motion are solved in an uncoupled form considering two steps: dynamical problem and constitutive model. An iterative procedure needs to be performed until a prescribed tolerance is assured.

The model parameters can be defined as a function of the material parameters, such as, transformation temperatures and the entropy difference per unit volume between the phases. Table XIII presents the expressions describing these SMA model parameters.

As an example of how the SMA behavior can change due to different heat transfer conditions, Fig. 39 shows normalized stress *vs.* strain and normalized temperature *vs.* non-dimensional time curves of a SMA subjected to isothermal, adiabatic, and non-isothermal conditions. The material parameters of a typical NiTi SMA wire,

Table XIII. Definitions of the model parameters of the normalized constitutive model with smooth hardening transitions

$$\hat{Y}^* = \tfrac{1}{2}\Delta\hat{s}_0\left(\hat{M}_s - \hat{A}_f\right)$$

$$\hat{a}_1 = \tfrac{1}{2}\Delta\hat{s}_0\left(\hat{M}_f - \hat{M}_s\right)$$

$$\hat{a}_2 = \tfrac{1}{2}\Delta\hat{s}_0\left(1 - \hat{A}_f\right)$$

$$\Delta\hat{u}_0 = \tfrac{1}{2}\Delta\hat{s}_0\left(\hat{A}_f + \hat{M}_s\right)$$

$$n_1 = 0.21, n_2 = 0.25, n_3 = 0.11, n_4 = 0.13$$

which will be used in this work, are given by Table XIV. The non-dimensional transformation temperatures at zero-stress are defined by $\hat{M}_s := M_s/A_s$, $\hat{M}_f := M_f/A_s$, and $\hat{A}_f := A_f/A_s$. The heat transfer coefficient for this simulation is selected to be $\hat{h} = -4.423 \cdot 10^{-8}$, while the temperature of the surrounding environment is chosen to be $T_\infty = 1.258$.

Figure 39 shows the case of complete phase transformation under loading and unloading. It can be noticed in Fig. 39a that non-isothermal conditions tends to increase the energy dissipation as the area of the hysteresis loop enlarges. Fig. 39b show the temperature variation during loading and unloading. The difference in the temperature variation of the adiabatic and non-isothermal heat conditions, and the impact of the temperature variation on the stress *vs.* strain response of the SMA is quite evident.

C. Numerical Simulations

In order to analyze the dynamical response of a single-degree of freedom pseudoelastic SMA oscillator, free and forced vibrations are carried out by employing the numerical

Table XIV. Normalized values of SMA material parameters used on the SMA oscillator

$\hat{S}^A = 1.0$	$\hat{S}^M = 1.333$
$\hat{\alpha}^A = 0.00513$	$\hat{\alpha}^M = 0.00513$
$\hat{c}^A = 0.0216$	$\hat{c}^A = 0.0216$
$H = 0.03$	$\dfrac{\partial \hat{\sigma}}{\partial \hat{T}} = 0.0416$
$\hat{T}_0 = 1.258$	$\Delta \hat{s}_0 = -8.113$
$\hat{M}_f = 0.914$	$\hat{M}_s = 1.154$
$\hat{A}_s = 1.0$	$\hat{A}_f = 1.258$

procedure discussed in the previous section. The SMA material parameters are given by Table XIV, representing a typical NiTi alloy.

1. Free Vibration

Free vibrations are first considered by vanishing the forcing term of the right-hand side of Eq. 8.1, and by giving appropriate initial conditions to the oscillator. Figure 40 shows results related to the free vibration of the isothermal SMA oscillator. Results are presented in the form of stress *vs.* strain and phase space curves. For a high energy initial condition $(x_1(0), x_2(0)) = (0.0, 0.04)$, and $\hat{T} = 1.258$ the system dissipates energy due the hysteresis loop. The level of energy dissipated per cycle is equivalent to the area of the hysteresis loop, defined by the amount of phase transformation that the SMA underwent. However, in the course of time, as the SMA dissipates energy, the system converges to the elastic regime. Since there is no phase transformation during the elastic regime, no energy dissipation due to hysteresis takes place. As a

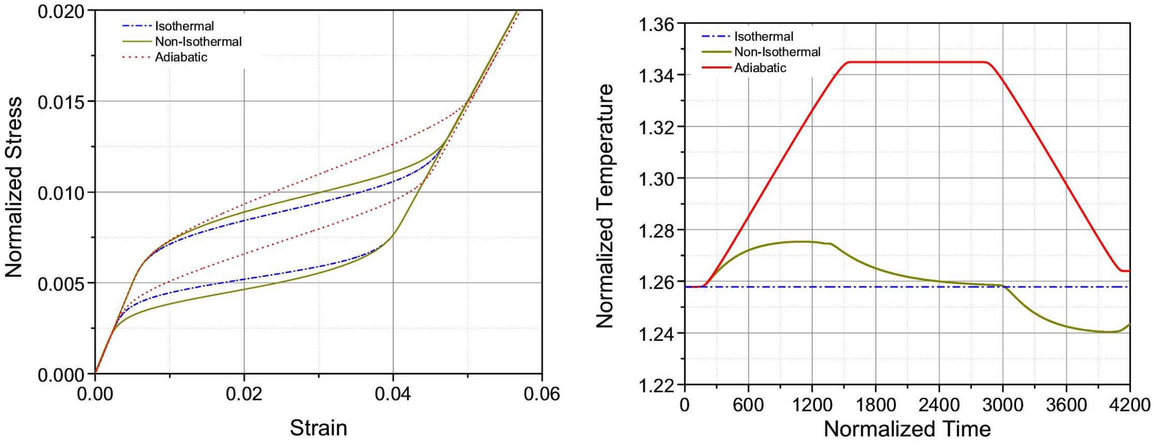

(a) $\hat{\sigma}$ *vs.* ε

(b) $\hat{T}$ *vs.* $\hat{t}$

Fig. 39. Stress *vs.* strain and temperature *vs.* time curves: comparison of isothermal, non-isothermal and adiabatic cases.

result, the oscillator motion converges to a periodic orbit and stays there. Similar results may be found for non-isothermal heat transfer conditions.

2. Forced Vibrations

Forced vibrations are now in focus. The SMA oscillator is subjected to a harmonic forcing excitation and two different situations are considered: isothermal and non-isothermal conditions. First, let us consider isothermal conditions.

a. Forced Vibration - Isothermal Conditions

Forced vibrations of the pseudoelastic SMA oscillator is investigated by considering a fixed amplitude of the excitation force and different values of the excitation frequency. Since, at first, we are assuming isothermal conditions, the temperature of the SMA element is fixed at $\hat{T} = 1.258$. In addition, the amplitude of the excitation force is selected to be $\hat{F} = 0.008$ for all simulations.

Figure 41a presents the bifurcation diagram of the SMA oscillator subjected to

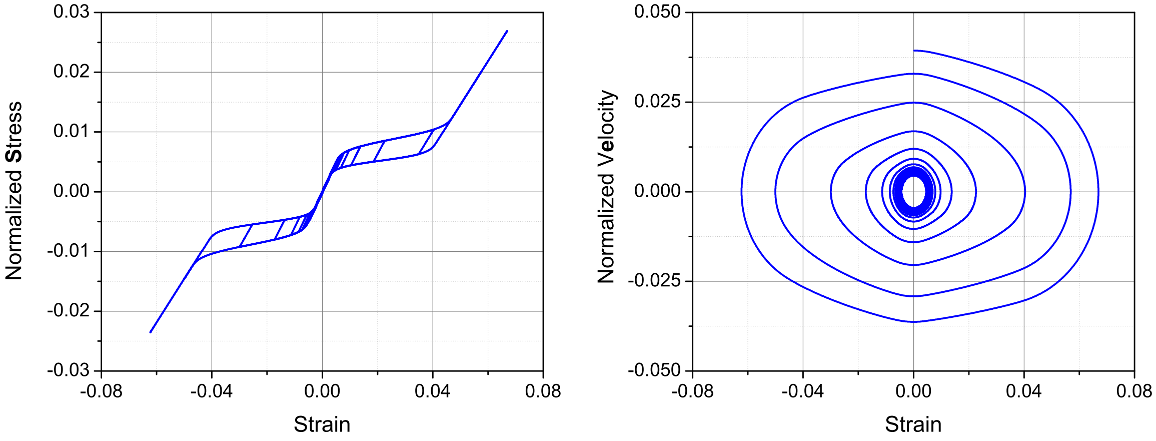

(a) $\hat{\sigma}$ *vs.* ε

(b) ε' *vs.* ε

Fig. 40. Free response of the SMA oscillator: stress *vs.* strain and phase portrait curves.

isothermal conditions, for the range of frequencies of $0.24 < \hat{\omega} < 0.76$. One can observe that Fig. 41 contains regions of clouds of points separated by regions with lines. Usually the regions of clouds of points are associated with chaotic regime, and the regions of lines are related to periodic regime. Figure 41b shows an enlargement of Fig. 41a for the interval of $0.35 < \hat{\omega} < 0.55$

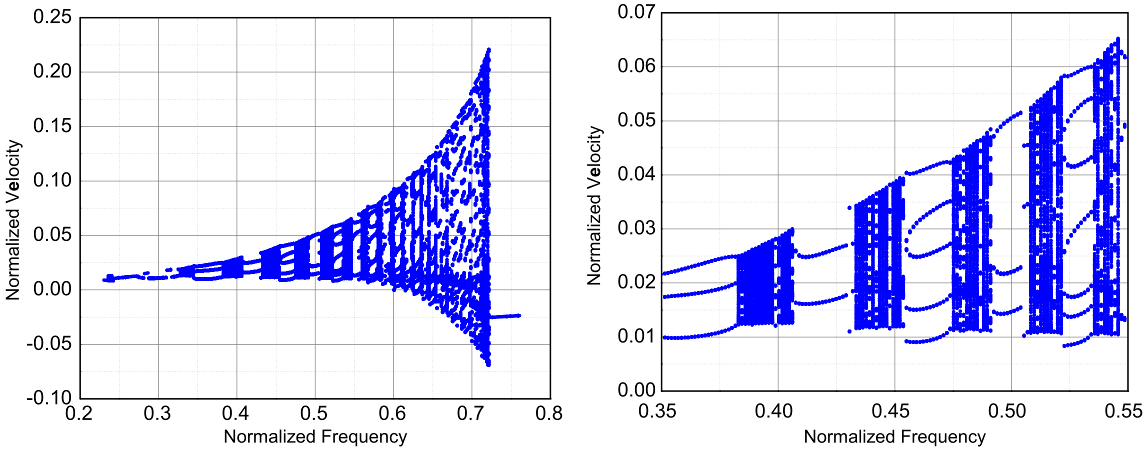

(a) Interval: $0.2 < \hat{\omega} < 0.8$

(b) Interval: $0.35 < \hat{\omega} < 0.55$

Fig. 41. Bifurcation diagram for isothermal conditions.

It is important to mention that if we consider two linear undamped oscillators, with elastic properties of austenite and martensite, the resonance frequencies of the these oscillators would be $\hat{\omega}_A = 1.0$ and $\hat{\omega}_N = 0.866$, respectively.

Next, we select two certain values of excitation frequencies to investigate the dynamical response of the SMA hysteretic oscillator. Figure 42 shows the oscillator dynamic response during steady state, for the case of $\hat{F} = 0.008$ and $\hat{\omega} = 0.356$. The stress *vs.* strain and the phase space curves are shown in Fig. 42a,b, respectively, while Fig. 42c presents the Poincaré map. Notice that the Poincaré map of Fig. 42c shows three points, that are related to a period-3 motion.

The next analysis is concerned to the oscillator's motion when the excitation frequency is $\hat{\omega} = 0.397$. Figure 43a presents stress *vs.* strain curve, while Fig. 43b presents phase space curve. The Poincaré section is shown in Fig. 43c. This time, the Poincaré map presents a cloud of points that can be associated to chaotic motion. However, only after the evaluation of the Lyapunov exponents one can claim that it is really chaos.

b. Forced Vibrations - Non-Isothermal Conditions

At this point, non-isothermal conditions are considered. The bifurcation diagram for non-isothermal conditions is presented in Fig. 44. The heat transfer coefficient for this simulation is selected to be $\hat{h} = -4.423 \cdot 10^2$, while the temperature of the surrounding environment is chosen to be $T_\infty = 1.258$. From the analysis of the bifurcation diagram, one can also identify regions with clouds of points and regions associated with periodic motion. Figure 44b shows an enlargement of Fig. 44a for the interval of $0.35 < \hat{\omega} < 0.55$.

In a similar way to the previous dynamic analysis of the SMA oscillator for isothermal heat transfer conditions, the exciting force amplitude is selected to be

$\hat{F} = 0.008$, while the two single frequency excitation cases are considered to be $\hat{\omega} = 0.356$ and $\hat{\omega} = 0.397$, respectively. Figure 45 shows the dynamic response of the oscillator during steady state for the case of $\hat{F} = 0.008$ and $\hat{\omega} = 0.356$. Figure 45a shows the stress *vs.* strain curve, while Fig. 45b presents the phase space curve. Figure 45c presents the Poincaré map, while the time history of the temperature is presented in Fig. 45d. It can be observed that the Poincaré map of Fig. 45c presents a cloud of points, that in principle, could be related to a chaotic motion.

Next, we analyze the oscillator's motion when the excitation frequency is $\hat{\omega} = 0.397$. Figure 46a presents stress *vs.* strain curve, while Fig. 46b shows the phase space curve. Figure 46c shows Poincaré section, and the time history of the temperature are presented in Fig. 46d. Notice that the Poincaré map presented in Fig. 46c might appear as a period-5 motion, since there are apparently 5 points in the Poincaré map. Figure 46d presents the temperature variation of the SMA element for this simulation, after it has reached its steady state.

It is important to mention that the observation of chaotic motion is not restricted to the displacement variable only. In fact, the dimension of the oscillator is not only related to the variables of displacement, and velocity, but also to stress, σ, temperature, T, and martensitic volume fraction ξ, since the free energy of the SMA hysteretic element is constructed by considering σ, T, and ξ as internal variables. Therefore, one can say that the SMA hysteretic oscillator has dimension six: displacement, velocity, stress, temperature, martensitic volume fraction, and time. This leads to the conclusion that the bifurcations diagrams in frequency presented before, are just projections of the complete bifurcation diagram. Figure 47 shows the other projections of the bifurcation diagrams. One should notice that all of them shows the same range of frequencies for which chaotic and periodic behavior take place.

D. Lyapunov Exponents

Lyapunov exponents evaluate the sensitive dependence to initial conditions, verifying the divergence of nearby orbits. In order to understand the idea related to these exponents consider an N-sphere of states that is transformed by the system dynamics in an N-ellipsoid. Lyapunov exponents are related to the expanding and contracting nature of different directions in phase space. The evaluation of the divergence of two nearby orbits is done considering the relation between the initial N-sphere and the N-ellipsoid related to a reference trajectory (Nayfeh and Balachandran [90], and Savi [93]).

The diameter variation at a generic time instant compared with the initial sphere (Fig. 48) can be calculated as:

$$d(\hat{t}) = d_0 \exp(\lambda \hat{t}), \tag{8.26}$$

where λ represents the Lyapunov exponent . Therefore, the i^{th} exponent of the spectrum is defined as follows (Wolf *et al.* [65]):

$$\lambda_i = \lim_{\hat{t} \to \infty} \frac{1}{\hat{t}} \ln \left(\frac{d_i(\hat{t})}{d_i(\hat{t}_0)} \right) \tag{8.27}$$

The signs of the Lyapunov exponents provide a qualitative picture of the system's dynamics and any system containing at least one positive exponent presents chaotic behavior. Notice that chaos may be geometrically understood considering a sequence of contraction-expansion-folder transformations, known as Smale horseshoes (Savi [93]). The expansion is related to an unstable direction being associated with a positive exponent. Beside the signs of the exponents, their magnitudes also provides information of the system's dynamics. Greater positive values, associated with greater divergence of nearby orbits, are related to greater instabilities.

The Lyapunov exponents estimation may be implemented by monitoring the evolution of the N-sphere principal axes evolving with the nonlinear equations of motion. One problem with this approach is that chaotic behavior presents an exponential divergence of nearby orbits. As pointed out by (Wolf *et al.* [65]), this problem may be avoided with the use of a phase space plus tangent space approach. A reference trajectory defines the N-sphere of states and the evolution of the N-sphere surface points are defined by the action of the linearized equations of motion. This procedure needs to calculate the reference trajectory by integrating the nonlinear equations of motion and simultaneously, the linearized equations of motion are integrated for N different initial conditions defining an arbitrary oriented frame of N orthonormal vectors. Since each vector will diverge in magnitude, and in a chaotic behavior, each vector tends to fall along the local direction of most rapid growth, it is necessary to repeatedly use the Gram-Schmidt reorthonormalization procedure on the vector frame, as shown in the schematic drawing of Fig.49.

Hence, when the distance $d(t)$ becomes large, a new $d_0(t)$ is defined, in order to evaluate the divergence and the exponents estimation is done by:

$$\lambda_i = \frac{1}{\hat{t}_n - \hat{t}_0} \sum_{k=1}^{N} \ln\left(\frac{d(\hat{t}_k)}{d_0(\hat{t}_{k-1})}\right), \tag{8.28}$$

1. Linearization Process of a SMA Dynamical Hysteretic System

Based on the previous discussion, the use of the algorithm proposed by Wolf *et al.* [65] needs to evaluate a system linearization in order to follow the nearby perturbed trajectory. We start the linearization process by writing the dynamical system described by Eqn. 8.25, in an autonomous form, as

$$\mathbf{x}' = \mathbf{F}(\mathbf{x}) \tag{8.29}$$

where **F** is a continuous differentiable vector function, with components:

$$\begin{aligned} F_1 &= x_2 \\ F_2 &= \hat{F}\sin\left(\hat{\theta}\right) - \frac{1}{\hat{S}}\left[x_1 - \hat{\alpha}\left(\hat{T} - \hat{T}_0\right) - \varepsilon^t\right] \\ F_3 &= \hat{\omega} \end{aligned} \tag{8.30}$$

where $\hat{\theta}$ is defined to be $\hat{\theta} := \hat{\omega}\hat{t}$

A solution of the system of Eqn. 8.29, starting from some initial condition $\boldsymbol{\phi}(t)$, leads the trajectory $\mathbf{x}(\hat{t})$. Then, applying a small perturbation $\boldsymbol{\zeta} = \boldsymbol{\zeta}(\hat{t})$ in the $\mathbf{x}(\hat{t})$, the perturbed trajectory becomes

$$\mathbf{x} = \boldsymbol{\phi} + \boldsymbol{\zeta}. \tag{8.31}$$

Substituting Eqn. 8.31 into Eqn. 8.29, and linearizing the resulting equation around the perturbation (Nayfeh and Balachandran [90]) gives the perturbed equation

$$\boldsymbol{\zeta}' = J\boldsymbol{\zeta}, \tag{8.32}$$

where J is the Jacobian matrix given by:

$$J = \frac{\partial \mathbf{F}}{\partial \mathbf{x}} \tag{8.33}$$

At this point it is important to discuss the dimension of the dynamical system for which we compute the Lyapunov exponents. Recall that the SMA oscillator is modeled as a dynamical system of dimension six. The state variables are the normalized displacement,ε, the normalized velocity, ε', the normalized stress, $\hat{\sigma}$, the normalized temperature, $\hat{T}$, and martensitic volume fraction ξ, in addition to normalized time, $\hat{t}$, as the independent variable. Therefore, a natural approach would be to compute six Lyapunov exponents, one for each dimension of the system. Even though this approach seems to be the appropriated one to follow, it is difficult to implement, especially since the dynamical system consist of a set of both ordinary differential and algebraic equations with multiple branches. The approach utilized in this work is to calculate only the Lyapunov exponents associated with the normalized displacement, normalized velocity and normalized time dimensions. Since the normalized stress does not appear explicitly in the equation of motion, Eqn. 8.4, but is eliminated through substitution from the stress-strain relation given in Eqn. 8.24, and the normalized temperature and martensitic volume fraction are computed separately through the return mapping algorithm from the equation of motion.

Under these assumptions, for each time step, the divergence of nearby orbits considering a reference orbit, governed by the equation of motion, and a perturbed orbit governed by the linearized system is verified. Since the reference trajectory evolves in time, the linearized system has time dependent coefficients. This is expressed by the time dependent Jacobian matrix. Therefore, for each time instant, the linearized system is governed by the following equation:

$$\begin{aligned} \zeta_1' &= \zeta_2 \\ \zeta_2' &= -\hat{k}\zeta_1 + \hat{F}sin(\theta) \end{aligned} \tag{8.34}$$

The non-dimensional linearized stiffness, $\hat{k}$, can be directly obtained from the derivative of $\hat{\sigma}$ with respect to ε from Eq. 8.30.

$$\hat{k} = \frac{\partial}{\partial x_1}(\hat{\sigma}) = \frac{1}{\hat{S}} = \frac{1}{\hat{S}^A - \xi(\hat{S}^M - \hat{S}^A)} \tag{8.35}$$

Notice that even though the linearization process captures the variable stiffness of the SMA element as a function of ξ, no damping term appears in Eqn. 8.34. The reason for this is that there is no term associated with ε' in Eqn. 8.25, since the only damping considered is the hysteretic damping provided by the SMA element, which is rate-independent. Moreover, because of the linearization, the transformation strain

, ε^t, is lost from the linearized equations of motion, Eqn. 8.34. As a consequence, the effect of hysteresis and the hysteretic damping are not considered. This is an important issue, since hysteresis plays a key role in the dynamical behavior of the system. Then, one can conclude that the linearized system of Eqn. 8.34 does not represent the original system, which has nonlinear stiffness and nonlinear hysteretic damping. If we carry on the estimation of the Lyapunov exponents based on the linearized system of Eqn. 8.34, the summation of the converged values of the Lyapunov exponents would be zero, instead of being negative, as expected for dissipative systems. Therefore, in order to overcome this linearization issue, we consider an equivalent viscous damping that dissipates the same amount of energy as the hysteretic SMA. We write the linearized system with the addition of a representative viscous damping as

$$\begin{aligned} \zeta_1' &= \zeta_2 \\ \zeta_2' &= -\hat{b}\zeta_2 - \hat{k}\zeta_1 + \hat{F}sin(\theta) \end{aligned} \tag{8.36}$$

where $\hat{b}$ is the viscous damping coefficient, representing the hysteretic but rate independent SMA system.

The equivalent viscous damping that is considered in the linearized system does not alter the solution of the original system. It is used only to compute the Lyapunov exponents. The procedure for obtaining the equivalent viscous damping is shown below.

2. Equivalent Viscous Damping

The linearized dissipation concerning the hysteretic behavior is performed by establishing a comparison of the dissipated energy in one motion cycle of the nonlinear hysteretic motion with a linear viscous damping motion (Inman [94]). The idea is to define an equivalent viscous damping that dissipates the same amount of energy as the hysteretic system. Therefore, It is assumed that the response of the oscillator is given by:

$$\varepsilon\left(\hat{t}\right) = \epsilon \sin\left(\hat{\omega}\hat{t}\right) \tag{8.37}$$

where ω is the frequency of the damper's response and $\bar{\varepsilon}$ is cycle amplitude related to the hysteresis loop.

The non-dimensional total energy dissipated by an SMA element during one cycle of tensile-compressive loop of hysteresis is defined as:

$$\hat{E}_D^{SMA} = \left[2\oint \hat{\pi}\mathrm{d}\xi\right] = \left[2\int_0^1 \hat{Y}^*\mathrm{d}\xi + 2\int_1^0 -\hat{Y}^*\mathrm{d}\xi\right] = 4\hat{Y}^*. \tag{8.38}$$

On the other hand, the non-dimensional energy dissipated by a linear viscous damping can be calculated as follow:

$$\hat{E}_D^V = \oint F_d\mathrm{d}\varepsilon = \oint b\varepsilon'\mathrm{d}\varepsilon = \int_0^{\frac{2\pi}{\hat{\omega}}} \hat{b}\dot{\varepsilon}^2\mathrm{d}\hat{t} = \pi\hat{b}\epsilon^2\hat{\omega} \tag{8.39}$$

Therefore, by comparing this result with the SMA hysteretic dissipation, it is possible to define a non-dimensional equivalent viscous damping coefficient as follows:

$$\hat{b} = \frac{4\hat{Y}^*}{\epsilon^2\hat{\omega}\pi} \tag{8.40}$$

It should be emphasized that the SMA can also undergo partial phase transformations, which leads to a variable energy dissipation. Consequently, we need to consider the amount of phase transformation that the SMA element underwent in every cycle. This aspect is considered by assuming a variation of variables ξ and $\bar{\varepsilon}$. Therefore, the energy dissipated by an SMA element is given by

$$\hat{E}_D^{SMA} = \left[2\int_0^{\xi} \hat{Y}^*\mathrm{d}\xi + 2\int_{\xi}^0 -\hat{Y}^*\mathrm{d}\xi\right] = 4\hat{Y}^*\Delta\xi \tag{8.41}$$

The equivalent viscous damping can be redefined as:

$$\hat{b} = \frac{4\hat{Y}^*}{\Delta\epsilon^2\hat{\omega}\pi}\Delta\xi \tag{8.42}$$

The equivalent viscous damping coefficient, $\hat{b}$, is not a constant and its value depends on the phase transformation level, which is evaluated by the terms $\Delta\xi$ and $\Delta\epsilon$.

3. Lyapunov Exponents Estimation

Next, we revisit the results from Section C for the cases of forced vibration under isothermal and non-isothermal heat transfer conditions. However, the analysis of the dynamical behavior of the SMA oscillator is completed by the estimation of the Lyapunov exponents.

a. Forced Vibrations - Isothermal Conditions

Figure 50 shows the estimation of the Lyapunov exponents for isothermal heat transfer conditions, for the cases with excitation frequencies of $\hat{\omega} = 0.356$ and $\hat{\omega} = 0.397$. The Lyapunov exponent time history show converged values of $((\lambda_1, \lambda_2) = (-0.0038, -0.0723))$ for the case of $\hat{\omega} = 0.356$ (Fig. 50a) confirm that the oscillator is undergoing a periodic motion, as indicated by the Poincaré map in Fig. 42. The time history of the Lyapunov exponents for the case of an exciting frequency of $\hat{\omega} = 0.356$ under isothermal conditions is shown in Fig. 50. For this simulation there is a positive exponent in the spectrum of the Lyapunov exponents $(\lambda_1, \lambda_2) = (+0.021, -0.074)$, indicating that the oscillator is undergoing a chaotic motion. It should be pointed out that the exponents calculation captures the dissipation characteristics of the motion since the sum of Lyapunov spectrum is less than zero. This is an important aspect since all dissipative phenomena are completely associated with the hysteresis loop and therefore, the proposed linearization captures this essential characteristics of the dynamical system.

In order to verify if the approach to compute the Lyapunov exponents provides a correct analysis of the behavior of the system, Fig. 51 revisits the bifurcation diagram of Fig. 41b along with the value of the largest Lyapunov exponent (big dots) of selected normalized frequencies. Note that the obtained values of the Lyapunov exponents are consistent with the behavior of the dynamical response observed in the bifurcation diagram. In other words, the Lyapunov exponents with positive values correspond to the regions with clouds of points in the bifurcation diagram, whereas the Lyapunov exponents with negative values are associated with periodic responses.

b. Forced Vibrations - Non-Isothermal Conditions

The next analysis is related to non-isothermal heat transfer conditions. Figure 52 presents the simulation of the Lyapunov exponents for the case of $\hat{\omega} = 0.356$. The analyzes of the spectrum of the Lyapunov exponents confirms this conclusion showing that converged values are $(\lambda_1, \lambda_2) = (+0.020, -0.086)$. Therefore, for the same value of frequency and force excitation amplitude, but different heat condition from Fig. 42, the system's response has changed from a periodic to a chaotic one, confirmed by the Lyapunov exponents. Once again, the dissipative system characteristics is captured by the Lyapunov exponent spectrum since the summation is less than zero.

Figure 52 show the Lyapunov exponents analysis for the case of $\hat{\omega} = 0.397$, under non-isothermal conditions. By analyzing the converged values of the Lyapunov exponents (Fig. 52b), one can see that highest exponent has a positive value $(\lambda_1, \lambda_2) = (+0.03, -0.078)$. This indicates that the oscillator is experiencing a chaotic motion, as opposed to what the Poincaré map of Fig. 46 might suggest. This represents a different chaotic pattern when compared to that of the isothermal condition.

Similarly to the case of isothermal conditions, Fig. 53 revisits the bifurcation diagram for non-isothermal conditions shown in Fig. 44b and plot the largest Lyapunov exponent (big dots) obtained for different normalized excitation frequencies. Note again that the obtained values of the Lyapunov exponents are consistent with the behavior of the dynamical response observed in the bifurcation diagram. In other words, the Lyapunov exponents with positive values correspond to the regions with clouds of points in the bifurcation diagram, whereas the Lyapunov exponents with negative values are associated with periodic responses.

The results of the current approach seem to be compatible with the bifurcation diagram results. However, further work on the full dynamical system is necessary to rigorously justify the above results.

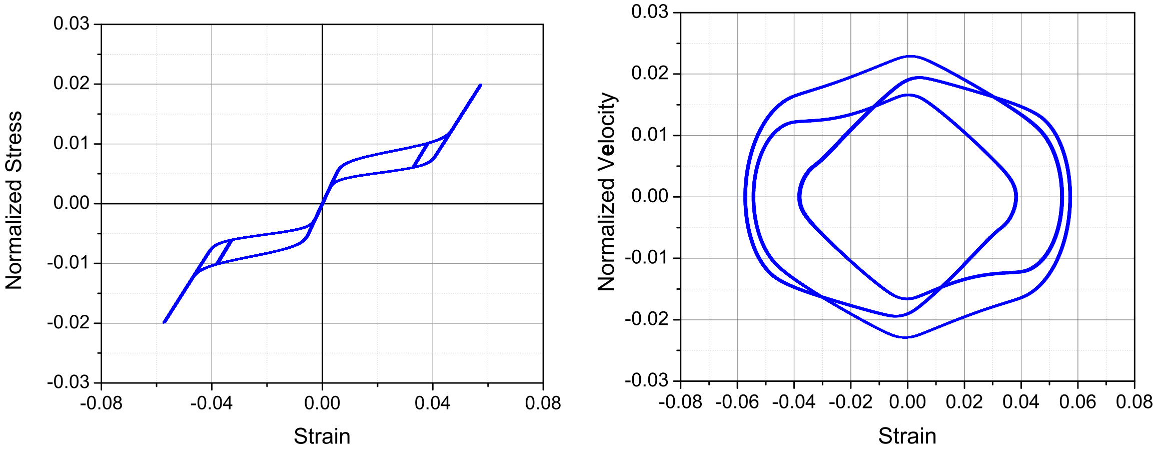

(a) $\hat{\sigma}$ *vs.* ε

(b) $\varepsilon' vs. \varepsilon$

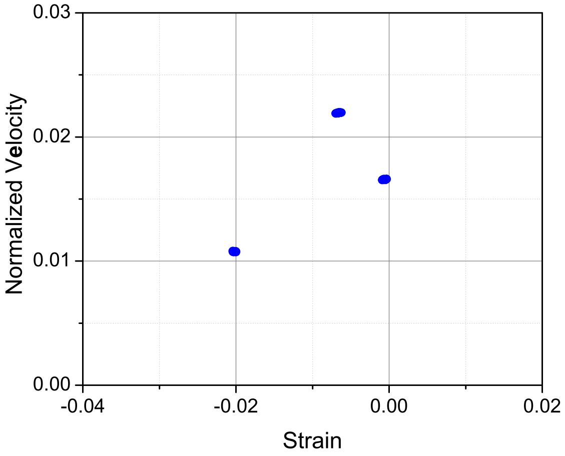

(c) Poincaré Map:ε' *vs.* ε

Fig. 42. Forced response of the SMA oscillator for $\hat{F} = 0.008$ and $\hat{\omega} = 0.356$, isothermal conditions.

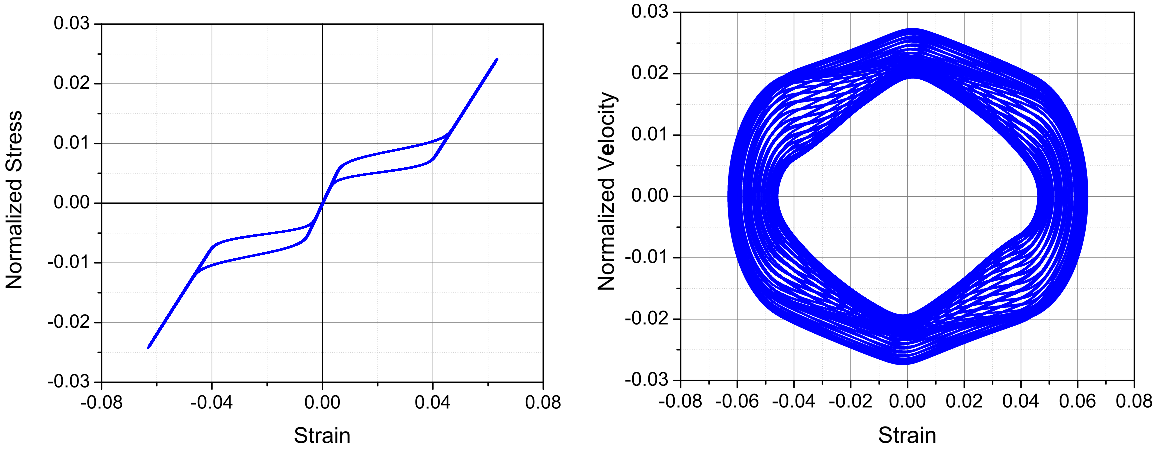

(a) $\hat{\sigma}$ *vs.* ε

(b) ε' *vs.* ε

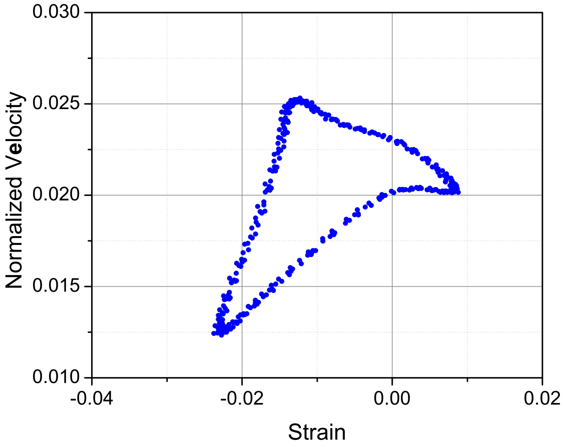

(c) Poincaré Map:ε' *vs.* ε

Fig. 43. Forced response of the SMA oscillator for $\hat{F} = 0.008$ and $\hat{\omega} = 0.397$Hz, isothermal conditions.

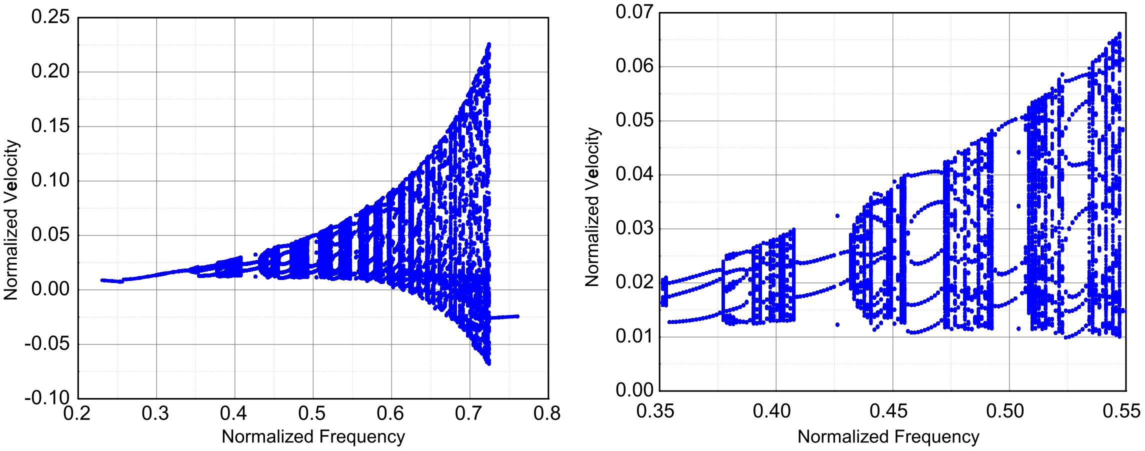

(a) Interval: $0.2 < \hat{\omega} < 0.8$

(b) Interval: $0.35 < \hat{\omega} < 0.55$

Fig. 44. Bifurcation diagram for non-isothermal conditions.

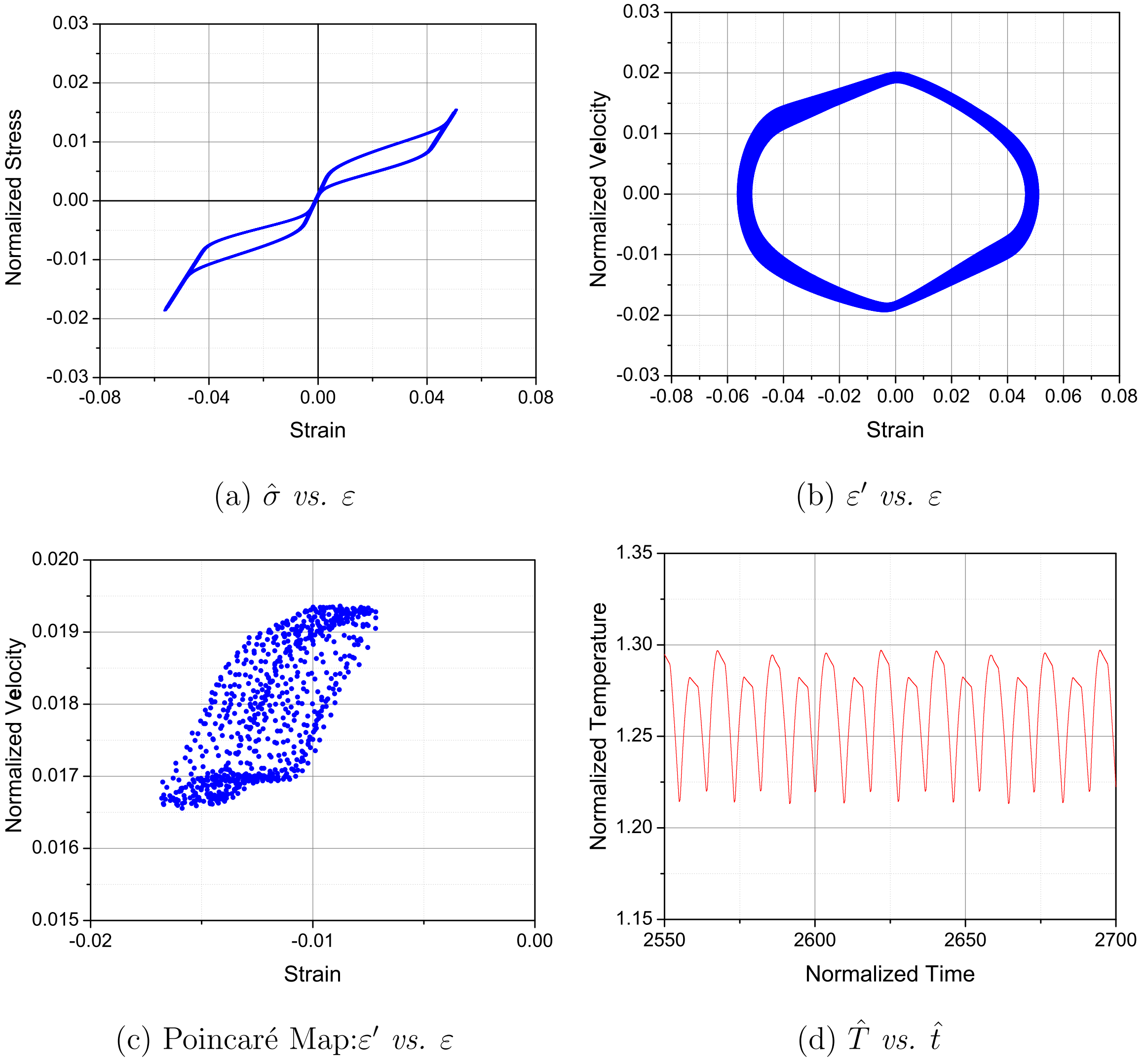

(a) $\hat{\sigma}$ *vs.* ε

(b) ε' *vs.* ε

(c) Poincaré Map:ε' *vs.* ε

(d) $\hat{T}$ *vs.* $\hat{t}$

Fig. 45. Forced response of the SMA oscillator for $\hat{F} = 0.008$ and $\hat{\omega} = 0.356$.

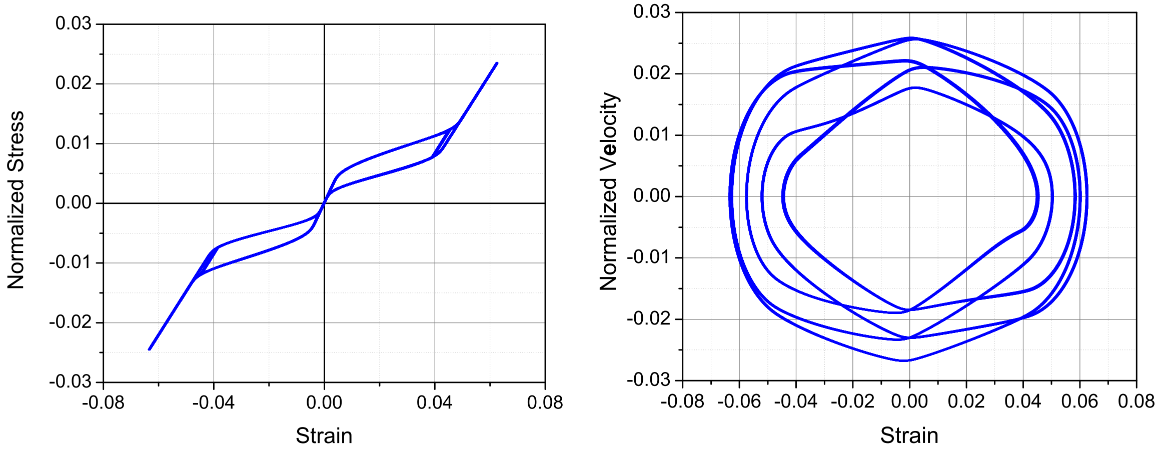

(a) $\hat{\sigma}$ *vs.* ε

(b) ε' *vs.* ε

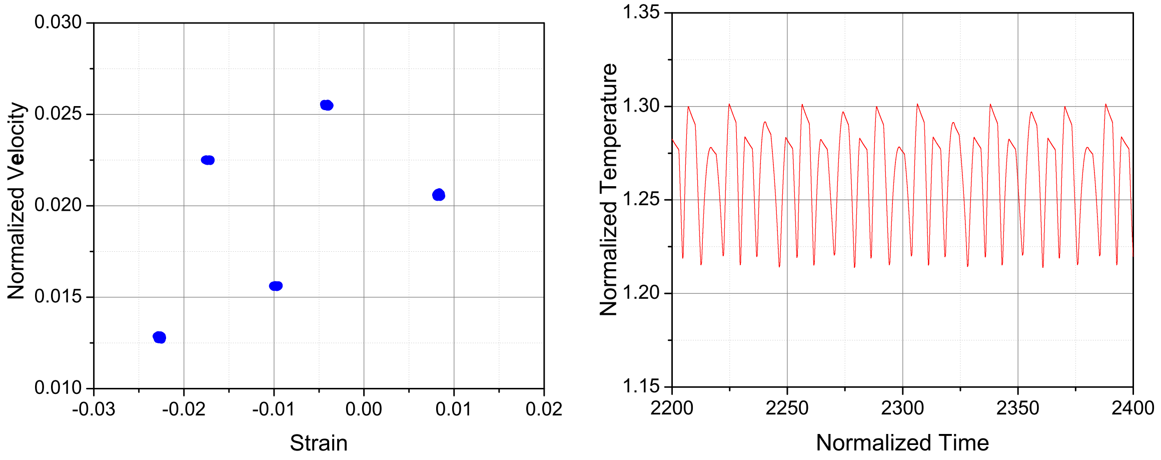

(c) Poincaré Map:ε' *vs.* ε

(d) $\hat{T}$ *vs.* $\hat{t}$

Fig. 46. Forced response of the SMA oscillator for $\hat{F} = 0.008$ and $\hat{\omega} = 0.397$.

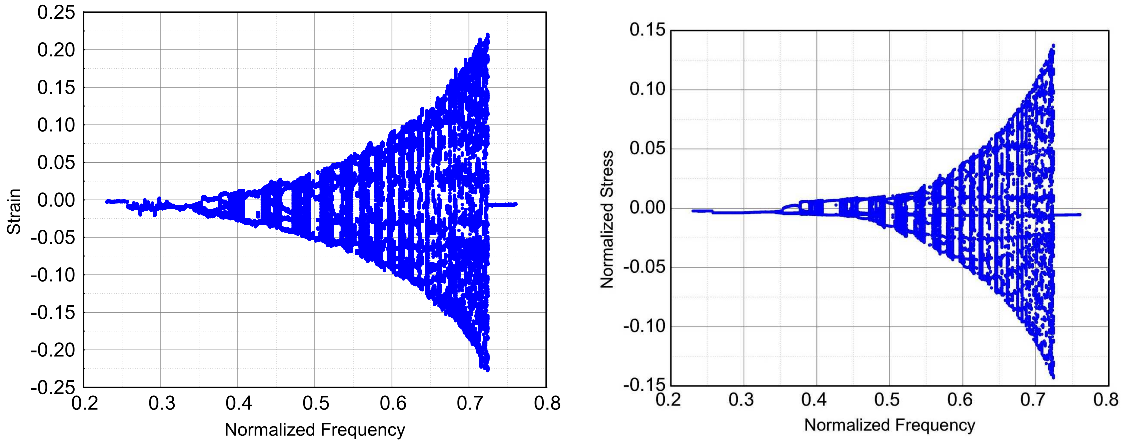

(a) ε *vs.* $\hat{\omega}$

(b) $\hat{\sigma}$ *vs.* $\hat{\omega}$

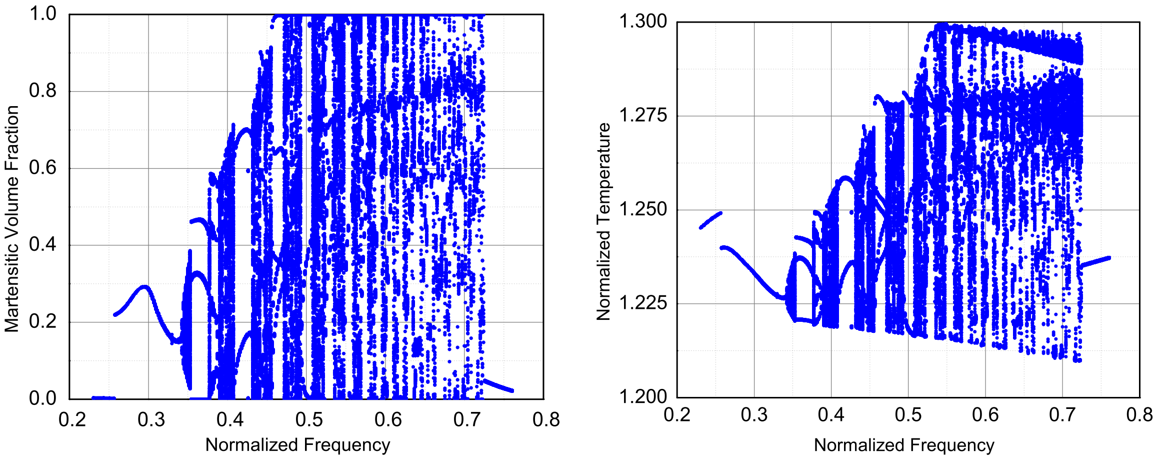

(c) Martensitic Volume Fraction *vs.* Normalized Frequency

(d) $\hat{T}$ *vs.* $\hat{\omega}$

Fig. 47. Bifurcation diagrams, non-isothermal conditions.

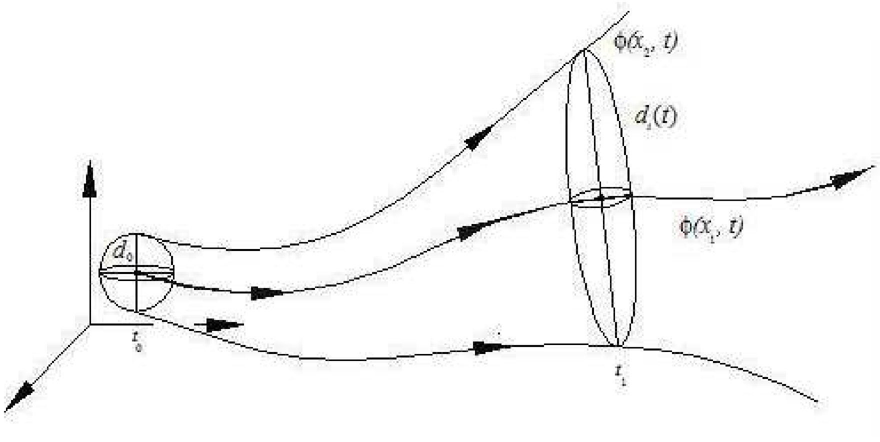
$\phi(x_2, t)$
$d_1(t)$
$\phi(x_1, t)$
d_0
t_0
t_1

Fig. 48. Lyapunov exponents.

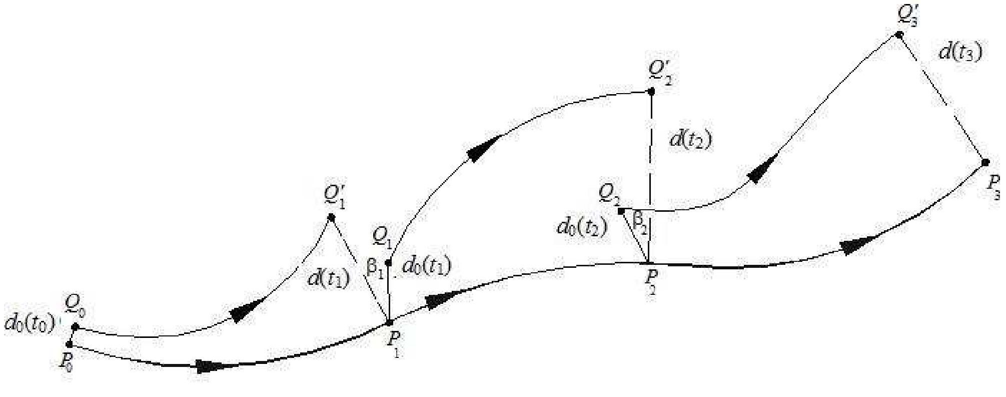
Q_3'
$d(t_3)$
Q_2'
$d(t_2)$
Q_2
β_2
$d_0(t_2)$
P_3
Q_1'
Q_1
β_1
$d_0(t_1)$
$d(t_1)$
P_2
Q_0
$d_0(t_0)$
P_0
P_1

Fig. 49. Lyapunov exponents calculation.

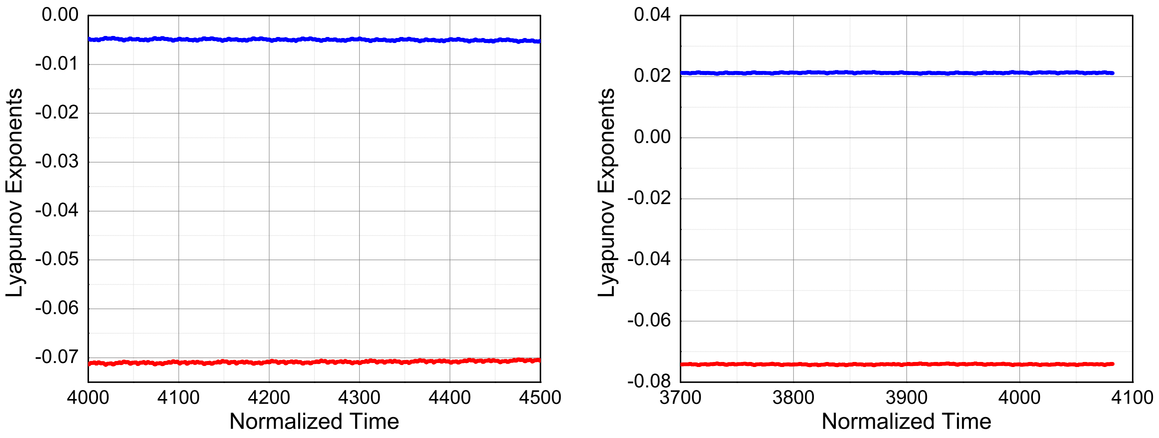

(a) Lyapunov Exponents for $\hat{\omega} = 0.356$ (b) Lyapunov Exponents for $\hat{\omega} = 0.397$

Fig. 50. Lyapunov exponents for $\hat{F} = 0.008$ and $\hat{\omega} = 0.356$ and $\hat{\omega} = 0.397$, isothermal conditions.

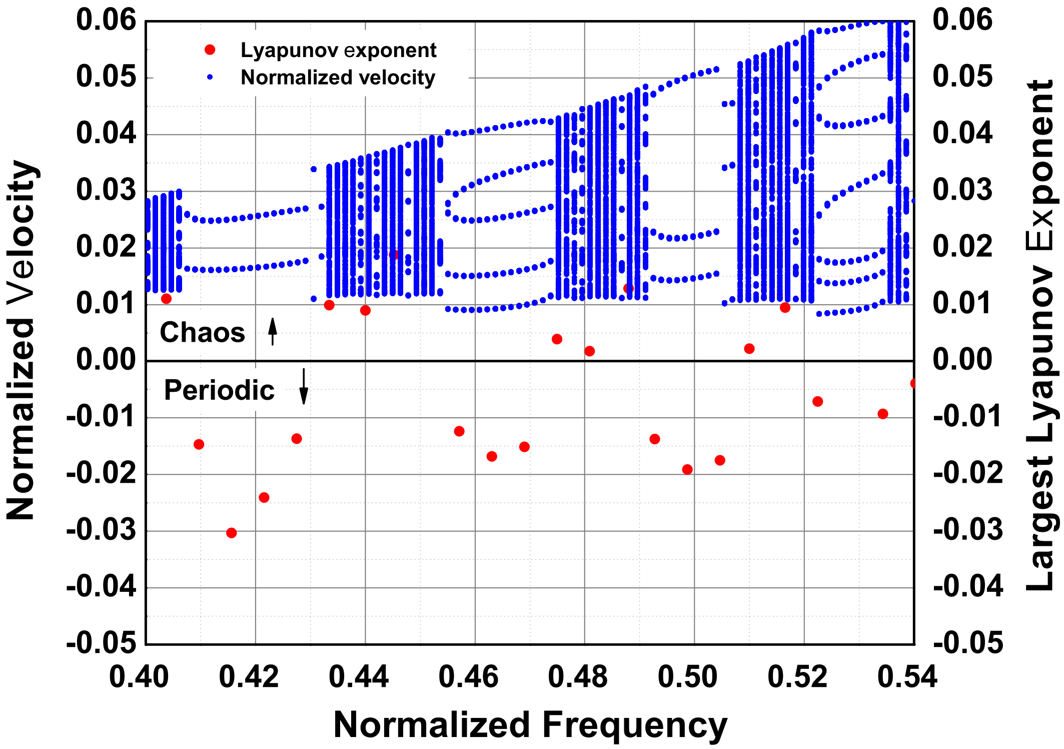

Fig. 51. Lyapunov exponents and bifurcation diagrams for the case of isothermal conditions.

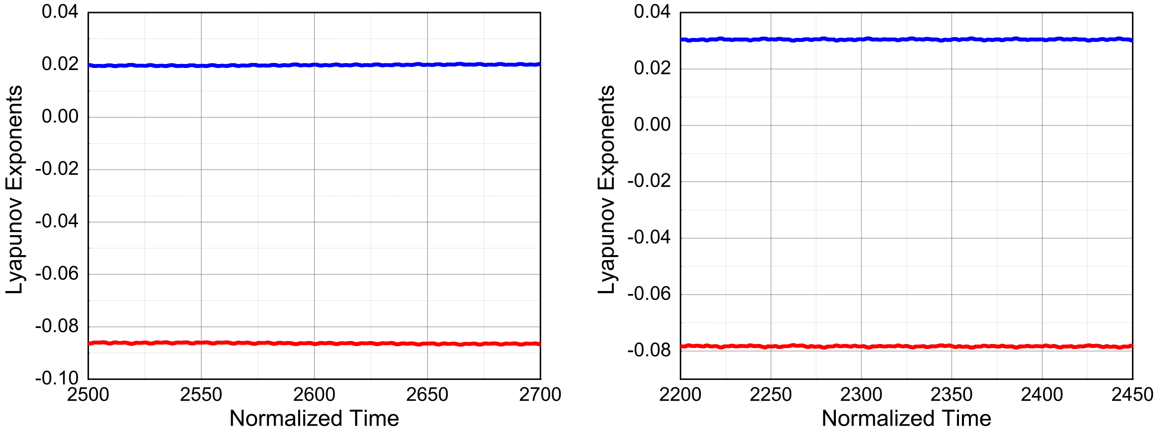

(a) Lyapunov Exponents for $\hat{\omega} = 0.356$ (b) Lyapunov Exponents for $\hat{\omega} = 0.397$

Fig. 52. Lyapunov exponents for $\hat{F} = 0.008$ and $\hat{\omega} = 0.356$ and $\hat{\omega} = 0.397$, non-isothermal conditions.

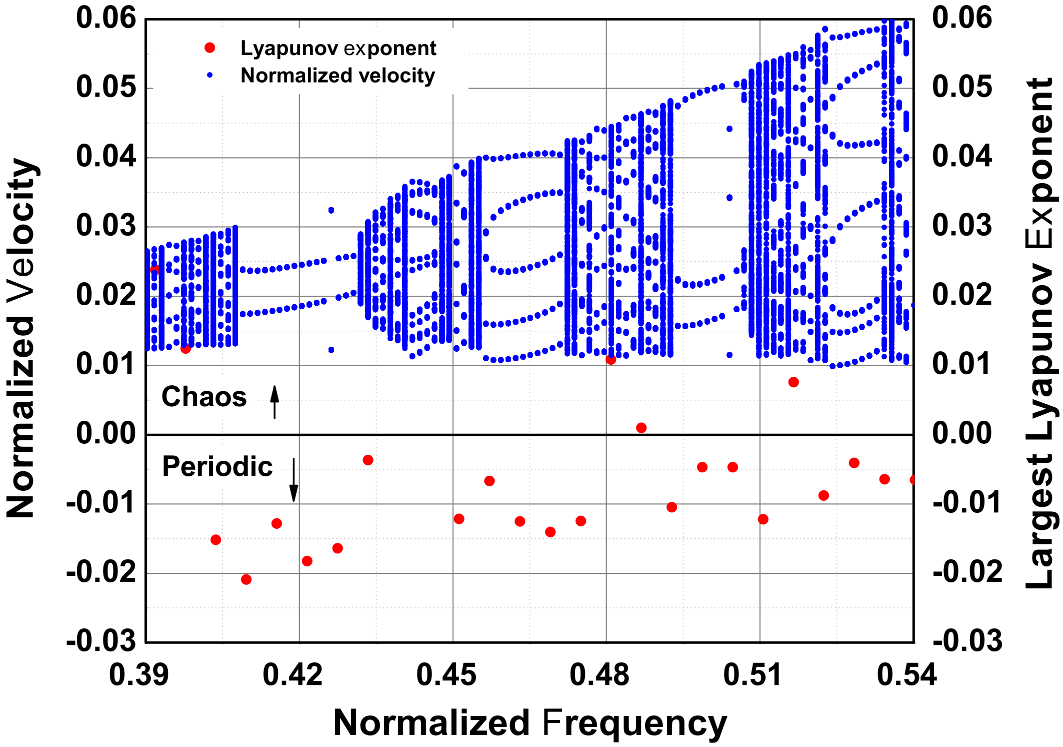

Fig. 53. Bifurcation diagram with Lyapunov exponents for the case of nonisothermal conditions.

CHAPTER IX

CONCLUSIONS AND FUTURE WORK

This work have discussed the use of shape memory alloys for vibration isolation and damping. This research effort was divided into two parts. The first part investigated the nonlinear dynamics of a SMA passive vibration isolation and damping (PVID) device, where the main elements are pseudoelastic SMA wires. Experimental vibration tests were conducted where the PVID device was subjected to a series of continuous acceleration functions in the form of sine sweep. Frequency responses and transmissibility of the device as well as temperature variations of the SMA wires are analyzed for the case where the SMA wires were pre-strained at 4.0% of their original length. The experimental results have shown that higher acceleration amplitudes result in higher additional hysteretic damping. The value of the transmissibility peak had a reduction of 23% when the acceleration amplitude increased from 1g to 2g, for the up sine sweep test. A further reduction of 37% in the value of the transmissibility peak occurred when the amplitude increased from 2g to 4g. Similarly, the transmissibility peak reduced approximately 10% when the acceleration amplitude increased from 1g to 2g in the down sine sweep test. It was also observed that the temperature of the SMA wires increased during the vibration tests. This increase in the temperature was caused by the stress-induced martensitic phase transformation that the wires underwent during the vibration tests. Higher acceleration amplitudes produced higher temperature variations, denoting a very strong thermomechanical coupling. The temperature of the SMA wires increased 48% for the acceleration amplitude of 1g of the up sine sweep test with respect to the environment temperature, which was surrounding the SMA. An increase of 96% in the temperature of the SMA wires was observed for an amplitude of 2g, and an increase of 112% for the amplitude of 4g, with respect to the environment temperature. For the down sine sweep tests, the temperature of the SMA wires increased 44% for the acceleration amplitude of 1g, and 108% with respect to the environment temperature for the amplitude of 2g.

Numerical simulations of a one-degree of freedom SMA oscillator have been conducted to corroborate the experimental results. The SMA oscillator had the same configuration of the PVID device, where a mass is balanced by two pre-strained pseudoelastic SMA elements. A rate-independent hysteretic constitutive model, originally proposed by Boyd and Lagoudas, was utilized to simulate the pseudoelastic behavior of the SMA material. The model was modified to consider the thermomechanical coupling caused by stress-induced martensitic phase transformations. The thermomechanical coupling induces the time-dependent behavior of the SMA due to latent heat production during phase transformations, and also due to the interaction of the SMA with the heat transfer medium that surrounds it. This time-dependent behavior can lead to the appearance of the transformation-induced stress relaxation phenomenon. Therefore, the heat transfer equation was incorporated into the constitutive model, where the case of heat convection was considered. The constitutive model was integrated using a modified version of closest point projection return mapping algorithm presented in Qidwai and Lagoudas [27]. Two different ways of integrating the constitutive model along with the heat equation were tested, where the same results were obtained. Numerical results showed that the modified constitutive model presented here, with the inclusion of the heat equation, was capable of predict all the nonlinearities observed on the dynamical tests of the SMA device, such as discontinuities (jumps) on the transmissibility curves, reduction of the transmissibility peak and the frequency of resonance with an increase of the amplitude of acceleration input. The modeling was also capable of capturing the large temperature variation of the wires next to the frequency of resonance caused by the effect of vibration.

The second part of this research effort investigated the occurrence of chaotic responses in a one-degree of freedom SMA oscillator, composed of a mass and a one-dimensional SMA element. A modified version of the constitutive model developed in the first part of this work was used to simulate the behavior of the SMA element. This new version of the constitutive model, which was also constructed under the same thermodynamic framework of Boyd and Lagoudas model, allowed smooth transitions between the austenitic and martensitic phases. Experimental thermomechanical and calorimetric results were compared with the model's prediction, where a very good agreement was observed.

The chaotic response of the SMA oscillator were evaluate through the analysis of phase space plots, Poincaré maps, and through the estimation of the Lyapunov exponents. The estimation of the Lyapunov exponents for the nonlinear hysteretic SMA system was done by adapting the classical algorithm by Wolf and co-workers. The main issue of using this algorithm for nonlinear, rate-independent, hysteretic systems is related to the procedure of linearization of the equations of motion. This work proposed a proper procedure to perform the linearization of the system, assuming an equivalent viscous damping, where the energy dissipation is related to the energy dissipated through the hysteresis loop. The proposed procedure was able to capture the dissipation characteristics of the hysteretic motion, allowing the adequate determination of the Lyapunov exponents. It was shown that periodic and chaotic responses can exist and also situations where a change in heat transfer conditions can dramatically alter the system dynamics.

There are several aspects in which this work could be extended. The first aspect of this work that could be extended is to consider different values of the mass of the SMA PVID device as well as different levels of pre-strain of the SMA wires. A parametric study could then be conducted in order to optimize the system's response according to some specific requirements, *e.g*, lower vibration isolation frequency. The second aspect that could be implemented is to excite the SMA PVID device with a single frequency sinusoidal function (dwell test), instead of a sine-sweep function, for selected values of frequency. These single-frequency excitation tests would help in the analysis of the nonlinear dynamics of the SMA device. The device could be excited by functions with frequency close to system's resonance, for example. Thus, the dynamic response of the system could be classified through the analysis of the acceleration time series. Moreover, the experimental results obtained from the single-frequency excitation tests could be compared with numerical results, where the values of frequency that the simulations predicted chaotic responses could be tested experimentally. Another aspect that could be considered is to test the SMA device with random excitation functions. The SMA could be used to not only attenuate undesirable vibrations of a structure from an earthquake event, for example, but also to restore the original configuration of the structure.

The constitutive model could also be extended to incorporate additional aspects of the SMA behavior, such as minor loops. The current version of the model does not properly consider minor hysteresis loops. Even though the model can simulate partial phase transformations, the model does not capture the rotation that minor hysteresis loop have with respect to the major loop. This is a point to consider, since the amount of energy dissipated by the SMA is related to the area of the hysteresis loop that has been utilized. Another point to be considered is to extend the capability of the model to simulate other forms of heat transfer conditions, such as heat conduction and radiation. These two additional forms of heat transfer are important to consider if the SMA is to be used in space applications, for example. Finally, the procedure to compute the Lyapunov exponents for a given dynamical system with known equations of motion could also be extended to estimate the Lyapunov exponents from an experimental time series. This procedure would be helpful to quantify the system response of the SMA device subjected to single-frequency excitations, for example, and investigate the possibility of chaotic responses.

REFERENCES

[1] D. C. Lagoudas, D. J. Hartl, P. Kumar, L. G. Machado, et al., Introduction to Modeling and Engineering Applications of Shape Memory Alloys, Springer, 2007, submitted.

[2] K. Otsuka, C. M. Wayman, Shape memory materials, Press Syndicate of the University of Cambridge, 1999.

[3] E. Patoor, D. C. Lagoudas, P. Entchev, L. C. Brinson, X. Gao, Shape memory alloys, part i: General properties and modeling of single crystals, Mechanics of Materials 38 (5–6) (2006) 391–429.

[4] G. Olson, M. Cohen, Stress assisted isothermal martensitic transformation: application to trip steels, Metallurgical and Material Transactions A 13 (1982) 1907–1914.

[5] K. Otsuka, X. Ren, Physical metallurgy of ti-ni-based shape memory alloys, Progress in Materials Science 50 (5) (2005) 511–678.

[6] D. Mandovani, Shape memory alloys: Properties and biomedical applications, JOM Journal of the Minerals, Metals and Materials Society 52 (10) (2000) 36–44.

[7] D. E. Hodgson, M. H. Wu, R. J. Biermann, Shape memory alloys, in: Metals Handbook, Vol. 2, ASM, 1990, pp. 897–902.

[8] W. Buehler, J. Gilfrich, R. Wiley, Effect of low-temperature phase changes on the mechanical properties of alloys near composition tini, Journal of Applied Physics 34 (5) (1963) 1475–1477.

[9] M. Wayman, J. Harrison, The origins of the shape memory effec, JOM Journal of the Minerals, Metals and Materials Society 41 (99) (1989) 26–28.

[10] L. G. Machado, M. A. Savi, Medical applications of shape memory alloys, Brazilian Journal of Medical and Biological Research 36 (683–691).

[11] Z. Nishiyama, Martensitic transformations, Academic Press, San Diego, 1978.

[12] L. Delay, Diffusionless transformations, Vol. 5 of Material Science and Technologies, VCH Publishers, New York, 1990, Ch. 6, pp. 339–404.

[13] J. Vos, E. Aernoudt, L. Delaey, The crystallography of the martensitic transformation of b. c. c. into 9 r: A generalized mathematical model, Zeitschrift fur Metallkunde 69 (7) (1978) 438–444.

[14] K. Otsuka, X. Ren, Recent developments in the research of shape memory alloys, Intermetallics 7 (5) (1999) 511–528.

[15] S. Wu, H. Lin, Recent development of tini-based shape memory alloys in taiwan, Material Chemistry and Physics 64 (2) (2000) 81–92.

[16] P. Popov, Constitutive modeling of shape memory alloys and upscaling of deformable porous media, Ph.D. thesis, Texas A & M University (May 2005).

[17] P. B. Entchev, Micromechanical modeling of porous shape memory alloys, Ph.D. thesis, Texas A & M University (May 2002).

[18] K. Tanaka, A thermomechanical sketch of shape memory effect: one-dimensional tensile behavior, Res Mechanica 18 (1986) 251–263.

[19] K. Tanaka, S. Kobayashi, Y. Sato, Thermomechanics of transformation pseudoelasticity and shape memory effect in alloys, International Journal of Plasticity 2 (1986) 59–72.

[20] C. Liang, C. A. Rogers, One-dimensional thermomechanical constitutive relations for shape memory materials, Journal of Intelligent Material Systems and Structures 1 (1990) 207–234.

[21] L. Brinson, One-dimensional constitutive behavior of shape memory alloys: thermo mechanical derivation with non-constant marterial functions, Journal of Intelligent Material Systems and Structures 1 (1990) 207–234.

[22] L. C. Brinson, One-dimensional constitutive behavior of shape memory alloys: thermomechanical derivation with non-constant material functions and redefined martensite internal variables, Journal of Intelligent Material Systems and Structures 4 (1993) 229–242.

[23] M. Berveille, E. Patoor, M. Buisson, Thermomechanical constitutive equations for shape memory alloys, Journal de Physique IV France 1 (C.4) (1991) 387.

[24] J. Boyd, D. C. Lagoudas, A thermodynamical constitutive model for shape memory materials. part i: the monolithic shape memory alloy, International Journal of Plasticity 12 (6) (1996) 805–842.

[25] D. C. Lagoudas, Z. Bo, M. A. Qidwai, A unified thermodynamic constitutive model for SMA and finite element analysis of active metal matrix composites, Mechanics of Composite Materials and Structures 3 (2) (1996) 153–179.

[26] P. Popov, D. C. Lagoudas, A 3-d constitutive model for shape memory alloys

incorporating pseudoelasticity and detwinning of self-accommodated martensite, International Journal of Plasticity 23 (10) (2007) 1679–1720.

[27] M. A. Qidwai, D. C. Lagoudas, Numerical implementation of a shape memory alloy thermomechanical constitutive model using return mapping algorithm, International Journal for Numerical Methods in Engineering 47 (2000) 1123–1168.

[28] F. Auricchio, E. Sacco, A temperature-dependet beam for shape-memory alloys: constitutive modeling, finite-element implementation and numerical simulations, Computer Methods in Applied Mechanics and Engineering 174 (1999) 171–190.

[29] S. Auricchio, E. Sacco, A one-dimensional model for superelastic shape-memory alloys with different elastic properties between austenite and martensite, International Journal of Non-Linear Mechanics 32 (6) (1997) 1101–1114.

[30] K. R. Rajagopal, A. R. Srinivasa, Mechanics of the inelastic behavior of materials. Part I: Theoretical underpinnings, International Journal of Plasticity 14 (10–11) (1998) 945–967.

[31] K. R. Rajagopal, A. R. Srinivasa, Mechanics of the inelastic behavior of materials. Part II: Inelastic response, International Journal of Plasticity 14 (10–11) (1998) 969–995.

[32] M. A. Savi, A. Paiva, A. P. Baeta-Neves, P. M. C. L. Pacheco, Phenomenological modeling and numerical simulation of shape memory alloys: A thermo-plastic-phase transformation coupled model, Journal of Intelligent Material Systems and Structures 13 (2002) 261–273.

[33] D. C. Lagoudas, P. B. Entchev, P. Popov, E. Patoor, L. C. Brinson, X. Gao,

Shape memory alloys - part ii: Modeling of polycrystals, Mechanics of Materials 38 (2006) 430–462.

[34] Q. P. Sun, K. C. Hwang, Micromechanics modelling for the constitutive behavior of polycrystalline shape memory alloys - i. derivation of general relations, Journal of the Mechanics and Physics of Solids 41 (1) (1993) 1–17.

[35] Q. P. Sun, K. C. Hwang, Micromechanics modelling for the constitutive behavior of polycrystalline shape memory alloys - ii. study of individual phenomena, Journal of the Mechanics and Physics of Solids 41 (1) (1993) 19–33.

[36] D. C. Lagoudas, A. Bhattacharrya, Modelling of thin layer extensional thermoelctric SMA actuators, International Journal of Solids and Structures 35 (3-4) (1998) 331–362.

[37] F. A. Nae, Y. Matsuzaki, T. Ikeda, Micromechanical modeling of polycrystalline shape-memory alloys including thermo-mechanical coupling, Smart Materials and Structures 12 (2003) 6–17.

[38] L. Anand, M. E. Gurtin, Thermal effects in the superelasticity of crystaline shape-memory materials, Journal of the Mechanics and Physics of Solids 51 (2003) 1015–1058.

[39] F. Falk, Model free energy, mechanics, and thermodynamics of shape memory alloys, Acta Metallurgica 28 (1980) 1773–1780.

[40] T. J. Lim, D. L. McDowell, Mechanical behavior of an Ni-Ti shape memory alloy under axial-torsional proportional and nonproportional loading, Journal of Engineering Materials and Technology 121 (1999) 9–18.

[41] P. H. Leo, T. W. Shield, O. P. Bruno, Transient heat transfer effects on the pseudoelastic behavior of shape-memory wires, Acta Metallurgica et Materialia 41 (8) (1993) 2477–2485.

[42] A. Bhattacharyya, D. C. Lagoudas, Y. Wang, V. K. Kinra, On the role of thermoelectric heat transfer in the design of SMA actuators: Theoretical modeling and experiment, International Journal of Solids and Structures 4 (1995) 252–263.

[43] H. Benzaoui, C. Lexcellent, N. Chaillet, B. Lang, A. Bourjault, Experimental study and modelling of a TiNi shape memory alloy wire actuator, Journal of Intelligent Material Systems and Structures 8 (1997) 619–629.

[44] S. Leclercq, C. Lexcellent, A general macroscopic description of the thermomechanical behavior of shape memory alloys, Journal of the Mechanics and Physics of Solids 4 (6) (1996) 953–980.

[45] R. Peyroux, A. Chrysochoos, C. Licht, M. Lobel, Thermomechanical coupling and pseudoelasticity of shape memory alloys, International Journal of Engineering Science 36 (4) (1998) 489–509.

[46] H. Prahlad, I. Chopra, Development of a strain-rate dependent model for uniaxial loading of SMA wires, Journal of Intelligent Material Systems and Structures 14 (2003) 429–442.

[47] R. Matsui, H. Tobushi, T. Ikawa, Transformation-induced creep and stress relaxation of tini shape memory alloy, Journal of Material: Design and Applications 218 (Part L) (2004) 343–353.

[48] T. J. Lim, D. L. McDowell, Cyclic thermomechanical behavior of a polycrystalline

pseudoelastic shape memory alloy, Journal of the Mechanics and Physics of Solids 50 (2002) 651–676.

[49] C. Lexcellent, Rejzner, Modeling of the strain rate effect, creep and relaxation of a Ni-Ti shape memory alloy under tension (compression)-torsional proportional loading in the pseudoelastic range, Smart Materials and Structures 9 (2000) 613–621.

[50] B. Raniecki, C. Lexcellent, Thermodynamics of isotropic pseudoelasticity in shape memory alloys, European Journal of Mechanics - A/Solids 17 (2) (1998) 185–205.

[51] X. . Balandraud, E. Ernst, E. Soos, Relaxation and creep phenomena in shape memory alloys.relaxation and creep phenomena in shape memory alloys. part ii: Stress relaxation and strain creep during phasetransformation, Zeitschrift fur Angewandte Mathematik und Physik 51 (2000) 419–448.

[52] X. Balandraud, E. Ernst, E. Soos, Relaxation and creep phenomena in shape memory alloys. part i: hysteresis loop and pseudoelastic behavior, Zeitschrift fur Angewandte Mathematik und Physik 51 (2000) 171–203.

[53] F. Auricchio, L. Petrini, A three-dimensional model describing stress-temperature induced solid phase transformations: stress-temperature induced solid phase transformations: thermomechanical coupling and hybrid composite applications, International Journal for Numerical Methods in Engineering 61 (2004) 716–737.

[54] K. Williams, G. Chiu, R. Bernhard, Adaptive-passive absorbers using shape-memory alloys, Journal of Sound and Vibration 249 (5) (2002) 835–848.

[55] Z. Salich, J. Hou, M. Noori, Vibration supression of structures using passive shape memory alloy energy dissipation devices, Journal of Intelligent Material Systems and Structures 12 (10) (2001) 671–680.

[56] S. Saadat, J. Salich, M. Noori, Z. Hou, H. Davoodi, I. Bar-on, Y. Suzuki, A. Masuda, An overview of vibration and seismic applications of NiTi shape memory alloy, Smart Materials and Structures 11 (2002) 218–229.

[57] D. C. Lagoudas, L. G. Machado, M. Lagoudas, Nonlinear vibration of a one-degree of freedom shape memory alloy oscillator: a numerical-experimental investigation, in: 46th AIAA/ ASME / ASCE / AHS / ASC Structures, Structural Dynamics and Materials Conference, Austin, TX. USA, 2005, pp. 1–18.

[58] L. G. Machado, D. C. Lagoudas, Nonlinear dynamics of a sma passive vibration damping device, in: Smart Structures and Materials 2006: Damping and Isolation, Vol. 6169, SPIE, 2006, p. 61690X.

[59] Z. C. Feng, D. Z. Li, Dynamics of a mechanical system with a shape memory alloy bar, International Journal of Intelligent Material Systems and Structure 7 (1996) 399–410.

[60] E. J. Graesser, F. A. Cozzarelli, Shape-memory alloys as new materials for aseismic isolation, Journal of Engineering Mechanics 117 (11) (1991) 2590–2608.

[61] M. A. Savi, A. M. B. Braga, Chaotic vibrations of an oscillator with shape memory, Journal of the Brazilian Society of Mechanical Sciences and Engineering XV (1) (1993) 1–20.

[62] M. A. Savi, P. M. C. L. Pacheco, Chaos and hyperchaos in shape memory systems, International Journal of Bifurcations and Chaos 12 (3) (2002) 645–657.

[63] L. G. Machado, M. A. Savi, P. M. C. L. Pacheco, Bifurcations and crises in a shape memory oscillator, Shock and Vibration 11 (2004) 67–80.

[64] L. G. Machado, M. A. Savi, P. M. C. L. Pacheco, Nonlinear dynamics and chaos in coupled shape memory oscillators, International Journal of Solids and Structures 40 (2003) 5139–5156.

[65] A. Wolf, J. B. Swift, H. L. Swinney, J. A. Vastano, Determining lyapunov exponents from a times series, Physica D 16 (1985) 285–317.

[66] M. A. Savi, M. A. N. Sa, A. Paiva, P. M. C. L. Pacheco, Tensile-compressive asymmetry influence on shape memory alloy systems, Chaos, Solitons and FractalsIn press.

[67] A. Paiva, M. A. Savi, A. M. B. Braga, P. M. C. L. Pacheco, A constitutive model for shape memory alloys considering tensile-compressive asymmetry and plasticity, International Journal of Solids and Structures 42 (11–12) (2005) 3439–3457.

[68] W. Lacarbonara, D. Bernardini, F. Vestroni, Nonlinear thermomechanical oscillation of shape-memory devices, International Journal of Solids and Structures 41 (2004) 1209–1234.

[69] I. Ivshin, T. J. Pence, A thermodynamical model for one-variant shape memory alloy material, Journal of Intelligent Material Systems and Structures 5 (1994) 455–473.

[70] D. Bernardini, G. Rega, Thermoemchanical modelling, nonlinear dynamics and chaos in shape memory oscillators, Mathermatical and Computer Modelling of Dynamical Systems 11 (3) (2005) 291–314.

[71] M. M. Khan, D. C. Lagoudas, J. J. Mayes, B. K. Henderson, Pseudoelastic SMA spring elements for passive vibration isolation. part i: Modeling, Journal of Intelligent Material Systems and Structures 15 (6) (2004) 415–441.

[72] D. C. Lagoudas, M. M. Khan, J. J. Mayes, B. K. Henderson, Pseudoelastic SMA spring elements for passive vibration isolation. part ii: Simulations and experimental correlation, Journal of Intelligent Material Systems and Structures 15 (6) (2004) 443–470.

[73] L. G. Machado, D. C. Lagoudas, Dynamical response of shape memory alloys, in: 2004 ASME International Mechanical Engineering Congress, Anaheim, CA. USA., 2004, pp. 13–19.

[74] W. M. Lai, D. Rubin, E. Krempl, Introduction to Continuum Mechanics, 3rd Edition, Butterworth-Heinemann, Woburn, MA, 1993.

[75] M. E. Gurtin, An Introduction to Continuum Mechanics, Vol. 158 of Mathematics in Science and Engineering, Academic Press, San Diego, 1981.

[76] L. E. Malvern, Introduction to the mechanics of a continuous medium, Prentice Hall, 1969.

[77] W. S. Slaughter, The Linearized Theory of Elasticity, Birkhäuser, Boston, 2002.

[78] B. Coleman, M. Gurtin, Thermodynamics with internal variables, The Journal of Chemical Physics 47 (2) (1967) 597–613.

[79] M. A. Qidwai, D. C. Lagoudas, On thermomechanics and transformation surfaces of polycrystalline NiTi shape memory alloy material, International Journal of Plasticity 16 (2000) 1309–1343.

[80] A. S. Khan, S. Huang, Continuum Theory of Plasticity, John Wiley & Sons, New York, 1995.

[81] J. C. Simo, T. J. R. Hughes, Computational Inelasticity, Vol. 7 of Interdisciplinary Applied Mathematics, Springer-Verlag, New York, 1998.

[82] M. Ortiz, E. Popov, Accuracy and stability of integration algorithms for elastoplastic constitutive relations, International Journal of Non-Linear Mechanics 21 (1985) 1561–1576.

[83] M. Ortiz, J. Simo, An analysis of a new class of integration algorithms for elastoplastic constitutive relations, International Journal of Non-Linear Mechanics 23 (353–366).

[84] J. C. Simo, T. J. R. Hughes, Computational Inelasticity, Springer-Verlag New York, Inc., 1997.

[85] J. A. Shaw, S. Kyriakides, Thermomechanical aspects of NiTi, Journal of the Mechanics and Physics of Solids 43 (8) (1995) 1243–1281.

[86] A. D. Dimarogonas, S. Haddad, Vibration for engineers, Prentice-Hall, Inc., 1992.

[87] K. Bathe, Finite element procedures, Englewood Cliffs, NJ: Prentice Hall, 1996.

[88] J. N. Reddy, An introduction to the finite element method, McGraw-Hill Singapore, 1993.

[89] B. Kiefer, H. E. Karaca, D. C. Lagoudas, I. Karaman, Characterization and modeling of the magnetic field-induced strain and work output in Ni2MnGa magnetic shape memory alloys, Journal of Magnetism and Magnetic Materials 312 (1) (2007) 164–175.

[90] A. Nayfeh, B. Balachandran, Applied nonlinear dynamics:analytical, computational, and experimental methods., John Wiley and Sons, Inc., 1995.

[91] L. G. Machado, P. A. Popov, D. C. Lagoudas, Constitutive model for polycrystalline shape memory alloys with smooth transformation hardening, International Journal of Engineering ScienceSubmitted.

[92] M. Ortiz, P. M. Pinsky, R. Taylor, Operator split methods for the numerical solution of the elastoplastic dynamic problem, Computer Methods in Applied Mechanics and Engineering 39 (1983) 137–157.

[93] M. A. Savi, Dinâmica N ao-Linear e Caos, Editora E-papers, 2006.

[94] D. J. Inman, Engineering Vibration, Prentice Hall, 1994.

VITA

Luciano G. Machado was born in Salvador-BA, Brazil. He enrolled at the Federal Center of Technological Education (CEFET) of Rio de Janeiro in 1995 and earned a Bachelor of Science degree in Mechanical Engineering in 2000. After completing his B.S. degree he entered graduate school at the Military Institute of Engineering (IME) earning a Master of Science degree in Mechanical Engineering in 2002, under the guidance of Dr. Marcelo Savi.

In the fall of 2002, Luciano Machado began his doctoral studies in the Aerospace Engineering Department at Texas A&M University under the guidance of Dr. Lagoudas. His research interests include continuum mechanics, computational mechanics, nonlinear dynamics and chaos of mechanical systems, modeling of shape memory alloys (SMAs) and nonlinear vibration of SMAs systems. A current curriculum vitae containing detailed lists of his publications is available by contacting Luciano Machado via email at machado.lucianog@gmail.com. He can be reached at the following permanent address: Rua Conde de Bonfim, 604 apt. 405, Tijuca, Rio de Janeiro, R.J - ZIP: 20520-055. Brazil.